REVIEW

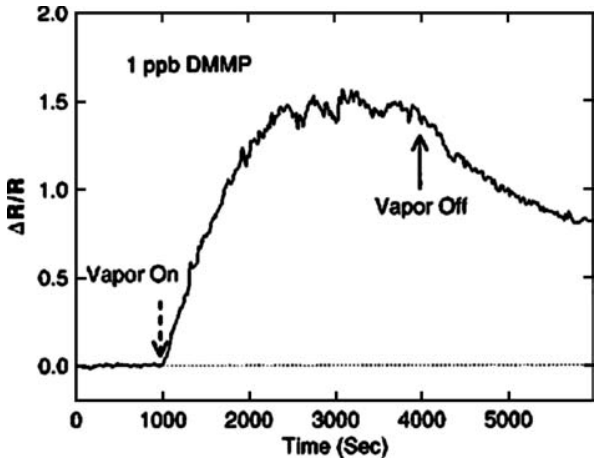

Fig. 45. Relative change in resistance versus time for a chemiresistive flow-cell exposed to a 1 ppb concentration of DMMP. Reprinted with permission from [70], J. P. Novak et al., *Appl. Phys. Lett.* 83, 4026 **(2003)**. © 2003, American Institute of Physics.

served as a back gate while two electrodes were working as drain and source. Moreover, one designed chemiresistor flow cells, in which the inner surface of a quartz tube served as a background for *in situ* growth (over and iron catalyst) of CNTs. The ends of the SWCNTs were then metallised to create electric contacts for end-to-end resistance measurements (Fig. 45). The deposited network of CNTs behaved like *p*-type semiconductor. According to the authors, the application of the SWCNTs-network made the sensors more stable than the devices employing single CNTs. The adsorption of DMMP (a strong electron donor) on the *p*-semiconductor CNTs resulted in a substantial increase of their electric resistance. It was attributed to the donor interaction of a DMMP molecule on the majority current carries in SWCNTs i.e., the capture of holes was expected due to the transfer of a negative charge from adsrobate to CNTs. It was also discovered that setting of a positive potential at the back gate (Si-background) was necessary to offset the negative charge induced in CNTs by the bonded DMMP molecules. The interaction between the negative charge on the phosphate oxygen atoms (in DMMP) and CNTs helps to explain the observed electric effects. The positive bias at the gate electrode was very helpful for the recovery of the starting resistance of the CNTs-based transistor. Simple recovery attempts by the exposure to pure air were not successful since the removal of residual DMMP molecules lasted for hours, however positive bias at the back gate shortened the recovery process. The sensors exhibited no response to some contaminants, such as vapours of water and hexane. Novak and co-workers presented another spectacular effect achieved by the application of a strong hydrogen-bonding polymer as pre-filter which differentiated the response of sensor to specific substances.

Cui and co-workers[71] reported a side wall osmylation of SWCNTs, i.e., immobilisation of an osmium tetraoxide

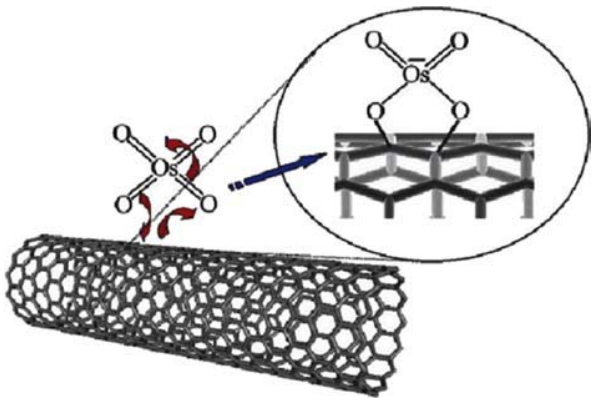

Fig. 46. Reaction scheme illustrating the cycloaddition of osmium tetroxide (OsO_4) to the sidewall of a Single-Walled Carbon Nanotube (SWCNT) leading to an osmyl ester of a 5-membered ring structure. Arrows indicate the flow of electrons during bond formation. Reprinted with permission from [71], J. Cui et al., *Nano Lett.* 3, 613 **(2003)**. © 2003, American Chemical Society.

on the tubes. The reaction was performed by cycloaddition of OsO_4 to double bonds in the rolled graphene sheets as presented in Figure 46. The sidewall functionalization of SWCNTs was achieved in the gas phase in the presence of oxygen. UV irradiation was necessary to initiate the reaction. The osmylation decreased the conductance of the SWCNTs by several orders of magnitude. The process of osmylation was found to be a reversible phenomenon, in which the simultaneous action of three factors caused the effect of enhanced sensitivity. That were: The presence of OsO_4, the presence of O_2 and UV irradiation (Fig. 47). When the action of one of them was terminated the process of osmylation was frozen (the lack of UV) or reversed (no contact with OsO_4). No reaction with O_2 was noticed

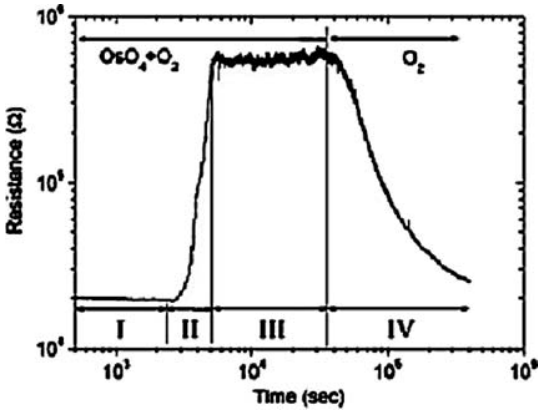

Fig. 47. Two-terminal resistance of the metallic SWCNT measured *in situ* for different gas-phase compositions. Regions I and II correspond to the tube in the $OsO_4 + O_2$ atmosphere without and with UV light irradiation (254 nm), respectively. Within region III, no UV light was used. After the removal of OsO_4, the sample was again irradiated with UV light, this time in a pure O_2 atmosphere (region IV). Reprinted with permission from [71], J. Cui et al., *Nano Lett.* 3, 613 **(2003)**. © 2003, American Chemical Society.

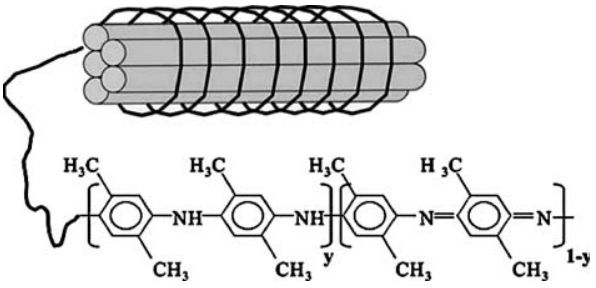

Fig. 48. Schematic of PDMA conducting polymer wrapped up around MWCNTs. Reprinted with permission from [72], V. Bavastrello et al., *Sens. Actuators B* 98, 247 **(2004)**. © 2004, Elsevier.

even if the treated sample was under UV irradiation. The experiment showed that some sidewall functionalisations could be reversible and might be employed for chemical sensing as in the case of volatile metal oxide (OsO_4).

Another non-conventional CNTs- based sensor was presented by Bavastrello et al.[72] They synthesized a nanocomposite consisting of poly(2,5-dimethylaniline) and MWCNTs. The authors suggested an interaction between the component that was characteristic because of chains of the conducting polymer (PDMA) wrapped around packages of aligned MWCNTs as it is depicted in Figure 48. The material was obtained in a multi-step procedure and was sensitive to the presence of acidic vapour like HCl. The adsorption of HCl strongly influenced the equilibrium between the doped and undoped form of the polymer. The doping-undoping transition affected electric conductivity of the investigated nanocomposite. In this study, the polymer was recognized to fulfill two roles: adsorption of the detected acidic vapours, and change its electrical properties upon adsorption of HCl.

2.2. Carbon Nanotubes as Sensitive Electrode Material

Carbon nanotubes have been investigated as a material for the construction of selective electrodes. Electrodes interact not only with the molecules of detected substances but can react with the solvent (in most cases water) particularly at high or low pH. Therefore electrode manufacturing that ensures long-term stability in liquid solutions is challenging task. The following section is focused on the preparation of carbon-based electrodes with particular emphasis on applications. Generally, carbon based electrodes can be fabricated in one of the following basic forms:

(1) A complex system consisting of a conductive background covered by a sensing carbon layer by means of a chemical glue or hardening agent.

(2) A complex system consisting of a conductive foundation being in contact with a powder of carbon materials (active carbon, carbon black, carbon nanotubes, graphite etc.).

(3) Monolithic carbon electrodes prepared in form of a rod or film where no separate carbon-based layer exists.

(4) Soft or solid carbon electrode consisting of small carbon particles assembled by means of an inert media (oil, polymer etc.).

Thus, in some electrodes one can expect two phases: a passive part that is responsible for charge transfer (carbon-based conductor, metal or conducting polymer) and an active carbon phase that is responsible for the electrode processes. Despite the role ascribed to carbon materials, all such electrodes are usually called carbon-electrodes with a little regard if the carbon component is passive or active.

Carbon in any of the mentioned forms can be applied as-prepared or in a chemically modified form, i.e., by means of some additional chemical treatments like oxidation, reduction, metallization, deposition of chemically active substances (or mixing with). In addition, the form of the active carbon phase can be very different and one may use active carbon, carbon black, graphite, fullerenes, or carbon nanotubes. Writing a complete survey on the application of carbon-based electrodes for chemical sensing seems to be quite a complicated matter due to the variety of possible electrode constructions, chemical treatments, and forms of carbon. Therefore, we present only selected problems with respect to electrode design and application.

Generally, CNT-containing electrodes may utilize them in form of a loose powder or as a solid deposit where single tubes are constrained by means of an inert substance. Gavalas et al.[73] immobilized MWCNTs (obtained by decomposition of methane over a dispersed iron catalyst) using the sol–gel method. Since the conventional sol–gel pathways like hydrolysis of a silane precursor require extreme pH conditions, Gavalas et al.[73] elaborated a modified method to avoid undesired reactions of CNTs in alkaline solution. The method relied on the application of sodium silicate solution (of strong base reaction) but it was stepwise neutralized by an acidic ion-exchange resin, HCl solution, and finally stabilized by a phosphate buffer containing a biologically active substance, the enzyme L-Aminoacid Oxidase (L-AAOx). At this stage, MWCNTs were added and the whole mixture was left until gelation. The resulting homogenous CNTs-based composites were packed into a Teflon tube affixed with a metal contact. Such fabricated electrodes were tested for the determination of the concentration of an amino acid (L-Phenylalanine). The overall electrode reaction was expressed by: L-Amino-Acid $+ H_2O + O_2 \rightarrow$ (L-AAOx) 2-Oxo-Acid $+ NH_3 + H_2O_2$. The H_2O_2 molecules underwent electrocatalytic oxidation on the MWCNTs yielding current when the sensing electrode was included into an amperometric experimental set-up and the potential of $+800$ mV versus Ag/AgCl electrode. Thus, one ascribed an active role to CNTs assuming their catalytic activity in

oxidation of hydrogen peroxide. Moreover, CNTs incorporated in the composite were responsible for current conduction within the electrode what was summarized in the expression "CNTs facilitated fast electron transfer."

Another approach to CNT-immobilisation was elaborated by Sotiropoulu et al.,[74] who worked on novel carbon materials for the construction of amperometric sensors for glucose detection. The background idea for the reported study was the combination of positive features of fullerenes and porous glassy carbon. Glassy carbon is a good candidate for electrode fabrication since it is mechanically stable, chemically resistant, effective current conductor. Fullerenes and CNTs offer unique electric and catalytic properties (frequently investigated and understood in part only) that have been utilized for the fabrication of chemically sensitive materials. Both materials i.e., porous glassy carbon and fullerenes are able to accommodate biologically active substances like proteins (particularly enzymes). The authors reported that the application of porous glassy carbon electrode loaded with fullerenes and glucose oxidase resulted in an enhanced electrode performance. Glucose detection in solution and oxidation of hydrogen peroxide were the test reactions to evaluate the performance of the electrodes. One attributed the immobilization of the enzyme to the properties of glassy carbon particularly to the presence of mezopores and to the presence of oxygen-containing surface functional groups. The sensitivity of the electrodes to the detection of dissolved glucose increased with the fullerene amount packed in the glassy carbon background.

Two basic factors rule the process of organic molecule immobilisation on carbons, geometrical (pore structure), and chemical (surface functionalization). The presence of micropores and mezopores means the existence of spaces on the carbon surface where the adsorption potential is high since the attraction forces cumulate inside the pores. The non-specific adsorption forces resulting from the curvature of the solid surface can be supported by specific interaction resulting from the existence of surface functional groups (also in the pores). Thus, the groups of various chemical compositions (containing oxygen, nitrogen, hydrogen, sulphur, etc.,) contribute significantly to the complex adsorption forces. Contrary to other porous materials, pores in carbon are slit-like ones what ease the adsorption of large molecules of organic substances. Moreover, all carbons are good electric current conductors and can work as an excellent mediator for processes involving charge transfer. The carbon matrix transmits electrical signals like electron capture (or release) to the encapsulated molecules (like enzymes) what would by extremely difficult in the case of insulating matrices.

Using water-based solutions of PTFE and MWCNTs Weinecke et al.[75] fabricated membrane-electrodes exhibiting an increased electrode sensitivity for gas sensor application. The composite electrode material was prepared by

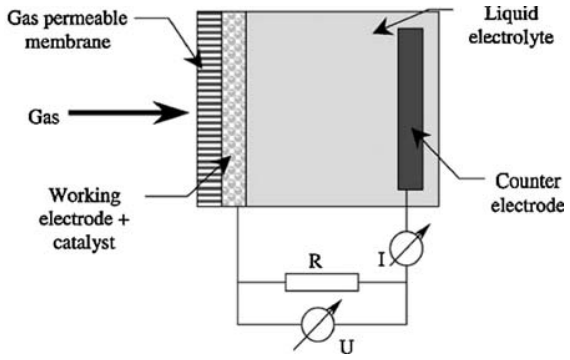

Fig. 49. Schematic presentation of an amperometric gas sensor with two electrodes. Reprinted with permission from [75], M. Wienecke et al., *Synth. Met.* 138, 165 **(2003)**. © 2003, Elsevier.

mixing water-based PTFE solution with MWCNTs aiming at the target CNTs concentration from 0.5 to 10% wt. The mixture was filtrated through a PTFE membrane and the whole material was sintered for 15 minutes at 150–300 °C. Metal particles were deposited by immersing of CNTs containing membranes in a solution of $AgNO_3$ and $SnCl_2$. Sintering and the presence of CNTs with metal particles provided low electrical resistance of the whole electrode. The membrane was in contact with gas and with liquid electrolyte in which a counter electrode was immersed. One could measure the current intensity and its changes versus the concentration of traced gas being in contact with the membrane-electrode (Fig. 49). The PTFE matrix was responsible for gas molecule separation, while the CNTs and metal particles ensured electrode conductivity and acted as an active catalyst. The membrane-electrode geometry helped to upgrade sensitivity from ppm to ppb level.

Male et al.[76] describe an electrode consisting of a glassy carbon conducting support covered by SWCNTs on which Cu particles were present (Fig. 50). The metal particles were deposited via the chemical reduction of cupper dodecyl sulphate ($Cu(DS)_2$). The cyclic voltammetry and TEM images confirmed that Cu particles were in contact with the glassy carbon background through SWCNTs. The electrodes were examined for the determination of glucose concentration in water up to 250 μM. The electrodes worked in an amperometric mode (+0.65 V put on the sensing electrode versus Ag/AgCl reference) and exhibited four-fold increase in the sensitivity when compared to a bare Cu disk electrode. One assumed a synergistic effect in the Cu-SWCNTs system that resulted in an enhanced sensitivity of the electrodes. Authors claimed that the reproducibility within a series of electrodes consisting of 30 elements was 5.7% at 100 μM glucose concentration. Additionally, some experiments were performed using monosacharides like galactose, arabinose, xylose, fructose, and mannose (similar current response as for glucose) and disaccharides maltose, lactose, sucrose, trehalose (reduced current response than for monosacharides). The presence of SWCNTs in the composite sensing layer improved

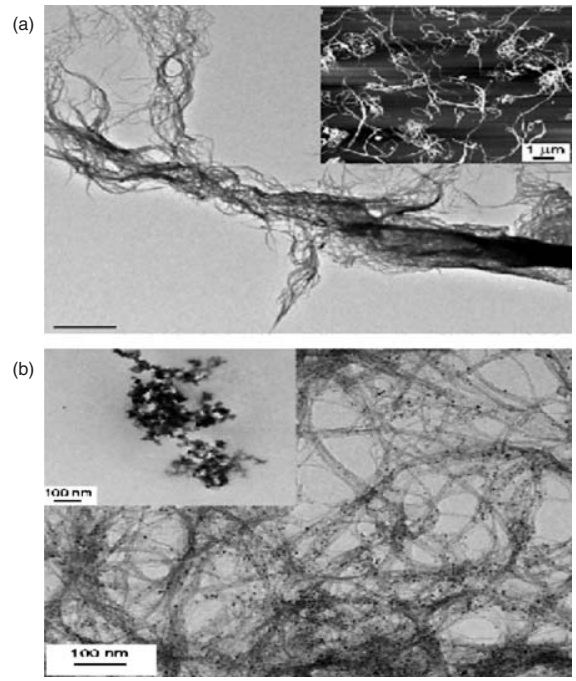

Fig. 50. (a) TEM micrograph of untreated SWCNTs dissolved in 0.5% Nafion, inset: AFM tapping-mode height image (size: 10 μm × 10 μm, data scale: 100 nm) of SWCNTs. (b) TEM micrograph of SWCNT in the presence of Cu nanoparticles, inset: TEM micrograph of Cu nanoparticles in the presence of Nafion. Reprinted with permission from [76], K. B. Male et al., *Anal. Chim. Acta* 516, 35 **(2004)**. © 2004, Elsevier.

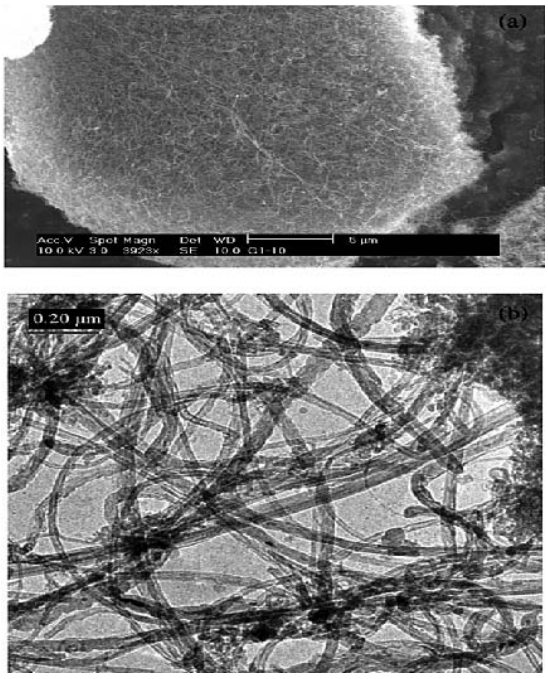

Fig. 51. STM (a) and TEM (b) images of carbon nanotubes used to fabricate the CNTPME. Reprinted with permission from [78], Y. D. Zhao et al., *Micromech. J.* 75, 189 **(2003)**. © 2003, Elsevier.

the selectivity of such electrodes to glucose when some test were performed to find out the influence of selected electroactive interferents (typical blood components like uric acid, ascorbic acid, acetaminophen) on the electrode performance.

Wu et al.[77] examined another way of fabrication of a CNTs-containing electrode, which later was tested as an amperometric sensor for indole-3-acetic acid (IAA), that is a substance known to regulate some basic biological processes like division, elongation, and differentiation of cell. MWCNTs were stuck on a glassy carbon background by means of hydrophobic surfactant dihexadecyl hydrogen phosphate (DHP) that was added to water dispersion of CNTs. After water evaporation the hydrophobic surfactant physically bonded a layer of randomly oriented CNTs to the surface of glassy carbon. The electrode with the CNTs layer was stable and its response to a fixed concentration of IAA was reproducible even after 36 measurements. The electrode resisted cyclic voltammetry tests at pH = 2. The presence of the MWCNTs layer significantly enhanced the current corresponding to oxidation of IAA compared to the behaviour of a bare glassy carbon electrode. The sensor found an application to the determination of IAA in plant leaves and the results were comparable with the results obtained by HPLC. From the experimental section of the paper one may assume that MWCNTs (synthesized by a catalytic pyrolysis) were cut, decapitated, and partially oxidized by HNO_3 treatment lasting for 10 hours.

Zhao et al.[78] applied CNTs as a sensing material for fabrication of sensing electrodes. The CNTs were not immobilised and were utilized as a powder for the electrooxidation and electroreduction of nitrite. The CNTs were prepared by catalytic chemical vapour decomposition of methane over Co/MgO catalyst. Such obtained CNTs were placed in a cavity first etched in a Pt microelectrode (Fig. 51). The sensing electrode was a part of a standard three-electrode cell (CNTs/Pt–Pt-Ag/AgCl). The test reactions were electro-oxidation and electro-reduction of nitrite that were found to be either 2-electron oxidation: $HNO_2 + H_2O \rightarrow NO_3^- + 3H^+ + 2e$ or 1-electron reduction. Reduction of nitrite was selected to detect its concentration since that helped to avoid the interference of other ions at high oxidation potential (above +0.7 V). One observed the change of limiting current and noticed short response times (ca. 10 s) when +0.3 V potential was established on the sensing electrode. The logarithm of limiting current (nitrite reduction on CNTs) was linearly growing with the growth of logarithm of the nitrite concentration in solution with the detection limit of 8 μM. The study demonstrated the catalytic properties of CNTs and an easy way how to fabricate a sensitive electrode without any binder.

He et al.[79] also investigated MWCNTs for the fabrication of a powder microelectrode. A Pt disk electrode was applied to ensure a good electric contact with the powder of MWCNTs (catalytic decomposition of methane over Ni/Mg catalyst). In this study, MWCNTs were subjected to

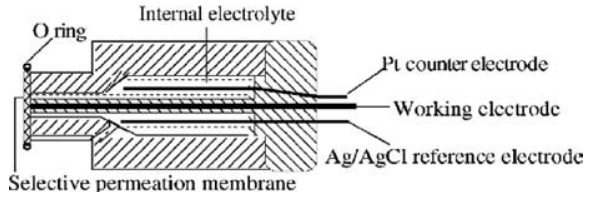

Fig. 52. Scheme of the CO gas sensor. Reprinted with permission from [79], J. B. He et al., *Sens. Actuators B* 99, 1 **(2004)**. © 2004, Elsevier.

a chemical pre-treatment consisting of backing at 550 °C (30 minutes) and a subsequent action of concentrated solutions of $HClO_4$ and HNO_3. In this way, the CNTs were purified, open at the ends and oxidized. The investigated CO gas sensor was a construction resembling the standard Clark electrode (Fig. 52). MWCNTs were stuck on a Pt rod in a small cavity. Additionally, the sensitive material was separated from the solution by a selective permeation membrane made of poly(ethylene). The response of the electrode was investigated towards CO concentration at constant potential of +0.7 V versus the Ag/AgCl reference electrode. The linear relationship of current versus the concentration of CO (in N_2 stream) was found for the range from 0.6 to 52 μg/ml. Comparative studies with the application of a bare Pt electrode confirmed the leading role of MWCNTs in oxidation of CO to CO_2. Overvoltage decreased for MWCNTs since some active oxygen containing species like $-OH_{ads}$ were easily generated and bonded to the surface of the tubes. The novel solution presented in this study consisted in the application of a selective membrane to solve the problem of selectivity.

Liu and Hu[80] constructed an electrochemical sensor for the detection of NO_2^- by means of MWCNTs encapsulated in a cavity that was etched at the tip of Pt disk. This concept, i.e., a direct utilization of CNTs powder placed on a Pt support, is similar to that it the previously mentioned studies however the MWCNTs were oxidised *in situ* by anodic polarization of the sensing electrode (+1.4 V vs. SCE) for 80 minutes in 0.05 M H_2SO_4. Assuming the behaviour of CNTs to be similar to glassy carbon, Liu, and Hu expected to create quinone type functionalities on the surface of the tubes. Anodically oxidized MWCNTs were shorter than before the treatment (proven by TEM investigations), and probably open at the ends since the energy needed to decapitate the tubes was lower than that one necessary for cutting. The oxidized MWCNTs were soaked in 5 mM $Os(bpy)_3^{+2}$ to adsorb these ions and modify the catalytic properties of the tubes towards the reduction of NO_2^-. They discovered that the adsorption of $Os(bpy)_3^{+2}$ catalyst on non-oxidized CNTs was weak and the osmium catalyst was easy to leach in water. The adsorption of the ions after anodic oxidation was more durable. The careful analysis of the $Os(bpy)_3^{+2}$ reduction peak led to the conclusion that the $Os(bpy)_3^{+2}$/MWCNT ratio is close to 1 suggesting that the ions were adsorbed at the open ends of the tubes.

The synthesis of CNTs created new opportunities for the construction of biosensors for the detection of biologically active molecules like DNA or proteins. The application of bare CNTs, however successful as presented above, is not the only possibility. A step ahead can be done provided one subjects CNTs to chemical manipulations. The detection of DNA is often based on the known ability of pairing interaction. The process of pairing of DNA chains is highly selective. Some attempts have been made towards the immobilization of single DNA molecules on various backgrounds. He and Dai[81] proposed a novel method of DNA immobilization on aligned SWCNTs. The problem of DNA attachment is not simple since the use of aligned CNTs in many chemical manipulations led to the destruction of the parallel alignment of the tubes. The novel method proposed by He and Dai[80] consisted of the synthesis of aligned SWCNTs on a gold support (thermal decomposition of iron (II) phthalocyanine) by acetic acid plasma treatment. In this way the CNTs preserved their alignment and underwent carboxylic functionalization at the ends in the same time. That step was followed by grafting single-strand DNA due to amide formation between −COOH groups and amino group at the 5′-phosphate end in the presence of [1-(3-dimethylaminopropyl)-3-ethylcarbodiimide hydrochloride] as it is depicted in Figure 53. Complementary DNA (cDNA) marked with ferrocenecarboxalehyde was used as for hybridization with the immobilized DNA stands. Thus, double strand DNA helices were formed on the aligned carbon nanotube electrode. The DNA helices grew not only at the ends of CNTs but also at the walls. Cyclic voltammetry studies let to observe a long-range electron

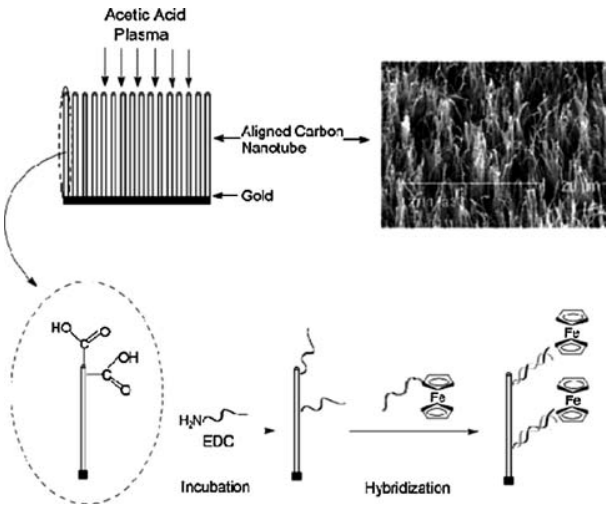

Fig. 53. A schematic illustration of the aligned nanotube–DNA electrochemical sensor. The upper right SEM image shows the aligned carbon nanotubes after having been transferred onto a gold foil. For reasons of clarity, only one of the many carboxyl groups is shown at the nanotube tip and wall, respectively. Reprinted with permission from [81], P. He and L. Dai, *Chem. Commun.* 3, 348 **(2004)**. © 2004, Royal Society of Chemistry.

transfer from the ferrocene marked DNA to the CNTs-electrode via the DNA duplex. Additionally, a strong oxidation peak of ferrocene was observed at the potential +0.29 V. Side effects like non-specific DNA paring and physical adsorption of marked DNA chains on CNTs-electrode could be neglected.

Ye and co-workers[82] proposed another analytically important functionalization of CNTs-based electrodes aiming at the fabrication of electrodes sensitive to dissolved oxygen. They assumed that hemin (iron (III) protoporphyrin) being a centre of heme-proteins like hemoglobin could act as an effective catalyst for dioxygen and hydrogen peroxide reduction. One may add that hemoglobin molecule contains a structure resembling hemin molecule. The central iron atom is capable (in hemoglobin) of reversible adsorption of molecular oxygen and CO_2. The important difference between the two substances consists in the oxidation state of iron, which is (III) in hemin and (II) in hemoglobin. The method of MWCNTs synthesis (pyrolysis of organic substances) provided that the tubes with diameter of 80–120 nm were long (ca. 10 μm) and well aligned (Fig. 54). One applied Ta plate covered with a thin layer of Co particles, with diameters ranging from 8 to 50 nm. The metal support with grown MWCNTs was stuck by means of Ag paste on the tip of a glassy carbon rod that was separated from the solution by a Teflon coating.

The hemin-fuctionalization consisted in the immersing of a bare MWCNTs-electrode in the hemin solution

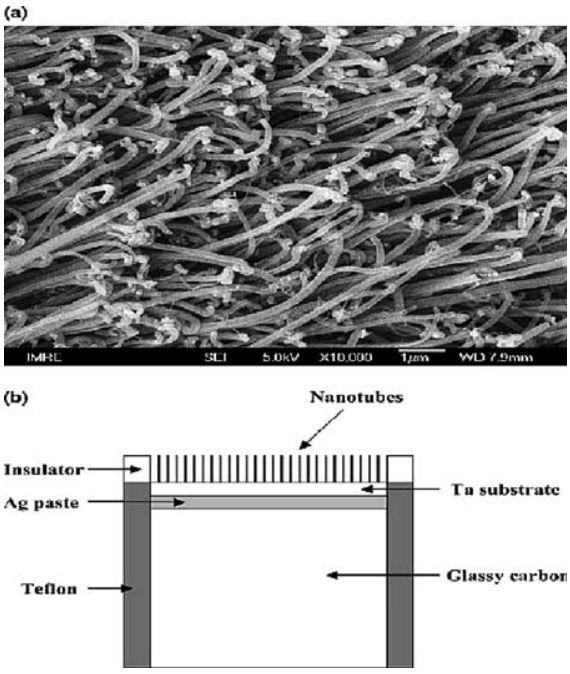

Fig. 54. (a) Scanning electron microscopy (SEM) images of the well-aligned MWCNTs. (b) Schematic of details showing the cross section of the MWCNT electrode. Reprinted with permission from [82], J. S. Ye et al., *J. Electroanal. Chem.* 562, 241 **(2004)**. © 2004, Elsevier.

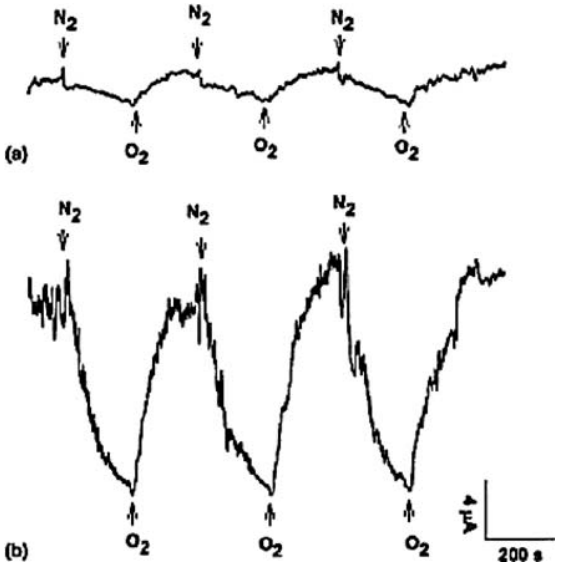

Fig. 55. Amperometric response of oxygen reduction in pH 7.4 PBS to the bubbling of N_2 or O_2 gas at either (a) the MWCNT electrode or (b) the hemin-modified MWCNT electrode. Applied potential: 0 V. Reprinted with permission from [82], J. S. Ye et al., *J. Electroanal. Chem.* 562, 241 **(2004)**. © 2004, Elsevier.

in 0.03 M KOH. Authors suggested that the performed functionalization was non-covalent and proceeded due to π-π interactions in the hemin—MWCNTs system. As-grown and hemin-modified MWCNTs electrodes were subjected to the influence of oxygen dissolved in a phosphate buffer (pH = 7.4). Hemin-modified MWCNTs electrodes gave three peaks corresponding to the reduction of O_2 at −0.087, −0.182, and −0.290 V versus Ag/AgCl (3 M KCl) reference electrode. The recorded reductive current was 4 times higher than for electrodes without hemin (Fig. 55). The influence of oxygen concentration on the electrode current was tested in a phosphate buffer solution when the hemin-modified and non-modified amperometric sensors were exposed to the bubbling N_2 and O_2. One observed a reversible increase of reducing current (at 0 potential) upon switching to pure oxygen. The recorded increase of current for the hemin-modified electrode was sevenfold greater than for the non-modified electrode.

2.3. Mass-Sensitive Devices Incorporating CNTS

Mass sensitive devices can be also constructed employing CNTs. Their operation requires only the adsorption of detected species and charge transfer is not necessary for sensor operation. The signal generated by the mass sensitive devices (a shift of resonant frequency) is usually caused by extremely small amounts of adsorbed species.

Ono et al.[83] reported the construction of a mass sensitive device for H_2 detection in air, which was designed by employing CNTs as sensitive material. CNTs are an attractive candidate for sensing materials because of known

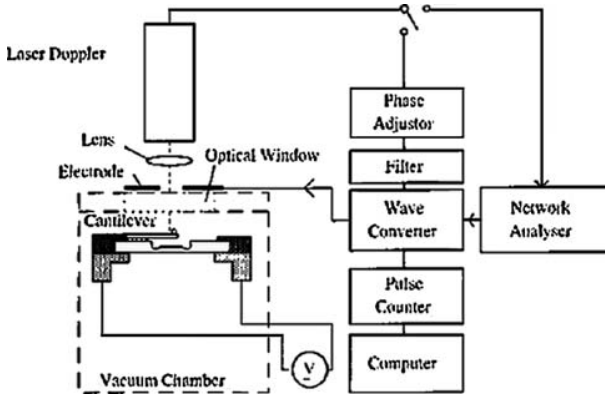

Fig. 56. Experimental set-up of the vibration measurement system. Reprinted with permission from [83], T. Ono et al., *Rev. Sci. Instrum.* 74, 1240 **(2003)**. © 2003, American Institute of Physics.

CNTs capability to the reversible hydrogen storage. In the study, thin (170 nm) cantilevers were used a resonant element for the deposition of 10^{-12}–10^{-13} g of CNTs. The CNTs were synthesised by a hot-filament CVD method using H_2/C_2H_2 and iron catalyst. The CNTs were of 2–8 nm diameter. A bundle of separately synthesised CNTs was trapped by mechanical manipulation with a sharp tip and the end of silicon cantilever as in Figure 56. The bundle needed to be cleaned from adsorbed species by heating up to 1000 °C in nitrogen. The cantilever was brought to oscillate due to electrostatic forces. Both the mass of CNTs and the amount of adsorbed hydrogen were calculated from the observed changes of the resonant frequency of the cantilever. The device exhibited an extreme mass sensitivity of 5×10^{-18} g with a 2–3 Hz drift per day atop the basic signal of ca. 100 kHz. One has to notice that bare CNTs can reversibly and effectively adsorb molecular hydrogen. Nevertheless, the results show that the device is quite far from a practical application.

Wei and co-workers[84] tried to detect CO, NO_2, H_2, and N_2 in air at the operation temperatures from 25 to 200 °C. It was discovered that temperatures above 100 °C upgraded the sensitivity of such sensors. The sensors' response noticed for lower temperatures were significantly less spectacular. Surprisingly, the adsorption of the investigated gases increased the resonant frequency of CNTs-coated crystals. In usual cases, quartz crystal microbalance sensing devices generate a decrease of its resonant frequency during detection. Due to the unexpected frequency increase, authors assumed that the sensing mechanism was more complex and based on the weight lost instead of increase. The given explanation implied the adsorption of oxygen prior to the adsorption of detected gases. It seems to be probably since the elevated temperature of operation (the best results were achieved at 200 °C) has to ease the oxidation of CNTs. The adsorbed oxygen molecules were later competing with detected molecules for occupation of the same adsorption sites. Thus, the detection mechanism should be seen as a mass change (parallel desorption and adsorption) resulting from gas exchange in adsorption complexes, or change in coating elasticity.

SAW sensors are another class of gas sensitive devices that can employ CNTs as a sensing material. Penza and co-workers[85] demonstrated that such a sensor reacted to the change in concentration of selected volatile organic liquids. For this purpose, MWCNTs and SWCNTs were applied. CNTs were deposited as a sensing layer onto a substrate by means of spray-painting method. The tubes were dispersed in ethanol or toluene and overlayed without any binder. Their adherence to the background and the mechanical stability of the oscillators was provided by coverage the substrate with a thin SiO_2 film (sputtered). The sensor design (Figs. 57, 58) is an example how

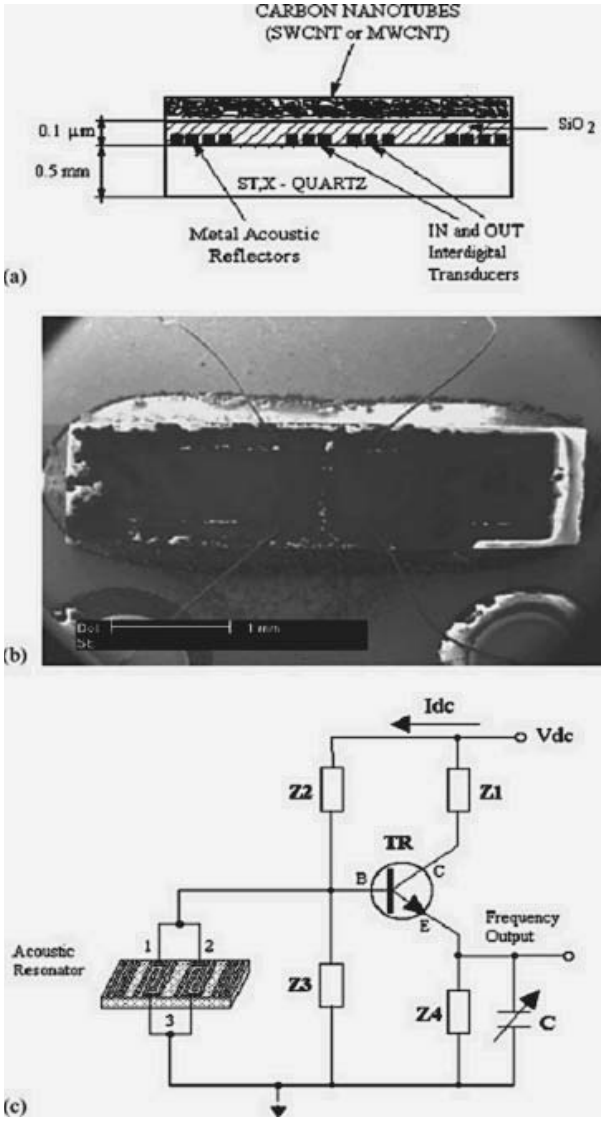

Fig. 57. (a) Cross-sectional view of the SAW sensor coated by carbon nanotubes; (b) top view SEM image of the SAW sensor coated by carbon nanotubes in a TO-39 open case; (c) scheme of SAW sensor oscillator with RF amplifier. Reprinted with permission from [85], M. Penza et al., *Sens. Actuators B* 100, 47 **(2004)**. © 2004, Elsevier.

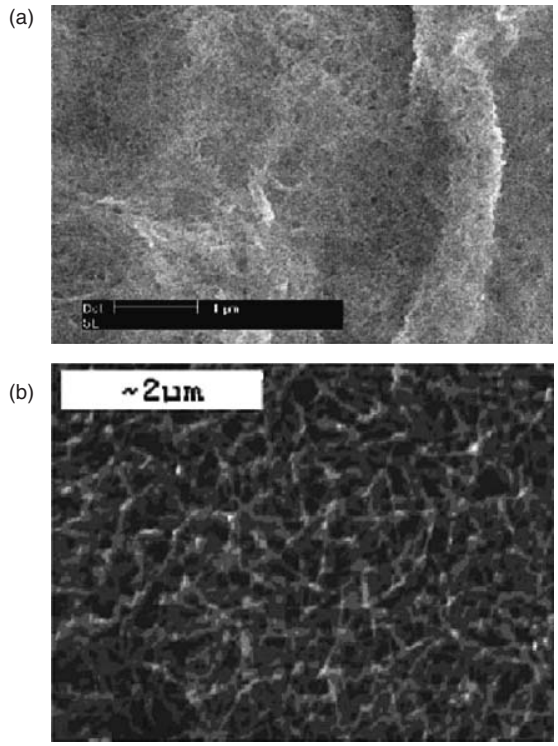

Fig. 58. SEM image of (a) SWCNTs and (b) MWCNTs coatings sprayed onto SAW quartz substrate. Reprinted with permission from [85], M. Penza et al., *Sens. Actuators B* 100, 47 **(2004)**. © 2004, Elsevier.

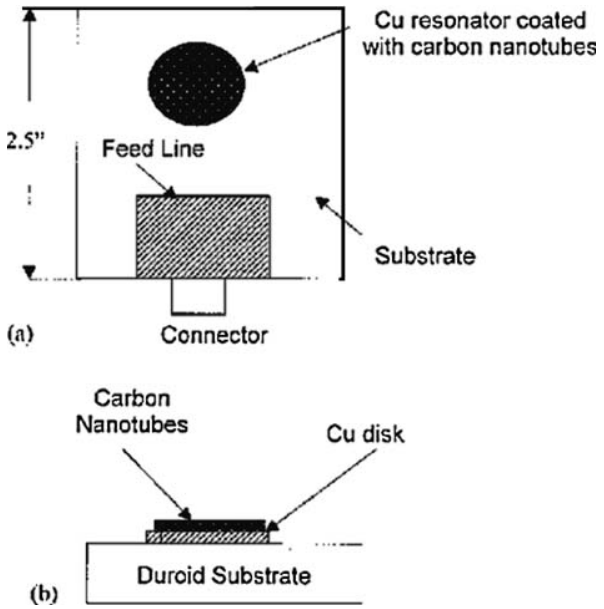

Fig. 59. (a) Schematic of the resonator sensor used in this study. The shaded regions represent copper metal on which the nanotube coating is applied. (b) Cross-sectional view of the resonator sensor. Reprinted with permission from [86], S. Chopra et al., *Appl. Phys. Lett.* 80, 4632 **(2002)**. © 2002, American Institute of Physics.

the nanotubes can be immobilized without any particular binder yielding a coherent layer. The SAW sensors exhibited a substantial downshift of the oscillation frequency due to adsorption of organic molecules. It has to be noticed that the adsorption of several organic species (vapours of ethanol, ethylacetate, and toluene) modulated the resonant frequency at room temperature. The lowest detection limit of ca. 1.3 ppm was achieved for toluene vapours that were interacting with SWCNTs deposited from the toluene dispersion and for ethanol vapour interacting with SWCNTs deposited from the ethanol dispersion. The tests were performed for the concentration range from single ppm to ca. 200 ppm (ethyl acetate) or to ca. 100 ppm (ethanol and toluene). The highest sensitivity was achieved for the substances that were also used for the preparation of CNTs dispersions. It was suggested that the phenomenon resulted from the presence of the solvent residuals on the surface of the CNTs. Thus, the detection was easier since the adsorbate and adsorbent surface had a high affinity to each other. Moreover, it was proven that oxygen chemisorbed first on CNTs helped to retain quite durably some ethanol molecules on the surface due the formation of hydrogen bonds. On the contrary, the chemisorbed oxygen promoted only weak attraction of non-polar solvents like toluene that was used for the dispersion of CNTs. The CNTs deposited from toluene dispersion did not retain toluene molecules as strongly as ethanol molecules were attracted by the oxidised carbon surface. It is reasonable that one may consider the contact of organic liquids (from a dispersion of CNTs) as a kind of a non-covalent functionalization of CNTs. The example points out the key role of CNTs functionalization and their surface state in design of chemical sensors containing the CNTs.

Chopra et al.[86] described a sensing device based on the downshift in resonant frequency of circular electromagnetic resonator as depicted in Figure 59. CNTs were stuck onto a copper resonator by means of a conductive epoxy resin. The resonant frequency of the sensing element was determined by the properties of dielectric materials, i.e., Duroid board and CNTs interacting with electromagnetic field generated by a RF transmitter. CNTs were supposed to change their dielectric properties upon adsorption of gases and vapours as it was presented by means of NH_3. Authors suggested that NH_3 molecules, when interacted with carbon atoms in CNTs, created surface charges leading to variations of the dielectric constant value. Thus, the phenomenon was based on the ability of adsorbed molecules towards the charge transfer to and from CNTs. The detection of NH_3 consisted in the continuous monitoring of the frequency downshift of the resonator by means of a remote antenna. Thus, the detection system did not need any direct electric connection between the sensitive element and the electronic device transmitting and receiving electromagnetic waves. This principle of operation enables a remote detection of chemical substance inside packages or other isolated spaces. In the study, one employed SWCNTs and MWCNTs as adsorbing material. The frequency shifts noticed for the NH_3 adsorption on

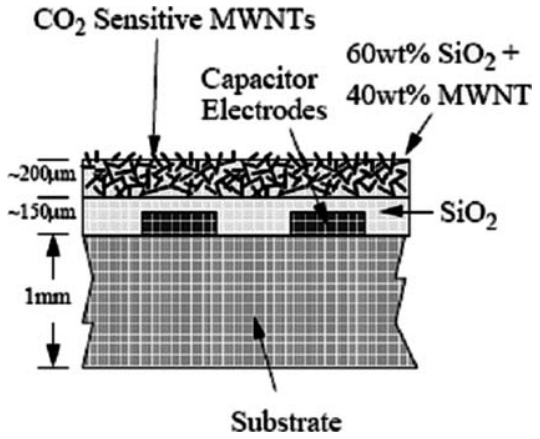

Fig. 60. Cross sectional view of the interdigital capacitor. An electrically insulating 150 μm hick SiO_2 layer is first applied to protect the sensor, followed by a 200 μm MWNT-SiO_2 gas sensing layer. Reprinted with permission from [87], K. G. Ong and C. A. Grimes, *Sensors* 1, 193 (**2001**). © 2001, MDPI Publ.

SWCNTs were ranging from 0.5 to 6 MHz when ammonia concentration changed from ca. 100 to 1400 ppm (base frequency 4 GHz).

The advantages remote-query sensing systems were utilized by Ong and Grimes[87] to trace CO_2 in isolated spaces; the resonator is depicted in Figure 60. The sensor structure has a certain capacitance (C) and inductance (L), which interact with electromagnetic signals using the resonant frequency ascribed to the resonators. The LC sensors did not need to be connected to any power supply. It provided a long and wireless operation of such sensors even if they were placed in a quite remote area. The fabricated sensors consisted of two electrodes deposited onto a substrate. The whole assembly was first covered with a layer of SiO_2 and then by a mixture of SiO_2 and MWCNTs (3 : 2 ratio). SiO_2 played the binding role for CNTs. The sensor's response was detected by measuring the impedance spectrum of a remote antenna that monitored the LC sensors. The analysis of the antenna impedance let to calculate the value of complex permittivity of the sensing material i.e., CNTs incorporated in the sensing layer. The phenomenon was ascribed to the interactions between the electron pairs in CO_2 molecules and CNTs. Authors found that complex permittivity of MWCNTs decreased upon the exposure to pure CO_2 due to higher adsorption rate of CO_2 on MWCNTs than for other competitive gases like N_2. Although not proven in the experimental way, the last assumption is fully justified since nitrogen is a poorly adsorbing gas at room temperatures despite the nature of adsorbing solid. Nitrogen adsorption increases significantly at liquid nitrogen temperature what is conventionally employed for the determination of pore structure of solids. The sensor's response to the changes of CO_2 concentration was fast (ca. 50 seconds) in adsorption and desorption cycle. No sensing hysteresis was noticed. A limited cross sensitivity occurred towards water vapour but the problem was solved by the construction of a sensor array employing additional sensors: SiO_2-coated and uncoated one. The last two sensors did not respond to CO_2. Therefore, the complex response of the array was possible to resolve aiming at the elimination of water vapour influence on the CO_2 readings. The MWCNTs used in the study were synthesised by thermal decomposition of ferrocene dissolved in xylene under Ar/H_2 atmosphere. Such obtained CNTs were dispersed in liquide SiO_2 solution and dropped onto the substrate forming a porous, 200 μm thick coverage.

Varghese and co workers[88] performed comparative studies on the application of MWCTs to the detection of humidity, carbon dioxide, carbon monoxide, and ammonia. Two different kinds of sensors we examined. The first category of sensors had structure identical as the sensor depicted in Figure 60. The sensing layer contained MWCNTs mixed with a silica-based binder. A pair of interdigital electrodes let to treat the sensor as gas sensitive capacitor. The second type of sensors had a different structure. A serpentine path of SiO_2 was created by photolithography on the surface of silicon plate (ca. 1.7 cm $\times$ 1.7 cm) first oxidized at elevated temperature. Then, the substrate with etched serpentine of SiO_2 served as a background for MWCNTs deposition from gas phase (pyrolysis of ferrocene and xylene, Ar/H_2 atmosphere, 750 °C). In those conditions one observed the growth of MWCNTs only on the surface of SiO_2 serpentine which length was close to 45 cm. No deposition of carbon tubes was observed on the Si surface between the SiO_2 serpentine. This kind of sensor was treated as a resistor-type chemical sensor. Impedance analyzer let to collect impedance data resulting from the exposure of both types of sensors to the above mentioned gases and water vapour. The measures total impedance of both sensors was deconvoluted by means of appropriate theoretical models. In this way, one could determine equivalent circuits consisting of several capacitances and resistances. The impedance of the capacitor-type sensor increased significantly upon the increase of humidity. The resistances of resistor-type sensors increased upon water vapour adsorption but the growth was rather minor. The presence of ammonia, carbon monoxide, and carbon dioxide increased the resistance of the sensors, too. The gases are considered as electron donors. Thus, the electrons may localize holes in *p*-type MWCNTs incorporated in the sensors. The authors indicated that the sensing performance of the sensors was strongly affected the composition of sensing layer. Both type of sensors did react to the presence of oxygen but it was associated to the instant and durable adsorption of oxygen after exposure of the tubes to air. It could not be desorbed by the performed vacuum treatment at 100 °C. One assumed that ammonia molecules replaced pre-adsorbed oxygen causing irreversible changes of electric properties of the tubes and sensors incorporating MWCNTs. A similar capacitor-type sensor was reported by Ong, Zeng, and Grimes.[89] The sensor exhibited reversible changes of complex permittivity

(dermined by relative permittivity and conductivity of the sensing layer) upon adsorption of oxygen and carbon dioxide. The adsorption of ammonia caused reversible and irreversible effects. When the sensors were cycled between nitrogen and oxygen one observed an increase of conductivity of MWCNTs due to electron localization of the *p*-type tubes. Also in this study it was confirmed that NH_3 and CO_2 were acting as donors of electrons that could localize majority current carriers. The difference between the above described studies consisted mainly in the response of the sensors to oxygen.

2.4. Other CNT Chemical Sensors

Wong and co-workers[90] fabricated a quite complex structure in a four-step procedure: sputtering deposition of a thin palladium film (catalyst for growing CNTs) on a highly conductive *n*-type silicon plate, growing of MWCNTs on the metallized *n*-Si surface by means of microvawe plasma enhanced CVD from CH_4/H_2 mixture, short annealing for better adhesion of CNTs to the silicon plate (900 °C in argon), sputtering deposition of a thin Pd-layer on the top of CNTs. The fabricated structure is presented in Figures 61 and 62. The whole device had the structure equivalent to a Schottky-diode Pd/CNTs/n^+-Si, in which the Pd/CNTs interface was an ohmic one while the diode junction existed at the CNTs/n^+-Si interface. The recorded *I–V* curves were shaped as for typical metal-semiconductor diodes. The device was sensitive to molecular hydrogen at room temperature. The run of *I–V* curves was dependent on the presence of hydrogen. Generally, the adsorption of H_2 increased the potential barrier at the sensitive interface. Pd served as a catalyst for dissotiative adsorption of hydrogen. Hydrogen atoms penetrated the outer Pd-layer reaching the sensitive interface. The atoms

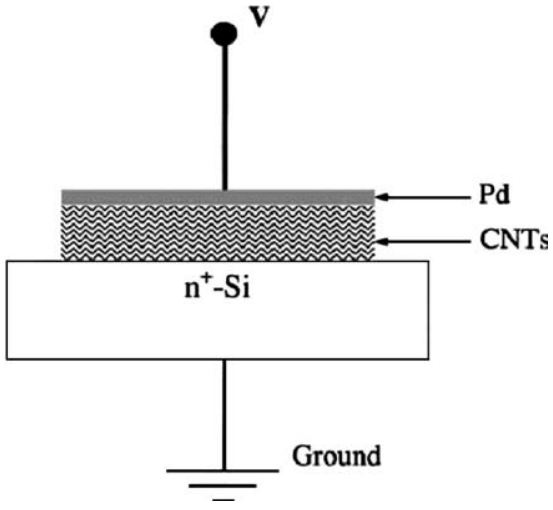

Fig. 61. Schematic diagram of the experimental setup of the CNTs-based gas sensor. Reprinted with permission from [90], Y. M. Wong et al., *Sens. Actuators B* 93, 327 **(2003)**. © 2005, Elsevier.

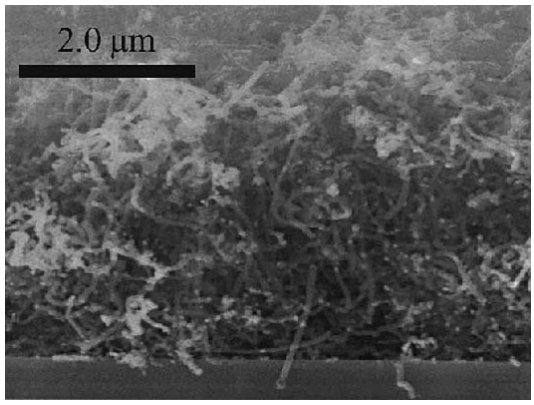

Fig. 62. SEM micrograph of the carbon nanotubes grown by MPECVD. Reprinted with permission from [90], Y. M. Wong et al., *Sens. Actuators B* 93, 327 **(2003)**. © 2003, Elsevier.

introduced dipoles at the interface. The induced voltage increased the potential barrier the Pd/CNTs interface. At elevated temperature of 170 °C the device lost its diode character since all the contacts became ohmic. Room operation and reversible response to hydrogen gas were the most important features of the described diode-type sensing devices.

Chen et al.[91] described non-covalent functionalization of CNTs for highly specific electronic biosensors that were sensitive to proteins. SWCNTs worked as platforms for the non-specific deposition of proteins. Protein sensitive devices were prepared by *in situ* synthesis of interconnected SWCNTs on a quartz substrate covered by an iron catalyst. The layer of SWCNTs behaved as a typical *p*-type semiconductor that bridged two metal electrodes. AFM and QCM studies revealed that 1 hour contact of CNTs with 10–50 nM buffered solution of a protein (streptavidin—SA, avidin, staphylococcal protein A-SpA, α-glucosidase-GCD, human IgG, BSA) resulted in a non-covalent attachment of some proteins due to hydrophobic interaction (Fig. 63). Non-specific bonding was found to be irreversible. Table IV indicates whether the mentioned proteins can be attached to as grown and modified CNTs. It is clear that pre-adsorption of some mentioned surfactants prevented the non-covalent bonding of some proteins that might be utilized for a selective adsorption of the desired proteins. The conductance of the inter-electrode layer of CNTs was gated by the voltages created by a Pt electrode immersed in a buffer solution above the sensitive area of the device (Fig. 64). The adsorption of protein molecules caused a significant shift in the conductance of CNTs layer versus gate voltage characteristics. Therefore, the whole device could be regarded as a FET device sensitive to protein adsorption. All adsorbed protein caused a decrease in conductance of the sensitive layer of as-grown CNTs. Authors expected a further progress in the application of such biosensitive devices basing on the synthesis of nanotube micro-arrays capable to detect a number of

REVIEW

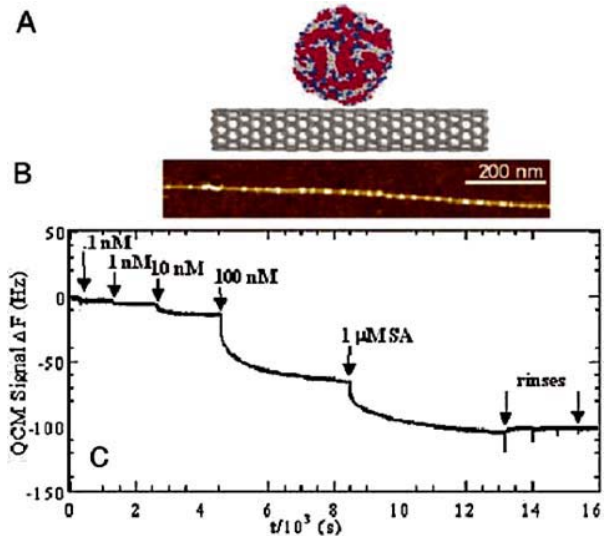

Fig. 63. Proteins tend to bind nonspecifically onto as-grown carbon nanotubes. (A) Schematic illustration of globular protein adsorption onto a nanotube. (B) An AFM image showing protein A (bright dot-like structures decorating the line-like nanotube) nonspecifically adsorbed on a nanotube. We have also observed a certain degree of NSB of proteins on regions of the (SiO_2) substrate free of nanotubes (data not shown). (C) QCM data (frequency shift Df vs. time t) revealing NSB of SA onto nanotubes at increasing protein concentrations. The NSB is irreversible upon rinsing. Reprinted with permission from [91], J. R. Chen et al., *PNAS* 100, 4984 (**2003**). © 2003, National Academy of Sciences.

Table IV. Selective bonding of proteins due to the pretreatment with some surfactants.

Nanotubes	SA	Avidin	BSA	GCD	SpA
As grown	Y	Y	Y	Y	Y
Tween 20-treated	N	N	N	N	N
Pluronic P103-tretaed	N	N	N	N	N
Triton X-100-treated	N	Y	Y	Y	N
Dextran-treated	Y	Y	Y	Y	Y

Source: Reprinted with permission from [91], R. J. Chen et al., *PNAS* 100, 4984 (**2003**). © (2003), National Academy of Sciences.

various proteins. The device would not need any labeling of proteins since the problem of selectivity could be solved by an appropriate pre-treatment with carefully selected surfactants.

Electric phenomena occurring in CNTs that might be induced by gas or vapour adsorption are not limited to the changes in electrical resistance. Sumanasekera and co-workers[92] investigated the influence of various gases and vapours on the thermoelectric power (TEP) generated in SWCNTs-based materials. The authors found that the thermoelectric power generated in CNTs was very sensitive to adsorption of gas even if the gas was inert. Thus, variation of TEP were observed upon the adsorption of oxygen, hydrogen, nitrogen, helium, methanol, ethanol, buthanol, benzene 1,3-cyclohexadiene, cyclohexane, and cyclohexene. A correlation between the number

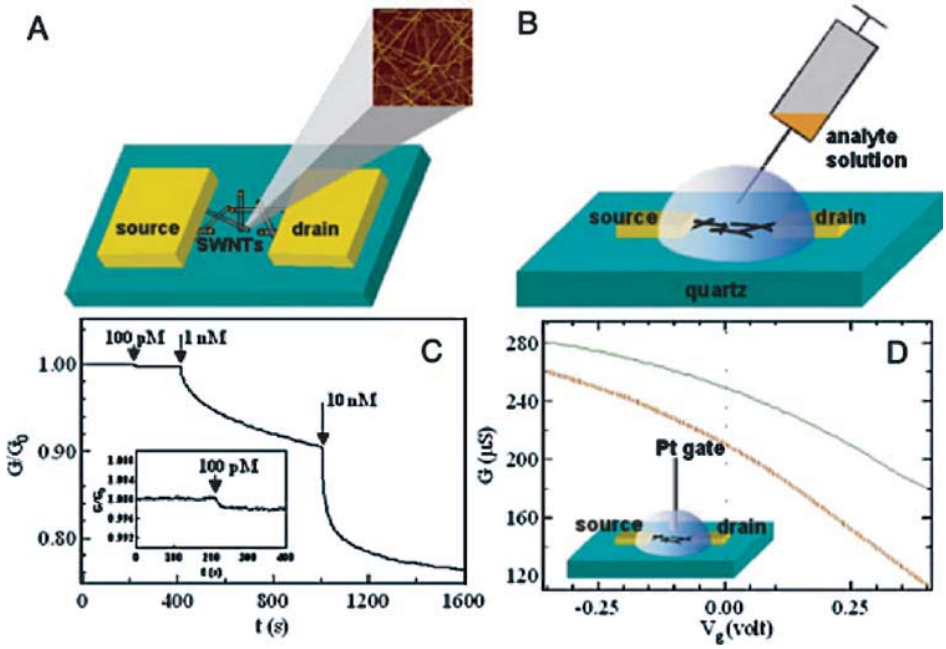

Fig. 64. Carbon nanotubes as electronic devices for sensing in aqueous solutions. (A) Schematic views of the electronic sensing device consisting of interconnected nanotubes bridging two metal electrode pads. An AFM image of a portion of the nanotube network (0.5 mm on a side) is shown. (B) Schematic setup for sensing in solution. (C) Conductance (G) evolution of a device for electronic monitoring of SA adsorption on nanotubes. The conductance is normalized by the initial conductance G_0. (*Inset*) Sensitivity to a 100-pM protein solution is shown. (D) Electrical conductance (G) versus gate voltage (V_g) for a device in a 10-mM phosphate buffer solution. The gate voltage is applied through a Pt electrode immersed in the solution (*Inset*). The green (solid) and orange (broken) curves are the G–V_g characteristics for the device before and after SA binding, respectively. The shift in the two curves suggests a change in the charge environment of the nanotubes. Reprinted with permission from [91], J. R. Chen et al., *PNAS* 100, 4984 (**2003**). © 2003, National Academy of Sciences.

of π-electrons in the organic rings (if a molecule contained such ones) and the magnitude of the registered TEP changes was found. The higher the number of π-electrons the more dramatic (larger) was the change of the TEP.

2.5. Electrodes and Chemiresitors

The physical properties of carbon pastes can differ significantly from the properties of solid carbon materials like glassy carbon, polycrystalline carbon, etc. Carbon pastes are soft substances that can be spread over a selected spot. The pastes are often self-sticking and do not need any other binder to stay on a covered spot. One may use different carbon powders or powdered carbons (grinded graphite, grinded active carbon, carbon black, CNTs, fullerenes) for fabrication of carbon pastes. Carbon pastes can be obtained by mixing of carbons in powdered form with a liquid component providing adhesion between the carbon particles and plasticity of the mixture. If the liquid component can harden upon polymerisation or evaporation of a solvent, such a carbon paste becomes a conductive solid preserving properties typical for carbons (good conductivity, chemical composition of the surface, porosity, and high surface area). The pastes before hardening can be mixed with other substances that can react more selectively with detected substances offering application to the construction of chemical and biological sensors. Often the sensitisation of a carbon paste by the admission of active substances like enzymes is much more easier and effective that the deposition of such substances on solid carbons like glassy carbon electrodes. There are many reports in the literature announcements on chemical sensors and biosensors fabricated by means of a carbon paste. Many of them do not consider the role nor pedigree of the carbon particles, with little attention paid to their chemical properties.

A recent report concerns the electrochemical reduction and oxidation of nucleic acids at carbon-based electrodes.[93] The electrodes exhibited the ability for interfacial accumulation of DNA or RNA molecules. Fabricating the carbon paste electrodes one utilized the possibility of mixing the paste with an appropriate reagent enhancing catalytic properties (oxidation/reduction) of bare carbon particles. As comparative samples one applied non-modified carbon electrodes believing that carbon particle also possessed natural ability to run elctrocatalytic processes. The addition of an organo-ruthenium catalyst upgraded significantly the sensing properties of the modified electrodes if comparing them to the behaviour of non-modified carbon-paste electrodes. The test reaction was electrocatalytic guanine oxidation of single-strand DNA in a cyclic voltammetry experimental set up. The carbon paste was prepared from graphite powder (not chemically characterized), mineral oil, and organo-ruthenium catalyst ($Ru(Bpy)_3^{2+}$). The electrodes worked in the three-electrode amperometric regime. Easy renewal of the surface was one the most important features of the bulk-modified electrodes. Ruthenium-modified electrodes exhibited a substantial current enhancement, which was related to the catalytic guanine oxidation of single-strand DNA molecules at +0.9 V potential. Calibration plots (electrode current vs. concentration) for the detection of single-strand DNA were linear up to 50 ppm. The study is a good example of an ordinary practice that assumes that carbon particles (graphite powder) plays only the role of electric conductor.

In the similar, way one can prepare enzyme-modified carbon electrodes. In such cases the electrodes are prepared by admission of dissolved enzyme like alcohol dehydrogenase.[94] Such electrodes were tested for measuring alcohol content in some food products like wine, sake, beers, and soy sauce. The obtained results were comparable with results obtained by widely approved methods. Authors modified the applied enzyme with poly(ethylene glycol) aiming at improving electrode lifetime. The successful usage of the electrodes needed mediators that were non-soluble in water. Authors pointed out that the short lifetime of the enzyme-containing electrodes could be the biggest drawback of them since many components of carbon pastes were water soluble and leached out from the sensing material. They also proved that a successful design of such electrodes required numerous components that had to be selected according to the needs of active organic species (alcohol dehydrogenase).

The ongoing drive for miniature biosensors turn the attention towards the application of carbon fibres and CNTs. Ge and co-workers[95] presented a series of micro-scale modifications by means of scanning electrochemical microscope. According to authors, microbiosensors often suffer from the imperfect immobilization of enzymes. Amination can follow the pathway starting from the attachment of nitrophenol (reduction of diazonim salts), and subsequent reduction to aminophenyl functional groups. Enzymes can be covalently bonded using biotin-avidin chemistry. The amine groups acted as anchors for some organic molecules like enzymes (glucose oxidase). Small dimensions of carbon fibres and precise chemical/instrumental methods allow the fabrication micro-enzymatic electrodes that are capable to direct investigation of biological objects.

The way in which carbon pastes are manufactured provides much space for manipulation like changing the proportions between carbon, hardening agent and chemically sensitive substance. That allows fabrication of carbon paste-based materials that can exhibit a wide spectrum of sensing properties changing gradually according to the relative compositions. Such a manipulation is hard to achieve in the case of other carbon-based materials where the implantation of an active component is not easy to control. The mentioned advantages of carbon pastes fit the needs of sensor arrays. It is a key point in the fabrication of sensor arrays that each single sensor differs from the other sensitive elements in the array, which is relatively easily

achieved with carbon pastes. Moreover, carbon paste-based sensitive materials being self-sticking and self-hardening, are ideal candidates for the deposition of active covers or layers on the substrates like plates, rods, or wires. The sensing materials prepared from a carbon paste mixed with an active (sensitive) substance can be considered as relatively homogenous. Thus, the bulk and the surface of such a material exhibit the same chemical properties. The sensing element surface (particularly electrodes) undergoes mechanical and chemical deterioration caused by some undesired by-reactions occurring when the sensors are in operation or stored for long. Bulk homogeneity of carbon paste-based sensors provide an unique opportunity to renew the original state of the surface by a gentle abrasion. Such a possibility does not exist in the case of sensitive electrodes that are not homogenous like glassy carbon electrodes covered by a thin layer of a sensitive material. Diffusion-based side effects that can occur in thick layers of carbon paste seem to be the main shortcoming of the application carbon pastes for chemical sensor design.

Sensor arrays fabricated by means of carbon black often rely on the phenomenon of polymer swelling upon adsorption of organic vapours. The phenomenon of swelling influences the geometry of the sensing composite layer and changes the contacts between carbon black particles. This affects the transduction of electric current through the swelled sensor. The presented principle of operation requires a careful selection of polymers to suite the properties of the detected species. In such a case the preparation of the composite material consists in mixing of carbon black particles with a dissolved polymer until a homogenous paste is obtained. Then the paste can be deposited on a desired substrate by spraying, spin coating, screen-printing, dip coating, etc.

Zee and Judy[96] investigated arrays of chemiresitors prepared from a carbon black-polymer composite to identify several organic vapours. The authors tried to find a way to prepare the composite-base sensors of possibly identical amount of sensing material between the electrodes. The problem was solved by a "well" design of each sensor as it is presented in the following pictures (Figs. 65, 66). The deposited film of composite after the evaporation of solvent excess had always a comparable geometry. Six polymers were applied for the array fabrication, with the reproducibility of samples' geometry and their sensing properties ensured by the injecting of dissolved composite into the "wells." Additionally, it was proven that the size of "wells" did not affect the obtained results. It indicated that the way of composite film deposition provided high homogeneity of the sensing films.

Lonergan and co-workers[97] reported an application of 17 polymers for the preparation of a carbon paste containing carbon black (see Table V). All the polymers were non-conductive in the pure form but became conductive

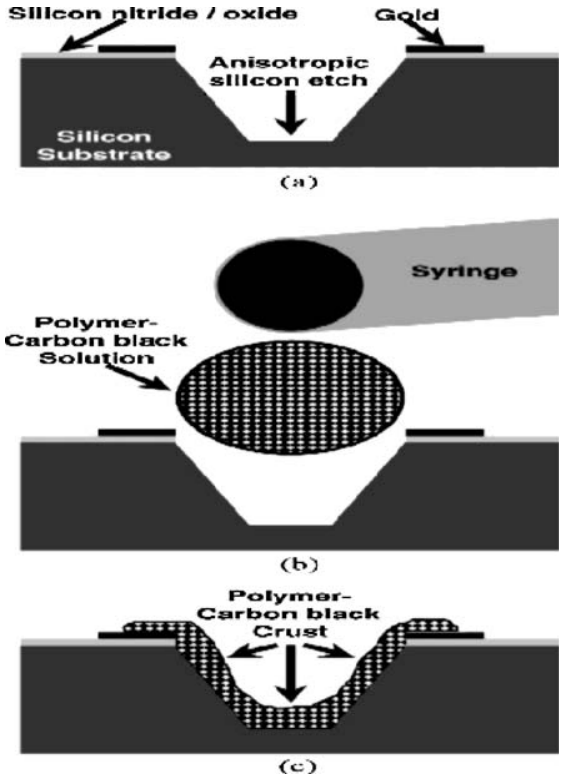

Fig. 65. Fabrication of the gas sensor using bulk-micromachining techniques: (a) anisotropically etched "well" into a silicon wafer with patterned silicon nitride/oxide insulation and gold metallization; (b) polymer-carbon black solution deposited into the "well" with a syringe, and (c) crust of polymer-carbon black film remains after drying. Reprinted with permission from [96], F. Zee and J. W. Judy, *Sens. Actuators B* 72, 120 **(2001)**. © 2001, Elsevier.

after the admission of carbon particles. The sensor array was exposed to the action of various vapours. The response of the array let them distinguish between a variety of substances (Fig. 67). The exposure to the mixed vapour of ethanol and methanol gave pathways between the responses to pure vapours of the alcohols. The response (increase of electric resistance of the sensors) was linear versus the concentration of organic vapours.

Uniform distribution of carbon black particle in carbon pastes, especially in these that were intensively diluted before use, is a serious problem. Dickson and Goddman[98] indicated that carbon black particles got restructured upon evaporation of solvent during drying of carbon pastes. The particles tended to accumulate at the edges of the drop forming a so called "coffee ring." After drying, the edge-accumulated carbon black particles formed highly conductive pathways between electrodes, which were not sensitive to the adsorption of detected species. A special electrode geometry was designed to overcome this problem. Sensor electrodes in a single chemiresitor had a concentric structure consisting of an inner ring-electrode and an outer square-ring electrode (135 micron on side) as it is shown on Figure 68 and Figure 69. The exterior part of

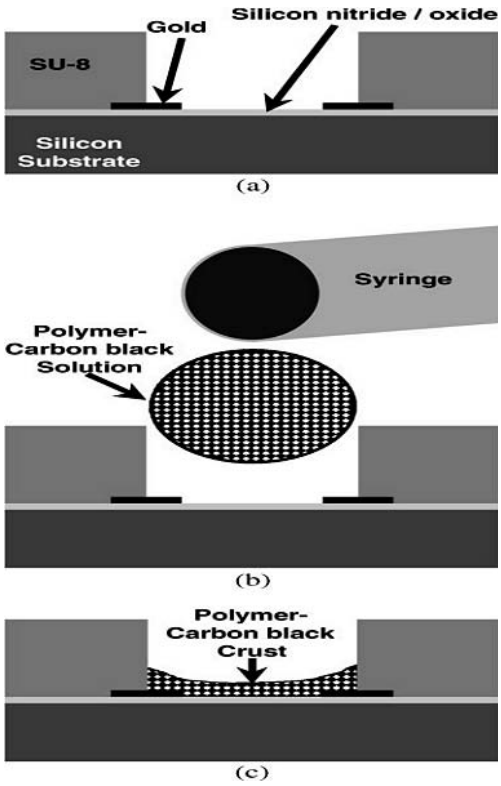

Fig. 66. Fabrication of the gas sensor using surface-micromachining techniques: (a) Patterned silicon nitride/oxide insulation, gold metallization and SU-8 photoresist to form "well" on silicon substrate; (b) polymer-carbon black solution deposited into the "well" with a syringe and (c) crust of polymer-carbon black film remains after drying. Reprinted with permission from [96], F. Zee and J. W. Judy, *Sens. Actuators B* 72, 120 **(2001)**. © 2001, Elsevier.

the sensors was common to all sensors. Thus, the conductors were shared among all the sensors and aggregation of carbon black particles at that spots decreased the contact resistance between the sensing material and the outer electrodes. According to authors, it helped to change carbon black agglomeration at the edges "from a problem to a benefit." The sensor array was successfully employed for the detection of some organic vapours (toluene, THF, acetone, methanol, octanol).

Some of the already reviewed papers were characteristic because the carbon black particles were considered as playing a secondary and rather passive role in the chemical sensing. This ignored the adsorption of the vapours on carbon black particles in the composite. However it is well known that carbon blacks exhibit high affinity towards organic vapours. The affinity of organic vapour towards carbon black, as well as towards other kinds of carbon, strongly depends on the chemical composition of the carbon surface. The variety of surface treatments and their resulting chemical properties of their surface suggests that the application of carbon black-based pastes or composites for sensing purposes should consider the fact that carbon blacks are different and are

Table V. Polymers applied for the fabrication of sensors array.

Sensor no.	Polymer
1	Poly(4-vinyl phenol)
2	Poly(styrene-*co*-allyl alcohol), 5.7% hydroxyl
3	Poly(α-methylstyrene)
4	Poly(vinyl chloride-*co*-vinyl acetate), 10% vinyl acetate
5	Poly(vinyl acetate)
6	Poly(*N*-vinylpyrrolidone)
7	Poly(carbonate bisphenol A)
8	Poly(styrene)
9	Poly(styrene-*co*-maleic anhydride0), 50% styrene
10	Poly(sulfone)
11	Poly(methyl methacrylate)
12	Poly(methyl vinyl ether-*co*-maleic anhydride), 50% maleic anhydride
13	Poly(vinyl butyral)
14	Poly(vinylidene chloride-*co*-acrylonitrile), 80% vinylidene chloride
15	Poly(caprolactone)
16	Poly(ethylene-*co*-vinyl acetate), 80% ethylene
17	Poly(ethylene oxide)

Source: Reprinted with permission from [97], M. C. Lonergan et al., *Chem. Mater.* 8, 2298 **(1996)**. © (1996), American Chemical Society.

not inert solids especially during adsorption of organic vapours. Fortunately, several studies were performed that considered the presence of carbon black surface functional groups and their role in the fabrication and application of such carbon black-polymer composites for chemical sensing. Tsubokawa and co-workers[99] applied the existence of surface functional groups on carbon black particles for the initiation of polymerisation of a selected polymer. Polymer chains were grafted by a direct condensation of carboxyl groups on the carbon black surface with terminal hydroxyl groups in polymer chains by means of a condensing agent. Hydroxyl groups were originally present on the carbon surface and were quantitatively characterized. In this way one obtained carbon black grafted with poly(ε-caprolactone)—PCL, poly(ethylehe glycol)—PEG and poly(ethylene adipate)—PEA. Grafting of carbon black particles provided good affinity of the modified particles to the same polymers utilized later as binding polymer for the preparation of sensing composites. It helped to prepare homogenous mixtures of the modified carbon black, the dissolved polymers and some amounts of THF. After mixing, the paste was deposited on solid substrates (with screen-printed interdigitated electrodes) forming after solvent evaporation a chemically sensitive resistor ready for use. The sensors exhibited rapid and reversible responses to the presence of organic contaminants added to hexane, which was selected as a basic solvent for tests. As expected, the polymers applied as binders for grafted carbon black particles swelled upon the contact with chloroform, trichloroethane and ethyl alcohol but the behaviour of the samples was significantly differentiated. The type of grafting polymer played an important role. Composites containing PCL-grafted carbon black (also PCL as binding polymer) swelled easily in hexane containing 10% vol. of

REVIEW

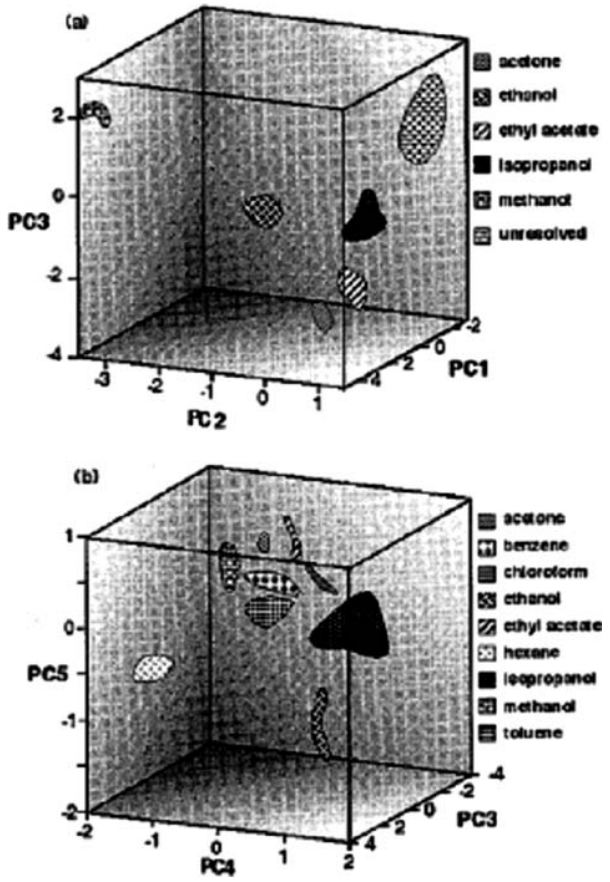

Fig. 67. Results from the exposure of the 17-element array to nine solvents as represented in (a) the first three dimensions of principal component space and (b) the third, fourth, and fifth dimensions of principal component space. These five principal components contain over 98% of the total variance in the data. Reprinted with permission from [97], M. C. Lonergan et al., *Chem. Mater.* 8, 2298 **(1996)**. © 1996, American Chemical Society.

chloroform at 20 °C, while samples that contained non-grafted carbon particles did not exhibit such a dramatic reaction. PCL-grafted carbon black/PCL composites were also sensitive to trichloroethane and ethanol dissolved in hexane (10% vol.). The logarithm of sensors' resistance (PCL-grafted carbon black/PCL) increased spectacularly in the linear mode versus the concentration of chloroform in hexane (test range 0–12%). Other investigations revealed that chloroform adsorbed by composites upon the contact with 10% solution of $CHCl_3$ was readily released after rinsing with pure hexane. Moreover, grafting with PEG changed the carbon black surface from a hydrophobic to hydrophilic one. PCL- and PEA-grafted carbon black particles were still hydrophobic. In other studies authors claimed that PEI- and PEG-grafted carbon black responded significantly (the change of electric resistance) to the contact with water and alcohol vapours which reacted (high affinity) with the grafted chains.

The study clearly shows that the chemical state of carbon black particles can play a key role in the enhancement

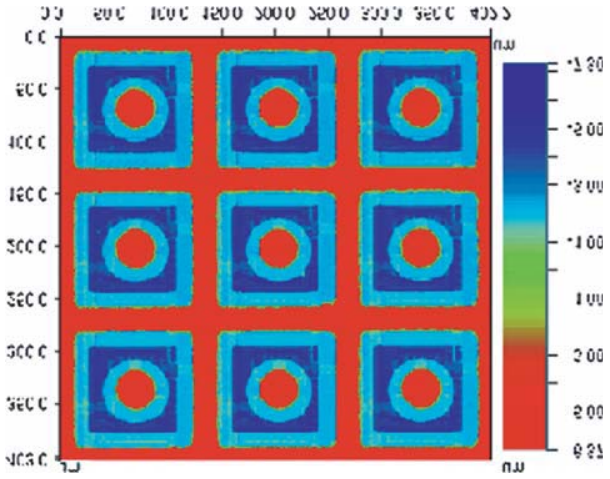

Fig. 68. Profilometry of a 3×3 section of array after the post-fabrication processing. The plating is approximated 10 microns high, and each sensor is 135 microns on a side. The internal contact is connected to the switch transistor, while the common perimeter contact is ground. Reprinted with permission from [98], J. A. Dickinson and R. M. Goodman, *IEEE International Symposium of Circuits and Systems* (*ISCAS'2000*), Geneva **(2000)**, p. 341. © 2000, IEEE.

or depressing of sensing properties of carbon black-polymer composites. However, the role of binding polymer cannot be neglected. Authors ascribed specific sensing properties of some composites to the phenomena occurring in polymer upon the contact with organic solvents like the change of crystalline structure of the polymers. The modelling of carbon black surface properties was also helpful in successful preparation of the composites. The problem of the influence of the carbon surface

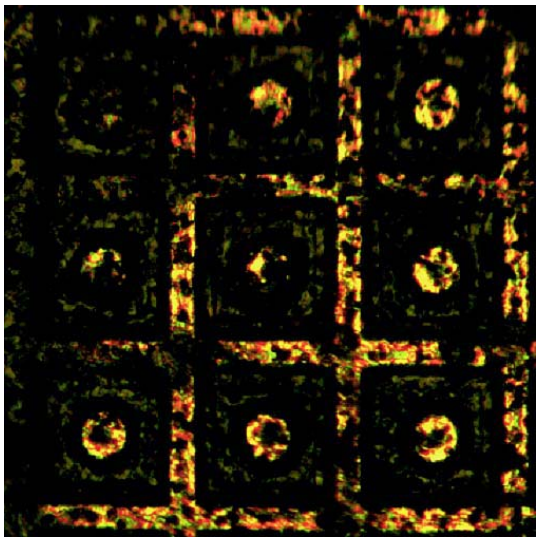

Fig. 69. Sensor material deposited on a plated chip. The active circuitry is located underneath each sensor. Reprinted with permission from [98], J. A. Dickinson and R. M. Goodman, *IEEE International Symposium of Circuits and Systems* (*ISCAS'2000*), Geneva **(2000)**, p. 341. © 2000, IEEE.

quality on the performance of enzyme modifies carbon black-based electrodes was investigated by Razumiene et al.[100] Their electrodes were fabricated from a series of home synthesised carbon blacks. The carbon black surface properties were modified by means of HNO_3, Br_2 + Fe, N_2H_2 2HCl, and H_2O_2. The treatment influenced the type and quantity of surface functional groups: carboxylic, lactone, and hydroxyl which concentration was estimated using the standard method of Boehm. Carbon black for electrode manufacturing was additionally modified by immobilisation of aldehyde dehydrogenase (ADH) and glucose dehydrogenase (GDH). The synthesis of carbon black was a complex process consisting of 11 technological operations including delamination of graphite structures, tailoring of surface properties, and particle size. The enzyme layers were additionally protected by the deposition of a permeable terylene film. Such electrodes were examined as amperometric sensors working in the three-electrode mode for the detection of ethanol and glucose dissolved in water (a flow-through experimental cell). It was proven that sensitivity and stability of the sensors were improved by increasing of the concentration of oxygen-containing surface functional groups. The authors ascribed the enhancement of sensing properties to the better contact between the carbon black particles and enzyme molecules. The close connection of both components resulted from the intermolecular binding forces that were more intensive when the polarity of carbon surface became a fact. Thus, the unique achievement of the study is showing the importance of the surface quality of carbon black particles applied for the fabrication of enzyme electrodes. According to the paper, carbon particles can play a complex role not limited to current conduction. The contacts between carbon black particles and enzyme molecules seem to be crucial for charge transfer during the electrode reactions. Therefore, the concentration and quality of the surface functionalities must influence the sensing properties of the electrodes.

Matthews et al.[101] reported the application of a composite consisting of carbon black with attached chains of poly(alkyl acrylate). The polymer-modified carbon black particles in solution were sprayed (after dilution) over an array of 42 pairs of electrodes of different size. In this way, one could investigate the influence of electrode size on the sensing performance towards toluene vapours (100, 500, 1000 ppm). The response magnitude, fundamental noise and signal-to-noise ratio of each sensor were considered as function of geometry of electrodes. No important influence of the geometrical factor on the mentioned sensing parameters was noticed. It suggested that carbon black-polymer composites were a homogenous resistive material suitable for fabrication of toluene vapour sensor of different size. Authors modified carbon black to increase its affinity to organic solvents aiming at easy paste preparation and improved sensitivity of the sensors.

Chen and McCreery[102] announced a detailed report on the role of surface oxygen species on glassy carbon electrodes in immobilisation of several organic substances. Surface modification of glassy carbon included oxidation (and oxygen removal), derivatization of surface oxides and adsorption of various organic substances. Some of the deposited substances were capable to specific interactions with surface functionalities while other ones were adsorbed in a non-specific form. Many of them like methylene blue were capable to form durable monolayers just by the adsorption from solution. One investigated several complex redox systems observing electron transfer kinetics. It was found, among other cases, that electron transfer to a particular redox system was dependent on oxygen-containing surface functionalities. The smaller the O/C ratio in the surface region the slower was the charge transfer. A negative influence on the charge transfer was noticed if a non-specific monolayer was adsorbed and if surface oxides were derivatized i.e., chemically transformed in other species. The chemical state of glassy carbon electrodes is depicted in Figure 70.

Graphite, which is highly conductive material, can find an application to chemical sensing not only as an electrode material. Miremadi and Colbow[103] constructed a hydrogen sensor basing on thin layer of graphite obtained be a two-step method. The first step started from intercalation of Li atoms into the pores and among graphite layers of graphite sample. The intercalation of Li atoms into graphite was run in two ways. Direct intercalation consisted in the action of Li vapours on carbon in vacuum while the second pathway was a "wet" chemical reaction (immersion of graphite samples in a hexane solution of *n*-bythyl lithium). The subsequent immersion of intercalated graphite samples in water (the second step) resulted in evolution of hydrogen due to the reaction: $2Li + 2H_2O \rightarrow 2LiOH + H_2$. The pressure of evolved hydrogen acted as a separation force causing the exfoliation of single graphite layers. The exfoliated graphite sheets were stuck on a solid substrate (glass or alumina) upon sintering above 300 °C. The obtained graphite films were highly resistive and their electric resistance depended strongly on the sintering temperature. Some reactive sites existed in the films and were connected with immobilized Pt (or Pd) particles that served as adsorption centres for molecular hydrogen and oxygen. The adsorption of hydrogen led to its dissociation and the release of electrons: $H_{2(gas)} + 2Pt^0 \leftrightarrow 2Pt{:}H \rightarrow 2Pt^0 + 2H^+ + 2e$.

Since the adsorption of hydrogen on Pt particles was a chemical process, it was accompanied by the formation of H^+ ions and the transfer of electrons from hydrogen to Pt. The fabricated graphite-based sensors exhibited good sensitivity to the chemical signal consisting of 300 ppm of hydrogen in air at 110 °C. The relation between sensors sensitivity and the concentration of H_2 in air was linear up to 300 ppm. Other reductive gases as CO, CH_4,

propane, alcohol vapours, and H_2S did not interfere the measurements of H_2 concentration probably since the temperature of operation was too low for the reduction of the mentioned species. The changes of electric conductance of the film upon hydrogen adsorption were significant since there was no inert "bulk" in the adsorbing film. In such conditions, the depth of surface zone of increased conductivity was comparable with the thickness of the whole film.

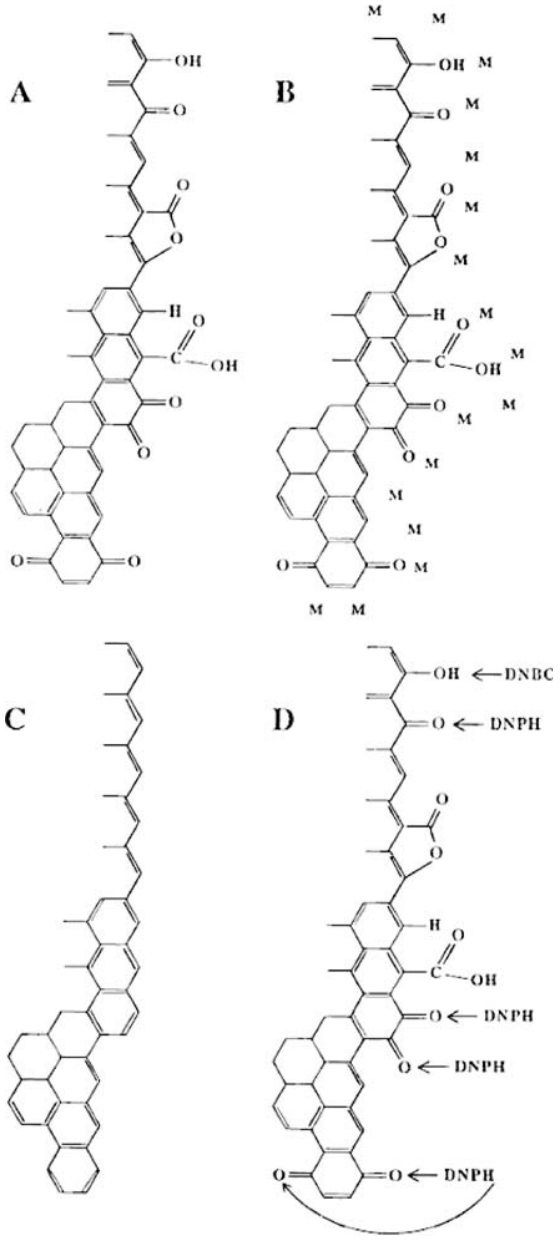

Fig. 70. Normally polished and desired GC surfaces: (A) normally polished GC surface, (B) GC surface covered by a monolayer absorber, (C) oxide-free GC surface, and (D) GC surface on which carbonyl and hydroxyl groups are derivatized. Reprinted with permission from [102], P. Chen and R. L. McCreery, *Anal. Chem.* 68, 3958 **(1996)**. © 1996, American Chemical Society.

3. CONCLUSIONS

Chemical sensors are of great importance for improved medical care, control of industrial processes, and ensuring environmental safety to name but a few applications. We review the field of chemical sensors based on the use of carbon-based materials; selected methods of carbon preparation are considered, as well as the most recent announcements on application of carbon to chemical sensing. We review how the chemical properties of the carbon surface can be controlled, and how these properties influence the application of carbon materials to the construction and use of chemical sensors. This paper reviews application of different carbon materials, including graphite, polycrystalline carbon, carbon black, and carbon nanotubes, to the construction of chemical sensors. Basic chemical properties of carbons are presented as well as selected synthesis methods. Different ways of carbon surface functionalization are considered in relation to chemical sensing properties.

Acknowledgments: The review was prepared based primarily on a grant by the Rector of Nicholas Copernicus University of Torun (Poland).

References and Notes

1. M. Inagak, New Carbons. *Control of Structure and Functions*, Elsevier, Amsterdam **(2000)**, p. 11.
2. J. C. Bokros, Chemistry and Physics of Carbon, edited by P. L. Walker, Jr., M. Dekker, New York **(1969)**, Vol. 5.
3. J. W. Gilman, D. L. Vander Hart, and T. Kashiwagi, Material and Test for Hazard Prevention, American Chemical Society. ACS Symposium Series 599, Thermal Decomposition Chemistry of Poly(vinyl alcohol), Washington **(1994)**.
4. M. Inagaki, New Carbons. *Control of Structure and Functions* Elsevier, Amsterdam **(2000)**, p. 9.
5. M. Inagaki, New Carbons. *Control of Structure and Functions* Elsevier, Amsterdam **(2000)**, p. 124.
6. C. N. R. Rao, B. C. Satishkumar, A. Govindaraj, and M. Nath, *Chem. Phys. Chem.* 2, 78 **(2002)**.
7. V. A. Garten and D. E. Weiss, *Australian J. Chem.* 10, 309 **(1957)**.
8. J. S. Mattson and H. B. Mark, Jr., Activated Carbon, M. Dekker, New York **(1971)**.
9. H. P. Boehm, *Adv. in Catalysis* 16, 179 **(1966)**.
10. K. Laszlo, K. Josepovits, and E. Tombacz, *Anal. Sci.* 17, i1741 **(2001)**.
11. H. Jankowska, A. Swiatkowski, L. Starostin, and J. Ławrinienko-Omiecynska, Adsorpcja jonów na weglu aktywnym (in Polish), PWN, Warsaw **(1991)**, p. 88.
12. S. Biniak, G. Szymanski, J. Siedlewski, and A. Swiatkowski, *Carbon* 35, 1799 **(1997)**.
13. M. Inagaki, New Carbons. *Control of Structure and Functions*, Elsevier, Amsterdam **(2000)**, p. 88.
14. G. Szymanski and G. Rychlicki, *Carbon* 29, 489 **(1991)**.
15. G. Szymanski and G. Rychlicki, *React. Kinet. Catal. Lett.* 43, 475 **(1991)**.
16. G. Szymanski, T. Grzybek, and H. Papp, *Catal. Today*, (in print).
17. J. P. Lukaszewicz, *J. Mater. Sci.* 32, 6063 **(1997)**.
18. S. Wang and G. Q. Lu, *Carbon* 36, 283 **(1998)**.
19. M. Molina-Sabio, F. Rodriguez-Reiniso, F. Caturla, and M. J. Selles, *Carbon* 34, 457 **(1996)**.
20. E. Auer, A. Freund, J. Pietsch, and T. Tacke, *Appl. Catalysis A: General* 173, 259 **(1998)**.

21. I. Mochida, Y. Korai, M. Shirahama, S. Kawano, T. Hada, Y. Seo, M. Yosikawa, and A. Yasutake, *Carbon* 38, 227 **(2000)**.
22. A. Kuznetsova, I. Popova, J. T. Yates, Jr., M. J. Bronikowski, Ch. B. Huffman, J. Liu, R. E. Smalley, H. H. Hwu, and J. G. Chen, *J. Am. Chem. Soc.* 123, 10699 **(2001)**.
23. A. Kuznetsova, J. T. Yates, Jr., J. Liu, and R. E. Smalley, *J. Chem. Phys.* 112, 9590 **(2000)**.
24. P. G. Collins, K. Bradley, M. Ishigami, and A. Zettl, *Science* 287, 1801 **(2000)**.
25. H. Hu, P. Bohowmik, B. Zhao, M. A. Hamon, M. E. Itkis, and R. C. Haddon, *Chem. Pys. Lett.* 345, 25 **(2001)**.
26. Y. S. Lee, T. H. Cho, B. K. Lee, J. S. Rho, K. H. An, and Y. H. Lee, *J. Fluor. Chem.* 120, 99 **(2003)**.
27. Y. K. Chen, A. Chu, J. Cook, M. L. H. Green, P. J. F. Harris, R. Heesom, M. Humphries, J. Sloan, S. C. Tsang, and J. F. C. Turner, *J. Mat. Chem.* 7, 545 **(1997)**.
28. C. N. R. Rao, G. U. Kulkarni, A. Govindaraj, B. C. Satishkumar, and P. J. Thomas, *Pure Appl. Chem.* 72, 21 **(2000)**.
29. Z. J. Liu, Z. Y. Yuan, W. Zhou, L. M. Peng, and Z. Xu, *Phys. Chem. Chem. Phys.* 3, 2518 **(2001)**.
30. P. M. Ajayan and Ijima, *Nature* 361, 333 **(1993)**.
31. B. C. Satishkumar, E. M. Vogl, A. Govindaraj, and C. N. R. Rao, *J. Phys. D: Appl. Phys.* 29, 3173 **(1996)**.
32. J. Sloan, J. Cook, M. L. H. Green, J. L. Hutchinson, and R. Tenne, *J. Mater. Chem.* 7, 1089 **(1997)**.
33. K. Bladh, L. K. L. Falk, and F. Rohmund, *Appl. Phys. A* 70, 317 **(2000)**.
34. P. Chen, X. Wu, J. Lin, and K. L. Tan, *Science* 285, 5424 **(1999)**.
35. W. Q. Han and A. Zettl, *Nano Lett.* 3, 681 **(2003)**.
36. J. W. Seo, E. Couteau, P. Umek, K. Hernadi, P. Marcoux, B. Lukic, C. Miko, M. Milas, R. Gaal, and L. Forro, *New J. Phys.* 5, 120.1 **(2003)**.
37. J. K. Lim, W. S. Yun, M. Yoon, S. K. Lee, C. H. Kim, K. Kim, and S. K. Kim, *Synth. Mater.* 139, 521 **(2003)**.
38. J. Liu, A. G. Rinzler, H. J. Dai, J. H. Hafner, R. K. Bradley, P. J. Boul, A. Lu, T. Iverson, K. Shelimov, C. B. Huffman, F. R. Macias, Y. S. Shon, T. R. Lee, D. T. Colbert, and R. E. Smalley, *Science* 280, 1253 **(1998)**.
39. W. Qikun, Z. Changchun, L. Weihua, and W. Ting, *Int. J. Hydr. Chem.* 27, 497 **(2002)**.
40. Y. Q. Wang, *J. Phys. Chem. B* 1999, 103, 4809 **(1999)**.
41. A. Star, D. W. Steuerman, J. R. Heath, and J. F. Stoddart, *Angew. Chem. Int. Ed.* 41, 2508 **(2002)**.
42. B. Zhao, H. Hu, and C. Haddon, *Adv. Funct. Mater.* 14, 71 **(2004)**.
43. M. Sano, A. Kamini, J. Okamura, and S. Shinkai, *Science* 293, 1299 **(2002)**.
44. M. M. Dubinin, Progress in Surface Membrane Science, Academic Press, New York **(1975)**.
45. O. K. Varghese, D. Gong, M. Paulose, K. G. Ong, C. A. Grimes, and E. C. Dickey, *J. Mater. Res.* 17, 1162 **(2002)**.
46. M. Inagaki, New Carbons. *Control of Structure and Functions* Elsevier, Amsterdam **(2000)**, p. 130.
47. H. Teng, T. S. Yeh, and L. Y. Hsu, *Carbon* 36, 1387 **(1998)**.
48. J. Ozaki, N. Endo, W. Ohizomi, K. Igarashi, M. Nakahara, A. Oya, S. Yoshida, and T. Iizuka, *Carbon* 35, 1031 **(1997)**.
49. A. Tamon, Personal communication to Kyotami.
50. T. Kyotami, N. Sonobe, and A. Tomita, *Nature* 331, 331 **(1988)**.
51. J. H. Knox and M. T. Gilbert, Preparation of Porous Carbon US Patent 4,263,268 **(1981)**.
52. S. Mrozowski, *J. Chem. Phys.* 21, 492 **(1953)**.
53. T. Koyama and M. Endo, *Jpn. J. Appl. Phys.* 13, 1175 **(1974)**.
54. K. Tsukagoshi, E. Watanabe, I Yagi, N. Yoneya, and Y. Aoyagi, *New J. Phys.* 6, 2 **(2004)**.
55. R. Saito, G. Dresselhaus, and M. S. Dresselhaus, Physical Properties of Carbon Nanotubes, Imperial College Press, London **(1998)**.
56. F. Kong and N. R. Franklin, *Science* 287, 622 **(2000)**.
57. L. Valentini, L. Lozzi, C. Cantalini, I. Armentano, J. M. Kenny, L. Ottaviano, and S. Santucchi, *Thin Solid Films* 436, 95 **(2003)**.
58. L. Valentini, C. Cantalini, L. Lozzi, I. Armentano, J. M. Kenny, and S. Santucchi, *Mater. Sci Engin.* C23, 523 **(2003)**.
59. C. Cantalini, L. Valentini, L. Lozzi, I. Armentano, J. M. Kenny, and S. Santucci, *Sens. Actuators B* 93, 333 **(2003)**.
60. J. Li, Y. Lu, Q. Ye, M. Cinke, J. Han, and M. Meyyappan, *Nano Lett.* 3, 929 **(2003)**.
61. J. Zhao and J. P. Lu, *Appl. Phys. Lett.* 82, 3746 **(2003)**.
62. W. L. Yim, X. G. Gong, and Z. F. Liu, *J. Phys. Chem B* 107, 9363 **(2003)**.
63. B. Y. Wei, M. C. Hsu, P. G. Su, H. M. Lin, R. J. Wu, and H. J. Lai, *Sens. Actuators B* 101, 81 **(2004)**.
64. K. H. An, S. Y. Jeong, H. R. Hwang, and Y. H. Lee, *Adv. Mater.* 16, 1005 **(2004)**.
65. J. Suehiro, G. Zhou, and M. Hara, *J. Phys. D: Appl. Phys.* 36, L109 **(2003)**.
66. Y. T. Jang, S. I. Moon, J. H. Ahn, Y. H. Lee, and B. K. Ju, *Sens. Actuators B* 99, 118 **(2004)**.
67. L. Valentini, I. Armentano, L. Lozzi, S. Santucchi, and J. M. Kenny, *Mater. Sci. Engin. C* 24, 527 **(2004)**.
68. M. Grujicic, G. Cao, and R. Singh, *Appl. Surf Sci.* 211, 166 **(2003)**.
69. Y. Lu, J. Li, J. Han, H. T. Hg, C. Binder, C. Partridge, and M. Meyyappan, *Chem. Phys. Lett.* 391, 344 **(2004)**.
70. J. P. Novak, E. S. Snow, E. J. Houser, D. Park, J. L. Stepnowski, and R. A. McGill, *Appl. Phys. Lett.* 83, 4026 **(2003)**.
71. J. Cui, M. Burghard, and K. Kern, *Nano Lett.* 3, 613 **(2003)**.
72. V. Bavastrello, E. Stura, S. Carrara, V. Erokhin, and C. Nicolini, *Sens. Actuators B* 98, 247 **(2004)**.
73. V. G. Gavalas, S. A. Law, J. C. Ball, R. Andrews, and L. G. Bachas, *Anal. Biochem.* 329, 247 **(2004)**.
74. S. Sotiropoulu, V. G. Gavalas, V. Vamvakaki, and N. A. Chaniotakis, *Biosens. Bioelectron.* 18, 211 **(2003)**.
75. M. Weinecke, M. C. Bunescu, M. Pietrzak, K. Deistung, and P. Fedtke, *Synth. Met.* 138, 165 **(2003)**.
76. K. B. Male, S. Hrapovic, Y. Liu, D. Wang, and J. H. T. Luong, *Anal. Chim. Acta* 516, 35 **(2004)**.
77. K. Wu, Y. Sun, and S. Hu, *Sens. Actuators B* 96, 658 **(2003)**.
78. Y. D. Zhao, W. D. Zhang, Q. M. Luo, and S. F. Y. Li, *Micromech. J.* 75, 189 **(2003)**.
79. J. B. He, C. L. Chen, and J. H. Lui, *Sens. Actuators B* 99, 1 **(2004)**.
80. P. Liu and J. Hu, *Sens. Actuators B* 84, 194 **(2002)**.
81. P. He and L. Dai, *Chem. Comm.* 348 **(2004)**.
82. J. S. Ye, Y. Wen, W. D. Zhang, H. F. Cui, L. M. Gan, G. Q. Xu, and F. S. Sheu, *J. Electroanal. Chem.* 562, 241 **(2004)**.
83. T. Ono, X. Li, and H. Miyashita, *Rev. Sci. Instrum.* 74, 1240 **(2003)**.
84. B. Y. Wei, C. S. Lin, and H. M. Lin, *Sens. Mater.* 15, 177 **(2003)**.
85. M. Penza, F. Antolini, and M. V. Antisari, *Sens. Actuators B* 100, 47 **(2004)**.
86. S. Chopra, A. Pham, J. Gaillard, A. Parker, and A. M. Rao, *Appl. Phys. Lett.* 80, 4632 **(2002)**.
87. K. G. Ong and C. Grimmes, *Sensors* 1, 193 **(2001)**.
88. O. K. Varghese, P. D. Kichambre, D. Gong, K. G. Ong, E. C. Dickey, and C. A. Grimes, *Sens. Actuators B* 81, 32 **(2001)**.
89. K. G. Ong, K. Zeng, and C. A. Grimes, *IEEE Sens. J.* 2, 82 **(2002)**.
90. Y. M. Wong, W. P. Kang, J. L. Davidson, A. Wisitsora-at, and K. L. Soh, *Sens. Actuators B* 93, 327 **(2003)**.
91. J. R. Chen, S. Bangsaruntip, K. A. Drouvalakis, N. W. S. Kam, M. Shim, Y. Li, W. Kim, P. J. Utz, and H. Dai, *PNAS* 100, 4984 **(2003)**.
92. G. U. Sumanasekera, B. K. Pradham, C. K. Adu, H. E. Romero, H. C. Foley, and P. C. Eklund, *Mol. Cryst. Liq. Cryst.* 387, 255 **(2002)**.
93. N. A. El-Maali and J. Wang, *Sens. Actuators B* 76, 211 **(2001)**.

94. Q. Yao, S. Yabuki, and F. Mitzutani, *Sens. Actuators B* 65, 147 **(2000)**.
95. F. Ge, R. C. Tenent, and D. O. Wipf, *Anal. Sci.* 17, 27 **(2001)**.
96. F. Zee and J. W. Judy, *Sens. Actuators B* 72, 120 **(2001)**.
97. M. C. Lonergan, E. Severin, B. J. Doleman, S. A. Beaber, R. H. Grubb, and N. S. Lewis, *Chem. Mater.* 8, 2298 **(1996)**.
98. J. A. Dickinson and R. M. Goodman, *IEEE International Symposium of Circuits and Systems* (*ISCAS'2000*), Geneva **(2000)**, p. 341.
99. N. Tsubokawa, M. Tsuchida, J. Chen, and Y. Nakazawa, *Sens. Actuators B* 79, 92 **(2001)**.
100. J. Razumiene, V. Gureviciene, V. Laurinavicius, and J. V. Grazulevicius, *Sens. Actuators B* 78, 243 **(2001)**.
101. B. Matthews, J. Li, S. Sunshine, L. Lerner, and J. W. Judy, *IEEE Sensor. J.* 2, 160 **(2002)**.
102. P. Chen and R. L. McCreery, *Anal. Chem.* 68, 3958 **(1996)**.
103. B. K. Miremadi and K. Colbow, *Sens. Actuators B* 46, 30 **(1998)**.

SENSOR LETTERS
Vol. 4, 99–119, 2006

REVIEW

Boron-Doped Diamond-Based Sensors: A Review

Orawon Chailapakul[1], Weena Siangproh[2], and Donald A. Tryk*, †

[1] Sensor Research Unit, Department of Chemistry, Faculty of Science, Chulalongkorn University, Bangkok 10330, Thailand
[2] Department of Chemistry, Faculty of Science, Srinakharinwirot University, Bangkok, Thailand

(Received: 13 January 2005. Accepted: 30 January 2006)

Electrically conductive, boron-doped diamond (BDD) films, prepared by means of chemical vapor deposition, have been studied intensively just over the past ten years as electrode materials for electrochemistry. During this time, it has become apparent that BDD films are in many ways ideal for high-sensitivity analytical measurements of a wide variety of inorganic and organic species, opening the door to a host of sensor applications. The techniques for preparing micro-scale and nano-scale electrodes have also been developed, which will further widen the sensor possibilities. Preparation and characterization techniques, as well as recent developments in specific inorganic and organic determinations, are reviewed.

Keywords: Boron-Doped Diamond, Electrochemistry, Diamond Electrodes, Amperometric Sensors.

CONTENTS

1. INTRODUCTION

Electrochemical sensors are electrical sensors that usually involve an interface between a solid or liquid electronically conducting phase (the electrode) and a solid or liquid ionically conducting phase (the electrolyte).[1–6] The types of electrical measurements that can be made include potential, current, charge, capacitance, conductance, and impedance. In the present review, we will focus on current-based measurements at solid electrodes in liquid electrolytes.

In the case of current-based electrochemical measurements, there is usually an electron transfer (ET) process that can occur at a discrete potential.[7] Often, the latter can be related, albeit indirectly at times, to the standard potential for the ET that involves the species of interest. This aspect can provide some chemical information, as in the oxidative (anodic) stripping of mixtures of metals deposited on the electrode. In many cases, however, this aspect is not important, as in the non-specific oxidation of organic compounds that have already been separated chromatographically or electrophoretically.

In current-based measurements, the electrode itself should interfere as little as possible with the measurement. There are several sources of current that can be traced to the electrode; these include

(1) oxidation and reduction of the solvent;

(2) oxidation and reduction of the electrolyte ions;

(3) adsorption of ions on the electrode surface accompanied by ET;

(4) bulk oxidation or reduction of the electrode material; and

(5) charging and discharging of the electrochemical double layer at the solid-liquid interface.

All of these sources are more or less electrode material-dependent. For example, platinum is highly catalytic for oxidation and reduction processes involving water as a solvent (type 1), processes involving hydrogen and hydroxide adsorption (type 3), a near-surface oxidation process that occurs at highly positive potentials (type 4), and double-layer charging (type 5). In fact, the intrinsic electrochemistry of platinum in aqueous solution has been intensively studied (see, e.g., the work of Clavilier and coworkers.[8]) In a second, contrasting example, glassy carbon and pyrolytic

*Corresponding author; E-mail: tryk@comp.metro-u.ac.jp
†Present Address: Department of Applied Chemistry, Metropolitan University, Minami-Ohsawa, Hachiohji, Tokyo 192-0397, Japan.

graphite have little catalytic activity for type 1 reactions involving water, little activity for type 3 processes,[9] but they can undergo progressive type 4 oxidation of the surface.[10] In addition, due to the slightly porous nature of the material, the current for type 5 (double layer charging) can be relatively large.

Recently, electrically conductive films of boron-doped chemical vapor-deposited (CVD) diamond have gained popularity in a variety of electrochemical applications, in large part due to the fact that the electrode-based currents are relatively small.[11–15] In fact, for very high quality films, the currents can be orders of magnitude smaller than those for other types of electrode materials.[16] The catalytic activity for water oxidation/reduction (type 1) is very small.[17] The ability to undergo hydrogen adsorption (type 3) is small. The ability to undergo covalent attachment of hydroxyl or carbonyl oxygen is significant at highly positive potentials, but it appears that the surface is not progressively oxidized (type 4), as in the case of sp^2-type carbons and graphites but stops after the modification of the top layer of carbon atoms.[18] The currents for double layer charging (type 5) are quite small, due to the low number of carriers and the nearly complete lack of porosity. These attributes make conductive diamond well suited for current-based electrochemical measurements. Recently, the use of diamond as an electrode material in electrochemistry has been extensively reviewed.[19]

In the next section, we shall briefly review the preparation and characterization of conductive diamond films, principally of the boron-doped type. In the subsequent two sections, we shall review the use of diamond film electrodes as electrochemical sensors for inorganic species and organic species, respectively.

2. PREPARATION AND CHARACTERIZATION

2.1. Preparation and Availability of Conductive Diamond Films by CVD Processes

There are several possible methods for preparing CVD diamond films, which have been reviewed recently.[20]

Orawon Chailapakul is an Associate Professor in the Department of Chemistry, Faculty of Science, Chulalongkorn University. She received her B.Sc. in Chemistry from Mahidol University in 1982, the M.Sc. from Chulalongkorn University in 1987, and the Ph.D. from the University of New Mexico in 1994. Presently, she is a member of the Materials Chemistry and Catalysis Research Unit and the Sensor Research Unit. Her research interests include diamond electrochemistry, chemical sensors and biosensors, labs-on-a-chip, and nanomaterials and their applications in food and environmental science.

Weena Siangproh received her Bachelor of Science (Chemistry) from Srinakharinwirot University in 1998. She is a Lecturer in the Department of Chemistry, Faculty of Science, Srinakharinwirot University, Thailand. At present, she is pursuing her doctoral research, supported by The Thailand Research Fund through the Royal Golden Jubilee Ph. D. Program, at the Department of Chemistry, Faculty of Science, Chulalongkorn University, Thailand, under the direction of Associate Professor Orawon Chailapakul. Her research interests include diamond electrochemistry, microchip capillary electrophoresis, and nanomaterials and their applications in electroanalysis.

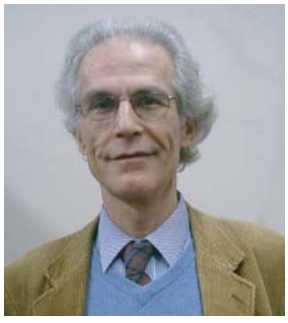

Donald A. Tryk graduated from the University of Florida in 1969 with a Bachelor of Science in Chemistry and from the University of New Mexico in 1980 with a Doctorate in Chemistry. From there, he went on to Case Western Reserve University, where he was a Senior Research Associate in the Chemistry Department until 1995. He was at the University of Tokyo as a Research Associate and Special Associate Professor in the group of Professor Akira Fujishima until 2001. He was then a Visiting Professor, first at Tokyo Metropolitan University in the Department of Applied Chemistry, in the group of Professor Haruo Inoue, then in 2003 at the University of Puerto Rio, and then again, in 2005, at Tokyo Metropolitan University. His research interests include analytical electrochemistry, electrocatalysis, photoelectrochemistry, and photocatalysis. He is particularly interested in the use of diamond as an electrode material, as well as the development of biomimetic electrocatalysts for redox reactions such as those involving dioxygen, dihydrogen, and carbon dioxide.

The principal methods are hot-filament CVD,[21] microwave plasma CVD,[22] radio-frequency plasma CVD[23] and arc-jet.[24] The hot filament and microwave methods have been used extensively to prepare boron-doped films. Boron can be introduced in any of several forms, e.g., solids that are placed in the CVD chamber, including boron metal,[25] boron nitride and boron-containing ceramics,[26] gases introduced into the chamber, including diborane[27] or trimethylborane,[28] or as a compound dissolved in a spray of liquid droplets, e.g., boron oxide, dissolved in a mixture of methanol and acetone entrained in the hydrogen feed gas.[29] Films can be prepared in one of several possible particle sizes, depending upon the growth conditions, ranging from microcrystalline (MCD), with crystallites typically in the 1–10 μm range[30] to nanocrystalline (NCD), with particles in the range below 1 μm,[27,31] down to ultra-nanocrystalline (UNDC), with particles in the range down to 1 nm.[32,33] There are several commercial suppliers of boron-doped MCD films, including Element Six (UK), Condias (Germany), Sumitomo (Japan) and sp3 Diamond Technologies (USA).

The most commonly used form of conductive diamond that has been used for analytical purposes is the boron-doped MCD CVD film, which we will refer to simply as boron-doped diamond (BDD). Films typically exhibit a somewhat random arrangement of crystal grains that are on the order of 1–10 μm in diameter (Fig. 1). The microcrystals usually present either a rectangular (100) or a triangular (111) face on the polycrystalline surface. These faces are known to incorporate boron from the gas phase at different rates during the growth process, with the (111) faces taking up a higher concentration.[34] This leads to a situation in which the ET process may be carried predominantly by the more highly doped (111) faces,[35] which can lead to electrochemical behavior that tends toward that of a microelectrode array, i.e., sigmoidal voltammograms at slow potential sweep rates.[36,37]

The microcrystalline surface can also be polished to a high degree of smoothness by combined chemical-mechanical techniques, for example. Not much work has been published on the electrochemical behavior of these polished surfaces, although some results have appeared as part of articles that have dealt with nanotextured surfaces.[38] In most cases, the analytical techniques that have been reported do not involve the need to mechanically polish the electrode surface. The range of possible applications will probably be greater if polished films are available. However, NCD and UNDC films are also highly smooth as deposited and circumvent the polishing process.

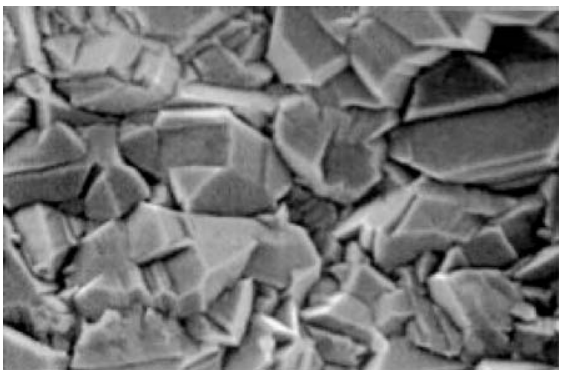

Fig. 1. Scanning electron micrograph of a microcrystalline, boron-doped CVD diamond film.

One of the attractive attributes of diamond films is that they have little tendency to adsorb species from solution and consequently there is little buildup of films,[39] so that there is not a strong incentive to physically polish the electrode. Any films that adhere can usually be removed by maintaining a positive, oxidizing potential for a few seconds to minutes.[40]

Another type of diamond surface that can be used in sensor devices is the non-doped, hydrogen-terminated film. This type of surface possesses surface conductivity that can be used as the basis for a conductimetric sensor directly in the gas phase[41,42] or in liquid solution phase, either as an electrode in a simple electrochemical measurement or with a fabricated metal-semiconductor field-effect transistor (MESFET), as described in a later section. Non-doped CVD films can be used after suitable preparation, which can involve treatment in strong acid to remove non-diamond carbon, followed by a brief rehydrogenation in a pure hydrogen plasma (see, e.g., Refs. [43–45]). Even non-doped synthetic and natural single crystals can be hydrogenated by placing them in a CVD chamber and treating them in a hydrogen-containing plasma.[45,46] The hydrogenation step converts the oxygen termination, which is typical for the acid-treated surface, as well as for polished diamond, to hydrogen termination. Some authors have argued that this type of procedure also introduces hydrogen into a thin region just below the surface, in a layer that could be on the order of a few nanometers[43,47] up to several hundred nanometers,[46,48–50] in which the hydrogen acts as a *p*-type dopant. Others have argued that the surface termination by itself is sufficient to impart conductivity.[45,51,52] Differences in the various types of pretreatments no doubt lead to differences in the resulting depth distribution or lack thereof. The subject of surface conductivity will be discussed later in terms of the types of specific sensors.

Another dopant that can be used to produce conductive films is sulfur, with *n*-type conduction. Sulfur is usually thought to be a deep donor, i.e., one that has an activation energy that is too large for room-temperature conductivity, but, after some initial controversy,[53–55] it has become recognized recently that it can be a shallow donor, i.e., a room-temperature conductor,[51,56–58] perhaps due to the formation of sulfur-hydrogen[59] or sulfur-vacancy pairs.[56] Thus far, sulfur-doped diamond films have not been used for electrochemistry, with the exception of one report,[60]

but there is preliminary work on its use in the surface conductance mode as a sensor (see later).

Modified diamond surfaces are becoming more and more extensively used recently. The modification techniques, which include chemical, electrochemical, and photochemical techniques, have been reviewed recently;[61] these include ways of attaching anything from terminating atoms, such as oxygen,[62–64] chlorine,[65,66] nitrogen,[65,66] or fluorine,[67–69] all the way to proteins[70] and DNA strands,[71–73] as well as metal particles[74–77] and metal oxides.[78–82] New ones are continually being reported. Some of the specific modified surfaces will be mentioned later in the context of the analytical methods.

2.2. Characterization of Conductive Diamond Films

2.2.1. Microscopy

The quality of microcrystalline CVD films is conveniently assessed with SEM, to ensure that the crystallinity is good. For example, in Figure 1, the presence of various types of crystalline morphologies can be seen. Typically, the (111)-type grains are darker, which correlates with the previously mentioned tendency of this grain type to incorporate higher levels of boron; the (100)-type grains are lighter. This produces a characteristic pattern of light and dark areas. SEM is also a good technique with which to examine the surface after the deposition of metal particles.[74–76,83]

2.2.2. Raman Spectroscopy

Raman is an essential characterization technique: one of the routine ways Raman is used is to gauge the presence of sp^2 carbon, which shows up typically as a very broad peak centered at ca. 1600 cm^{-1}, while diamond itself has a highly characteristic peak, due to the principal phonon mode, at very close to 1332 cm^{-1} Refs. [84–86]. This peak is extremely intense for highly crystalline diamond. The presence of a high concentration of boron as a dopant leads to an increase in a broad peak at ca. 1200 cm^{-1}. This peak is thought to be due to the presence of either very small crystalline domains of diamond or disordered diamond,[84] either of which could result from the perturbation of the structure by the boron dopant atoms.

2.2.3. X-Ray Photoelectron Spectroscopy

The surface termination of the diamond film, whether hydrogen or oxygen, can affect the electrochemical properties greatly.[62–64,87–90] This can be established through the use of x-ray photoelectron spectroscopy (XPS). The O 1s/C 1s peak area ratio typically reaches a maximum of 0.10 to 0.15 with increased time of oxidizing treatment, for example, electrochemical oxidation.[64] This may correspond approximately to a monolayer coverage with oxygen-containing functional groups. It is possible to attain higher O/C ratios with oxygen plasma treatment, but this type of aggressive treatment may lead to surface damage, e.g., graphitization,[18] similar to the type of damage observed even with bombardment with light ions such as D^+ and He^+ Refs. [18, 91]. XPS is a useful technique for the examination of chemically modified diamond surfaces, particularly if the modifier contains characteristic elements, e.g., N, Si[18] or F.[92]

3. DETECTION AT BORON-DOPED DIAMOND ELECTRODES

3.1. Detection of Inorganic Species

The use of BDD films for the detection of inorganic species makes particular use of the extremely wide potential range. Such films have been used as working electrodes to detect various kinds of metals, including Pb, Cd, Cu, Ag, and Hg, typically with the use of anodic stripping voltammetry (ASV). Cations such as Ce^{3+} and anions such as nitrite and azide were also investigated. In the context of such analyses, new methods, including abrasive anodic stripping voltammetry, as well as ultrasonic activation (sonoelectroanalysis) and microwave activation, have also been introduced.

3.1.1. Detection of Ionic Species and Dissolved Gases

Because of the extended potential range in the positive direction, the cyclic voltammetric response of Ce^{3+} ions in aqueous sulfuric acid, nitric acid, and perchloric acid solutions was investigated at highly doped BDD electrodes.[93] The concentration dependence was studied voltammetrically, as shown in Figure 2. The diffusion coefficients and electron transfer kinetic parameters can be conveniently determined in a way that is not possible with other types

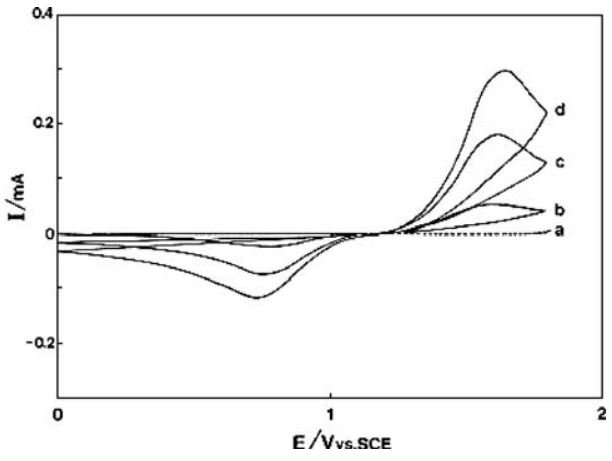

Fig. 2. Cyclic voltammograms in 0.1 M H_2SO_4 at a BDD electrode for various $Ce_2(SO_4)_3$ concentrations: (a) 0 mM, (b) 1 mM, (c) 3 mM, and (d) 5 mM; potential sweep rate, 10 mV s^{-1}; temperature, 25 °C.

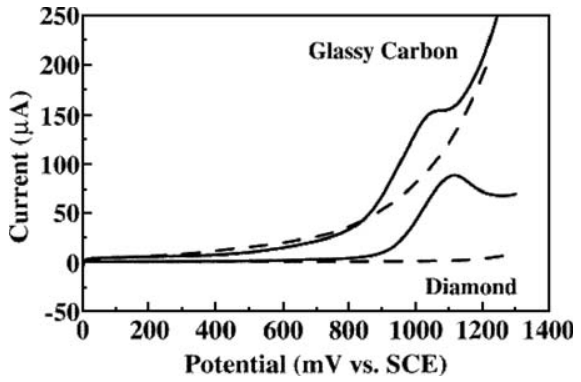

Fig. 3. Linear sweep voltammetric $i-E$ curves for freshly polished glassy carbon and a diamond thin film (D803961) in 1 mM NaN_3/0.1 M phosphate buffer, pH 7.2. The total and background currents are shown for both electrodes; sweep rate, 100 mV s^{-1}.

of electrodes, due to the interference of the background current. It was concluded that highly doped BDD is an excellent electrode material for the electrochemical analysis of species with highly positive redox potentials in aqueous solutions.

The azide anion dissolved in aqueous media was determined by Xu et al. with high-quality BDD thin-film electrodes.[94] The linear sweep, differential pulse voltammetric technique was employed to study the reaction at neutral pH as a function of the potential sweep rate, analyte concentration, and electrolyte composition. Figure 3 shows linear sweep voltammetric current-potential curves for glassy carbon (GC) and BDD in 1 mM NaN_3/0.1 M phosphate buffer (pH 7.2). A peak-shaped oxidation response was observed for both electrodes, but the background currents, upon which the Faradaic response is measured, were dramatically different. The background current for the GC electrode was significantly larger than that for BDD, with the difference at 1200 mV being a factor of approximately 200.

The lower background current for diamond at the potential for azide oxidation is a great advantage in its electroanalysis. Furthermore, when a BDD-based detector is coupled with a hydrodynamic system such as that for flow-injection analysis (FIA) or high-performance liquid chromatography, in the amperometric mode, it can be used to detect azide with very high sensitivity. This idea will be discussed in greater detail in the section on organic species. Thus, BDD can serve as an analytically useful sensor for the detection of azide anion and exhibits superior performance characteristics compared with GC.

The detection of sulfide through the electrocatalytic oxidation of ferrocyanide to ferricyanide at a BDD electrode with the use of both cyclic voltammetry and chronoamperometry was reported by the Compton group.[95] The analytical utility has been compared with that of other common electrode substrates (Pt, Au, glassy carbon). The high oxidation potential for the direct oxidation of sulfide at a BDD electrode allows clear resolution of the ferrocyanide and sulfide oxidation waves, with the result being a clearly distinguishable analytical signal at the oxidation peak potential for ferrocyanide. This procedure was used to determine the % recovery of a sulfide spike in a sewage effluent ($102 \pm 4.5\%$).

The surface conductivity phenomenon has been used to develop sensors for ionic species in solution, including the chloride ion by the Kawarada group,[96,97] and the hydrogen ion (pH) by Garrido et al.,[98] both with the use of MESFET devices. For the chloride ion response, the authors developed essentially an electrostatic model, in which the chloride ion attracts the majority carrier holes to the surface, creating higher surface conductivity. Increasingly negative drain-source currents at given drain-source voltages are observed for increasing chloride concentrations. In contrast, for the pH sensor, the authors report *decreasingly* negative drain-source currents for increasing hydrogen ion concentrations (decreasing pH values), again at given drain-source voltages, because the positively charged hydrogen ions repel the holes away from the surface. It is interesting to note that the chloride response requires a hydrogen-terminated surface, whereas the hydrogen ion response requires a partially oxygenated surface (via ozone treatment).

Not only can cations and anions be detected at BDD electrodes but also gases such as nitrogen oxides (NO and NO_2) dissolved in aqueous solution can be detected voltammetrically.[99] The voltammetric curves exhibit well-defined anodic peaks, with a response that is superior to that obtained with GC electrodes. In addition, it was found that the anodic voltammetric peak for the oxidation of the nitrite anion is well defined and suitable for analytical applications. The conclusion was that BDD is promising for the detection of these nitrogenous species.

The surface conductivity effect can also be used to detect species in the gas phase, with the conductivity being measured by use of a two-point probe technique. Ri et al. studied this effect in a series of papers.[41,100,101] In their first paper, they examined the effects of acidic vapors (HCl) and basic vapors (NH_3) and found that the former increased the conductivity, whereas the latter decreased it.[101] Their model was essentially the same as that discussed above, i.e., electrostatic attraction or repulsion of holes from the surface. In their second paper, they examined a set of oxidizing gases (NO_2, HCl, and O_3), finding increased conductivity, and a reducing gas (NH_3), which decreased the conductivity.[41] Here, the model is more complicated, because it is considered to involve electron transfer; for example, NO_2 is reduced to NO_2^- at the surface, whereupon it acts electrostatically to attract holes to the surface. In a third paper, the authors support their model with Hall effect measurements of the carrier concentrations in the presence of NO_2 and NH_3.[100]

In recent work by Gonzalez et al., a similar effect has been studied with oxygen gas dissolved in aqueous

solution.[102] This work is based on the suggestion by Chakrapani et al. that oxygen should be an oxidizing species,[42] in the same sense as used by Ri et al. above.[41, 100] Indeed, it was found that dissolved oxygen leads to higher electrochemical currents for hydrogen evolution for non-doped (*p*-type) films, whereas it leads to lower currents for sulfur-doped (*n*-type) films. The proposed mechanism involves the reduction of O_2 to the superoxide radical anion $O_2^{\cdot-}$, which can then electrostatically attract the majority carrier holes toward the surface of *p*-type non-doped films, whereas it repels the electrons in sulfur-doped *n*-type films. When the carriers are close to the electrode surface, they are more easily transferred to the protons in solution, and thus the hydrogen evolution current increases. Clearly, when the carriers are further from the surface, ET is more difficult, and the current is smaller. The possible relationship of these results to the surface conductivity effect and the "transfer-doping model" of Ristein et al.[51, 52] has not been entirely established.

3.1.2. Chemically Modified Diamond Electrodes

The chemical modification of the BDD surface can provide enhanced sensitivity and selectivity for the detection of various species. Several approaches for modification have been developed thus far; these include surface oxidation, attachment of organic functional groups, attachment of biomolecules and the deposition of metal or metal oxide particles. These approaches have been reviewed recently.[61] These modified surfaces have been used more extensively for the analysis of organic and biochemical compounds, but some have also been used for inorganic species.

For example, hydrous iridium oxide (IrO_x) electrodeposition has been used for the modification of the BDD surface to selectively detect peroxide.[103] The electrodeposition technique allows the amount deposited to be precisely controlled, and thus highly reproducible electrochemical behavior can be achieved. The detection limit for H_2O_2 was ca. 10 times lower than that for bulk platinum electrodes. It was also found that IrO_x/BDD electrodes exhibit excellent, highly stable pH response over a wide pH range. The idea of using iridium oxide-modified BDD was also later taken up by the Compton group, for the trace analysis of As(III).[82]

3.1.3. Trace Metal Detection

The Fujishima group was the first to utilize unmodified BDD films for the electrochemical detection of trace concentrations of lead dissolved in aqueous solution by differential pulse anodic stripping voltammetry (DP-ASV).[104] Thus, this was one of the earliest, most successful examples of anodic stripping analysis of metals carried out without benefit of mercury. The stripping peak current was observed to increase linearly with increasing lead concentration, as shown in Figure 4. Lead concentrations down to

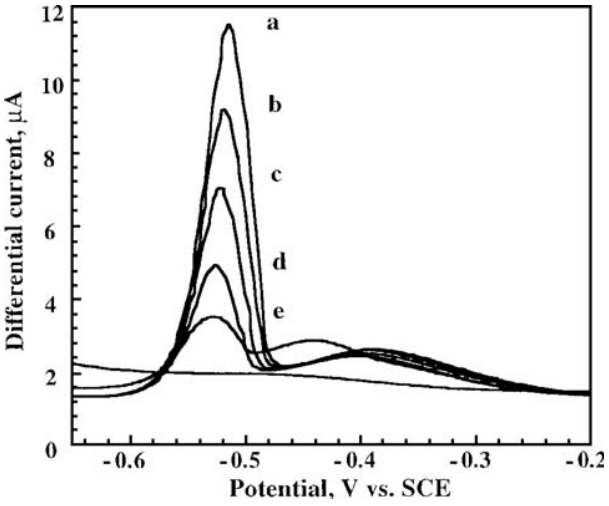

Fig. 4. DPASV for $Pb(NO_3)_2$ in 0.1 M KCl (pH 1), obtained for a highly doped diamond electrode after holding the potential at −1.0 V versus SCE for 2 min. The concentrations were (a) 2×10^{-6} M; (b) 1.6×10^{-6} M; (c) 1.2×10^{-6} M; (d) 8×10^{-7} M; (e) 4×10^{-7} M; and (f) background. The sweep rate was 20 mV s^{-1}, the pulse amplitude was 100 mV, and the sampling time was 10 ms.

4×10^{-9} M were detected. It should be noted that Goeting et al. had already examined lead deposition on BDD, but the concentrations used were higher, and the particles were probably larger, so that the stripping was not quantitative, due to possible problems with adhesion or poor electronic contact.[25] In the work of Manivannan et al., the stripping was found to be quantitative, probably because the particles were small enough to avoid problems with adhesion or contact.

The Compton group also found that boron-doped diamond can be used for mercury-free lead detection, but they used a slightly different approach, in which they anodically deposited the lead as lead dioxide and then cathodically stripped by reducing the PbO_2 to soluble Pb^{2+} Ref. [105]. These workers also used ultrasonic enhancement of the mass transport in order to achieve lower detection limits, as discussed later. The same group also developed a method for the detection of lead in blood using a bismuth film-modified BDD electrode.[106]

The Compton group examined the simultaneous detection of lead and copper in solution using ASV with BDD electrodes.[107] Peaks due to Cu and Pb were identified, and interactions between the two metals were studied. The results indicated that this technique could be used for the independent detection of Cu and Pb via conventional standard addition procedures. The Fujishima group also examined the problem of the simultaneous detection of two metals in solution, first with Pb and Cd[108] and then with Pb and Cu.[109] These workers also concluded that it is straightforward to simultaneously quantify two metals if the interactions are specifically taken into account. Foord et al. have also recently examined the interactions between Pb and Ag in detail.[110]

Interestingly, BDD electrodes were also used for the detection of mercury itself. Linear behavior was obtained in the mercury concentration range from 10^{-10} to 10^{-9} M with the use of the co-deposition of a small amount of gold, which was purposely added to the analyte solution in order to enhance the deposition of Hg.[111] Thus, the ASV technique, which makes use of bare polycrystalline diamond electrodes, shows great promise for the analysis of trace toxic metals.

3.1.4. Abrasive Stripping Voltammetry

The Fujishima group developed a novel approach for the electrochemical "fingerprinting" of a wide range of materials using abrasive stripping voltammetry (AbrSV) at BDD electrodes.[112] The rough, microcrystalline BDD surface was used to abrade the surfaces of metals and alloys, and small particles of the material were found to adhere to the electrode. These were then analyzed with anodic stripping. The abrasive stripping voltammetry of Pb and Fe samples and of a brass alloy sample was investigated.

The Compton group also investigated metal samples containing silver and tin using abrasive stripping voltammetry at BDD electrodes.[113] The mechanical and electrical contact of the abraded particles was dependent on the contact force used during the abrasion. Silver was found to be yield useful analytical results from the ASV measurements, but tin was found to be less reproducible.

3.1.5. Ultrasonic and Microwave Enhancement

The use of ultrasonic agitation of the analyte solution with BDD electrodes (sonoanalysis) is an interesting new approach to the enhancement of mass transport. As already mentioned, it has been used for the determination of lead via cathodic stripping.[105] It has also been used for the determination of silver, with the use of both cathodic and anodic stripping.[114] It was found that, after deposition of metallic silver on the bare BDD electrode surface under ultrasonic agitation, anodic stripping square-wave voltammetry could be used for the sensitive analysis of silver ions. The detection limit for Ag^+ was 10^{-9} M with a deposition time of 300 s.

The same group also determined Pb^{2+} using another novel technique, i.e., microwave activation.[115] The detection of Pb^{2+} in a 0.1 M HNO_3 solution was strongly enhanced by microwave activation of the deposition and stripping processes at the BDD electrode. The anodic stripping was carried out with square wave voltammetry. Pb concentrations in a water sediment sample were also measured; the results agreed well with those of two other independent analytical techniques, ICP mass spectroscopy and sono-cathodic stripping voltammetry.

3.2. Detection of Organic Compounds

BDD electrodes provide a very attractive means of measuring inorganic species; in many cases, these undergo reversible electron transfer. In addition, they can be used to measure a great variety of organic compounds; as well shall see, these can undergo either reversible or, in many cases, due to the complexity of the processes, irreversible electrochemical reactions. Many specific examples have been reported, and those published through 2003 have been summarized in earlier review articles.[11, 116–122] In the present review, we highlight some important developments and review more recent work.

3.2.1. Voltammetry, Flow Injection Analysis and Related Techniques

This section can be separated into separate topics based on the type of heteroatom contained in the organic compound: nitrogen, sulfur, and others, including oxygen and halogens.

3.2.1.1. Detection of Nitrogen-Containing Compounds Cyclic voltammetry was first used to examine the electron transfer reactions of organic redox-active analytes such as dopamine (DA) at BDD electrodes. In an early paper, the effect of surface pretreatment was studied at as-deposited and chemically oxidized diamond thin-film electrodes.[123] The measurement of the background current response and capacitance of interfaces formed at as-deposited polycrystalline BDD thin-film electrodes in contact with aqueous electrolytes was also performed.

In order to enhance the selectivity for dopamine detection in the presence of ascorbic acid (AA), cyclic voltammetric and chronoamperometric measurements were carried out at anodically treated BDD surfaces in alkaline solution.[11, 89, 117] These treatments resulted in the incorporation of substantial amounts of oxygen on the surface and substantial shifting in the positive direction for the peak potential for AA oxidation, as shown in Figure 5. Linear

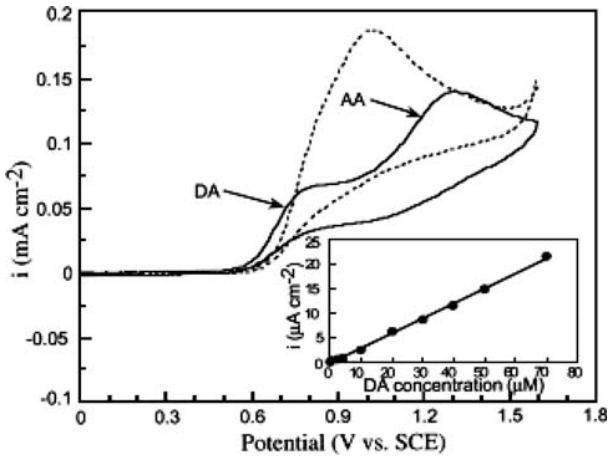

Fig. 5. Cyclic voltammograms for a mixture of 0.1 mM dopamine and 1 mM ascorbic acid in 0.1 M $HClO_4$ at untreated (dashed line) and treated diamond electrodes; sweep rate, 100 mV s^{-1}. Inset shows the calibration curve for dopamine in the presence of 1 mM ascorbic acid. Reprinted with permission from [11], T. N. Rao and A. Fujishima, *Dia. Rel. Mater.* 9, 384 (**2000**). © 2000, Elsevier Science.

calibration curves were obtained for both a higher concentration range (1–70 μM DA, 1 mM AA) and a lower range (0.1–1 μM DA, 0.1 mM AA), respectively. The detection limit appears to be on the order of 50 nM, which is among the lowest values reported.

To increase the sensitivity and efficiently eliminate interferences, highly boron-doped diamond microfiber electrodes (BDDMF) modified with highly oxidized polypyrrole were successfully fabricated and used as microsensors for the detection of dopamine in the presence of AA.[124] The limit of detection (signal/noise ratio, S/N = 3) for dopamine was 0.1 nM, which is one order of magnitude lower than that observed for carbon microfiber electrodes (CMFE), and a linear dynamic range was obtained from 0.5 nM to 100 μM ($r^2 = 0.997$). The amperometric response for 0.5 nM dopamine showed high stability, with a relative standard deviation (RSD) of 5.4% ($n = 5$). Highly reproducible results were obtained with an RSD of 6.2% for 10 measurements for 1 nM DA obtained over a 10-h period.

FIA with diamond thin-film detectors was employed to detect amines such as ethylamine, and ethylenediamine by the Swain group.[125] These redox reactions were studied by cyclic voltammetry, hydrodynamic voltammetry, and FIA with electrochemical detection (FIA-EC) at a BDD electrode. These workers proposed that the oxidation reactions involve the anodic transfer of an oxygen from H_2O. The cyclic voltammetry and FIA results for ethylamine are shown in Figure 6.

The oxidation of polyamines such as putrescine, cadaverine, spermine, and spermidine was investigated at polycrystalline BDD thin-film electrodes with the use of cyclic voltammetry and FIA with amperometric detection.[26] Well-resolved oxidation waves with respect to the background signal were observed. The mechanism proposed involved oxygen transfer from reactive OH radicals electrogenerated at non-diamond carbon impurity sites. The results showed that the BDD electrode can be used to effectively detect

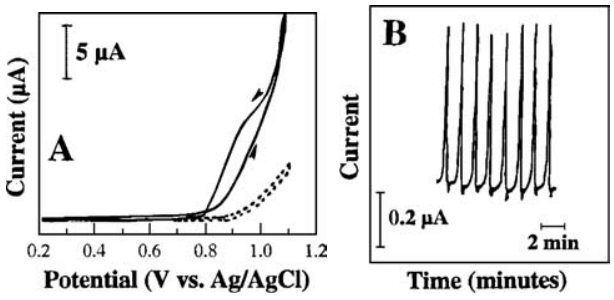

Fig. 6. (A) Cyclic voltammetric $i - E$ curves (background and total current) for a diamond film (D72696) in 1 mM ethylamine + 0.1 M $NaClO_4$/0.01 M carbonate buffer, pH 10; sweep rate, 20 mV s^{-1}. (B) FIA-EC results for a diamond film (D120795) using 20-μL injections of 0.25 mM ethylamine in 0.1 M carbonate buffer, pH 10. The mobile phase was 0.1 M carbonate buffer, pH 10, at a flow rate of 0.5 mL min^{-1}. Reprinted with permission from [125], S. Jolley et al., *Anal. Chem.* 69, 4099 (**1997**). © 1997, American Chemical Society.

polyamines with a detection limit of approximately 1 μM (S/N $\geq$ 3) and a linear dynamic range from 10^{-3} to 10^{-6} M ($r^2 > 0.97$).

The FIA-EC results for cadaverine (CAD), putrescine (PUT), spermine (SPM) and spermidine (SPMD) were reported with particular emphasis on the electrode response variability and stability.[126] Hydrodynamic voltammograms for these amine compounds are shown in Figure 7. A linear dynamic range from 1.0 μM to 1.0 mM and a detection limit of 1.0 μM (S/N $\geq$ 3) were found for CAD, PUT, and SPMD. For SPM, a linear dynamic range from 0.32 μM to 1.0 mM and a detection limit of 0.32 μM were observed. The improvement was achieved by introducing a 3–6-min delay period between injections; thereby, a response variability, as low as 2–4%, was observed. The extension of these results to include a chromatographic separation stage is straightforward, for example, with the use of a simple reverse-phase column.

The electrochemical detection of chlorpromazine and catecholamines was studied with high quality polycrystalline, hydrogen-terminated BDD thin films (3–6 μm thick).[127] Some preliminary results obtained in the amperometric detection mode, coupled with FIA and liquid chromatography (LC), were presented. BDD exhibited superior detector performance; for example, the detection limit (S/N = 3) for chlorpromazine at BDD was 4 nM, and the response variability was 0.3%, while for a GC electrode, the detection limit was 40 nM, and the response variability was 1%.

An important biogenic nitrogen-containing compound, nicotinamide adenine dinucleotide (NADH), was studied at as-deposited BDD electrodes with cyclic voltammetry, amperometry, and the rotating disk electrode technique in neutral pH solution. NADH is an important cofactor in a large number of dehydrogenase-based reactions. With GC and other types of electrodes, reproducible results cannot be obtained for this compound due to the strong adsorption of NAD^+, the principal oxidation product. However, with BDD, highly reproducible, stable, sensitive cyclic voltammograms were obtained for NADH oxidation. The amperometric results for NADH for the BDD electrode at 0.58 V in the nM concentration range are shown in Figure 8. After each injection of an aliquot of NADH stock solution, which caused a concentration step of 10 nM, a sharp rise in the current was observed. A linear calibration plot was obtained up to 500 nM. The results indicate that BDD is an attractive electrode material for use in sensors based on enzyme-catalyzed reactions involving NADH as a cofactor.[128–130]

Histamine (HI) and serotonin (5-hydroxytryptamine (5-HT)) are important biogenic amines that act as chemical messengers. Histamine is also present in many food products. The electrochemical detection of serotonin and histamine was investigated for the first time at BDD thin film electrodes by use of voltammetry and FIA

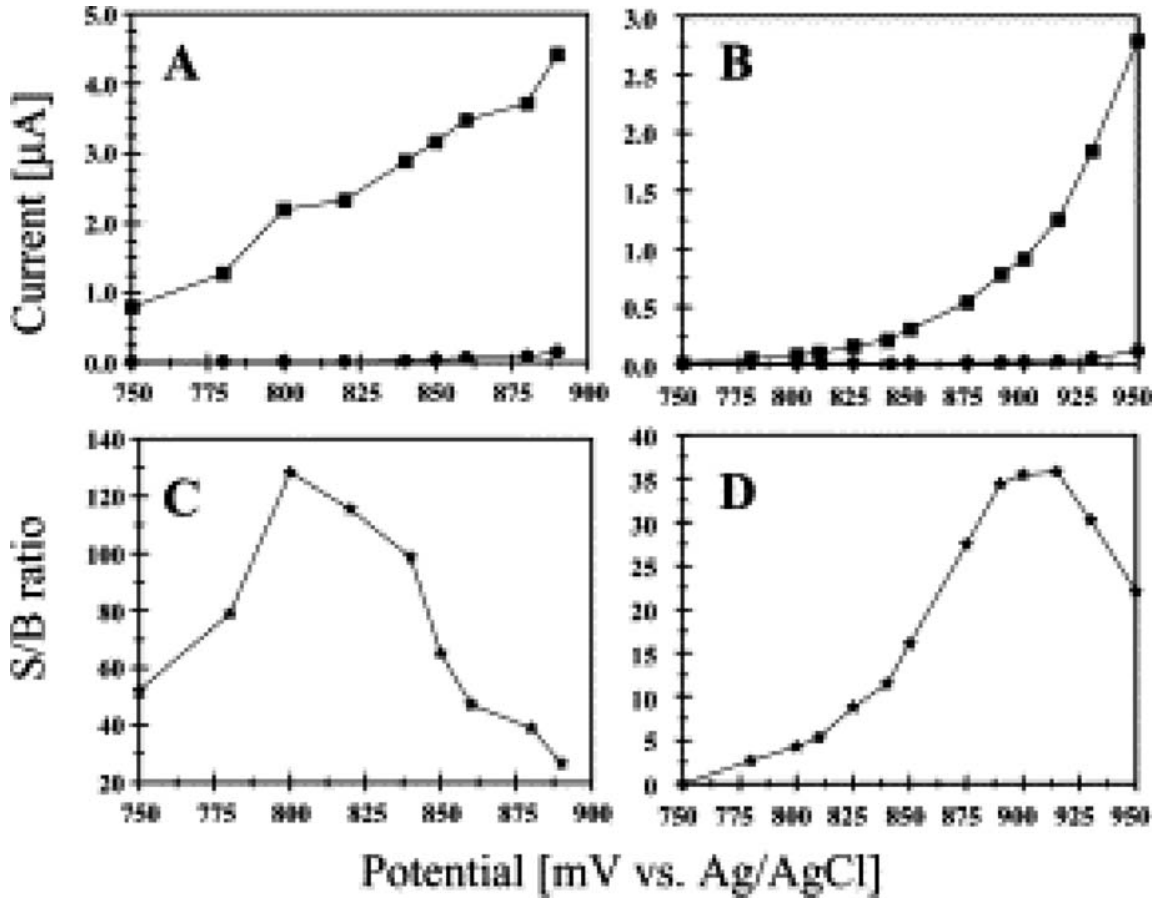

Fig. 7. Hydrodynamic voltammetric $i-E$ curves for 20-μL injections of (A) 1.0 mM SPMD; and (B) 1.0 mM CAD. The carrier solution was in 0.1 M $NaClO_4 + 0.01$ M carbonate buffer, CBpH10. The total current responses are shown as (•) and the background current responses as ( ). Plots of the S/B ratio versus the applied potential are shown for (C) SPMD; and (D) CAD. Working electrodes: unused 0.50% C/H films. The S/B ratio was calculated as $I_{tot} - I_{bkg}/I_{bkg}$; flow rate, 1.0 mL min^{-1}. Reprinted with permission from [126], M. A. Witek and G. M. Swain, *Anal. Chim. Acta* 440, 119 (**2001**). © 2001, Elsevier Science.

with amperometric detection . In comparison to the GC electrode, it was found that BDD provides very low background currents and a low tendency to adsorb the oxidative products on the electrode surface. Figure 9 shows linear sweep voltammograms for 100 μM HI together with the corresponding background voltammograms in 0.1 M phosphate buffer (pH 7) at the GC and BDD electrodes. At the GC electrode, the oxidation of HI occurred at ~1.2 V versus SCE. A rapid increase in the current at this potential was also observed in the background voltammogram due to oxygen evolution and carbon oxidation. For this reason, the voltammogram was ill defined. In the case of the diamond electrode, a very well defined oxidation peak at 1.40 V versus SCE was observed. The voltammetric signal-to-background ratios (S/B) obtained at diamond were one order of magnitude higher than those obtained for GC electrodes at and above histamine concentrations of 100 μM. A linear dynamic range of 3–4 orders of magnitude and a detection limit of 1 μM were observed in the voltammetric measurements. Well-defined sweep rate-dependent voltammograms were also obtained for 5-HT. A detection limit of 0.5 μM (S/N = 13.8) for HI was obtained by use of the FIA technique with the BDD electrode. A very low detection limit (10 nM) was obtained for 5-HT on BDD by the same method. A detection limit of 10 nM (0.2 pmol) was obtained for the FIA technique, indicating that BDD is a stable and sensitive electrode for 5-HT determination.[131, 132]

Selective voltammetric and amperometric detection of uric acid (UA) in the presence of high concentrations of AA was reported for oxidized diamond film electrodes by differential pulse voltammetry and chronoamperometry. A differential pulse (DP) voltammogram obtained for 50 μM UA in the present of AA at electrochemically treated diamond electrodes is shown in Figure 10. The chronoamperometric results show linear calibration curves obtained for UA over the concentration range up to 1×10^{-6} M in 0.1 M $HClO_4$ solution, A statistical analysis of the calibration curve yielded a detection limit of 1.5×10^{-8} M (S/N = 3). The possibility of practical use is shown by the direct measurement of UA in human urine and serum with no electrode pretreatment.[88]

REVIEW

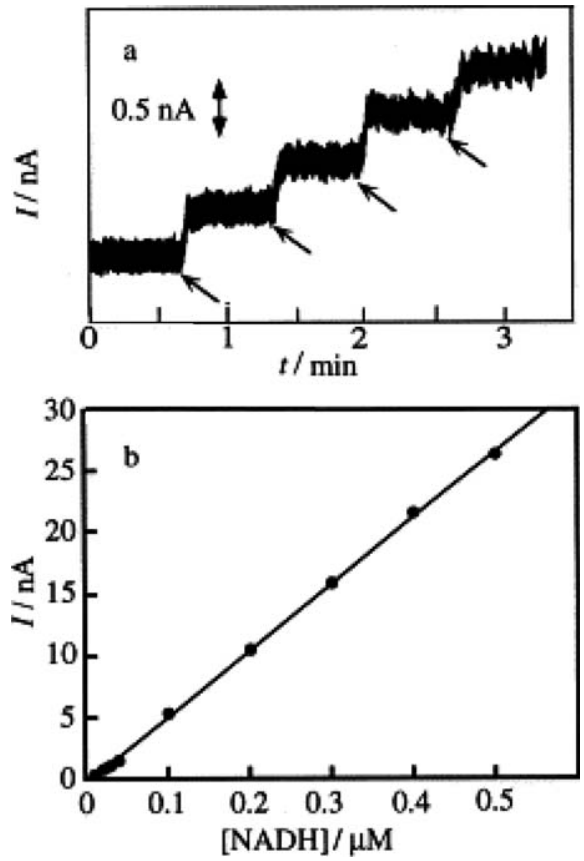

Fig. 8. (a) Amperometric response of a diamond electrode to NADH additions in a stirred solution containing 0.1 M phosphate buffer (pH 7.0) at an applied potential of 0.58 V versus SCE (each addition increased the concentration by 10 nM). (b) Calibration plot. Reprinted with permission from [128], A. Fujishima et al., *J. Electroanal. Chem.* 473, 179 (**1999**). © 1999, Elsevier Science.

Several tricyclic antidepressant drugs (tricyclic antidepressants or TCAs), imipramine, desipramine, clomipramine, amitriptyline, nortriptyline, and doxepin, were

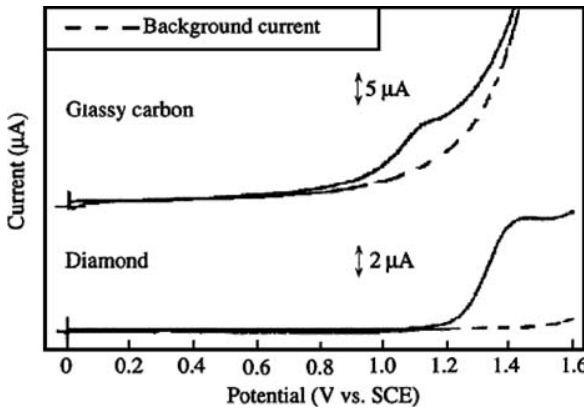

Fig. 9. Linear sweep voltammograms for 100 μM histamine in 0.1 M phosphate buffer (pH 7). (1) GC electrode (0.196 cm^2); (2) diamond electrode (0.189 cm^2). The potential sweep rate was 100 mV s^{-1}. Reprinted with permission from [132], B. V. Sarada et al., *Anal. Chem.* 72, 1632 (**2000**). © 2000, American Chemical Society.

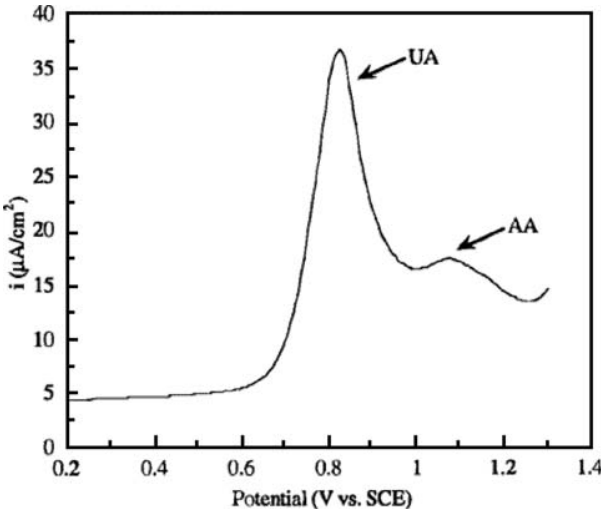

Fig. 10. Differential pulse voltammogram for a mixture of 50 μM UA and 0.25 mM AA at an oxidized diamond electrode in 0.1 M $HClO_4$ solution; sweep rate, 20 mV s^{-1}; pulse amplitude, 50 mV; pulse width, 50 ms; repetition time, 500 ms. Reprinted with permission from [88], E. Popa et al., *Anal. Chem.* 72, 1724 (**2000**). © 2000, American Chemical Society.

reported to be electrochemically detectable by cyclic voltammetry, FIA and HPLC with BDD electrodes.[133] These compounds belong to one of the largest groups of drugs for the treatment of psychiatric disorders such as depression. The function of these drugs is thought to involve blocking the uptake of norepinephrine at nerve endings in the central nervous system. For this group of drugs, distinct ranges of optimal plasma concentration for therapy are required. The therapeutic concentration range for most TCAs is approximately from 280 to 850 nM, while toxic effects can occur when plasma concentrations exceed 1.4 μM. It was found that using FIA-EC, at an operation potential of 0.85 V versus Ag/AgCl, BDD exhibited a background current of 7 nA with rapid stabilization (15 min), in contrast to the case of GC, which appeared to stabilize only after 1 h. Linear calibration curves were from 0.05 to 100 μM. The limits of detection (S/N = 3) were 3 nM for imipramine and desipramine, 0.5 nM for clomiprarmine, 163 nM amitriptyline, 1080 nM for nortriptyline and 92 nM for doxepin. The amperometric response (Fig. 11) obtained for a BDD electrode for 20-μL injections of 100 μM imipramine gave reproducible peaks, with a peak variability of ~3% ($n = 18$), which suggests a lack of adsorption of oxidation products on the electrode surface.

Reproducible results over several days of analysis were obtained. Moreover, this approach has been applied for determinations in plasma samples for imipramine and desipramine. The results demonstrate the promise of the use of BDD as an amperometric detector in HPLC for the analysis of these types of compounds.

Nitrogen-containing pesticides such as *N*-methylcarbamate pesticides (carbaryl, carbofuran, methyl 2-benzimidazolecarbamate, bendiocarb) were electrochemically

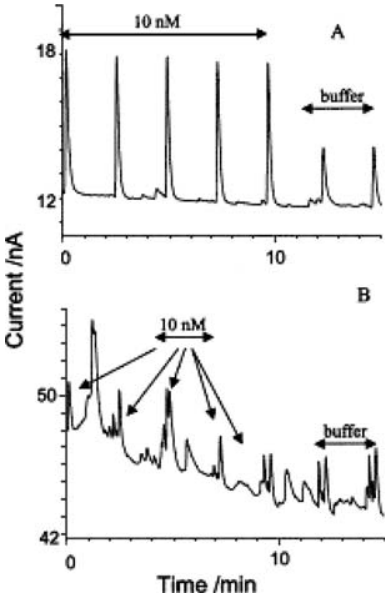

Fig. 11. FIA-ED results for 20-μL injections of: (A) 10 nM imipramine at a BDD electrode and (B) 10 nM imipramine at a GC electrode. The mobile phase was 0.1 M phosphate buffer pH 6.9; the flow rate was 1 mL min^{-1}. Reprinted with permission from [133], T. A. Ivandini et al., *J. Electroanal. Chem.* 521, 117 **(2002)**. © 2002, Elsevier Science.

detected at BDD thin-film electrodes after LC separation. Two kinds of detection methods were adopted in this study. First was a direct detection of the underivatized pesticides carried out at an operating potential of 1.45 V versus Ag/AgCl. The results provided detection limits of 5–20 ng mL^{-1} (or 5–20 ppb) with S/N = 2, due to the low background current and wide potential window of the diamond electrode. In the second method, the pesticide samples were prepared by alkaline hydrolysis in a separate step prior to injection in order to produce the phenolic derivatives. The latter, which oxidized at lower potentials (approximately 0.9 V vs. Ag/AgCl), gave very low detection limits and improved drastically the sensitivity. On-line reactivation of the diamond electrode surface was shown to be possible by an anodic treatment of the electrode at +3 V for 30 min in case of electrode fouling, which may occur after prolonged use. Such treatment can damage GC, Kel-graf (Kel-F resin plus graphite) and metal electrodes, while the diamond electrode is stable. These results suggest that the BDD electrode is better than other, previously used electrodes for the highly sensitive, stable detection of carbamate pesticides.[134] Figure 12A shows the hydrodynamic voltammograms at the diamond electrode for carbaryl, carbofuran, and bendiocarb after the prehydrolysis step. The mobile phase used was a solution of 0.01 M $NaClO_4$ in acetic acid/water/acetonitrile, 0.5%:59.5%:40%. The background current did not rise in the potential region where the phenolic derivatives of three pesticides underwent oxidation. The derivative of carbaryl, 1-naphthol, oxidized much earlier than those of carbofuran and bendiocarb. The potential for the amperometric detection was set at

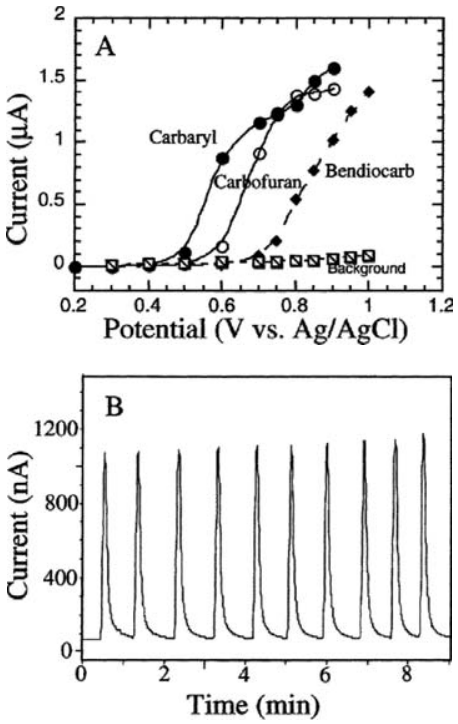

Fig. 12. (A) Hydrodynamic voltammograms for phenolic derivatives of 50 μM carbamates at diamond electrode. The injection volume was 20 μL. (B) FIA-ED results for diamond electrode using 20-μL injections of 50 μM prehydrolyzed carbaryl; applied potential, 0.9 V versus Ag/AgCl. The mobile phase was a mixture of acetic acid/water/acetonitrile, 0.5:59.5:40; the flow rate was 1 mL min^{-1}. Reprinted with permission from [134], T. N. Rao et al., *Anal. Chem.* 74, 1578 **(2002)**. © 2002, American Chemical Society.

0.9 V versus Ag/AgCl, where the derivatives of all three pesticides gave current responses. Figure 12B shows the amperometric response for repetitive 20-μL injections of 50 μM prehydrolyzed carbaryl. As expected, the response was very stable, with a RSD of 2.5% for 10 injections.

The electrochemical oxidation of other important nitrogen-containing compounds such as xanthine and its naturally occurring *N*-methyl derivatives, theophylline, theobromine, and caffeine was also investigated[135] Caffeine and theophylline are methylxanthine derivatives that are widely distributed in plant products and beverages. Theophylline and caffeine have been widely used for the treatment of asthmatic manifestations, neonatal apnea and bronchial spasms. Therefore, it is very important to determine accurately the content of these compounds in foods and pharmaceutical preparations. The effects of pH, concentration and potential sweep rate on the voltammetric response were thoroughly examined. It was found that BDD exhibits excellent behavior, in terms of very well defined, reproducible oxidation peaks, for xanthine, theophylline, theobromine, and caffeine determination. The results enabled BBD electrode to be used as the electrochemical sensor to detect the investigated compounds, within a concentration range of 1 to 400 μM

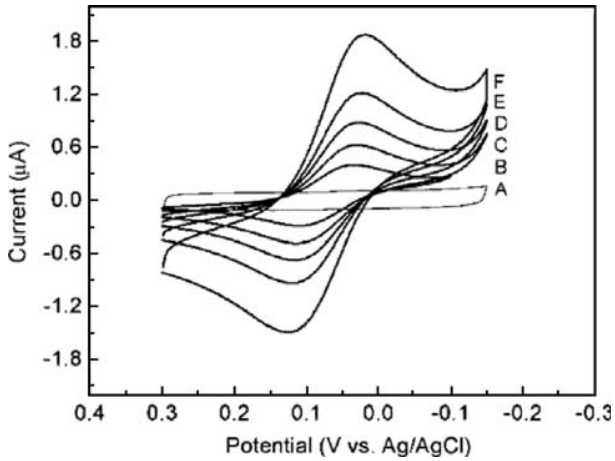

Fig. 13. (A) Background CV at 20 mV s^{-1} for a 20 mM NaCl aqueous solution and (B-F) CVs for 200 μM horse heart cytochrome *c* in 20 mM NaCl, 1 mM Tris HCl pH 7 buffer at different scan rates: (B) 2 mV s^{-1}, (C) 5 mV s^{-1}, (D) mV s^{-1}, (E) 20 mV s^{-1}, and (F) 50 mV s^{-1}; electrode area, 0.2 cm^2. Reprinted with permission from [136], S. Haymond et al., *J. Am. Chem. Soc.* 124, 10634 (**2002**). © 2002, American Chemical Society.

for theophylline, theobromine and caffeine, and of 1 to 100 μM for xanthine. Results obtained for caffeine detection in real samples of commercially available products, without separation from the matrix were promising for quantitative studies.

Figure 13 shows a series of cyclic voltammetric curves for 200 μM horse heart cytochrome *c* in 1 mM Tris HCl buffer (pH 7) containing 20 mM NaCl at a nanocrystalline BDD electrode at various potential sweep rates from 2 to 50 mV s^{-1}.[136] A well-defined, quasi-reversible voltammetric response, characteristic of a diffusion-controlled reaction, was observed in the potential range of 0.3 to −0.2 V. The peak currents varied linearly with the concentration, as shown in Figure 14 and importantly, there was no

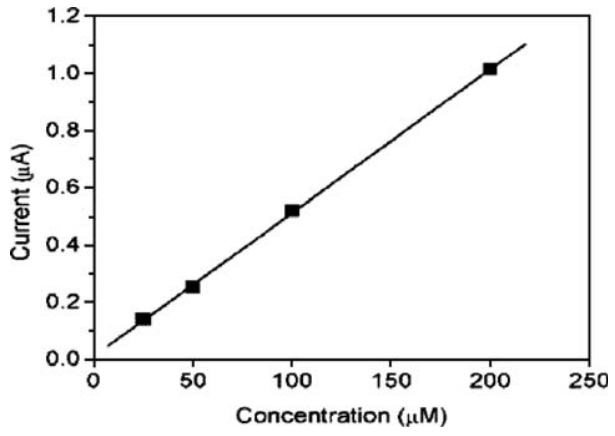

Fig. 14. Plot of cathodic peak current versus cytochrome *c* concentration from 25 to 200 μM at 10 mV s^{-1}; linear regression coefficient, 0.9995; slope, 5.03×10^{-3} μA μM^{-1}. Reprinted with permission from [136], S. Haymond et al., *J. Am. Chem. Soc.* 124, 10634 (**2002**). © 2002, American Chemical Society.

electrode fouling. The results are interesting from the standpoint of the interactions between the diamond surface and cytochrome *c* and their influence on the ET kinetics.

BDD electrodes were used to study the electrochemical analysis of nucleic acids in aqueous solution by Prado et al.[137] The advantages of this electrode material included reproducibility and small background currents observed at very positive potentials. From other work of this group, it is clear that BDD is quite robust under extreme conditions, including ultrasound, so that such conditions could also be used in future applications. tRNA, single and double stranded DNA and 2′-deoxyguanosine 5′-monophosphate (dGMP) were studied, and well defined peaks were observed in all cases and were assigned to the oxidation of deoxyguanosine monophosphate.

BDD is a most useful electrode material with which to examine the electrochemical oxidation of underivatized-nucleic acids in terms of single-stranded and double-stranded DNA. Cyclic voltammetry and square wave voltammetry were used to study the oxidation reactions and to detect DNA without derivatization or hydrolysis steps.[138] Linear calibration results showed linearity of oxidation current with concentrations in the range of 0.1–8 μg mL^{-1} for both guanine and adenine residues at as-deposited BDD. Detection limits (S/N = 3) of 3.7 and 10 ng mL^{-1} for adenine and guanine residues in single-stranded DNA, respectively, and 5.2 and 10 ng mL^{-1} for adenine and guanine residues in double-stranded DNA, respectively, were observed. The results also show the promise of using the oxidation peak current for the adenine moiety for the direct detection of nucleic acids.

The determination of aminonaphthalenes and aminobiphenyls by liquid chromatography with amperometric detection on BDD film electrodes was reported.[139] The noise, background current, signal stability, linearity of the calibration curve and detection limits obtained for the GC electrode were compared with the parameters obtained at the BDD electrode. The calibration curves were linear in the whole range 10^{-7}–10^{-4} mol L^{-1}, and the sensitivity was higher for the GC electrode. The signals for these analytes were reproducible and stable for at least 8 h for both electrode materials. The detection limits for aminonaphthalene and aminobiphenyl were at least a factor of five lower for the BDD electrode due to the lower noise and background current.

The detection of leucine-enkephalinamide (LEA) and its metabolites, tyrosine (T), tyrosyl-alanine (TA), tyrosyl-alanine-glycine (TAG) and leucine-enkephalin (LE) was reported at the BDD electrode with the use of cyclic voltammetry, FIA, and gradient LC with amperometric detection.[140] At BDD electrodes, well-defined and highly reproducible cyclic voltammograms were obtained with S/B ratios 5–10 times higher than those observed for GC electrodes. The analytical peaks of LC for LEA and its metabolites were well resolved. No deactivation of the

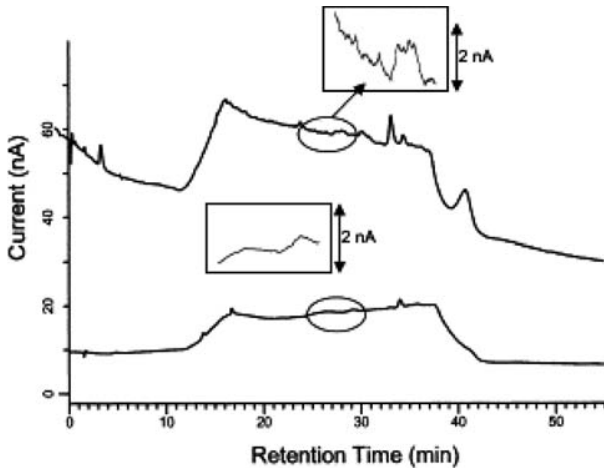

Fig. 15. Baseline obtained at BDD and GC electrodes with gradient elution using an Inertsil ODS-3 column. Operating potentials were 1.2 and 0.9 V versus Ag/AgCl for BDD and GC electrodes, respectively; the flow-rate was 1 mL min^{-1}. Reprinted with permission from [140], T. A. Ivandini et al., *J. Chromatogr. B* 791, 63 **(2003)**. © 2003, Elsevier Science.

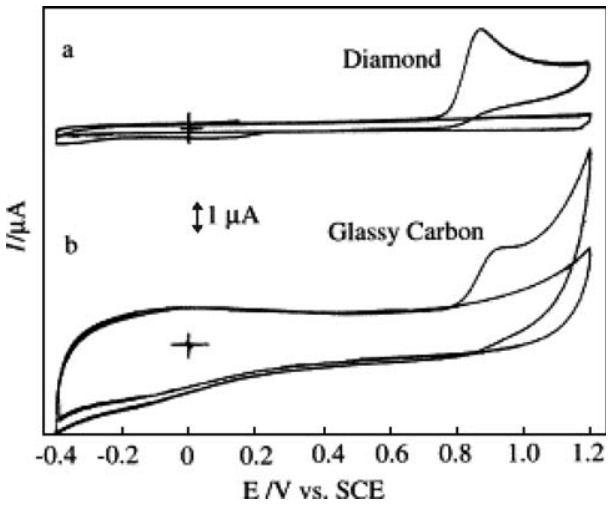

Fig. 16. Cyclic voltammograms for 50 μM sulfadiazine in 0.1 M phosphate buffer (pH 7.1) at (a) diamond electrode (area, 0.12 cm^2) and (b) GC electrode (area, 0.07 cm^2) The sweep rate was 100 mV s^{-1}. Background voltammograms are also shown in the figure. Reprinted with permission from [161], T. N. Rao et al., *J. Electroanal. Chem.* 491, 175 **(2000)**. © 2000, Elsevier Science.

BDD electrodes was found after several experiments with standard as well as plasma samples, indicating high stability of the electrode. The calibration curves were linear over a wide range from 0.06 to 30 μM with regression coefficients of 0.999 for all compounds. The limits of detection obtained based on a S/N ratio of 3 were 3, 2.2, 2.7, 20, and 11 nM for T, TA, TAG, LE, and LEA, respectively. In this work, it was reported that high stability and no fouling were observed with the BDD electrode during analysis, whereas for the GC electrode, the baseline current continuously decreased during the analysis, as shown in Figure 15. The results show the promising use of conducting diamond as an amperometric detector in gradient LC, especially for the analysis of enkephalinamide and its metabolites.

3.2.1.2. Detection of Sulfur-Containing Compounds Sulfa drugs were investigated at diamond electrodes, and their determination by HPLC with amperometric detection was described for the first time by Rao et al. For example, Figure 16 shows the cyclic voltammograms for 50 μM sulfadiazine together with the corresponding background voltammograms in 0.1 M phosphate buffer (pH 7.1) at BDD and GC electrodes. Highly reproducible and well-defined cyclic voltammograms were obtained not only sulfadiazine but also for the other two drugs, sulfamerazine and sulfamethazine, with a S/B ratio of a factor of ten greater than that obtained at two types of freshly polished GC electrodes. With the use of amperometry coupled with an FIA system, BDD exhibited a highly reproducible amperometric response, with a peak variation of approximately 5%. A detection limit of 50 nM and a linear dynamic range of three orders of magnitude were obtained. An important observation in this study was that BDD yields a well-defined chromatogram with a flat baseline (background current), unlike the other two types of GC electrodes, as shown in the Figure 17.

The electrooxidation L-cysteine was first examined at BDD and GC electrodes by use of cyclic voltammetry.[141]

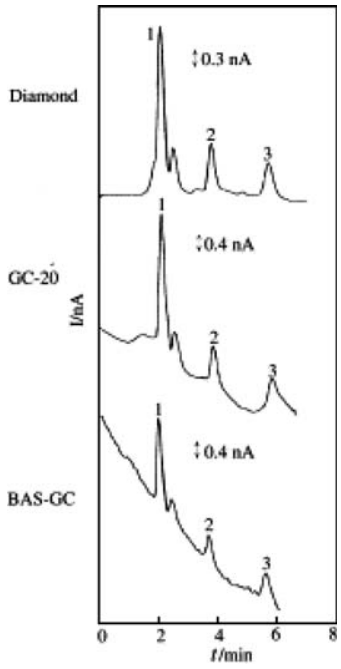

Fig. 17. Chromatograms of a standard mixture containing 100 nM concentrations of (1) sulfadiazine, (2) sulfamerazine and (3) sulfamethazine at diamond and GC electrodes. The mobile phase was 85% 0.1 M phosphate buffer (pH 7.1) + 15% methanol (v/v). The injection volume was 20 μL, and the flow rate was 1 mL min^{-1}. Reprinted with permission from [161], T. N. Rao et al., *J. Electroanal. Chem.* 491, 175 **(2000)**. © 2000, Elsevier Science.

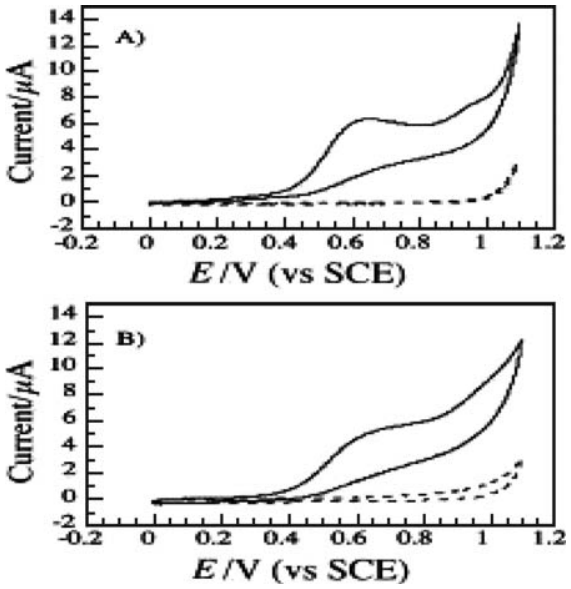

Fig. 18. Cyclic voltammograms for (A) boron-doped diamond and (B) glassy carbon electrodes in L-cysteine + 0.5 M $KHCO_3$ (solid lines) and 0.5 M $KHCO_3$ (dashed lines); potential sweep rate, 20 mV s^{-1}; electrode area, 0.07 cm^2. Reprinted with permission from [141], O. Chailapakul et al., *Electrochem. Commun.* 2, 422 **(2000)**. © 2000, Elsevier Science.

Well-defined, irreversible peaks were obtained for the oxidation of cysteine, as shown in Figure 18. This preliminary study showed that BDD has better sensitivity than GC. The mechanism oxidation reaction of L-cysteine (CySH) was also studied in alkaline media.[142] The results of the voltammetric and polarization measurements showed that the overall CySH oxidation reaction at BDD electrodes was controlled by the initial electrochemical step, i.e., the oxidation of the CyS^- electroactive species. In contrast, under the same conditions, the reaction at GC electrodes was controlled by the desorption of the reaction products. It was found that BDD exhibits excellent behavior for CySH detection.

Interestingly, Nekrassova et al. developed a voltammetric method, using the BDD electrode, for the study of the homogeneous oxidation mechanism of cysteine by aqueous ferricyanide.[143] It was shown that, on the BDD electrode, unlike other electrodes, e.g., platinum, the voltammetric responses of the ferrocyanide and the cysteine were distinctly different, with the ferrocyanide oxidizing at a lower potential, so that the kinetics could be examined via voltammetric methods. Cyclic voltammetry with the BDD electrode was used to show that an electron transfer followed by a chemical reaction (EC' mechanism) occurs, and the appropriate rate constants were determined. Both the protonated and de-protonated forms of cysteine underwent oxidation by ferricyanide. The cyclic voltammetric results obtained with a conventional electrode configuration also agreed well with those obtained with a channel flow cell. The latter was found to provide a simple means of controlling the hydrodynamics at BDD electrodes.

The electrooxidation of homocysteine, glutathione (GSH), 2-mercapto ethanesulfonic acid and cephalexin at BDD and GC electrodes was investigated for the first time by cyclic voltammetry.[144] This preliminary voltammetric study showed that BDD had better sensitivity than GC, as shown in Figure 19. The concentration dependence was studied and indicated the promise of using BDD electrodes for quantitative determination. All of the compounds displayed recognizable oxidation peaks with the BDD electrode at millimolar concentration levels. The scan rate dependence of GSH was examined. It was found that there was negligible adsorption on the surface of the BDD electrode for low concentrations.

At anodized (electrochemically oxidized) BDD electrodes, highly reproducible, well-defined cyclic voltammograms for homocysteine oxidation were obtained in acidic media, while as-deposited BDD did not provide a detectable signal.[145] In alkaline media, however, oxidation peaks were obtained at both as-deposited and anodized electrodes. In the flow system, BDD exhibited a highly reproducible amperometric response, with a peak variation less than 2%. An extremely low detection limit (1 nM) was obtained at 1.6 V versus Ag/AgCl. Homocysteine was also determined in a standard mixture with aminothiols and disulfide compounds with isocratic reverse-phase HPLC with amperometric detection at BDD electrodes. The detection limit was 1 pmol, and the linear dynamic range was three orders of magnitude.

Anodized BDD was also used for the first time to detect disulfides in aqueous acidic media.[146, 147] Cyclic voltammetric signals for 1 mM glutathione disulfide (GSSG) were observed at 1.39 and 1.84 V versus SCE; these values were less positive than those for as-deposited BDD and GC electrodes. It was proposed that an attractive electrostatic interaction between the anodically oxidized diamond surface and the positively charged GSSG caused a positive shift in the peak potential in acidic media. Electrolysis results showed that the oxidation reaction mechanism for glutathione (GSH) and GSSG involves oxygen transfer. Following separation by LC, the determination of both GSH and GSSG in whole rat blood (Fig. 20) was achieved at a constant potential (1.50 V versus Ag/AgCl), and the limits of detection for GSH and GSSG were found to be 1.4 nM (0.028 pmol) and 1.9 nM (0.037 pmol), with a linear dynamic range up to 0.25 mM. These detection limits were much lower than those reported for Bi-PbO_2 electrodes or for LC-mass spectrometry and were comparable with those for enzymatic assay for real samples.

The electrochemically initiated catalytic oxidation of 5-thio-2-nitrobenzoic acid (TNBA) by thiols was examined at a BDD electrode with chronoamperometry.[148] This method provided the basis for the detection of a range of biologically relevant thiols. The method was shown to be capable of measuring total thiol concentration, since the sensitivities of the standard addition plots are independent of the individual thiols. Detection limits of 5.7 μM,

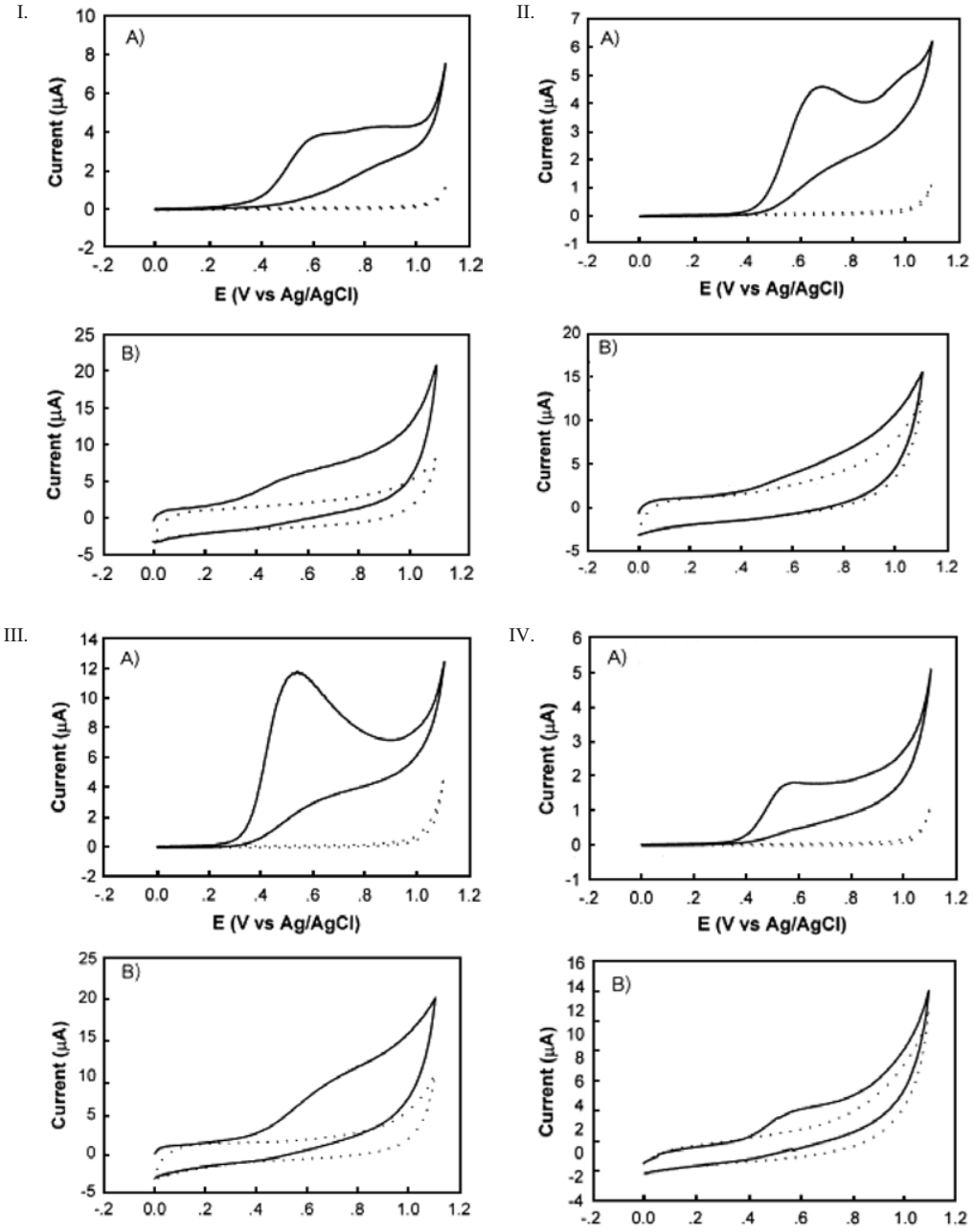

Fig. 19. Cyclic voltammograms for I. homocysteine, II 0.67 mM glutathione, III 1.0 mM 2-mercapto ethanesulfonic acid, IV. 10.0 mM cephalexin (A) BDD electrode and (B) GC electrode versus Ag/AgCl in 0.1 M carbonate buffer (pH 9.2) in the presence (solid lines) and absence (dotted lines) of analytes; sweep rate, 50 mV s^{-1}; area of electrode, 0.07 cm^2.

4.4 μM, and 5.8 μM for the detection of cysteine, homocysteine, and glutathione, respectively, were obtained.

D-penicillamine, a thiol drug, was detected for the first time at a BDD-based electrode with cyclic voltammetry for a range of concentrations and pH.[149] The results were compared with those for a GC electrode. The BDD electrode exhibited a well resolved, irreversible oxidation voltammetric peak, but the GC electrode exhibited an ill defined response. The BDD electrode provided a linear dynamic range from 0.5 to 10 mM and a detection limit of 25 μM (S/B = 3) in the voltammetric measurements. In addition, penicillamine was studied by hydrodynamic voltammetry and FIA with amperometric detection at the BDD electrode. The FIA results indicated a linear dynamic range from 0.5 to 50 μM and a detection limit of 10 nM (S/N approximately 4). The proposed method was applied to the determination of D-penicillamine in dosage form (capsules); the results obtained in the recovery study (255 $\pm$ 2.50 mg per tablet) were in agreement with the nominal values (250 mg per tablet).

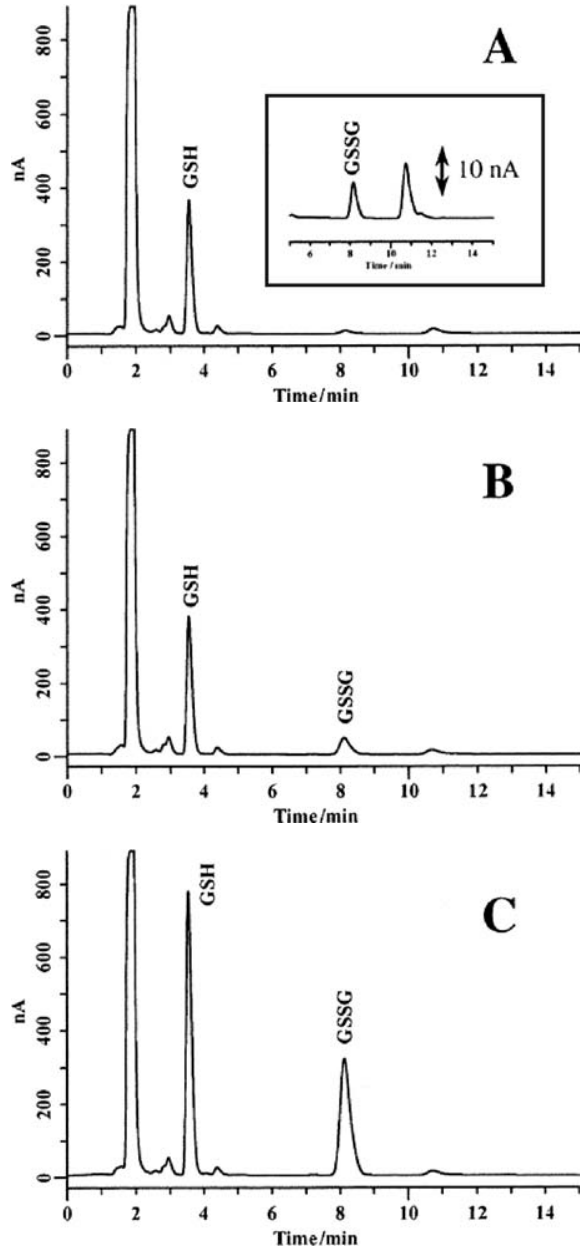

Fig. 20. Chromatograms of rat whole blood (1:80 dilution) showing peaks for GSH and GSSG. (A) No addition of standard GSH and GSG, (B) 82.5 μM each, and (C) 825 μM each of GSH and GSSG was added prior to deproteinization. Separation column: Inertsil ODS-3 (4.6-mm i.d. × 75 mm, dp = 3 μm); mobile phase, MeCN/0.1% TFA = 2/98; temperature, 25 °C; flow rate, 0.7 mL min^{-1}; injection volume, 20 μL. Anodically oxidized (AO) diamond was prepared by applying a potential of 1.50 V versus Ag/AgCl. Reprinted with permission from [146], C. Terashima et al., *Anal. Chem.* 75, 1564 (**2003**). © 2003, American Chemical Society.

A quantitative study of tiopronin, a drug used to prevent kidney stones, was carried out with BDD electrodes with cyclic voltammetry and FIA coupled with amperometry.[150] At the diamond electrode, it was found that tiopronin provided highly reproducible and well-defined cyclic voltammograms, with a peak potential of +0.8 V versus Ag/AgCl. In contrast, tiopronin gave ill-defined cyclic voltammograms at the GC electrode. Linearity at the BDD film electrode was observed over a range of 0.05–10 mmol L^{-1}, with a detection limit of 50 μmol L^{-1} (S/B $\geq$ 3). In addition, the amperometric hydrodynamic voltammetry with FIA with the BDD was studied. A detection potential of +0.8 V was chosen, at which tiopronin exhibited the highest S/B ratios. The FIA results showed the low detection limit of 10 nmol L^{-1} (S/N = 3) and a linear dynamic range of 0.5–50 μmol L^{-1}. This method was applied to the determination of tiopronin in a pharmaceutical formulation. With the use of the standard addition technique, the recoveries obtained were 96.5–108.3%, and the RSD values were 1.10–1.62% (n = 10).

Several techniques, including cyclic voltammetry, hydrodynamic voltammetry and FIA with amperometric detection, were used with the BDD electrode to study the electroanalysis of captopril in phosphate buffer (pH = 9). Catopril is a drug that is used to treat hypertension, congestive heart disease and diabetic kidney disease. Cyclic voltammetry was used to study the reaction as a function of analyte concentration. The results were compared with those obtained with a GC electrode under the same conditions. Captopril undergoes an irreversible reaction at both electrodes. However, the BDD electrode provided a highly reproducible, well-resolved cyclic voltammogram and a higher S/B ratio compared with GC. A linear range from 50 μM to 3 mM and a detection limit of 25 μM (S/B $\approx$ 3) were obtained from the BDD electrode with cyclic voltammetry. The potential sweep rate (υ) dependence for the captopril oxidation peak currents for 1 mM captopril was linear with $\upsilon^{1/2}$, within the range of 0.01 to 0.3 V s^{-1}, which indicates that the oxidation current was diffusion-controlled, with negligible adsorption on the BDD surface. The FIA measurements for the BDD electrode in the concentration range from 0.5 to 100 μM exhibited a linear dynamic range and the very low detection limit of 10 nM (S/N $\approx$ 3). In addition, the determination of captopril in commercial tablets by FIA with amperometric detection at BDD electrodes was also carried out. The results showed good precision (1.21–2.15%).[151]

3.2.1.3. Detection of Other Heteroatomic Compounds The detection of anthraquinone-2,6-disulfonate (2,6-AQDS) at GC, hydrogenated glassy carbon (HGC), the basal plane of highly oriented pyrolytic graphite (HOPG), and BDD electrodes was investigated by use of cyclic voltammetry and chronocoulometry.[152] Quantitative determination of the surface coverage and qualitative assessment of the physisorption strength of 2,6-AQDS adsorption on each of these electrode surfaces were carried out. The diamond and HGC surfaces were nonpolar and hydrogen terminated. The polar 2,6-AQDS did not adsorb on these surfaces, and the electrochemical process was diffusion-controlled. In contrast, the GC and HOPG surfaces were polar, with a significant coverage of carbon-oxygen functionalities. 2,6-AQDS adsorbed strongly on both of these

surfaces at high coverage, and the electrochemical behavior was typical for an adsorbed layer. The initial adsorbed layer could not be completely removed by rinsing, which indicated strong physisorption. The results demonstrated that BDD electrodes are more difficult to foul by polar molecules, in comparison to GC, which is beneficial for a reproducible response.

An ultrasonically facilitated BDD electrochemical technique was developed to analyze the priority pollutant 4-chlorophenol by Saterlay et al.[153] The electroanalysis of this compound is hampered by the formation of a polymeric film on the electrode surface. The combination of ultrasound with the highly robust BDD electrode facilitated the measurement of 4-chlorophenol in aqueous solution. The surface film was removable due its ultrasonic breakup. The ultrasonic field also yielded an enhanced oxidation current signal due to more efficient mass transport of 4-chlorophenol. A detection limit of 1 μM and a linear range of 1–300 μM were reported; this range is useful for environmental measurements.

The detection of chlorophenols (CP) in aqueous solution was also examined with a hydrodynamic channel flow cell and a BDD electrode by Prado et al.154 Due to the film formation problem mentioned above, the use of the channel flow cell was proposed. The results showed linear ranges up to 20 μM. Thus, this technique is useful for environmental applications. Laser ablation voltammetry with a Nd:YAG laser indicated that there was negligible adsorption of oxidation products. The similarity of the sensitivities for 4-chlorophenol, 2-chlorophenol, phenol, 2,4-dichlorophenol, and 4-chloro-3-methylphenol makes it possible to measure a summed total CP concentration, presumably with a simplified separation stage. No interferences were observed for nitrite or sulfite.

In the same year, Terashima et al. reported a detailed study of the electrochemical oxidation of CPs at anodically pretreated BDD electrodes and their determination by HPLC with amperometric detection.[40] The anodization of as-deposited boron-doped polycrystalline diamond thin-film electrodes enabled the CPs to be determined stably over a wide concentration range. The oxidative behavior was compared for ordinary GC, as-deposited BDD, and anodized BDD by cyclic voltammetry and FIA with amperometric detection. At anodized BDD electrodes, reproducible, well-defined cyclic voltammetric peaks were obtained, even at CP concentrations as high as 5 mM, due to the lack of adsorption of oxidation products on the surface. After prolonged use, there was partial deactivation of the BDD surface due to filming, but the electrode was able to be reactivated *in situ* by applying a highly oxidizing potential (2.64 V vs. SCE) for 4 min; this treatment is effective in removing the polymeric film, due to the action of electrogenerated hydroxyl radicals. With FIA, the anodized BDD electrode exhibited excellent stability, with a response variability of 2.3% ($n = 100$), for the oxidation of a high concentration (5 mM) of chlorophenol. In contrast, GC exhibited a response variability of 39.1%. After 100 injections, the relative peak intensity for BDD decreased by 10%, compared to 70% for GC. The detection limit obtained in the FIA mode for 2,4-dichlorophenol was found to be 20 nM (S/N = 3), with a linear dynamic range up to 100 μM. By use of a column-switching technique, which enabled on-line preconcentration , the, detection limit was lowered to 0.4 nM (S/N = 3). With this technique, anodized BDD electrodes were also used for the analysis of CPs in a real sample, specifically, drainwater condensed from the flue gas of a waste incinerator.

The BDD thin film electrode was used to determine acetaminophen in phosphate buffer solution (pH 8) with cyclic voltammetry, hydrodynamic voltammetry, and FIA with amperometric detection.[155] Cyclic voltammetry was used to study the reaction as a function of analyte concentration. The BDD electrode exhibited a linear dynamic range from 0.1 to 8 mM and a detection limit of 10 μM (S/B $\approx$ 3) for the voltammetric measurement. The FIA results indicated a linear dynamic range from 0.5 to 50 μM and a detection limit of 10 nM (S/N $\approx$ 4). Acetaminophen was also measured for syrup samples. The reported recoveries (24.68 ± 0.26 mg mL^{-1}) were comparable to the nominal value of 24 mg mL^{-1}.

Metal-modified diamond electrodes have interesting characteristics in terms of the catalysis of multi-step electrochemical reactions, which can be quite sluggish on unmodified diamond. For example, the oxidation of alcohols and carbohydrates is quite difficult without a metal catalyst but becomes feasible with the addition of small amounts of metals. For example, nickel and copper were used to modify BDD, and the resulting electrodes yielded well-defined, reproducible voltammmetric peaks for the oxidation of 1 mM glucose in alkaline media.[156] These electrodes exhibited excellent electrochemical stability, with low background current for at least one week in an FIA system, indicating good adhesion of the metal clusters to the diamond surface. These results indicate the promising use of nickel- and copper-modified BDD electrodes for the detection of carbohydrates.

A new type of metal-modified BDD surface involves the use of ion implantation; specifically, nickel-implanted BDD electrodes (Ni-DIA) were prepared in order to examine their usefulness for carbohydrate detection. This type of electrode produced well-defined, reproducible voltammograms for the oxidation of 1 mM glucose in alkaline media. The electrode exhibited excellent electrochemical stability, with low background current, even after ultrasonic treatment, which indicated strong bonding of nickel with diamond. These results suggest that ion implantation of metals into BDD electrodes might show promise for the detection of carbohydrates and perhaps amino acids.

Due to the insensitivity of the unmodified BDD surface for the oxidation of alcohols, it is possible to measure a variety of analytes in alcohol solutions without interference. Additional benefits are the lack of electrode

deactivation from fouling and the ability to withstand highly positive electrochemical potentials. For example, the detection of ascorbic acid (AA) was carried out in an ethanol-water mixed solution (0.1 M $NaClO_4$) with a BDD electrode.[157] During FIA of AA in this solution, there was little interference from ethanol oxidation, in contrast to the behavior of a Pt electrode. Moreover, the detection limit for AA observed was lower than that for a GC electrode, because BDD exhibited lower background current, background noise, and lower injection noise. These findings suggest that BDD electrodes may be applied in the detection of other redox-active impurities and added substances in alcohol or alcohol-water solutions, such as chlorophyll, nicotinamide, caffeine, riboflavin, and dl-alpha-tocopherol.

The use of enzyme modification of diamond, as already mentioned, is a highly promising approach to the preparation of analytical electrodes with special selectivity. It was reported that tyrosinase-modified BDD electrodes can be used for the determination of phenol derivatives.[158] BDD electrodes were modified covalently with tyrosinase by the introduction of hydroxyl groups onto the surface and were then treated with (3-aminopropyl)triethoxysilane and finally coated with a tyrosinase film cross-linked with glutaraldehyde. These electrodes were designed for the determination of estrogenic phenol derivatives. The amperometric response of these modified electrodes was measured for bisphenol-A and 17-β-estradiol at -0.3 V versus Ag/AgCl. Interference from dioxygen reduction was nearly negligible. These electrodes were used in an FIA system, and the detection limit for bisphenol-A was found to be 10^{-6} M.

3.2.2. Detection Based on Other Techniques

Shin et al. reported the application of diamond microelectrodes for end-column electrochemical detection in capillary electrophoresis (CE). Diamond microline electrodes were fabricated from BDD thin films (exposed surface area, 300×50 μm), and their analytical performance as CE detectors was evaluated in a laboratory-made CE apparatus. The CE-ED system exhibited high separation efficiency for several catecholamines, including dopamine (DA), norepinephrine (NE), and epinephrine (E). The analytical performance was excellent, e.g., 155,000 theoretical plates for DA. The detection limits were quite low (approximately 20 nM for E at S/N = 3), and current response was highly reproducible for ten repetitive injections of mixtures containing DA, NE, and E (each 50 μM), with relative standard deviations of approximately 5%.

The performance of the BDD electrochemical detector for CE was also evaluated in the detection of CPs. When compared to the carbon fiber microelectrode, the BDD electrode exhibited lower detection limits in an end-column CE detection, as a result of the very low noise levels and high reproducibility. In addition, there was no need for electrode polishing, because analyte fouling was negligible; this makes the analysis significantly more convenient and also leads to higher stability.

Cvacka et al. also studied the use of BDD microelectrodes for CD with electrochemical detection.[159] The microelectrodes were prepared by coating thin films of CVD polycrystalline BDD on electrochemically sharpened platinum wires (76, 25, and 10-μm diameter. The BDD-coated wires were then attached to copper wires. These microelectrodes were characterized by scanning electron microscopy, Raman spectroscopy, and cyclic voltammetry. They exhibited low, stable background currents and voltammetric behavior typical of microelectrodes, i.e., sigmoidal curves for $Ru(NH_3)_6^{3+/2+}$ and $Fe(CN)_6^{3-/4-}$ at low potential sweep rates. The microelectrodes were fabricated by sealing in polypropylene pipet tips. Dopamine, catechol, and ascorbic acid were used to evaluate the performance of the CE-EC system in 10 mM phosphate buffer, pH 6.0, run buffer, and a 30-cm-long fused-silica capillary (75-μm I.D.). The background current ($\sim$100 pA) and noise ($\sim$3 pA) were measured at various detection potentials and were found to be quite stable. Reproducible separation (elution time) and detection (peak current or area) of dopamine, catechol, and ascorbic acid were observed with response precisions of 4.1% or less. Calibration curves constructed from the peak area were linear over 4 orders of magnitude, up to a concentration between 0.1 and 1 mM. Mass limits of detection for dopamine and catechol were 1.7 and 2.6 fmol, respectively (S/N = 3). The separation efficiency was 33,000, 56,000, and 98,000 plates/m for dopamine, catechol, and ascorbic acid, respectively. In addition, the separation and detection of 1- and 2-naphthol in 160 mM borate buffer, pH 9.2, was investigated. Separation of these two analytes was achieved with efficiencies of 118,000 and 126,000 plates/m, respectively.

Wang et al. discussed the advantages of a diamond electrode detector for a micromachined capillary electrophoresis (CE) system.[160] A chemically vapor-deposited BDD film band (0.3×6.0 mm) electrode was used for end-column amperometric detection. The performance of the BDD electrode detector was superior to that for a commonly used thick-film carbon detector. BDD provided enhanced sensitivity, lower noise levels, and sharper peaks for several groups of important analytes (nitroaromatic explosives, organophosphate nerve agents, phenols). The advantages of the BDD-based CE detector included the superior S/B ratios and the much higher resistance to surface fouling. The enhanced stability was evidenced by the RSD of 0.8% for 60 repetitive measurements of 5 ppm 2,4,6-trinitrotoluene (compared to an RSD value of 10.8% at the thick-film carbon electrode). A linear response was obtained for the explosives 1,3-dinitrobenzene and 2,4-dinitrotoluene over the 200–1400 ppb range, with detection limits of 70 and 110 ppb, respectively. BDD is thus quite a promising electrode material for electrochemical detection in CE and micromachined flow systems.

4. CONCLUDING REMARKS

Based on its range of superior characteristics for sensitive electroanalytical measurements, BDD as an electrode material and electrochemical sensor material may constitute one of the more important developments in this area in recent years. In addition, the range of possible analytes is great, as demonstrated in the present review. As the availability of high quality BDD samples becomes greater, there will doubtless be increasing numbers of applications. The ability to chemically tailor the surface with various species, including metals, functional molecules, oligonucleotides and enzymes, continues to grow as well, which further support the development of new applications.

Acknowledgments: The authors would like to acknowledge the Thailand Research Fund, the Rachadapiseksompot Endowment and the National Research Council of Thailand (NRCT) through the Nanopolymer Project (kor-sor-sor 52/2547). The authors would also like to thank Professor Akira Fujishima, Kanagawa Academy of Science and Technology, and his group at the University of Tokyo, for their encouragement and guidance, and to the Ministry of Education, Culture, Sports, Science, and Technology (MEXT) of Japan for support.

References and Notes

1. J. Wang, *Analytical Electrochemistry* Wiley-VCH, New York **(2000)**.
2. D. Diamond (Ed.), Principles of Chemical and Biological Sensors, Chemical Analysis: A Seried of Monographs on Analytical Chemistry and its Applications, Wiley-Interscience, New York **(1998)**, Vol. 150.
3. B. R. Eggins, Chemical Sensors and Biosensors, John Wiley and Sons, New York **(2002)**.
4. G. S. Wilson (Ed.), Bioelectrochemistry, Encyclopedia of Electrochemistry, Wiley-VCH, New York **(2002)**, Vol. 9.
5. R.-I. Stefan, J. F. V. Staden, and H. Y. Aboul-Enein, Electrochemical Sensors in Bioanalysis, Marcel Dekker, New York **(2001)**.
6. C. M. A. Brett, *Pure Appl. Chem.* 73, 1969 **(2001)**.
7. A. J. Bard and L. R. Faulkner, Electrochemical Methods: Fundamentals and Applications, Wiley, New York **(2000)**.
8. J. Clavilier, D. Armand, S. G. Sun, and M. Petit, *J. Electroanal. Chem.* 205, 267 **(1986)**.
9. M. S. Hossain, D. Tryk, and E. Yeager, *Electrochim. Acta* 34, 1733 **(1989)**.
10. K. Kinoshita, Carbon: Electrochemical and Physicochemical Properties, John Wiley and Sons, New York **(1988)**.
11. T. N. Rao and A. Fujishima, *Dia. Rel. Mater.* 9, 384 **(2000)**.
12. Y. Einaga, R. Sato, H. Olivia, D. Shin, T. A. Ivandini, and A. Fujishima, *Electrochim. Acta* 49, 3989 **(2004)**.
13. A. E. Fischer, Y. Show, and G. M. Swain, *Anal. Chem.* 76, 2553 **(2004)**.
14. M. C. Granger, M. Witek, J. Xu, J. Wang, M. Hupert, A. Hanks, M. D. Koppang, J. E. Butler, G. Lucazeau, M. Mermoux, J. W. Strojek, and G. M. Swain, *Anal. Chem.* 72, 3793 **(2000)**.
15. A. Fujishima, C. Terashima, K. Honda, B. V. Sarada, and T. N. Rao, *New Diamond Frontier Technol.* 12, 73 **(2002)**.
16. T. Kondo, Y. Einaga, B. V. Sarada, T. N. Rao, D. A. Tryk, and A. Fujishima, *J. Electrochem. Soc.* 149, E179 **(2002)**.
17. N. Vinokur, B. Miller, Y. Avyigal, and R. Kalish, *J. Electrochem. Soc.* 143, L238 **(1996)**.
18. T. Kondo, K. Honda, D. A. Tryk, and A. Fujishima, *J. Electrochem. Soc.* 152, E18 **(2005)**.
19. A. Fujishima, Y. Einaga, T. N. Rao, and D. A. Tryk (Eds.), Diamond Electrochemistry, BKC, Inc. (Tokyo), Elsevier (Amsterdam) **(2005)**.
20. T. A. Ivandini, Y. Einaga, K. Honda, and A. Fujishima, Diamond Electrochemistry, edited by A. Fujishima, Y. Einaga, T. N. Rao, and D. A. Tryk, BKC, Inc., (Tokyo), Elsevier (Amsterdam) **(2005)**, p. 11.
21. A. Argoita, C. S. Kovach, and J. C. Angus, Handbook of Industrial Diamond and Diamond Films, edited by M. A. Prelas, G. Popovici, and L. K. Bigelow, Marcel Dekker, Inc., New York **(1998)**, p. 797.
22. P. K. Bachmann, Handbook of Industrial Diamond and Diamond Films, edited by M. A. Prelas, G. Popovici, and L. K. Bigelow, Marcel Dekker, Inc., New York **(1998)**, p. 821.
23. S. L. Girshick, Handbook of Industrial Diamond and Diamond Films, edited by M. A. Prelas, G. Popovici, and L. K. Bigelow, Marcel Dekker, Inc., New York **(1998)**, p. 851.
24. M. A. Cappelli, Handbook of Industrial Diamond and Diamond Films, edited by M. A. Prelas, G. Popovici, and L. K. Bigelow, Marcel Dekker, New York **(1998)**, p. 865.
25. C. H. Goeting, F. Jones, J. S. Foord, J. C. Eklund, F. Marken, R. G. Compton, P. R. Chalker, and C. Johnston, *J. Electroanal. Chem.* 442, 207 **(1998)**.
26. M. D. Koppang, M. Witek, J. Blau, and G. M. Swain, *Anal. Chem.* 71, 1188 **(1999)**.
27. Y. Show, M. A. Witek, P. Sonthalia, and G. M. Swain, *Chem. Mater.* 15, 879 **(2003)**.
28. N. Mizuochi, H. Watanabe, J. Isoya, H. Okushi, and S. Yamasaki, *Diamond Rel. Mater.* 13, 765 **(2004)**.
29. K. Okano, H. Naruki, Y. Akiba, T. Kurosu, M. Iida, Y. Hirose, and T. Nakamura, *Jpn. J. Appl. Phys.* 6, 1066 **(1989)**.
30. R. S. Clausing, Handbook of Industrial Diamond and Diamond Films, edited by M. A. Prelas, G. Popovici, and L. K. Bigelow, Marcel Dekker, New York **(1998)**, p. 19.
31. J. Philip, P. Hess, T. Feygelson, J. E. Butler, S. Chattopadhyay, K. H. Chen, and L. C. Chen, *J. Appl. Phys.* 93, 2164 **(2003)**.
32. J. Birrell, J. E. Gerbi, O. Auciello, J. M. Gibson, D. M. Gruen, and J. A. Carlisle, *J. Appl. Phys.* 93, 5606 **(2003)**.
33. J.-Y. Raty and G. Galli, *Nature Mater.* 2, 792 **(2003)**.
34. T. Kolber, K. Piplits, R. Haubner, and H. Hutter, *Fres. J. Anal. Chem.* 365, 636 **(1999)**.
35. K. Honda, T. Noda, M. Yoshimura, K. Nakagawa, and A. Fujishima, *J. Phys. Chem. B* 108, 16117 **(2004)**.
36. D. Becker and K. Juettner, *J. Appl. Electrochem.* 33, 959 **(2003)**.
37. K. B. Holt, A. J. Bard, Y. Show, and G. M. Swain, *J. Phys. Chem. B* 108, 15117 **(2004)**.
38. K. Honda, T. N. Rao, D. A. Tryk, M. Watanabe, K. Yasui, and H. Masuda, *J. Electrochem. Soc.* 147, 659 **(1999)**.
39. D. Shin, D. A. Tryk, A. Fujishima, A. Merkoci, and J. Wang, *Electroanalysis* 17, 305 **(2005)**.
40. C. Terashima, T. N. Rao, B. V. Sarada, D. A. Tryk, and A. Fujishima, *Anal. Chem.* 74, 895 **(2002)**.
41. S. G. Ri, T. Ishikawa, S. Tanaka, T. Kimura, Y. Akiba, and M. Iida, *Jpn. J. Appl. Phys.* 36, 2057 **(1997)**.
42. V. Chakrapani, S. C. Eaton, A. B. Anderson, M. Tabib-Azar, and J. C. Angus, *Electrochem. Solid-State Lett.* 8, E4 **(2005)**.
43. K. Tsugawa, H. Umezawa, and H. Kawarada, *Jpn. J. Appl. Phys.* 40, 3101 **(2001)**.
44. O. A. Williams and R. B. Jackman, *J. Appl. Phys.* 96, 3742 **(2004)**.
45. C. E. Nebel, C. Sauerer, F. Ertl, M. Stutzmann, C. F. O. Graeff, P. Bergonzo, O. A. Williams, and R. Jackman, *Appl. Phys. Lett.* 79, 4541 **(2001)**.
46. T. Maki, S. Shikama, M. Komori, Y. Sakaguchi, K. Sakuta, and T. Kobayashi, *Jpn. J. Appl. Phys.* 31, L1446 **(1992)**.

47. N. Jiang and T. Ito, *J. Appl. Phys.* 85, 8267 (**1999**).
48. K. Hayashi, H. Watanabe, S. Yamanaka, T. Sekiguchi, H. Okushi, and K. Kajimura, *Diamond Rel. Mater.* 6, 303 (**1997**).
49. K. Hayashi, S. Yamanaka, H. Watanabe, T. Sekiguchi, H. Okushi, and K. Kajimura, *J. Cryst. Growth* 183, 338 (**1998**).
50. J. Chevallier, D. Ballutaud, B. Theys, F. Jomard, A. Deneuville, E. Gheeraert, and F. Pruvost, *Phys. Stat. Solid. A* 172, 73 (**1999**).
51. J. Ristein, M. Riedel, and L. Ley, *J. Electrochem. Soc.* E315 (**2004**).
52. F. Maier, M. Riedel, B. Mantel, J. Ristein, and L. Ley, *Phys. Rev. Lett.* 85, 3472 (**2000**).
53. R. Kalish, A. Reznik, C. Uzan-Saguy, and C. Cytermann, *Appl. Phys. Lett.* 76, 757 (**2000**).
54. M. Nishitani-Gamo, E. Yasu, C. Xiao, Y. Kikuchi, K. Ushizawa, I. Sakaguchi, T. Suzuki, and T. Ando, *Diamond Rel. Mater.* 9, 941 (**2000**).
55. S. C. Eaton, A. B. Anderson, J. C. Angus, Y. E. Evstefeeva, and Y. V. Pleskov, *Diamond Rel. Mater.* 12, 1627 (**2003**).
56. R. Kalish, C. Uzan-Saguy, R. Walker, and S. Prawer, *J. Appl. Phys.* 94, 3923 (**2003**).
57. S. Gupta, B. R. Weiner, and G. Morell, *Appl. Phys. Lett.* 83, 491 (**2003**).
58. K. Nakazawa, M. Tachiki, H. Kawarada, A. Kawamura, K. Horiuchi, and T. Ishikura, *Appl. Phys. Lett.* 82, 2074 (**2003**).
59. T. Nishimatsu, H. Katayama-Yoshida, and N. Orita, *Physica B* 302–303, 149 (**2001**).
60. S. C. Eaton, Y. E. Evsteeva, J. C. Angus, A. B. Anderson, and Y. V. Pleskov, *Russ. J. Electrochem.* 39, 170 (**2003**).
61. D. A. Tryk, T. Kondo, and A. Fujishima, Diamond Electrochemistry, edited by A. Fujishima, Y. Einaga, T. N. Rao, and D. A. Tryk, BKC, Inc., (Tokyo), Elsevier, (Amsterdam) (**2005**), p. 174.
62. H. Notsu, T. Fukazawa, T. Tatsuma, D. A. Tryk, and A. Fujishima, *Electrochem. Solid State Lett.* 4, H1 (**2001**).
63. H. Notsu, I. Yagi, T. Tatsuma, D. A. Tryk, and A. Fujishima, *J. Electroanal. Chem.* 492, 31 (**2000**).
64. H. Notsu, I. Yagi, T. Tatsuma, D. A. Tryk, and A. Fujishima, *Electrochem. Solid-State Lett.* 2, 522 (**1999**).
65. K. I. Sotowa, T. Amamoto, A. Sobana, K. Kusakabe, and T. Imato, *Diamond Rel. Mater.* 13, 145 (**2004**).
66. J. B. Miller and D. W. Brown, *Langmuir* 12, 5809 (**1996**).
67. S. Ferro and A. DeBattisti, *J. Phys. Chem. B* 107, 7567 (**2003**).
68. S. Ferro and A. DeBattisti, *Anal. Chem.* 75, 7040 (**2003**).
69. A. Freedman and C. D. Stinespring, *Appl. Phys. Lett.* 57, 1194 (**1990**).
70. A. Hartl, E. Schmich, J. Garrido, J. Hernando, S. Catharino, S. Walter, P. Feulner, A. Kromka, D. Steinmuller, and M. Stutzmann, *Nature Mater.* 3, 736 (**2004**).
71. W. Yang, J. E. Butler, J. N. Russell, Jr., and R. J. Hamers, *Langmuir* 20, 6778 (**2004**).
72. W. Yang, O. Auciello, J. E. Butler, W. Cai, J. A. Carlisle, J. E. Gerbi, D. M. Gruen, T. Knickerbocker, T. L. Lasseter, J. John N. Russell, L. M. Smith, and R. J. Hamers, *Nature Mater.* 1, 253 (**2002**).
73. T. Knickerbocker, T. Strother, M. P. Schwartz, J. N. Russell, Jr., J. Butler, L. M. Smith, and R. J. Hamers, *Langmuir* 19, 1938 (**2003**).
74. J.-S. Gao, T. Arunagiri, J.-J. Chen, P. Goodwill, O. Chyan, J. Perez, and D. Golden, *Chem. Mater.* 12, 3495 (**2000**).
75. D. Roy, Z. H. Barber, and T. W. Clyne, *J. Appl. Phys.* 91, 6085 (**2002**).
76. J. Wang and G. M. Swain, *Electrochem. Solid-State Lett.* 5, E4 (**2002**).
77. F. Montilla, E. Morallon, I. Duo, C. Comninellis, and J. L. Vazquez, *Electrochim. Acta* 48, 3891 (**2003**).
78. K. J. McKenzie, D. Asogan, and F. Marken, *Electrochem. Commun.* 4, 820 (**2002**).
79. S. Ferro and A. DeBattisti, *J. Phys. Chem. B* 106, 2249 (**2002**).
80. A. DeBattisti, S. Ferro, and M. D. Colle, *J. Phys. Chem. B* 105, 1679 (**2001**).
81. N. Spataru, C. Terashima, K. Tokuhiro, I. Sutanto, D. A. Tryk, S.-M. Park, and A. Fujishima, *J. Electrochem. Soc.* 150, E337 (**2003**).
82. A. Salimi, M. E. Hyde, C. E. Banks, and R. G. Compton, *Analyst* 129, 9 (**2004**).
83. I. González-González, D. A. Tryk, and C. R. Cabrera, *Diamond Rel. Mater.* 15, 275 (**2006**).
84. A. M. Zaitsev, Handbook of Industrial Diamond and Diamond Films, edited by M. A. Prelas, G. Popovici, and L. K. Bigelow, Marcel Dekker, New York (**1998**), p. 227.
85. K. M. Rutledge and K. K. Gleason, Handbook of Industrial Diamond and Diamond Films, edited by M. A. Prelas, G. Popovici, and L. K. Bigelow, Marcel Dekker, New York (**1998**), p. 413.
86. D. S. Knight and W. B. White, *J. Mater. Res.* 4, 385 (**1989**).
87. T. Kondo, D. A. Tryk, and A. Fujishima, *Electrochim. Acta* 48, 2739 (**2003**).
88. E. Popa, Y. Kubota, D. A. Tryk, and A. Fujishima, *Anal. Chem.* 72, 1724 (**2000**).
89. E. Popa, H. Notsu, T. Miwa, D. A. Tryk, and A. Fujishima, *Electrochem. Solid State Lett.* 2, 49 (**1999**).
90. I. Yagi, K. Tsunozaki, D. A. Tryk, and A. Fujishima, *Electrochem. Solid-State Lett.* 9, 457 (**1999**).
91. K. Niwase, Y. Kakimoto, I. Tanaka, and T. Tanabe, *Nucl. Instrum. Meth. Phys. Res. B* 91, 78 (**1994**).
92. R. J. Hamers, J. E. Butler, T. Lasseter, B. M. Nichols, J. N. R. Jr., K.-Y. Tse, and W. Yang, *Diamond Rel. Mater.* 14, 661 (**2005**).
93. Y. Maeda, K. Sato, R. Ramaraj, T. N. Rao, D. A. Tryk, and A. Fujishima, *Electrochim. Acta* 44, 3441 (**1999**).
94. J. Z. Xu and G. M. Swain, *Anal. Chem.* 70, 1502 (**1998**).
95. N. S. Lawrence, M. Thompson, C. Prado, L. Jiang, T. G. J. Jones, and R. G. Compton, *Electroanalysis* 14, 499 (**2002**).
96. T. Sakai, Y. Araki, H. Kanazawa, H. Umezawa, M. Tachiki, and H. Kawarada, *Jpn. J. Appl. Phys.* 41, 2595 (**2002**).
97. K.-S. Song, T. Sakai, H. Kanazawa, Y. Araki, H. Umezawa, M. Tachiki, and H. Kawarada, *Biosens. Bioelectron.* 19, 137 (**2003**).
98. J. A. Garrido, A. Härtl, S. Kuch, M. Stutzmann, O. A. Williams, and R. B. Jackmann, *Appl. Phys. Lett.* 86, 073504 (**2005**).
99. N. Spataru, T. N. Rao, D. A. Tryk, and A. Fujishima, *J. Electrochem. Soc.* 148, E112 (**2001**).
100. S. G. Ri, K. Tashiro, S. Tanaka, T. Fujisawa, H. Kimura, T. Kurosu, and M. Iida, *Jpn. J. Appl. Phys.* 38, 3492 (**1999**).
101. S. G. Ri, T. Mizumasa, Y. Akiba, Y. Hirose, T. Kurosu, and M. Iida, *Jpn. J. Appl. Phys.* 34, 5550 (**1995**).
102. I. González-González, J. De Jesús, D. A. Tryk, G. Morell, and C. R. Cabrera, *Diamond Rel. Mater.* 15, 221 (**2006**).
103. C. Terashima, T. N. Rao, B. V. Sarada, N. Spataru, and A. Fujishima, *J. Electroanal. Chem.* 544, 65 (**2003**).
104. A. Manivannan, D. A. Tryk, and A. Fujishima, *Electrochem. Solid State Lett.* 2, 455 (**1999**).
105. A. J. Saterlay, C. Agra-Gutierrez, M. P. Taylor, F. Marken, and R. G. Compton, *Electroanalysis* 11, 1083 (**1999**).
106. J. Kruusma, C. E. Banks, and R. G. Compton, *Anal. Bioanal. Chem.* 379, 700 (**2004**).
107. C. Prado, S. J. Wilkins, F. Marken, and R. G. Compton, *Electroanalysis* 14, 262 (**2002**).
108. A. Manivannan, R. Kawasaki, D. A. Tryk, and A. Fujishima, *Electrochim. Acta* 49, 3313 (**2004**).
109. D. Dragoe, N. Spataru, R. Kawasaki, A. Manivannan, T. Spataru, D. A. Tryk, and A. Fujishima, *Electrochim. Acta* 51, 2437 (**2006**).
110. J. S. Foord, K. Eaton, W. Hao, and A. Crossley, *Phys. Chem. Chem. Phys.* 7, 2787 (**2005**).
111. A. Manivannan, M. S. Seehra, D. A. Tryk, and A. Fujishima, *Anal. Lett.* 35, 355 (**2002**).

112. A. Manivannan, D. A. Tryk, and A. Fujishima, *Chem. Lett.* 851 (**1999**).
113. A. Chatterjee, R. Wiltshire, K. B. Holt, R. G. Compton, J. S. Foord, and F. Marken, *Diamond Rel. Mater.* 11, 646 (**2002**).
114. A. J. Saterlay, S. J. Wilkins, C. H. Goeting, J. S. Foord, R. G. Compton, and F. Marken, *J. Solid State Electrochem.* 4, 383 (**2000**).
115. Y.-C. Tsai, B. A. Coles, K. Holt, J. S. Foord, and F. Marken, *Electroanalysis* 13, 831 (**2001**).
116. T. N. Rao, T. A. Ivandini, C. Terashima, B. V. Sarada, and A. Fujishima, *New Diamond Frontier Carbon Technol.* 13, 79 (**2003**).
117. H. Notsu, I. Yagi, and A. Fujishima, *Electrochemistry* 67, 389 (**1999**).
118. A. Fujishima and T. N. Rao, *Diamond Rel. Mater.* 10, 1799 (**2001**).
119. R. G. Compton, J. S. Foord, and F. Marken, *Electroanalysis* 15, 1349 (**2003**).
120. J. Xu, M. C. Granger, Q. Chen, J. W. Strojek, T. E. Lister, and G. M. Swain, *Anal. Chem.* 69, 591A (**1997**).
121. A. Fujishima, T. N. Rao, and D. A. Tryk, *Electrochim. Acta* 45, 4683 (**2000**).
122. G. M. Swain, A. B. Anderson, and J. C. Angus, *MRS Bull.* 56 (**1998**).
123. S. Alehashem, F. Chambers, J. W. Strojek, and G. M. Swain, *Anal. Chem.* 67, 2812 (**1995**).
124. H. Olivia, B. Sarada, D. Shin, T. Rao, and A. Fujishima, *Analyst* 127, 1572 (**2002**).
125. S. Jolley, M. Koppang, T. Jackson, and G. M. Swain, *Anal. Chem.* 69, 4099 (**1997**).
126. M. A. Witek and G. M. Swain, *Anal. Chim. Acta* 440, 119 (**2001**).
127. M. C. Granger, J. S. Xu, J. W. Strojek, and G. M. Swain, *Anal. Chim. Acta* 397, 145 (**1999**).
128. A. Fujishima, T. N. Rao, E. Popa, B. V. Sarada, I. Yagi, and D. A. Tryk, *J. Electroanal. Chem.* 473, 179 (**1999**).
129. B. V. Sarada, T. N. Rao, D. A. Tryk, and A. Fujishima, *New Diamond Frontier Carbon Technol.* 9, 365 (**1999**).
130. T. N. Rao, I. Yagi, T. Miwa, D. A. Tryk, and A. Fujishima, *Anal. Chem.* 71, 2506 (**1999**).
131. B. V. Sarada, T. N. Rao, D. A. Tryk, and A. Fujishima, *Chem. Lett.* 1213 (**1999**).
132. B. V. Sarada, T. N. Rao, D. A. Tryk, and A. Fujishima, *Anal. Chem.* 72, 1632 (**2000**).
133. T. A. Ivandini, B. V. Sarada, C. Terashima, T. N. Rao, D. A. Tryk, H. Ishiguro, Y. Kubota, and A. Fujishima, *J. Electroanal. Chem.* 521, 117 (**2002**).
134. T. N. Rao, B. H. Loo, B. V. Sarada, C. Terashima, and A. Fujishima, *Anal. Chem.* 74, 1578 (**2002**).
135. N. Spataru, B. V. Sarada, D. A. Tryk, and A. Fujishima, *Electroanalysis* 14, 721 (**2002**).
136. S. Haymond, G. T. Babcock, and G. M. Swain, *J. Am. Chem. Soc.* 124, 10634 (**2002**).
137. C. Prado, G. Flechsig, P. Grundler, J. Foord, F. Markenc, and R. Compton, *Analyst* 127, 329 (**2002**).
138. T. Ivandini, B. Sarada, T. Rao, and A. Fujishima, *Analyst* 128, 924 (**2003**).
139. J. Cvacka, G. M. Swain, J. Barek, and J. Zima, *Chemicke Listy* 96, 33 (**2002**).
140. T. A. Ivandini, B. V. Sarada, C. Terashima, T. N. Rao, D. A. Tryk, H. Ishiguro, Y. Kubota, and A. Fujishima, *J. Chromatogr. B* 791, 63 (**2003**).
141. O. Chailapakul, E. Popa, H. Tai, B. V. Sarada, D. A. Tryk, and A. Fujishima, *Electrochem. Commun.* 2, 422 (**2000**).
142. N. Spataru, B. V. Sarada, E. Popa, D. A. Tryk, and A. Fujishima, *Anal. Chem.* 73, 514 (**2001**).
143. O. Nekrassova, G. D. Allen, N. S. Lawrence, L. Jiang, T. J. Jones, and R. G. Compton, *Electroanalysis* 14, 1464 (**2002**).
144. O. Chailapakul, P. Aksharanandana, T. Frelink, Y. Einaga, and A. Fujishima, *Sens. Actuators B: Chem.* 80, 193 (**2001**).
145. O. Chailapakul, W. Siangproh, B. V. Sarada, C. Terashima, T. N. Rao, D. A. Tryk, and A. Fujishima, *Analyst* 127, 1164 (**2002**).
146. C. Terashima, T. N. Rao, B. V. Sarada, Y. Kubota, and A. Fujishima, *Anal. Chem.* 75, 1564 (**2003**).
147. C. Terashima, T. N. Rao, B. V. Sarada, and A. Fujishima, *Chem. Lett.* 32, 136 (**2003**).
148. O. Nekrassova, N. S. Lawrence, and R. G. Compton, *Electroanalysis* 15, 1655 (**2003**).
149. N. Wangfuengkanagul and O. Chailapakul, *Talanta* 58, 1213 (**2002**).
150. W. Siangproh, N. Wangfuengkanagul, and O. Chailapakul, *Anal. Chim. Acta* 499, 183 (**2003**).
151. W. Siangproh, P. Ngamukot, and O. Chailapakul, *Sens. Actuators B: Chem.* 91, 60 (**2003**).
152. J. Xu, Q. Chen, and G. M. Swain, *Anal. Chem.* 70, 3146 (**1998**).
153. A. J. Saterlay and J. S. Foord, *Electroanalysis* 13, 1065 (**2001**).
154. C. Prado, G. G. Murcott, F. Marken, J. S. Foord, and R. G. Compton, *Electroanalysis* 14, 975 (**2002**).
155. N. Wangfuengkanagul and O. Chailapakul, *J. Pharm. Biomed. Anal.* 28, 841 (**2002**).
156. R. Uchikado, T. N. Rao, D. A. Tryk, and A. Fujishima, *Chem. Lett.* 144 (**2001**).
157. M. Komatsu and A. Fujishima, *Bull. Chem. Soc. Japan* 76, 927 (**2003**).
158. H. Notsu, T. Tatsuma, and A. Fujishima, *J. Electroanal. Chem.* 523, 86 (**2002**).
159. J. Cvacka, V. Quaiserova, J. Park, Y. Show, A. Muck, and G. Swain, *Anal. Chem.* 75, 2678 (**2003**).
160. J. Wang, G. Chen, M. P. Chatrathi, A. Fujishima, D. A. Tryk, and D. Shin, *Anal. Chem.* 75, 935 (**2003**).
161. T. N. Rao, B. V. Sarada, D. A. Tryk, and A. Fujishima, *J. Electroanal. Chem.* 491, 175 (**2000**).

SENSOR LETTERS
Vol. 4, 120–128, 2006

RESEARCH ARTICLE

A Transcutaneous Hydrogen Sensor: From Design to Application

Oomman K. Varghese[1,*], Xiping Yang[2], James Kendig[3], Maggie Paulose[2], Kefeng Zeng[2], Charles Palmer[3], Keat Ghee Ong[2], and Craig A. Grimes[1]

[1] *Department of Electrical Engineering, Department of Materials Science and Engineering, The Pennsylvania State University, 217 Materials Research Laboratory, University Park, PA 16802, USA*
[2] *Sentechbiomed Corporation, 200 Innovation Boulevard, State College, PA 16803, USA*
[3] *Penn State Milton S. Hershey Medical Center, Division of Newborn Medicine, 500 University Drive, Hershey, PA 17033, USA*

(Received: 4 April 2006. Accepted: 10 May 2006)

A transcutaneous hydrogen gas sensor of unprecedented sensitivity was fabricated and applied as a diagnostic tool for determining lactose intolerance due to lactase deficiency. The sensor, based on the use of highly-ordered titania nanotube arrays made by anodization of a 250 μm thick titanium foil, shows a change in electrical resistance of 8.7 orders of magnitude when cycled between air and nitrogen containing 1000 ppm of hydrogen. The sensor is completely reversible with a response time of about 30 seconds. Lactose intolerance tests were conducted at the Pediatric Gastroenterology Clinic of the Penn State Children's Hospital, where the transcutaneous hydrogen gas concentration from lactose intolerant patients was monitored and compared to hydrogen levels in exhaled breath. Results indicate a direct correlation between the transcutaneous and exhaled-breath hydrogen gas concentrations.

Keywords: Titania Nanotubes, Transcutaneous, Hydrogen, Lactose Intolerance, Sensor, Gas.

1. INTRODUCTION

Nano-structured metal oxides fabricated via anodization have been increasingly applied as gas sensors in recent years due to their remarkable gas-sensing properties which include large sensitivity, fast response time, controllable selectivity, and low hysteresis and drift. Varghese and coworkers,[1] for example, incorporated nanoporous alumina onto a surface acoustic wave device for the precise detection of ammonia gas. Lately considerable attention has been paid to the application of highly-ordered titania nanotube arrays[2–8] to measurement of hydrogen gas concentrations, achieved by monitoring the changes in electrical resistance of the nanotube-array sensors in response to hydrogen. Such hydrogen sensors have been incorporated into a sentinel wireless hydrogen sensor network for possible application in neonatal intensive care units.[9] In this work we focus on the optimization and application of the nanotube-array sensors for measurement of transcutaneous hydrogen levels.

Transcutaneous gas monitoring has been used as a means for diagnosing disease, as well as monitoring treatment effectiveness. For example, transcutaneous carbon dioxide is routinely monitored for bronchopulmonary dysplasia, apnea, upper airway obstruction, mechanical ventilation, and respiratory problems associated with hypercapnia.[10] Transcutaneous carbon dioxide is also routinely used in neonatal intensive care units[11,12] or in the preclinical detection of pneumothorax.[13] However, to our knowledge, there has been no effort on using transcutaneous hydrogen gas for diagnosing diseases. As far as we know, this is the first work to use measurement of transcutaneous hydrogen concentrations for detection of lactose intolerance,[14,15] and beyond that can be viewed as an enabling technology that might have a variety of useful clinical applications.

Lactose intolerance is caused by the inability to digest significant amounts of lactose, a major sugar in milk, due to the lack of enzyme lactase produced by the cells in the small intestine.[16] The function of lactase is to break down milk sugar into glucose and galactose, which are then absorbed into the bloodstream. Failure to digest

*Corresponding author; E-mail: dkv3@psu.edu

 1546-198X/2006/4/120/009 doi:10.1166/sl.2006.022

lactose into glucose and galactose causes the person to feel uncomfortable after consuming milk products, exhibiting symptoms such as nausea, cramps, bloating, gas, and diarrhea. Symptoms begin about 30 s to 2 hours after eating or drinking foods containing lactose. Currently, lactose intolerance is diagnosed with the Lactose Tolerance Test,[17, 18] where a patient's blood samples are taken over a 2-hour period to measure the blood glucose levels after lactose consumption to indicate how well the body is able to digest lactose. Alternatively, the Hydrogen Breath Test[14] can be performed to measure the amount of hydrogen present in the patient's breath since undigested lactose in the colon is fermented by bacteria and produces various gases including hydrogen, that is absorbed from the intestines, carried through the bloodstream to the lungs where it is exhaled. As indicated by the enabling work of Gerlach,[19] we hypothesize that a portion of hydrogen in the bloodstream releases through the skin, thus allowing hydrogen detection with a noninvasive, transcutaneous hydrogen sensor.

Our hydrogen sensor is based on the use of highly-ordered titania nanotube arrays, made by anodization of a Ti foil.[6, 20, 21] Micron-length un-doped titania nanotube-arrays exhibit an unprecedented variation in electrical resistance of up to ≈8.7 orders of magnitude, at room temperature, when exposed to alternating atmospheres of nitrogen containing 1000 ppm hydrogen and air.[8] The highly sensitive room, or skin, temperature operation of the sensor is critical for transcutaneous operation without risk of damaging the adjacent skin. The 8.7 orders of magnitude change in response to 1000 ppm hydrogen of the sensor represents the largest known change in electrical properties of any material, to any gas, at any temperature. The dramatic change in resistance is believed to be due to the highly active surface states on the nanoscale walls of the tubes, high surface area of the nanotube architecture, and the well-ordered geometry allowing for hydrogen-sensitive tube-to-tube electrical connections.[6, 8, 22]

The sensor response is characterized by measuring the change in its resistance through electrical contacts. Using a mask, platinum circular electrode pads (500 μm diameter, 100 nm thick, 1 mm edge-to-edge spacing) are sputter-coated onto the nanotube-array samples. Gold wire (1 mil), used for making electrical connections between the material and the measurement electronics, is bonded onto the platinum pads with a Mech-El-907 ultrasonic wire bonder. We have developed a robust electronic interface suitable for handing sensor resistances from 50 GΩ to the metallic range.

Since metal oxides, or indeed most materials, to some extent respond to a variety of environmental parameters, i.e., demonstrate unwanted cross-sensitivities, it is necessary to use other sensors, and cross-correlate the responses of these different sensors to obtain an absolute measurement of the target gas from within a complex environment. Therefore, we incorporated a humidity-temperature sensor along with the hydrogen sensor. The packaged sensor array is displayed in Figure 1. The hydrogen sensor and humidity-temperature sensor are secured in a white teflon housing, which screws onto the adhesive-backed ring that is applied to the skin of the patient undergoing the test.

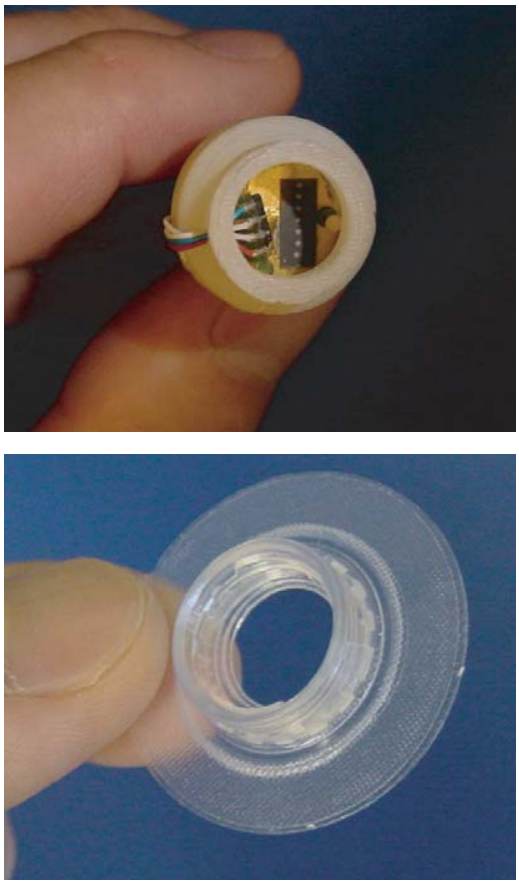

Fig. 1. (a) Packaging of our sensors comprised of a hydrogen sensor and a humidity-temperature sensor. The connector twists onto the adhesive-backed ring. (b) Vent holes (not visible) on the side prevent the accumulation of water vapor and gases in the housing.

2. SYSTEM IMPLEMENTATION

2.1. Fabrication of Titania Nanotube Array by Anodization

Figure 2 illustrates the anodization process; the target metal, in this case titanium, is used as the anode in an electrochemical cell with a platinum cathode. Upon application of a voltage potential across the terminals there is field-enhanced oxidation of the metal. While there is both field-enhanced oxidation of the metal, and field-enhanced dissolution of the oxide, the electric field at the bottom of the pore at the metal-oxide interface is much higher than that at the wall, hence the metal will be consumed at a higher rate near the bottom of the pore allowing continuous growth of the pore depth.

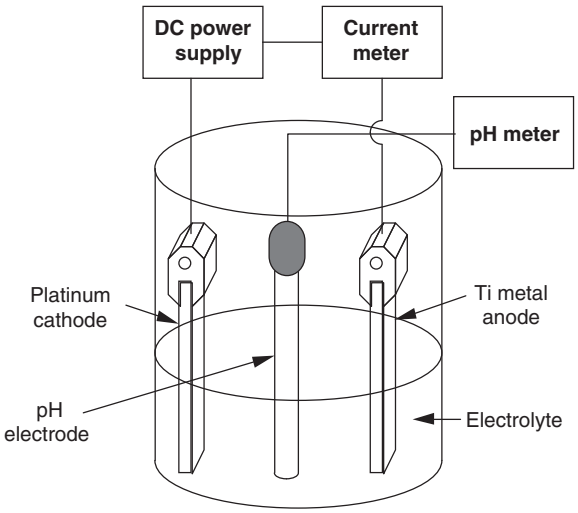

Fig. 2. Anodization setup comprising a glass beaker, some chemicals, and a dc power supply.

Titania nanotube arrays fabricated by anodic oxidation of titanium thick-film foils and thin films in hydrofluoric acid (pH 4.0) containing potassium fluoride, sodium hydrogen sulfate monohydrate, and sodium citrate tribasic dehydrate arrays were reported[20, 21] having lengths up to 400 nm and pore diameters from 22 nm to 90 nm depending on the anodization voltage. The structure consists of adjacent, parallel-oriented nanotubes separated from the un-anodized titanium foil by a thin oxide layer (barrier layer), the initial thickness of which is approximately equal to the nanotube pore radius. Nanotube-arrays of length 200 nm and pore diameter 22 nm coated with a thin palladium layer showed a resistance variation of about five orders in magnitude on exposure to 1000 ppm hydrogen at 290 °C.[22] However device performance was limited by the very low thickness of the array structure, which provided a low resistance path for the current to flow between the platinum-film electrodes on the nanotube surface and the underlying titanium metal layer. Furthermore, it is difficult to make electrical connections to this material, accomplished by wire bonding, since the wire bonder head would commonly break through the barrier layer to the underlying metal resulting in an electrical short.

We have improved the anodization process to fabricate nanotube-array architectures with lengths up to 6.5 μm using a KF or NaF electrolyte, pore diameters from 22 nm to 110 nm, and wall thicknesses from 9 nm to 34 nm. Our ability to control nanotube-array dimensions has enabled our ability to meaningfully test the gas sensing properties of the nanotube arrays. More importantly, these highly stable nano-structures withstand the mechanical handling necessary to transform them from materials to sensors. Figure 3 shows a FESEM image of a hydrogen responsive titania nanotube array sample made by anodization of titanium in a KF-containing electrolyte. The length of the nanotube array is dependent upon the pH, with higher

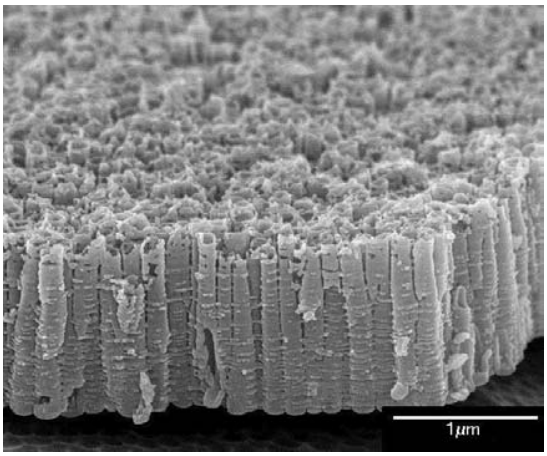

Fig. 3. FESEM images of illustrative TiO_2 nanotube-array grown in a KF based electrolyte of pH 3 using 25 V.

pH values that remain acidic resulting in longer nanotubes. The wall thickness is dependent upon the anodization bath temperature, and the pore diameter is a function of the anodization voltage. At a particular pH value, the pore size and length of the tube increase with the increase in voltage. For example, a 10 V anodization in pH 1.1 results in a nanotube array of 350 nm length and 30 nm pore diameter. A 25 V anodization in pH 5.0 results in a nanotube array of 6.5 μm length, with a 110 nm pore diameter. The longest nanotube array we have achieved to date is 25 μm.

Nanotube-arrays were prepared by anodization of 250 μm-thick titanium foil (99.7% Aldrich, Milwaukee, WI) samples in an electrolyte containing 1 M sodium hydrogen sulfate monohydrate, 0.1 M potassium flouride (ACS reagent 99% Alfa Aesar, Ward Hill, MA) and 0.2 M sodium citrate tribasic dihydrate (ACS reagent 99% Aldrich). Electrolyte pH was adjusted by the addition of sodium hydroxide (97% Aldrich). Nanotube lengths varied from 380 nm to 6.5 μm and pore diameters from 30 nm to 110 nm as dependent on the electrolyte pH (1.11 to 5) and the anodization potential (10–25 V). The samples, upon anodization, are amorphous demonstrating essentially no gas sensing properties. The samples were annealed at 480 °C for 6 hours for crystallization[21] to achieve suitable gas sensing properties.

2.2. Sensor Fabrication

To transform the nanotube-arrays into gas sensors it is necessary to achieve electrical contact with the material, so that the resistance or impedance of the material can be measured as a function of gas ambient. This is accomplished by depositing, through a mask, metal contacts onto the material of interest: Platinum circular electrodes (500 μm diameter, 100 nm thick, 1 mm edge-to-edge spacing) onto the top of the nanotube-array samples. Increasing the electrode separation increases the baseline resistance but does not affect sensitivity. Upon depositing

the electrodes, gold wires (1 mil) were bonded onto the pads with a Mech-El -907 ultrasonic wire bonder. We noticed that with short nanotubes, i.e., approximately 200 nm long, the nanotubes easily broke during the wire bonding stage. However, this problem was averted by making longer nanotube arrays using a KF or NaF electrolyte. These longer nanotube arrays demonstrated greater gas sensitivities, and were also mechanically more robust hence they could be easily connected to the outside world.

A further complicating factor is that the baseline resistance of metal oxide materials can be well over 100 GΩ, an impedance so large that it is virtually impossible to make interface electronics. We found that a post-anodization acid rinse could be used to controllably reduce the thickness of the oxide barrier layer between the nanotubular region and the underlying metal substrate, thus lowering the baseline resistance of the sensor.

2.3. Fabrication of the Sensor Reader

We have developed a robust electronic interface suitable for handling sensor resistances from 50 GΩ to the metallic range. Figure 4 shows a block diagram of the sensor interface electronics. For sensor measurement, a constant current I is applied to the sensor and the resulting dc voltage V is measured. The sensor resistance R is then calculated by $R = V/I$. In order to track the sensor resistance over a wide range (from 0 to 50 GΩ), the microcontroller is programmed to precisely and automatically tune the dc current value as well as the amplifier gain for optimal measurement accuracy. The measured data, including resistance of the hydrogen sensor, humidity, and temperature (the output of these two sensors is a microprocessor compatible voltage) are sent to a PC for storage and processing. Figure 5 shows the transcutaneous hydrogen measurement system.

Figure 6 shows the schematic diagram of the circuit that measures the resistance of the hydrogen sensor. A voltage generation circuit, which uses an ADR380 voltage reference chip (from Analog Devices), is designed to generate two accurate voltages: 2.048 V and 0.2048 V. The two voltages are selectable by an analog switch MAX4526

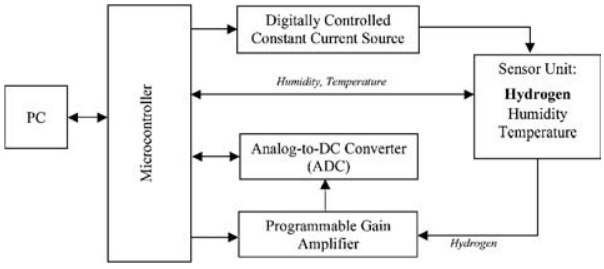

Fig. 4. Block diagram of the sensor interface electronics. The system generates a constant current to the hydrogen sensor, and measures the resulting voltage to determine the resistance. The response of a humidity-temperature sensor is also measured.

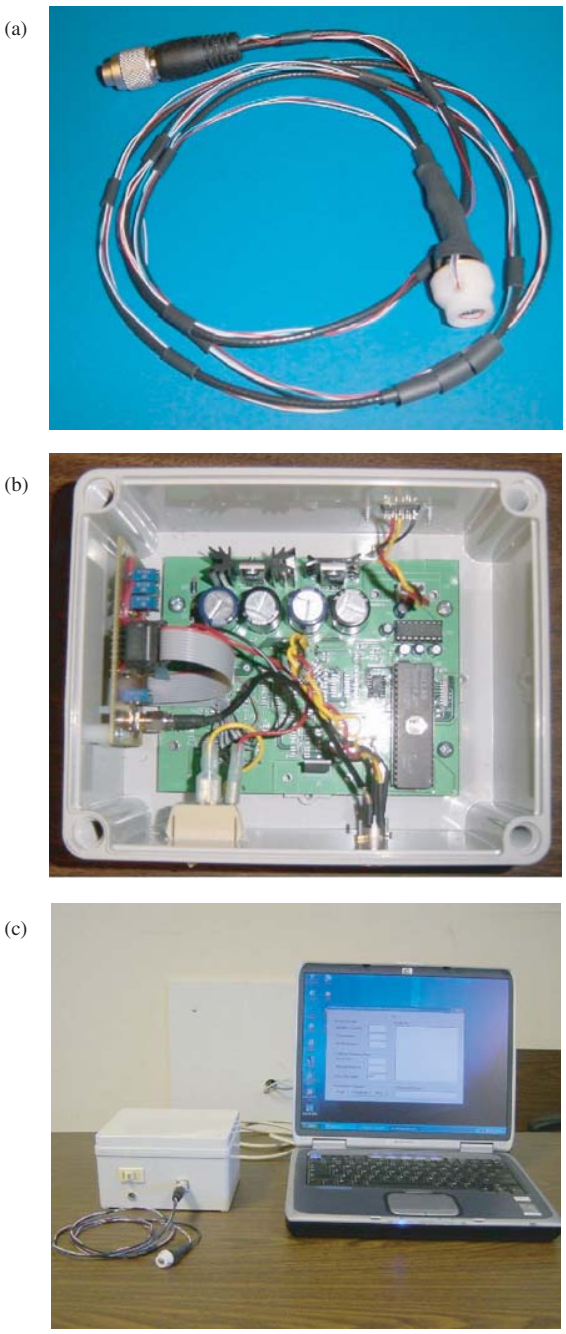

Fig. 5. (a) Packaged sensor with cable connecting sensor to electronics. (b) Internal view of sensor electronics. (c) The sensor, electronics box, and computer interface for data display.

(from Maxim/Dallas Semiconductor). The selected reference voltage is fed to a constant current generation circuit, which uses an analog switch MAX4666 (from Maxim/Dallas Semiconductor) to select the desired constant current value. With the combination of the two analog switches, the circuit can generate four digitally controlled current values: 2.048×10^{-6} A, 2.048×10^{-7} A, 2.048×10^{-9} A, and 2.048×10^{-10} A. The constant current source of a selected value is applied to the sensor under

RESEARCH ARTICLE

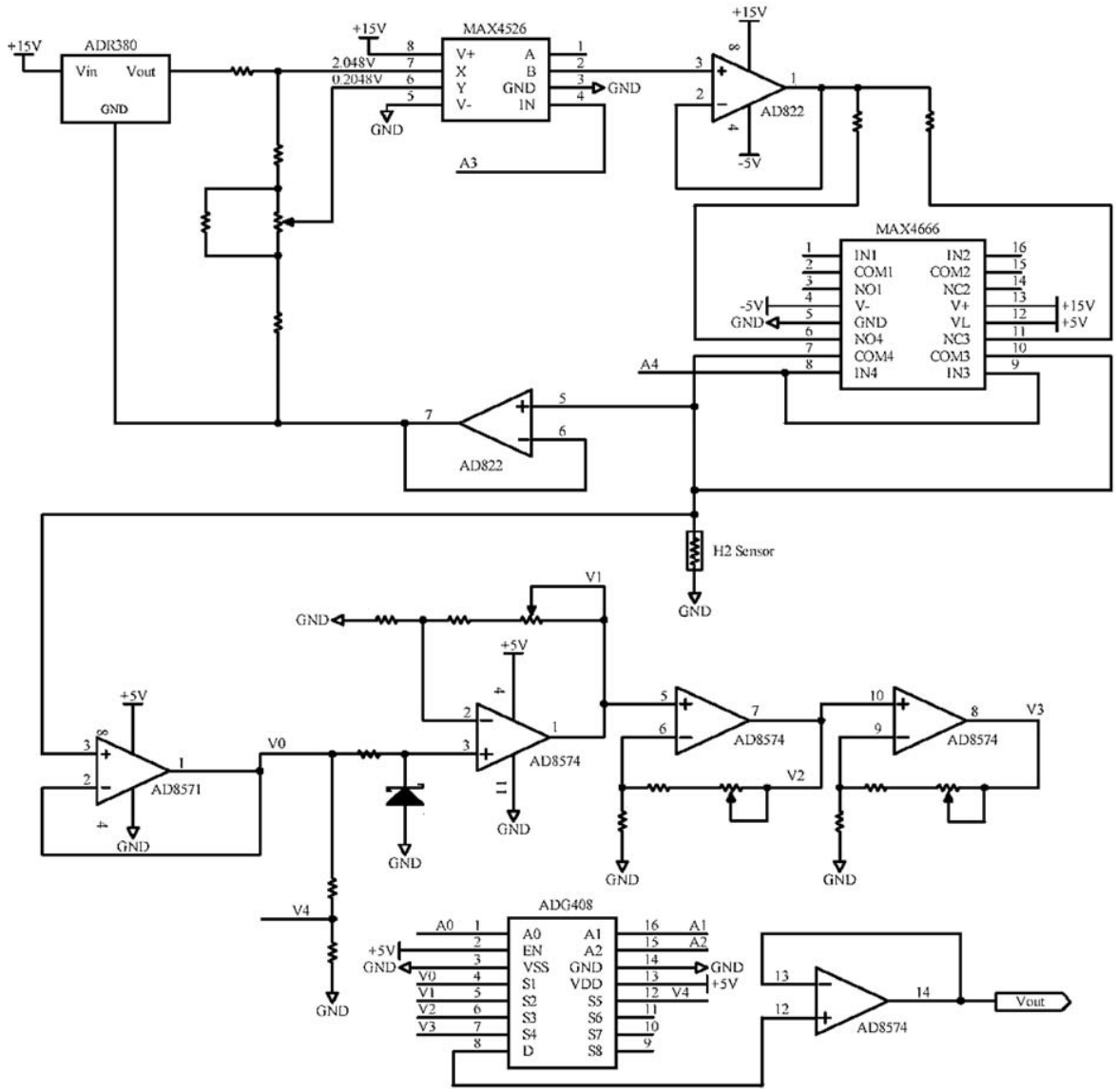

Fig. 6. Schematic diagram of the circuit for measuring the resistance of the hydrogen sensor.

measurement, and the sensor voltage is amplified by an amplifier bank consisting of five op-amps, with five voltage gains of 0.5, 1, 10, 100, and 1000 selectable by an analog multiplexer ADG408. The amplified voltage is sent to an ADC converter AD7817, which is part of the back-end microcontroller control circuit (not shown in the figure). A Dallas Microcircuits multiplexer chip is used to sequence between the difference sensors, with a Visual Basic interface allowing the user to input desired parameters.

The hydrogen sensor is packaged with a humidity/temperature sensor into a single sensor housing so that hydrogen, relative humidity, and temperature can be simultaneously monitored. The humidity sensor, SHT15 from Sensorian Inc., uses a two-wire serial interface to directly send measurements to the microcontroller, which are then processed and sent to a PC for storage.

3. RESULTS AND DISCUSSION

3.1. Hydrogen Sensitivity

The behavior of the nanotube samples in the presence of different gases was tested in a sealed Plexiglas chamber of 110 cm^3 volume. Titania, an n-type semiconductor, decreases its resistance in the presence of reducing gases and hence gas sensitivity S is defined as:[23]

$$S = \frac{G_{gas} - G_{air}}{G_{air}} \approx \frac{G_{gas}}{G_{air}} \quad \text{when} \quad G_{air} \ll G_{gas} \qquad (1)$$

where G_{air} and G_{gas} are, respectively, the conductance of the nanotubes in air and the test gas.

The greatest hydrogen sensitivities are achieved with the 30 nm pore diameter samples fabricated at 10 V,

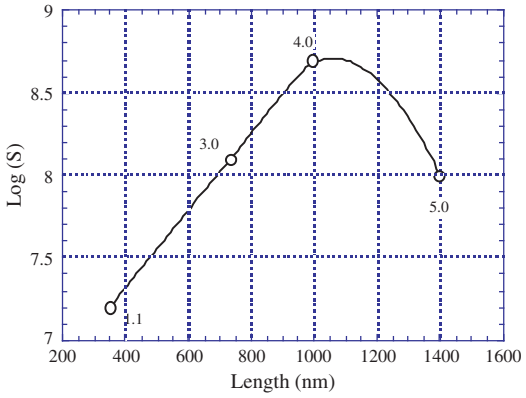

Fig. 7. The sensitivity of the hydrogen sensor depends on the length of the nanotubes. The pH of the electrolyte is listed for each sample.

Consequently the majority of our discussion is focused on these samples. Figure 7 plots the maximum room temperature hydrogen sensitivity, log(S), of the 30 nm pore diameter nanotube arrays in response to 1000 ppm hydrogen, as a function of length, which in turn is determined by electrolyte pH. We note that maximum hydrogen sensitivity was achieved with a 480 °C annealing that crystallizes the initially amorphous nanotube array samples. It can be seen from the figure that the highest resistance variation, 8.7 orders of magnitude was obtained for nanotube samples prepared using electrolyte pH 4.0 (length ∼1 μm, pore diameter ∼30 nm and wall thickness ∼13 nm). To the best of our knowledge, this is the largest change in electrical resistance of any material, to any gas, at any temperature. Sensitivity S is not greatly influenced by nanotube length; for the 10 V samples a sensitivity shift of 7 orders to 8.7 orders is found with an increase in length from 380 nm to 1 μm. It was found that 6 μm long samples (25 V, pH 5.0) showed less sensitivity, with significantly longer response/recovery times due to the time required for hydrogen to diffuse inside the long pores.

We make note that a test chamber capable of accurately flowing less than, approximately, 10 ppm of any gas is a difficult challenge requiring considerable resources. Consequently, we are not able to directly measure the low-level sensitivity of the sensor. The lower limit of our test chamber is approximately 20 ppm, at which we see 7.2 orders of magnitude variation in electrical resistance to 20 ppm hydrogen. The response of the sensor is linear to, approximately, 1000 ppm when it begins to demonstrate a non-linear response.

Figure 8 shows the variation in hydrogen sensitivity of the 10 V samples as a function of electrolyte pH. The response/recovery time (duration for the signal to change to 90% of its final value) of the sensor increases from 30 s to 200 s when the electrolyte pH increases from 1.13 to 4.5 due to the increase in tube length. There is no observable difference in the response time (air-to-hydrogen) and recovery time (hydrogen-to-air). The typical response of

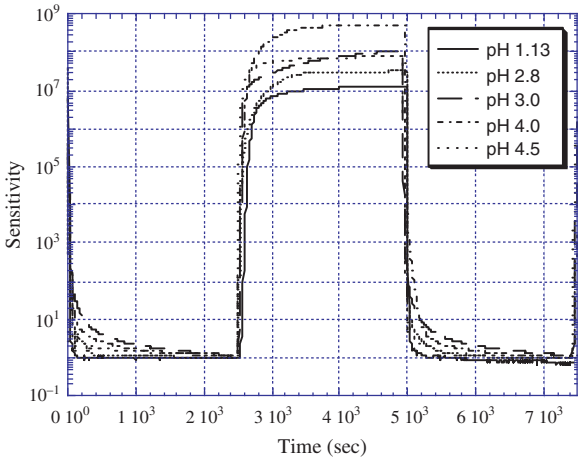

Fig. 8. Variation in hydrogen sensitivity S of 30 nm pore diameter nanotube-array samples as a function of electrolyte pH.

a pH 4.0 sample on repetitive switching of the ambient atmosphere between air and 1000 ppm hydrogen in nitrogen is shown in Figure 9. On exposure to hydrogen a rapid reduction in resistance from several hundred Giga-Ohms to a few hundred Ohms is observed; there is no indication of measurement hysteresis.

3.2. Cross Interference and Calibration

To determine which parameters affect the resistance of the hydrogen sensor, we placed the sensor inside the test chamber and varied the test environment (humidity, a variety of interfering gases, temperature) observing the change, if any, in the sensor resistance.

Temperature: As shown in Figure 10, temperature has a large impact on the resistance of the hydrogen sensor. Nevertheless, in practice the operating temperature of the

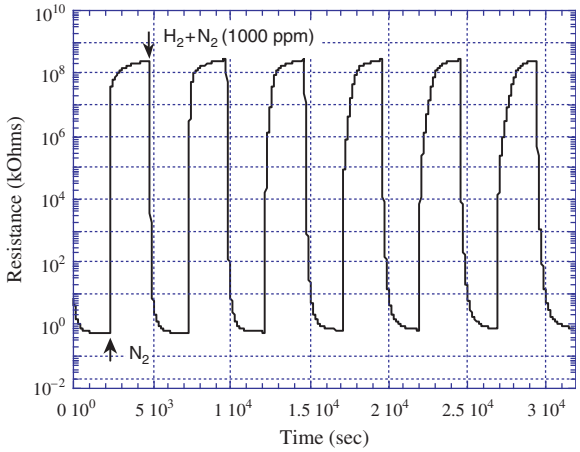

Fig. 9. Room temperature resistance variation of a nanotube-array sample prepared in a pH 4.0 electrolyte using 10 V (30 nm pore diameter), annealed at 480 °C, alternately exposed to air and 1000 ppm hydrogen in nitrogen.

RESEARCH ARTICLE

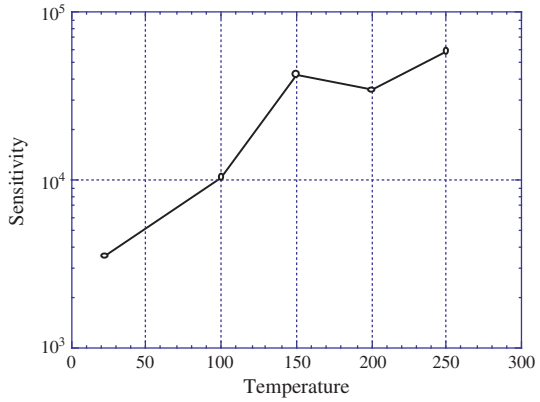

Fig. 10. The sensitivity of a 200 nm long nanotube-array hydrogen sensor increases with temperature.

transcutaneous sensor is near or at body temperature. As indicated in Figure 10, the change in the sensor sensitivity is only ≈0.08 order of magnitude (from 3800 to 4600) from 25° to 37 °C. As a result, although the temperature of the hydrogen sensor was also measured during the experiments, no calibration was performed.

Humidity: Figure 11 plots the change in sensor sensitivity (at 1000 ppm hydrogen) as a function of relative humidity. Between relative humidity of 3% and 56%, the sensitivity of the hydrogen sensor varies from 2.5×10^8 to 7×10^4, a change of more than 3 orders of magnitude. Therefore to ensure measurement integrity, we always measured the humidity level inside the sensor package, and used the humidity readings for calibration.

Oxygen: The addition of oxygen into the test environment reduces the sensitivity of the sensor as indicated in Figure 12. However, results show that the difference in the sensor sensitivity is only about 1 order of magnitude between zero (a pure nitrogen environment) and 20% of oxygen (atmospheric condition). As a result, variations in oxygen concentration do not represent a significant cross-sensitivity to the measurement since the hydrogen sensor

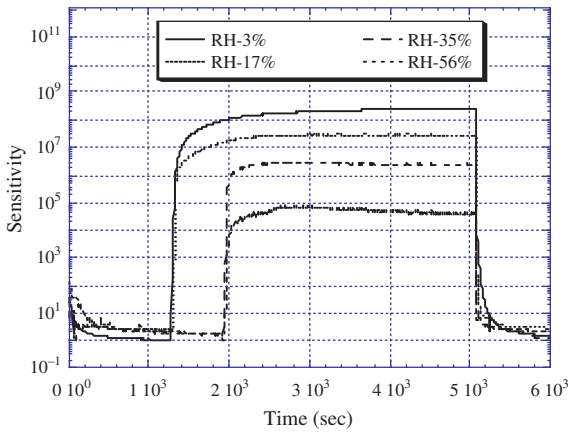

Fig. 11. The sensitivity of the hydrogen sensor reduces with increasing humidity.

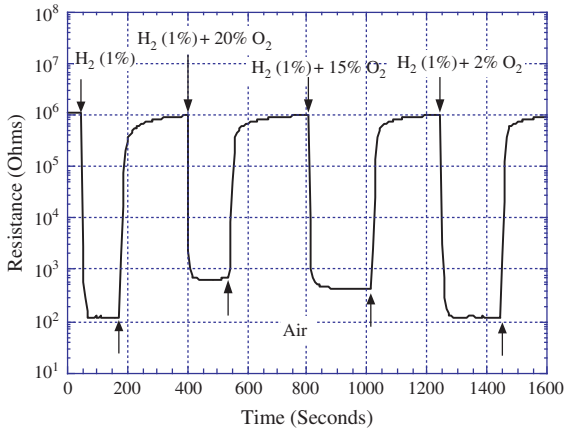

Fig. 12. The sensitivity of the hydrogen sensor reduces with increasing oxygen concentration.

was usually exposed to a near-atmospheric condition, with vent holes in the sensor housing allowing for the free flow-through of gases.

Carbon Dioxide: Figure 13 plots the resistance of the hydrogen sensor when it was switched from a pure nitrogen environment and nitrogen with 10% of CO_2. As clearly indicated in the plot, there is no difference between these two environments. This is expected because carbon dioxide is neither a strong reducing gas nor a strong oxidizing gas.

Carbon Monoxide: Figure 14 plots the change in the sensitivity when the sensor is exposed to 1000 ppm of carbon monoxide. Results show the sensitivity of the sensor to be approximately two orders or magnitude when exposed to 1000 ppm CO. Consequently, the material might usefully serve as a carbon monoxide sensor, however for this application CO cross-sensitivity is not a concern since it is highly unlikely for gas to be released by a patient.

Methane: Figure 14 plots the sensitivity of the sensor when it was exposed to 1000 ppm of methane. Results

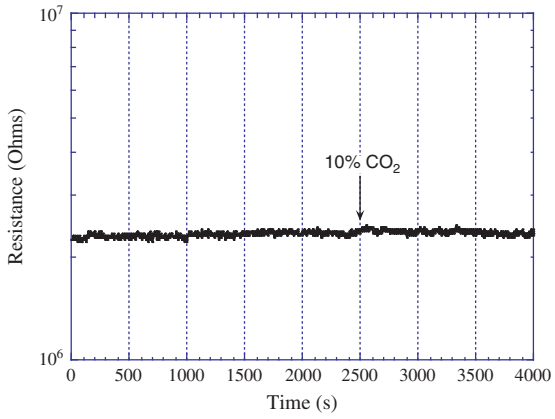

Fig. 13. Carbon dioxide has no effect on the sensor. The sensor was in a pure nitrogen atmosphere with 1000 ppm hydrogen. Ten percent of CO_2 was introduced at 2500 seconds.

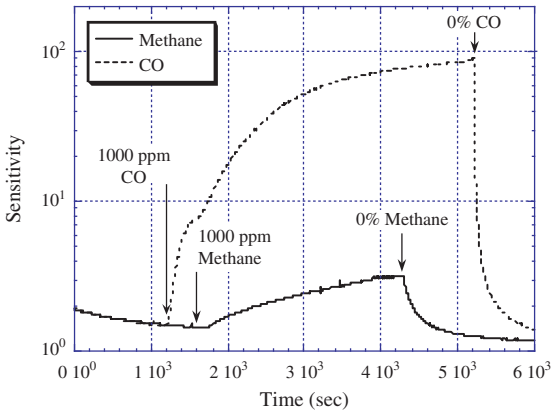

Fig. 14. The introduction of 1000 ppm carbon monoxide causes the sensor sensitivity to increase for about two orders of magnitude, while methane only changes the sensor sensitivity by half order of magnitude.

show that 1000 ppm of methane causes a change in electrical resistance of about a half order of magnitude, much smaller than the effect of hydrogen.

Upon evaluating the performance of the hydrogen sensor against various gases and operating conditions, we have concluded that for transcutaneous hydrogen measurement, the only significant potentially interfering parameter for our test application is humidity, hence we have generated a calibration lookup table to compensate for its effect. Before use, the resistance of the same sensor was measured as a function of humidity and hydrogen concentration, and the results were stored in a database. When taking a measurement, the operating software first obtained the humidity and hydrogen sensor measurements (resistance) from the microcontroller. It then determined the closest humidity and resistance values by going through the lookup table, and found the corresponding hydrogen concentration. The calibrated hydrogen concentration was printed on the screen of the PC in real time.

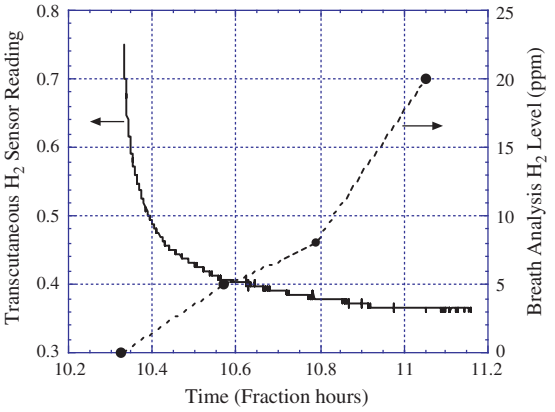

Fig. 15. Measurement of transcutaneous hydrogen concentrations using the described sensor (y-axis on LHS), and exhaled breath hydrogen levels (y-axis on RHS) measured by a gas chromatograph from a lactose intolerant adult volunteer.

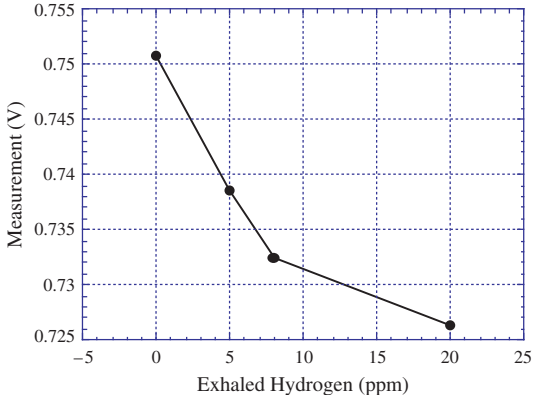

Fig. 16. Correlation between the response of the transcutaneous hydrogen sensor and exhaled hydrogen concentration.

3.3. Transcutaneous Hydrogen and Lactose Intolerance

Our transcutaneous hydrogen sensor was evaluated in the Pediatric Gastroenterology Clinic of the Penn State Children's Hospital with the full approval of the Institutional Research Subjects Review Board. The transcutaneous hydrogen sensor was placed on the forearm of children and adult volunteers who were referred for breath hydrogen testing for the evaluation and diagnosis of possible lactose intolerance due to lactase deficiency. In these patients the sensor has documented the transcutaneous excretion of hydrogen. Moreover in those patients with documented lactose intolerance, there is a good correlation between the transcutaneous sensor readings and the exhaled breath hydrogen levels as measured by the commercial gas chromatography Quintron instrument. We have studied 14 patients, some of whom had no detectable transcutaneous hydrogen excretion or detectable levels of exhaled breath hydrogen. Negative results in some patients have helped to reassure us that the novel hydrogen sensor is not responding to some volatile molecule that might be excreted through the skin. Figure 15 shows illustrative measurement of transcutaneous hydrogen levels using the described transcutaneous sensor, note the sensor measurement is continuous in operation, and the hydrogen levels (ppm) in exhaled breath as measured using a gas chromatograph, from a lactose intolerant adult volunteer who drank a small sample of milk. Figure 16 shows the decrease in the sensor measurement, which indicates an increase in transcutaneous hydrogen, coincides with an increase in exhaled breath hydrogen concentration.

4. CONCLUSIONS

We describe the fabrication, and systematic integration, of a hydrogen sensor based on the use of titania nanotube-arrays and its application to measurement of transcutaneous hydrogen levels. The titania nanotube array sensor shows an unprecedented sensitivity of 8.7 orders

RESEARCH ARTICLE

of magnitude when cycled between air and nitrogen containing 1000 ppm of hydrogen. Experimental results show the sensor is relatively insensitive to other gases such as oxygen, carbon dioxide, and methane. This sensor is significantly affected by changes in humidity, consequently we generated a calibration lookup table to ensure accurate hydrogen sensor operation over a range of humidity levels. By measuring the transcutaneous hydrogen concentration of a lactose intolerant patient, we have demonstrated a good correlation between the transcutaneous sensor reading and the exhaled breath hydrogen level using a commercially available gas chromatograph.

In addition to lactose intolerance, the transcutaneous hydrogen sensor can also be applied to other diseases such as necrotizing enterocolitis (NEC), a devastating disease of uncertain etiology and pathogenesis that causes high levels of mortality and morbidity in about 10% of preterm infants in neonatal intensive care units throughout the world.[24] Almost 20 years ago, several investigators[25, 26] demonstrated that elevated levels of exhaled breath hydrogen gas precede the onset of the clinical and radiographic signs of NEC. From a practical standpoint, it is very difficult to measure gas levels in exhaled breath of preterm infants because of their small tidal volumes and rapid respiratory rates. In neonatal intensive care units, the use of endotracheal tubes, nasal CPAP systems and nasal cannula flow systems are all barriers to the successful collection of undiluted end expiratory gas samples for gas analysis. Therefore, we expect transcutaneous measurement of hydrogen gas in preterm infants has the potential to facilitate the early identification and treatment of cases of NEC. This would permit the early withdrawal of enteral feeds and the early initiation of systemic antibiotics and supportive therapy with fluids, pressors, and blood products. In addition to saving lives, NEC mortality rate is about 35%, the early detection of NEC may also significantly reduce hospital costs, which according to an analysis published in 2002[27] is $95 million per year in the US.

Acknowledgments: O. K. Varghese and C. A. Grimes wish to thank the National Science Foundation, grant CTS-0518269 for support of their efforts associated with this project. X. Yang, M. Paulose, K. Zeng, and K. G. Ong wish to thank the National Institutes of Health, grant 1 R43 HD04233-01, for support of their efforts associated with this project. J. Kendig, C. Palmer, and C. A. Grimes wish to thank a Commonwealth of PA grant, affiliated with the Tobacco fund settlement, for additional financial assistance for this project.

References and Notes

1. O. K. Varghese, D. Gong, W. R. Dreschel, K. G. Ong, and C. A. Grimes, *Sens. Actuators B* 94, 27 **(2003)**.
2. O. K. Varghese and C. A. Grimes, *J. Nanosci. Nanotechnol.* 3, 277 **(2003)**.
3. O. K. Varghese, D. Gong, M. Paulose, K. G. Ong, and C. A. Grimes, *Sens. Actuators B*, 93, 338 **(2003)**.
4. G. K. Mor, O. K. Varghese, M. Paulose, and C. A. Grimes, *Sens. Lett.* 1, 42 **(2003)**.
5. O. K. Varghese, G. K. Mor, C. A. Grimes, M. Paulose, and N. Mukherjee, *J. Nanosci. Nanotechnol.* 4, 733 **(2004)**.
6. Q. Cai, M. Paulose, O. K. Varghese, and C. A. Grimes, *J. Mater. Res.* 20, 230 **(2005)**; G. K. Mor, K. Shankar, M. Paulose, O. K. Varghese, and C. A. Grimes, *Nano Lett.* 5, 191 **(2005)**.
7. G. K. Mor, O. K. Varghese, M. Paulose, K. G. Ong, and C. A. Grimes, *Thin Solid Films* 496, 42 **(2006)**.
8. M. Paulose, O. K. Varghese, G. K. Mor, C. A. Grimes, and K. G. Ong, *Nanotechnology* 17, 398 **(2006)**.
9. C. A. Grimes, K. G. Ong, O. K. Varghese, X. Yang, G. Mor, E. C. Dickey, C. Ruan, M. V. Pishko, J. W. Kendig, and A. J. Mason. *Sensors* 3, 69 **(2003)**.
10. J. Capovilla, C. VanCouwenberghe, and W. A. Miller, *Critical Care Nursing Quarterly* 23, 79 **(2000)**.
11. B. G. Carter, D. Wiwczaruk, M. Hochmann, A. Osborne, and R. Henning, *Anaesthesia and Intensive Care* 29 260 **(2001)**.
12. J. D. Tobias, W. R. Wilson, and D. J. Meyer, *Anesthesia and Analgesia* 88, 531 **(1999)**.
13. N. McIntosh, J. C. Becher, S. Cunningham, B. Stenson, I. A. Laing, A. J. Lon, and P. Badger, *Pediatric Research* 48, 408 **(2000)**.
14. D. E. Hammerschmidt, *Journal of Laboratory and Clinical Medicine* 144, 279 **(2004)**.
15. M. Pimentel, Y. Kong, and S. Park, *Am. J. Gastroenterology* 98, 2700 **(2003)**.
16. A. C. Adam, M. Rubio-Texeira, and J. Polaina, *Critical Reviews in Food Science and Nutrition* 44, 553 **(2004)**.
17. D. M. Goldberg, *Clinical Biochemistry* 20, 63 **(1987)**.
18. L. T. Cavalli-Sforza, P. Menozzi, and A. Strata, *Int. J. Bio-Medical Computing* 14, 31 **(1983)**.
19. P. Gerlach, *Arch. Anat. Physiol.* 431 **(1851)**.
20. D. Gong, C. A. Grimes, O. K. Varghese, W. Hu, R. S. Singh, Z. Chen, and E. C. Dickey, *J. Mater. Res., Rapid Commun.* 16, 3331 **(2001)**.
21. O. K. Varghese, M. Paulouse, D. Gong, C. A. Grimes, and E. C. Dickey. *J. Mater. Res.* 18, 156 **(2003)**.
22. O. K. Varghese, M. Paulose, K. G. Ong, E. C. Dickey, and C. A. Grimes, *Adv. Mater.* 15, 624 **(2003)**.
23. O. K. Varghese, D. Gong, M. Paulose, C. A. Grimes, and E. C. Dickey, *J. Mater. Res.* 17, 1162 **(2002)**.
24. J. A. Bisquera, T. R. Cooper, and C. L. Berseth, *Pediatrics* 109, 423 **(2002)**.
25. R. R. Engel and N. L. Virnig, *Pediatric Research* 7, 292A **(1973)**.
26. G. Godoy, C. Truss, J. Philips, M. Young, K. Coffman, and G. Cassady, *Pediatric Research* 20, 348A **(1986)**.
27. W. I. H. Garstin and V. E. Boston, *Pediatric Research* 22, 208 **(1987)**.

SENSOR LETTERS
Vol. 4, 129–134, 2006

Sensorial System to Detect Chloroform in Water

Eduarda R. Carvalho[1], Nelson Consolin Filho[1], Alessandra Firmino[1,2], O. N. Oliveira, Jr.[2], Luiz Henrique C. Mattoso[1], and Ladislau Martin-Neto[1,*]

[1] *Embrapa Instrumentação Agropecuária, P.O. Box 741, 13560-970, São Carlos-SP, Brazil*
[2] *Universidade de São Paulo, PPG Interunidades em Ciências e Engenharia de Materiais, São Carlos-SP, Brazil*

(Received: 5 April 2006. Accepted: 19 April 2006)

RESEARCH ARTICLE

A sensor system adapted to detect chloroform, a potentially carcinogenic compound, in water was fabricated and tested. Interdigitated gold-coated microelectrodes were covered with various conducting polymers, single, or mixed, under several different conditions, and the resulting sensors characterized and tested on the analyte in question. Polymer films were laid down by a self-assembly technique and their impedance was analyzed over a range of frequencies from 1 Hz to 1 MHz. For practical reasons, the capacitance was also measured, at a fixed frequency of 1000 Hz, which allowed data-acquisition to be simplified. Some of the systems tested were able to detect chloroform in water and to distinguish different concentrations, the detection limit being of the order of 0.01 mg L^{-1}. These results demonstrate the sensitivity of conducting polymers and show that they can be used in the fabrication and assembly of a sensor system capable of detecting by-products of water disinfection, such as chloroform, that exhibit carcinogenic properties.

Keywords: Sensors, Conducting Polymers, Drinking Water, Carcinogenic By-Products, Chloroform.

1. INTRODUCTION

Chlorinated water contains a large number of by-products, formed during the chlorination of organic matter and just a fraction of these have been tested for carcinogenicity in animal experiments.[1] The main focus has been on compounds and classes of compounds produced in greater quantities during chlorination.[1]

The classes of by-products on which most research is done are trihalomethanes, halogenated acetic acids, and chlorinated furanones (CHFs).[1] However, the carcinogenicity of the majority of the by-products has not been tested, even in laboratory tests with animals. Among the trihalomethanes, chloroform has been investigated most intensively, owing to its well-known carcinogenic properties, established in the laboratory in various tests on animals. The International Agency for Research on Cancer (IARC) has described the evidence from animal experiments for the carcinogenicity of chloroform as "sufficient" and classified this by-product as potentially very carcinogenic to humans.[1–2] The long-term effects of its carcinogenicity are chiefly related to damage to the liver, kidneys, and heart. Chloroform provoked tumor formation is strongly associated with cytotoxicity and excessive proliferation of tissue regenerative cells, considered a determining factor in carcinogenicity.[1] Concentrations of chloroform of the order of 2 mg L^{-1} give positive results in bioassays for cancer development.[3]

The general population is exposed to chloroform by ingesting water and food, inhaling contaminated air, and possibly through dermal contact with chloroform-containing water. Drinking water levels as high as 311 mg L^{-1} have been reported in public water supplies.[4] Measurements of chloroform in drinking water ranged from 0.022 to 0.068 mg L^{-1} also has been found.[5]

Thus, in light of the impact of such products on the environment and public health, it is important to research methods of detecting them in water–treatment plants. The growing demand for measures to protect the environment and the elaboration of new directives in this respect have had a very great impact on the development of novel materials, instruments, and sensing devices for the detection and measurement of by-products of disinfection.

The detection of individual substances by means of specific sensors is one of the most active fields in current research and development, owing to its great relevance to a variety of technological applications. The main features required in any sensor are high sensitivity, stability, and selectivity. The control and testing of the quality of air, soil,

*Corresponding author; E-mail: martin@cnpdia.embrapa.br

or water calls for sensors that detect particular molecules in small amounts in a complex mixture; thus, the detection needs to be specific and selective, as well as sensitive. However, currently available commercial sensors made from inorganic semiconductors like tin oxide, while inexpensive, possess very little selectivity. For this reason, new kinds of sensor are being explored[6] and, among these, conducting polymers are attracting a lot of interest.[7] Extensive work has been done in nose and tongue sensors[8–10] aimed at controlling pollutants in the environment and at monitoring the quality of foodstuffs. Most of the devices are based on electrical changes induced by bulk absorption or surface adsorption of molecules in conducting polimeric films.[11]

Conducting polymers stand out as excellent candidate materials for use in chemical and electrochemical sensors, both as sensitive components and as electrodeposited films. Owing to their intrinsic conducting properties, they can be made to sense given chemical species by employing diverse electrochemical techniques. Moreover, one-step electrosynthesis allows an adherent film of polymer to be made on the surface of electrodes (enabling microelectrodes to be built), with chosen anions included in the doping matrix.[12]

Chemical sensors are a viable solution to the problem of the high cost of devices used at present in the detection of by-products and water-quality monitoring. A chemical sensor can be defined as a device that, when exposed to a given type of substance (the analyte), transforms characteristic chemical information, such as polarity, stereochemical form, concentration and so on, to an analytical signal that can be measured, such as electrical resistance, current, potential difference, and frequency.[13]

Over the last few decades, many articles have been published referring to the use of electronic noses and, more recently, tongues.[14] In this context, therefore, a system of various sensory units, modified with natural and conducting polymers, has been tested for the detection and estimation of potentially carcinogenic compounds such as chloroform.

2. EXPERIMENTAL DETAILS

2.1. Conducting and Natural Polymers

The polymers used were: Polyaniline (PANI), poly(o-ethoxyaniline) (POEA), humic substances (HS), sulphonate lignine (SL), and mixtures of these. Polymers PANI and POEA were synthesized as described in Refs. [15–16] and polymer SL was obtained from Melbar S.A.

The POEA chemically synthesized using ammonium peroxydisulfate in solution of 1.0 mol L^{-1} HCl at 0 °C. The humic substances (HS) were isolated from a water sample collected in River João Pereira. This river is a tributary of the River Itapanhaú, located downstream-upstream. The River Itapanhaú is located in an environmentally protected area near the city of Bertioga, in the south coast of São Paulo state/Brazil.[17] The extraction and the fractioning were made according to the International Society of Humic Substances,[18] as well as recommendations made by Malcolm.[19] The HS solutions were prepared in the concentrations of 5, 10, and 30 mg L^{-1}. All the aqueous solutions of POEA, SL, and HS were prepared using ultra pure water from a Milli-Q system (MilliPore®). The pH adjustment of the solutions was made adding amounts of 0.1 M of HCl or 0.1 M of NH_4OH.

2.2. Chloroform Sample

A chloroform sample (PA) with the following characteristics obtained from Supelco was used: 1000 concentration mg (pure); purity degree (99.90%). From the pure solution, a stock solution of 10 mg L^{-1} was prepared. From the stock solution were prepared different solutions in the concentrations of 0.05 mg L^{-1} to 8.0 mg L^{-1}, for the analysis and pH (s) of the solutions were adjusted to 5.0 which coincides with the value presented for the stock solution.

2.3. Experimental Details

The specifications of deposition of polymers in each sensor and films for formation of the sensorial system are presented in Table I.

The conducting polymers based fine films (PANI and POEA) and natural polymers (HS and SL) were manufactured by the Self-Assembly (SA) technique, through monolayers (e.g., only POEA), bilayers (e.g., a layer of POEA over SL—POEA/SL) or complexed mixtures (e.g., solutions of same concentration together- PANI+HS) over solid substrate (interdigitated microelectrodes of gold deposited on glass).[20–23]

In SA technique, the number of deposited layers and the time of deposition of polymers, in the microelectrodes, were effected as follows:

(1) monolayer/3min (POEA and SL);
(2) monolayer/5min (PANI and HS);
(3) complexed mixture/3min (POEA+SL and POEA+HS) and
(4) bilayer/3min (POEA/SL, HS/POEA, PANI/SL).

Table I. Sensing units used in sensor system to analyze the chloroform.

Sensing Unit	Type of Material
S1	no film
S2	POEA
S3	POEA/SL
S4	POEA+SL
S5	SL
S6	HS/POEA
S7	POEA+HS
S8	PANI
S9	HS
S10	PANI/SL

The experiments were conducted at pH 5.0 using POEA, HS, and SL in the concentration of 1×10^{-3} mol L^{-1} and settling time 3 and 5 minutes in aqueous solution. As PANI is insoluble in aqueous medium, this was dissolved in NMP (N-Methyl-2-Pyrrolidone) in the concentration of 1×10^{-3} mol L^{-1}.

The limit of detection (DL) of the system was determined according to the following equation: DL = K.SB/S, where S = sensitivity of the method, SB = shunting line standard of the measures of the white, and K = constant numerical (value recommended for the IUPAC, $K = 3$).[24] The DL is defined as the lowest amount of analyte that can be detected with a trustworthiness level statistics.

The interdigitated gold microelectrodes (without film) were manufactured through the photolythographic method. The characteristics of these interdigitated microelectrodes are: gold microelectrodes containing 50 pairs of digits, each containing 10 μm wide, 10 μm of spacing between the microelectrodes and 0.1 μm thick of the deposited gold layer. Ten sensors were prepared per this technique, and an analysis system was mounted, according to Figure 1. Then the films containing polymers (POEA, PANI, HS, and SL) were deposited. The device used in the data acquisition was an impedance analyzer Solartron SI 1260 installed on a microcomputer. The amplitude of the input signal was 50 mV, with the scanning at intervals of 1 Hz to 1 MHz. The data treatment was made by analyses on the main components (PCA), along with software MATLAB

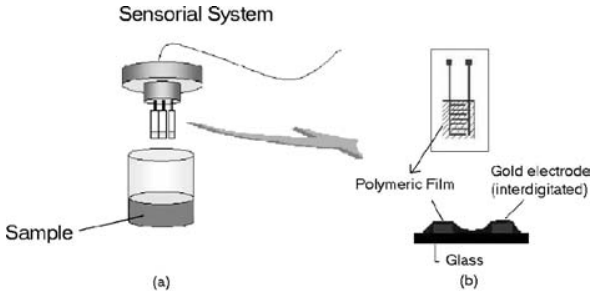

Fig. 1. Diagram illustrating the sensorial system.

version 5.2. The PCA analysis is a mathematical manipulation of the data matrix, in order to reduce its original dimensionality and it is founded on the correlation between the variables.[25]

3. RESULTS AND DISCUSSION

The frequency response for the various sensorial units in the different test conditions and solutions, are presented in the chart in Figure 2. For better visualization the extremes of the chloroform concentrations were chosen. In Figure 2(a) response obtained for solution in the presence of 0.1 mg L^{-1} of chloroform and in Figure 2(b) for 8.0 mg L^{-1}.

It was observed that the capacitance decreases with the increase of the frequency at an almost constant value

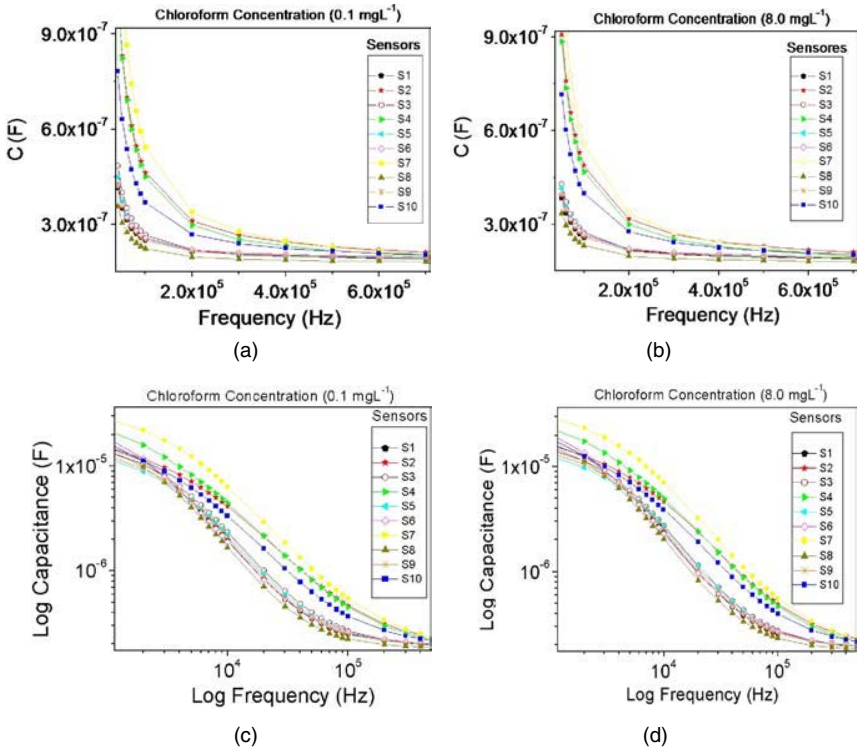

Fig. 2. Capacitance versus frequency: in (a) 0.1 mg L^{-1} of chloroform; (b) 8.0 mg L^{-1} of chloroform; (c) capacitance in function of frequency log for 0.1 mg L^{-1} of chloroform; (d) capacitance in function of frequency log of the frequency for 8.0 mg L^{-1} of chloroform.

RESEARCH ARTICLE

(ranging 10^{-7} F). Similar results were observed for all test solutions, i.e., a general decrease of the capacitance with the increase of the frequency, and an increase of the capacitance with the increase of the concentration of the solutions.

In Figures 2(c) and (d) the data relative to the dependence of the capacitance with the frequency log are presented, for the chloroform solutions in the concentrations of 0.1 mg L^{-1} and 8.0 mg L^{-1}, respectively. With the frequency log, a separation of the lines relative to the each sensor is observed. Each electrode has a specific electric response for the solutions and supplies a distinct signal for the different chloroform concentrations. Consequently, the evaluated disposition of the sensors can be used to detect substances with different properties.

The capacitance measurement can be obtained by selecting a specific frequency (e.g., 10^3 Hz), which simplifies the acquisition of data and, for practical purposes, it facilitates the application. Figure 3 shows to a chart of the capacitance obtained for each sensorial unit at 10^3 Hz, for which, the variations in the measurements better reflect the difference in charge and conductance storage of several films.

The relative sensitivity of the sensorial units is modified, when the chloroform concentration is increased in the solution. That is observed in Figure 3, where for a fixed frequency of 10^3 (Hz), an increase of the capacitance is observed, with the increase of the chloroform concentration in the 0.1 mg L^{-1} solution for 8.0 mg L^{-1}.

However, as conducting and natural polymers were deposited in the sensorial units, in different architectures and concentrations, the selectivity and the response of each sensor regarding the increase in the value of the capacitance, with the increase of the chloroform concentration, was better observed for specific sensorial units. As seen in Figure 3, sensorial units 4 and 7, which represent depositions: POEA complex with SL and, POEA complex with HS respectively, presented better response, that is, higher capacitance value, as to concentration increase and chloroform detection in the solution.

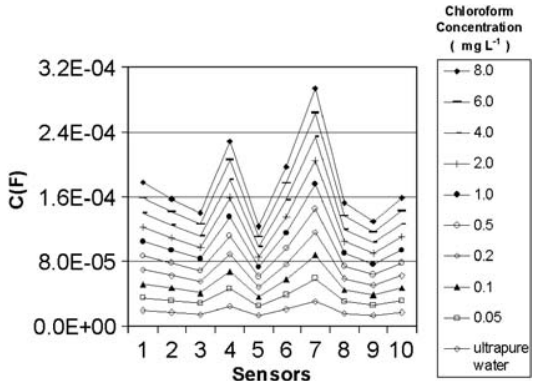

Fig. 3. Capacitance measurements at 10^3 Hz, obtained for chloroform solutions with different concentrations.

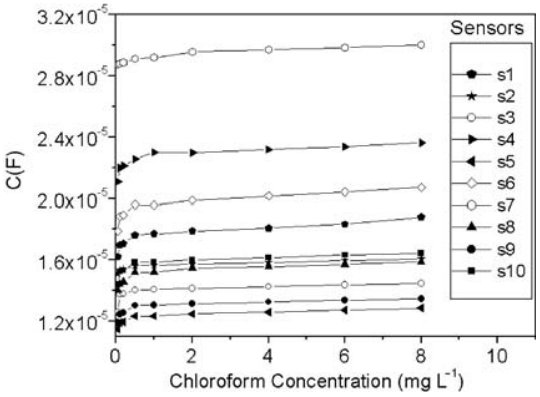

Fig. 4. Analytical curves plotted for the determination of the detection limit.

The analytical curves plotted to determine the detection limit are shown in Figure 4. From the analytical curves the Detection Limits (DL) were obtained for each microelectrode (interval from 0 to 2.0 mg L^{-1}), which are shown in Table II. The limit of detection (DL) was calculated by the equation: $DL = 3 \cdot SD/B$ where SD is the standard deviation average values of the reference sample (in absence of chloroform) and B is the slope of the straight line (analytical curve) obtained, respectively.

Figure 5 shows a bar chart, where we have a better visualization of the detection limits for each microelectrode. As shown in Figure 5, microelectrode 7 was the one that presented the best detection limit, (0.010 mg L^{-1}) followed by microelectrode 4 (0.012 mg L^{-1}). The worst detection limit was 0.190 mg L^{-1}, observed for microelectrode 8. This difference between the microelectrodes is related with the molecular structure of each film.

Microelectrode 7, is made up of a layer of a complexed mixture of POEA and HS. It has been shown that in the interaction between HS and POEA, the HS induces a dopage of the POEA by protonation. In the complex POEA+HS, the carboxylic groups and phenolic acid groups of the HS induce a primary dopage by protonation of imine groups of the POEA.[26]

The presence of HS in the complex with POEA, possibly contributes for a better interaction with chloroform, since the presence of aromatic groups in the HS, which are strongly reactive substrate in substitution and oxidation reactions, favoring this interaction. Substitution and oxidation reactions are typical in the aquatic chlorination, and contribute for the formation of organochlorinated compounds.[27]

In the case of microelectrode 4, the chemical groups contained in the POEA (–NH=) are linked with the SL by electrostatic attraction that involves the interaction between the ionized groups of the poliions and substratum, as well as by interaction by hydrogen linking, that can occur both for doped POEA, and for the non-doped POEA, between the groups $-NH =$ of the POEA and groups HSO_3^- of the SL.[26]

Table II. Results obtained from the analytical curves.

Linear Equation: Y = A + BX						
Sensors	A	Slope B	R	Standard deviation (SD)	Detection limit (DL) mg L^{-1}	Detection limit-Err (yEr±)
S1	1.68346×10^{-5}	6.03999×10^{-7}	0.94	4.86×10^{-9}	0.020	5.000×10^{-3}
S2	1.53323×10^{-5}	3.56633×10^{-7}	0.90	4.86×10^{-9}	0.040	1.000×10^{-2}
S3	1.37611×10^{-5}	3.43776×10^{-7}	0.90	4.86×10^{-9}	0.042	2.000×10^{-2}
S4	2.19418×10^{-5}	1.16592×10^{-6}	0.95	4.86×10^{-9}	0.012	5.000×10^{-4}
S5	1.19043×10^{-5}	4.94898×10^{-7}	0.90	4.86×10^{-9}	0.030	5.000×10^{-3}
S6	1.89754×10^{-5}	5.09950×10^{-7}	0.95	4.86×10^{-9}	0.028	1.000×10^{-2}
S7	2.87201×10^{-5}	1.39798×10^{-6}	0.99	4.86×10^{-9}	0.010	1.000×10^{-3}
S8	1.29905×10^{-5}	7.75714×10^{-8}	0.98	4.86×10^{-9}	0.190	1.350×10^{-1}
S9	1.50660×10^{-5}	1.88286×10^{-7}	0.96	4.86×10^{-9}	0.077	2.50×10^{-3}
S10	1.53830×10^{-5}	3.72347×10^{-7}	0.95	4.86×10^{-9}	0.040	5.90×10^{-2}

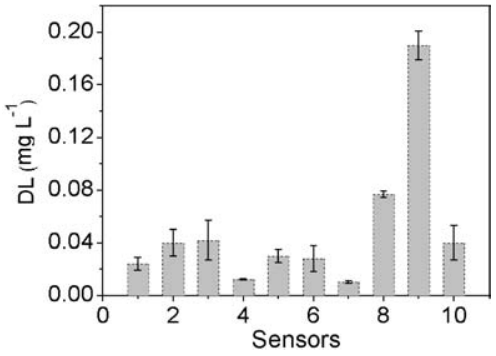

Fig. 5. Detection limits versus modified sensors.

Possibly these groups present both in the SL, and in the POEA, link more strongly to the chloroform and due to this the microelectrode 4 also presented good detection limit. In the case of microelectrode 8, that had the worst detection limit, we saw that the PANI dissolved in NMP (*N*-Methyl-2-Pyrrolidone) does not interact so strongly with chloroform. This is probably associated with the fact that this polymer is insoluble in some solvents[28] which would possibly be contributing to a lesser interaction with chloroform in aqueous medium.

With the application of the PCA, it was possible to notice a clear separation between the different types of polymer deposition and conditions, on the interdigitated microelectrodes, as in Figure 6. It was observed the formation of three (3) distinct groupings. In grouping I, are the sensors that presented the best results for the detection limit, with values below 0.02 mg L^{-1}. In grouping II, the sensors that presented an intermediate band (above 0.02 mg L^{-1} and below 0.05 mg L^{-1}). In grouping III, are the sensors that presented the worst values for the DL, with values above 0.10 mg L^{-1}. Sensor S1 corresponds to the reference microelectrode, that is, without film.

Plotting the score factors on the same PC1-PC2 plan (Fig. 6), we can observe excellent discrimination between the sensors. The sensors present good stability, reproducing the results in more than one measure and, they were able to discriminate the different chloroform concentrations present in the samples.

The samples with different chloroform concentrations were also evaluated using the 10 sensors and the

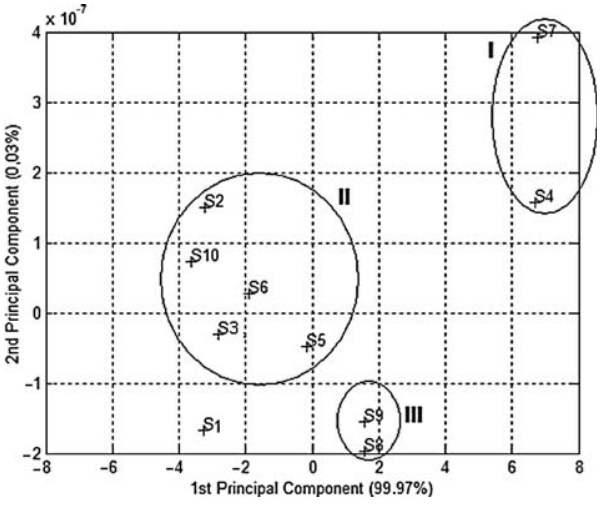

Fig. 6. PCA obtained for the sensors relative to the different polymeric complexes deposited over the interdigited microelectrodes.

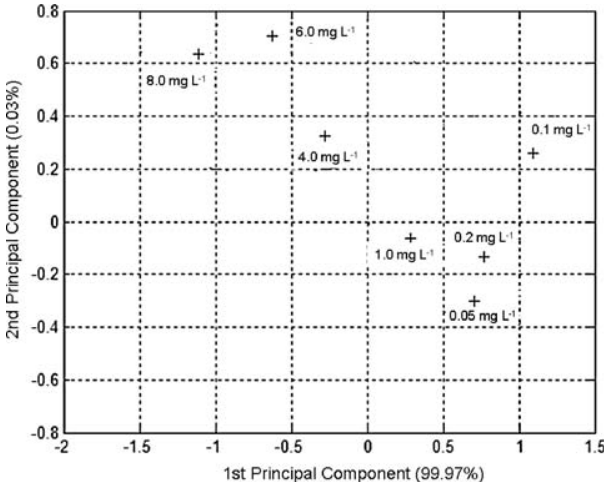

Fig. 7. PCA obtained for the different chloroform concentrations, relative to the different polymeric complexes deposited over the interdigitated microelectrodes.

impedance results also analyzed by PCA (Fig. 7). The sensorial system was able to differentiate the samples, due to their different compositions, which interact in different forms with the polymeric films, producing different impedance values in each sensor, as was previously observed in Figure 3.

The PCA analysis showed that to the values for first and second component represents about 100% of the total variance (PC1 = 99.97%; PC2 = 0.03%) of the observations. These results suggest that the sensors respond in a selective form, when in contact with chloroform, with practically 100% reliability.

4. CONCLUSIONS

A sensorial system using interdigitated microelectrodes and nanostructured conducting polymers allowed a statistical discrimination in the determination and detection of carcinogen compounds as chloroform, a by-product generated from water disinfection processes, in public supply systems. The polymeric films interacted distinctly with the compound present in the water. The use of this system for the evaluation of the water quality shows itself as a potential tool, making it possible, according to the database generated, in a selective way, the implementation of an on-line monitoring system.

Acknowledgments: The authors acknowledge the financial support from Conselho Nacional de Desenvolvimento Científico e Tecnológico (CNPq—Proc. 150042/2004-3, Proc. 302935/2004-3, CT-HIDRO: 550188/2002-9), Fundação de Amparo à Pesquisa do Estado de São Paulo (FAPESP—Proc. 02/07724-0) and Embrapa Instrumentação Agropecuária.

References and Notes

1. H. Komulainen, *Toxicology* 198, 239 **(2004)**.
2. International Agency for Research on Cance 73, 131 **(1999)**.
3. J. Fawell, *Food and Chemical Toxicology* 38, 91 **(2000)**.
4. http://www.atsdr.cdc.gov/toxprofiles/tp6-c5.pdf.
5. Agency for Toxic Substances and Disease Registry (ATSDR). Toxicological Profile for Chloroform. Public Health Service, U.S. Department of Health and Human Services, Atlanta, GA **(1997)**.
6. A. Barraud, *Vaccum* 41, 1624 **(1990)**.
7. J. N. Barisci, C. Conn, and G. G. Wallage, *Trends in Polymer Science* 4, 307 **(1996)**.
8. H. Toko, *Biosen. Bioelectron.* 13, 701 **(1998)**.
9. A. Riul, Jr., D. S. dos Santos, K. Wohnrath, R. Di Tommazo, A. C. P. L. F. Carvalho, F. J. Fonseca, O. N. Oliveira, Jr., D. M. Taylor, and L. H. C. Mattoso, *Langmuir* 18, 239 **(2002)**.
10. A. Riul, Jr., A. M. Gallardo Soto, S. V. Mello, S. Bone, D. M. Taylor, and L. H. C. Mattoso, *Synthetic Metals* 132, 109 **(2003)**.
11. C. J. L. Constantino, P. A. Antunes, E. C. Venâncio, N. Consolin, F. J. Fonseca, L. H. C. Mattoso, R. F. Aroca, O. N. Oliveira, Jr., and A. Rail, Jr., *Sens. Lett.* 2, 95 **(2004)**.
12. J. Janata, Principles of Chemical Sensors, Plenum Press, New York **(1989)**.
13. R. W. Cattrall, Chemical Sensors, Oxford University Press **(1997)**.
14. D. Anil K., D. C. Stone, and M. Thompson, *Int. Journal of Food Science and Technology* 39, 587 **(2004)**.
15. W. J. Zhang, J. Feng, A. G. MacDiarmid, and A. J. Epstein, *Synth. Met.* 84, 119 **(1997)**.
16. L. H. C. Mattoso, S. K. Manohar, A. G MacDiarmid, and A. J. Epstein, *J. Polym. Sci. Part A: Polym. Chem.* 33, 1227 **(1995)**.
17. E. R. Carvalho, L. Martin-Neto, D. M. B. P. Milori, J. C. Rocha, and A. H. Rosa, *J. Braz. Chem. Soc.* 15, 421 **(2005)**.
18. G. R. Aiken, Humic Substances in Soil, Sediment and Water, edited by John Wiley and Sons, New York **(1985)**.
19. R. L. Malcolm, Humic Substances in the Aquatic and Terrestrial Environment, edited by Springer-Verlag, Berlin **(1989)**.
20. W. Kern, *Semicond. Int* 94, **(1984)**.
21. L. G. Paterno, L. H. C. Mattoso, and O. N. Oliveira, Jr., *Quim. Nova* 24, 228 **(2001)**.
22. L. G. Paterno and L. H. C. Mattoso, *Polymer* 42, 5239 **(2001)**.
23. C. J. L. Constantino and O. N. Oliveira, Jr., *Colloids Surf. B: Biointerfaces* 23, 257 **(2002)**.
24. E. B. J. Rupp, *Agricult. Food Chem.* 40, 2016 **(1992)**.
25. S. Wold, *Chemom. Intell. Lab. Sys.* 2, 37 **(1987)**.
26. E. C. Venâncio, N. C. Filho, C. J. L. Constantino, L. Martin-Neto, and L. H. C. Mattoso, *J. Braz. Chem. Soc.* 16, 24 **(2005)**.
27. I. V. Dianova, N. A. Sinikova, and A. T. Lebedev, International Meeting of the International Humic Substances Society, 10th (Toulouse-França) Proceedings Toulouse **(2000)**, pp. 1039–1042.
28. M. G. Han, K. S. Cho, S. G. O. H, and S. S. Im, *Synth. Met.* 126, 53 **(2002)**.

SENSOR LETTERS
Vol. 4, 135–138, 2006

Comparison of ZnO/64° $LiNbO_3$ and ZnO/36° $LiTaO_3$ Surface Acoustic Wave Devices for Sensing Applications

K. Kalantar-Zadeh[1,*], D. A. Powell[1], A. Z. Sadek[1], W. Wlodarski[1], Q. B. Yang[2], and Y. X. Li[2]

[1] *School of Electrical and Computer Engineering, RMIT University, Melbourne, Australia*
[2] *State key Laboratory of High Performance Ceramics and Superfine Structures, Shanghai Institutes of Ceramics, Shanghai 200050, China*

(Received: 9 April 2006. Accepted: 19 April 2006)

The performance of ZnO/64°-YX $LiNbO_3$ and ZnO/36°-YX $LiTaO_3$ layered SAW structures was compared in terms of mass sensitivity and acoustic wave velocity. It was found that the ZnO/64° $LiNbO_3$ structure has a few distinct advantages over ZnO/36° $LiTaO_3$. For ZnO/64° $LiNbO_3$, the mass sensitivity is ~2.5 times larger. Additionally, the optimum thickness of the ZnO guiding layer is approximately half that of the ZnO/36° $LiTaO_3$ structure, which reduces the cost of fabrication.

Keywords: 64° $LiNbO_3$, 36° $LiTaO_3$, ZnO, Layered SAW, Mass Sensing.

RESEARCH ARTICLE

1. INTRODUCTION

Layered Surface Acoustic Wave (SAW) devices are of great interest for physical, chemical, and biochemical sensing applications. Their high mass sensitivity, robustness, ease of immobilization of bio-components on the active surface and low fabrication cost make them attractive for these applications. In this work, devices with different ZnO thicknesses were fabricated both on 64° $LiNbO_3$ and 36° $LiTaO_3$ substrates and their performance was compared. The most commonly utilised piezoelectric material orientations which allow the propagation of shear waves are 90° rotated ST-quartz, 64°-YX $LiNbO_3$, and 36°-YX $LiTaO_3$.[1–4] As a result, they are suitable for sensing applications in liquid media.

By depositing a wave guiding layer onto such substrates, mass sensitivity can be increased as the acoustic energy is more confined towards the surface. Layered SAW sensors for liquid media applications using SiO_2 on 90° rotated ST-quartz have been intensively studied.[5,6] SiO_2 on 36° YX-$LiTaO_3$ layered structure is another SAW structure that offers potential for liquid sensing applications.[7,8] However, such devices have lower sensitivity than devices based on ST cut quartz.

It has been shown that replacing the SiO_2 layer with ZnO, which is a piezoelectric material, results in considerable improvement of mass sensitivity.[9–11] Shoji et al.[10,11] showed that deposition of ZnO layer on $LiNbO_3$ or $LiTaO_3$ results in an improved electromechanical coupling coefficient (K^2). The authors[1] have conducted a comprehensive study regarding the sensitivity of ZnO/36° $LiTaO_3$ and found that maximum K^2 of 0.075 at thickness of $h/\lambda_0 = 0.05$ and maximum mass sensitivity of -70 cm^2/g. Chu et al.[12] investigated on the dependence of ZnO film on the sensitivity of love mode sensor in ZnO/90° rotated ST-cut quartz structure and found that the devices which are unheated during sputtering have higher sensitivity than those which are heated. They also found that the sensitivity of ZnO/90° rotated ST-cut quartz structure is higher than the SiO_2/90° rotated ST-cut quartz structure. Jian et al.[2] investigated the preferred orientation of ZnO films deposited onto a 64° $LiNbO_3$ substrate to apply as a liquid sensor. Zhang et al.[13] investigated a ZnO nanotip guiding layer grown by metal-organic chemical vapor deposition on the 128° Y-cut $LiNbO_3$ for biosensing applications. They claimed that the ZnO nanotip array enhanced DNA immobilization due to its large surface to volume ratio.

In this paper, the performance of the ZnO/36°-YX $LiTaO_3$ and ZnO/64°-YX $LiNbO_3$ SAW devices for sensing applications will be compared.

2. SENSOR FABRICATION

The sensor consists of a two-port resonator with 38 electrode pairs in input and output inter-digital transducers (IDTs), 160 electrodes in each reflective array, 700 μm

*Corresponding author; E-mail: kourosh@kalantar.org

Fig. 1. A typical sensor showing two identical resonators.

aperture width and a periodicity of 40 μm. A two-port resonator structure was chosen over a delay line as its higher phase slope increases oscillation stability. The IDTs and reflectors were formed by patterning an 80 nm Au layer. The Au layer was deposited upon 20 nm Ti for improved adhesion to the substrate. The ZnO guiding layer was deposited by RF magnetron sputtering. The sputtering gas was 40% O_2 in Ar at 1×10^{-2} Torr, substrate temperature was 220 °C, giving a deposition rate of $\sim$1.2 μm/hour. The ZnO thin film was employed as the acoustic wave-guiding layer on both the 64° $LiNbO_3$ and 36° $LiTaO_3$ substrates, with thickness ranging from 0 to 8 μm. Figure 1 shows a $LiTaO_3$ sensor before deposition of the ZnO.

3. MATERIAL ANALYSIS

ZnO films were micro-characterised using the X-Ray Diffraction (XRD) and Scanning Electron Microscopy (SEM) methods. It was observed from the XRD patterns (Fig. 2), that the ZnO thin film grows on $LiNbO_3$ and $LiTaO_3$ substrate with *c*-axis alignment normal and parallel to the surface, respectively.[10] For $LiNbO_3$, the strong (002) peak indicates that the *c*-axis orientation is normal to the substrate. The small peak which appears at 72.6° corresponds to the (004) plane. However, for $LiTaO_3$ the (110) peak indicates that the *c*-axis lies in the plane of the substrate. A smaller (102) peak is also present, but it is much smaller than the (110) peak.

It can be seen from the SEM micrographs (Fig. 3) that the formation of ZnO crystallites differs on $LiNbO_3$ and $LiTaO_3$ (Fig. 2), as does the corresponding crystal orientation, being (002) and (110), respectively as confirmed by XRD.

4. ACOUSTIC WAVE PROPERTIES

The acoustic wave propagation velocity within the structures and their mass sensitivity were studied. The

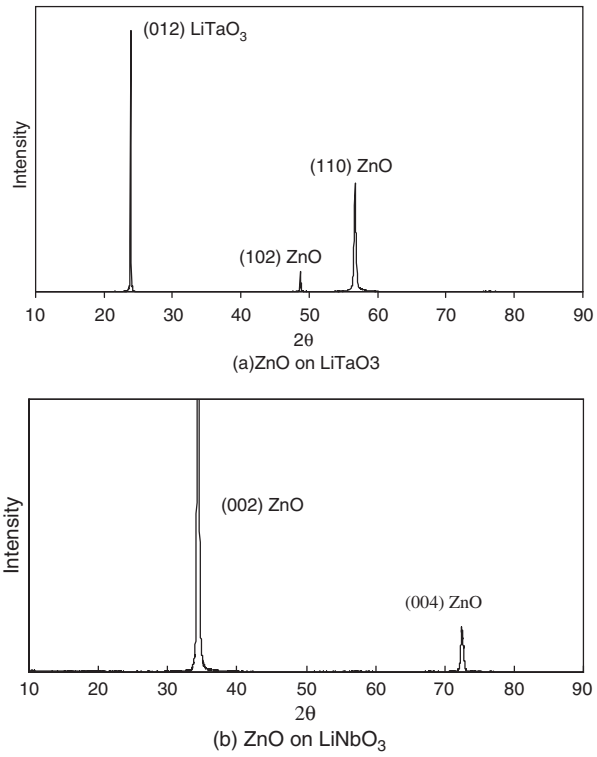

Fig. 2. XRD patterns.

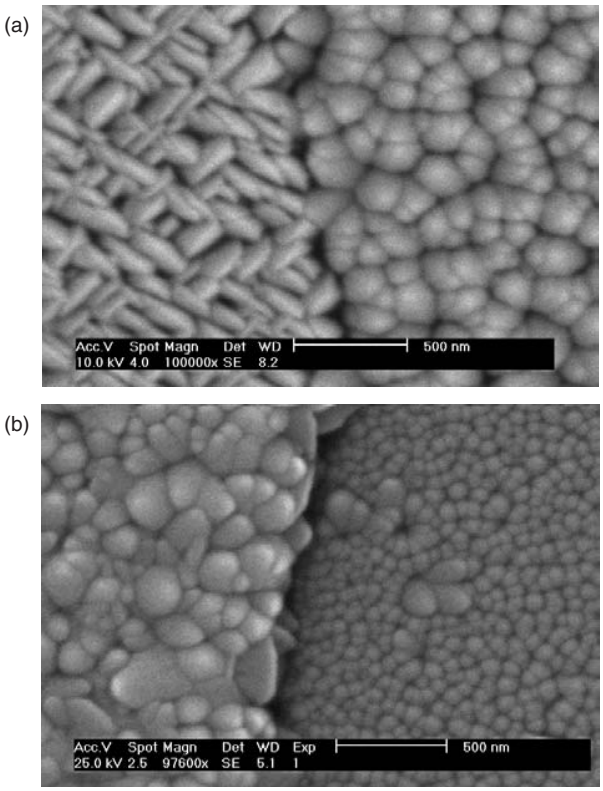

Fig. 3. (a) ZnO growth on bare $LiTaO_3$ (left) and gold (right), (b) ZnO growth on aluminium (left) and bare $LiNbO_3$ (right).

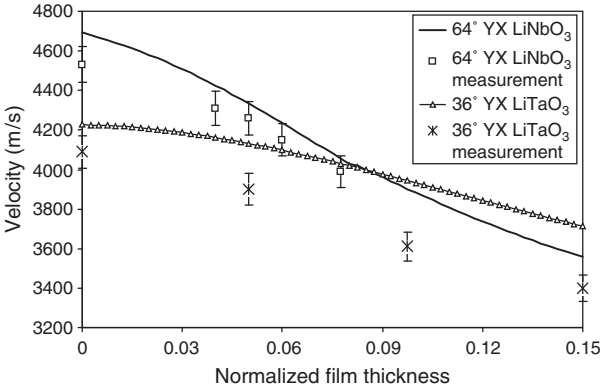

Fig. 4. Acoustic wave propagation velocity versus normalized layer thickness.

theoretical values were calculated using a numerical search technique.[1, 14] A determinant scan was performed in order to find the phase velocity which satisfies the boundary conditions.[15, 16] Theoretical values for propagation velocity are in good agreement with the measured values (Fig. 4). As can be observed, the change in the propagation velocity with the addition of the ZnO layer is much larger for the ZnO/64° $LiNbO_3$ structure than for the ZnO/36° $LiTaO_3$ structure. Each point is the average of three measurements. The deviation of the measurements from the average was less than 2%. The velocity shift with increasing layer thickness is correlated to the mass sensitivity, since the mass sensitivity is influenced by the group velocity, which relates to the change in group velocity with layer thickness.[5]

Theoretical and measured values for mass sensitivity for these two structures are shown in Figure 5. Theoretical values for mass sensitivity were obtained by calculating the phase velocity before and after addition of a perturbing mass layer. Measured values were obtained by spin coating a polymer with a thickness of 0.25 μm onto the active area of the sensors. Each point is the average of three measurements. The deviation of the measurements from the average was less than 15%. It can be seen that

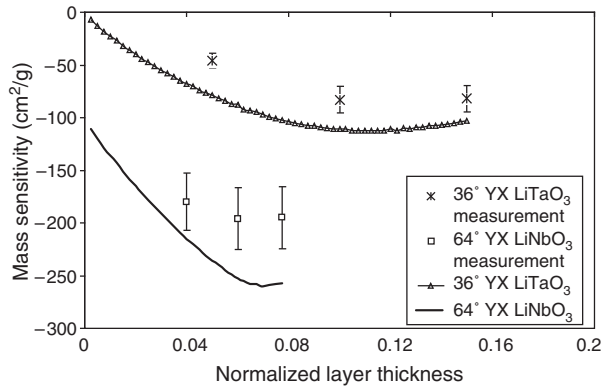

Fig. 5. Mass sensitivity versus the normalized layer thickness.

mass sensitivity reaches a maximum when the normalized layer thickness is 0.07 of the wavelength for the ZnO/64° $LiNbO_3$ structure and when it is 0.12 of the wavelength for the ZnO/36° $LiTaO_3$ structure. The ZnO/64° $LiNbO_3$ device's mass sensitivity of approximately 250 cm^2/g is larger than that of the ZnO/36° $LiTaO_3$ device, which is approximately 100 cm^2/g. Mass sensitivity measurements are in a good agreement with the calculations.

The authors have previously shown that the differing orientations of ZnO which occur on free and metallised regions of the SAW device result in different values for propagation velocity, mass sensitivity and electromechanical coupling coefficient.[1] Additionally, the authors have also shown[15, 16] that the crystal structure of sensitive layers have significant effect on the magnitude of the response of layered SAW devices for gas sensing applications. It is believed that the difference of ZnO crystal structures deposited on various surfaces causes the deviation from the calculated magnitude for mass sensitivities.

5. CONCLUSIONS

The performance of ZnO/$LiTaO_3$ and ZnO/$LiNbO_3$ were compared and for each structure, the ZnO thickness of maximum mass sensitivity was both theoretically and experimentally obtained. For a device operating at approximately 100 MHz the ZnO/64° $LiNbO_3$ structure reaches a maximum mass sensitivity of 250 cm^2/g when the normalized layer thickness is 0.07 of the wavelength. Such a structure is an excellent candidate for the fabrication of micro-mass sensors with numerous applications in immunosensing.

Acknowledgment: Authors would like to thank CRC (cooperative Research Centre) for Micro-technology, Australia, for the financial support.

References and Notes

1. D. A. Powell, K. Kalantar-Zadeh, and W. Wlodarski, *Sens. Actuators A* 115, 456 (**2004**).
2. S.-J. Jian, S.-Y. Chu, T. Y. Huang, and W. Water, *J. Vacuum Sci. Technol. A* 22, 2424 (**2004**).
3. K. Kalantar-Zadeh, W. Wlodarski, Y. Y. Chen, B. N. Fry, and K. Galatsis, *Sens. Actuators B*, 91, 143 (**2003**).
4. K. Kalantar-Zadeh, W. Wlodarski, Y. Y. Chen, B. N. Fry, and K. Galatsis, *Sens. Actuators B* 91, 303 (**2003**).
5. G. Kovacs, G. W. Lubking, M. J. Vellekoop, and A. Venema, *Proc. IEEE Ultrason. Symp.* 281 (**1992**).
6. J. Du, G. L. Harding, A. F. Collings, and P. R. Dencher, *Sens. Actuators A* 60, 54 (**1997**).
7. F. Herrmann and M. Weihnacht, *IEEE Trans. Ultrason. Ferroelec. Freq. Contr.* 48, 268 (**2001**).
8. J. Freudenberg, M. von Schickfus, and S. Hunklinger, *Sens. Actuators B* 76, 147 (**2001**).
9. K. Kalantar-Zadeh, A. Trinchi, W. Wlodarski, and A. Holland, *Sens. Actuators A* 100, 135 (**2002**).
10. K. Nakamura, T. Shoji, and H. B. Kang, *Proc. Int. Symp. App. Ferroelec.* 467 (**2000**).

RESEARCH ARTICLE

11. T. Shoji, K. Nakamura, and D. Yamazaki, *Proc. IEEE Ultrason. Symp.* 215 **(2001)**.
12. S.-Y. Chu, W. Water, and J.-T. Liaw, *Ultrasonics* 41, 133 **(2003)**.
13. Z. Zhang, N. W. Emanetoglu, G. Saraf, Y. M. Chen, P. Wu, J. Zhong, Y. C. Lu, J. Q. Chen, O. Mirochnitchenko, and M. Inouye, *IEEE Trans. Ultrason. Ferroelec. Freq. Contr.* 53, 786 **(2006)**.
14. D. A. Powell, K. Kalantar-Zadeh, and W. Wlodarski, *Proc. IEEE Ultrason. Symp.* 146 **(2003)**.
15. K. Kalantar-Zadeh, D. A. Powell, S. Ippolito, and W. Wlodarski, *Proc. IEEE Ultrason. Symp.* 191 **(2004)**.
16. D. A. Powell, K. Kalantar-Zadeh, S. Ippolito, and W. Wlodarski, *Sens. Lett.* 3, 66 **(2005)**.

SENSOR LETTERS
Vol. 4, 139–143, 2006

Fluorescence Behavior of Pyrene-1-Butylic Acid Chemisorption Layer onto Nano-Porous Anodic Oxidized Aluminum with Myristic Acid Layer for Optical Oxygen Sensing

Yuki Fujiwara and Yutaka Amao*

Department of Applied Chemistry, Oita University, Dannoharu, Oita 8701192, Japan

(Received: 10 February 2006. Accepted: 13 February 2006)

The fluorescence behavior of pyrene-1-butylic acid (PBA) chemisorption layer onto nano-porous anodic oxidized aluminum with a myristic acid layer was investigated and its device was applied as a fluorescence oxygen sensing material. When the ratio of [myristic acid]/[PBA] onto anodic oxidized aluminum plate increased, the fluorescence intensity due to monomer emission increased and the intensity due to excimer emission decreased. These results show that the polarity of the microenvironment around PBA molecules increased by chemisorption of myristic acid and the excimer formation between PBA molecules was suppressed by the myristic acid layer onto nano-porous anodic oxidized aluminum plate. Both of fluorescence attributed to monomer and excimer were quenched by oxygen. The I_0/I_{100} values, where I_0 and I_{100} represent the detected fluorescence intensities from a substrate exposed to 100% argon and 100% oxygen, respectively, in monomer emission increased with increasing the ratio of myristic acid to PBA. In contrast, the I_0/I_{100} values in excimer emission decreased with increasing the ratio of myristic acid to PBA. The PBA onto anodic oxidation of aluminum plates with myristic acid layer obey the modified Stern-Volmer equation and the Stern-Volmer constant, K_{SV} at 376 nm attributed to monomer and 461 nm attributed to excimer increased and decreased with increasing the ratio of myristic acid to PBA.

Keywords: Optical Oxygen Sensing, Pyrene, Nano-Porous Anodic Oxidized Aluminum, Fluorescence.

RESEARCH ARTICLE

1. INTRODUCTION

Ultrathin films such as chemisorption layer, self-assembled monolayer, Langmuir-Blogett (LB) film and layer by layer film have been used for development of molecular devices.[1–3] Among the these techniques, chemisorption layer technique has attracted considerable attention. Chemisorption layers are formed using spontaneous binding between a mercapto group and a noble metal (e.g., Au, Ag, or Pt)[1,4,5] or between a carboxyl group and a metal oxide (e.g., Al_2O_3, Fe_2O_3, or TiO_2).[6,7] The chemisorption technique is very convenient and so is widely used for optical and optoelectronic devices. Recently, a variety of devices and sensors based on luminescence quenching of organic dyes, polycyclic aromatic hydrocarbons (PAHs) such as pyrene or decacyclene immobilized in an oxygen permeable polymer (e.g., silicone polymer and polystyrene) were developed to measure oxygen concentration.[8–11] Since organic dye molecules directly interact with polymer molecules, the properties of sensing films depend strongly on the properties of polymer matrices. To improve these problems, layer of organic dye molecules directly chemisorbed onto substrate without polymer matrices are useful for oxygen sensing devices of no interaction. As the sensing dye molecules are arranged on the solid surface directly using chemisorption layer technique, a highly sensitive device for oxygen sensing will be obtained by using chemisorption layers.

Among PAHs, pyrene and its derivatives display strong fluorescence with high quantum yield and long lifetime.[12] Among pyrene derivatives, pyrene molecules with a carboxyl group are suitable for optical oxygen sensing devices using chemisorption layer because of the formation of a stable layer onto anodic oxidized aluminum and carboxyl

*Corresponding author; E-mail: amao@cc.oita-u.ac.jp

group of pyrene carboxylic acid. We previously reported the properties of optical oxygen sensor using various pyrene carboxylic acid modified onto anodic oxidized aluminum and improvement of oxygen sensitivity of pyrene carboxylic acid modified onto anodic oxidized aluminum by co-adsorption of hydrocarbon layer such as perfluorocarboxylic acid.[13–16] Moreover the fine structures of fluorescence spectrum of pyrene are strongly dependent on its microenvironment. Thus, the pyrene and pyrene derivatives also have been used to investigate the microenvironment of the fluorescent molecule.[17–20] There are two processes in the fluorescence mode of pyrene and pyrene derivatives. One is the emission attributed to monomer of pyrene molecules and the other is attributed to excimer formation of pyrene molecules. The both fluorescence mode depend on the microenvironment of pyrene molecules. The excimer formation of pyrene will be controlled by the co-chemisorbed hydrocarbon with a long alkyl chain such as myristic acid, because the hydrocarbon with a long alkyl chain layer makes a hydrophobic environment around pyrene molecules.

In this work we describe the fluorescence behavior of pyrene-1-butylic acid (PBA) chemisorption layer onto nano-porous anodic oxidized aluminum with myristic acid layer and its application as a fluorescence oxygen sensing material.

2. EXPERIMENTAL DETAILS

2.1. Materials

Pyrene-1-butylic acid (PBA) was obtained from Tokyo Kasei Inc (Tokyo, Japan). Myristic acid was obtained from Wako Pure Chemicals. (Osaka, Japan). Other materials were of the highest grade available obtained from Wako Pure Chemicals (Osaka, Japan).

2.2. Preparation of the Anodic Oxidation of Aluminum Plate

The aluminum plate (1.2 × 4 cm) was washed with 0.5 mol dm^{-3} NaOH aqueous solution for 2 min and then was electrically oxidized in H_2SO_4 solution. The aluminum plate was anodized galvanostatically in a thermostated with stirred bath of 1.0 mol dm^{-3} H_2SO_4 at a temperature of 10 °C for 30 min, a current density of 15 mA cm^{-2}. The applied potential was 20 V. After oxidation, the plate was washed with 0.3 mol dm^{-3} H_3PO_4 solution for 10 min. The anodic oxidized aluminum plates were dried in vacuum at 80 °C for 5 h and stored in vacuum prior to use. By using this method, the depth of pore of anodic oxidized aluminum prepared was 1.5 μm. The anodic oxidized aluminum is nano-porus structure as shown in Figure 1. As the surface of anodic oxidized aluminum plates were observed using scanning electron microscope (SEM), the mean diameter and the surface area of a pore of anodic oxidized aluminum prepared was estimated to be 30 nm and 7.1×10^{12} cm^2. The surface area of one anodic oxidized aluminum pore prepared is c.a. 1.4×10^{-9} cm^2. Thus, the total area of pore of anodic oxidized aluminum per 1 cm^2 is estimated to be c.a. 197 cm^2.

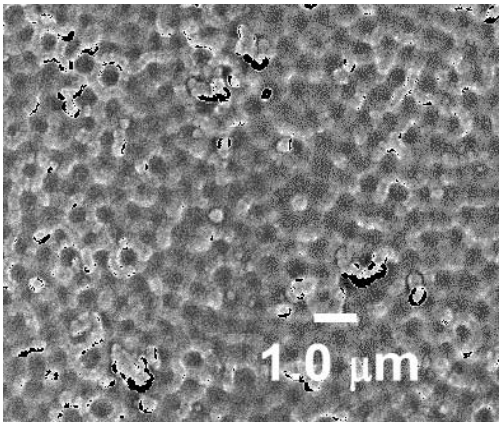

Fig. 1. Scanning electron microscope image of the surface of anodic oxidation of aluminum plate.

2.3. Preparation of PBA and Myristic Acid Chemisorption Layer

Anodic oxidized aluminum plate was dipped into methanol solution with different molar composition ratios of PBA to myristic acid at room temperature for 10 min. After dipping, the plate was washed with water and methanol several times. PBA and myristic acid physically adsorbed onto anodic oxidized aluminum plate were removed by ultrasonication and then dried under vacuum overnight. The PBA concentration was fixed to 0.1 mmol dm^{-3}. The molar composition ratios of PBA to myristic acid were changed 0 to 10. The amount of PBA chemisorbed onto anodic oxidized aluminum plate was determined using a spectrophotometer (Multispec-1500 Shimadzu) according to previous reported method.[21]

2.4. Spectroscopic Measurement

Steady state fluorescence spectra and excitation spectra of the PBA and myristic acid layers were measured using a Shimadzu RF5300-PC fluorescence spectrometer with a 150 W xenon lamp as an excitation light source. Excitation and emission bandpasses were 5.0 nm.

2.5. Characterization of Oxygen Sensor Using PBA and Myristic Acid Chemisorption Layer

The sample substrates were mounted at 45° angle in the quartz cell, for steady state fluorescence experiments, to minimize light scatter from the sample and substrate. Different oxygen standards (in the range 0–100%) in a gas stream were produced by controlling the flow rates of oxygen and argon gases entering a mixing chamber. The total pressure was maintained at 760 Torr. All the experiments

were carried out at room temperature. Oxygen sensing properties of PBA and myristic acid chemisorption layer were characterized by Stern-Volmer quenching constant, K_{SV}, obtained from following equation.

$$I_0/I = 1 + K_{SV}[O_2] \quad (1)$$

where I_0, I and $[O_2]$ are fluorescence intensities in the absence and in the presence of oxygen and oxygen concentrations, respectively. K_{SV} was obtained from a linear plot of (I_0/I)-1 versus $[O_2]$.

3. RESULTS AND DISCUSSION

3.1. Fluorescence Behavior of PBA onto Anodic Oxidation of Aluminum Plate with Myristic Acid Layer

PBA and myristic acid co-chemisorbed layer onto the anodic oxidized aluminum plate showed fluorescence at 376, 396 (attributed to monomer emission) and 474 nm (attributed to excimer emission) when excited at 340 nm under argon saturated condition as shown in Figure 2. The spectra (1), (2), and (3) showed the 0, 2, and 10 of [myristic acid]/[PBA] value, respectively. When the [myristic acid]/[PBA] value increased, the fluorescence intensities at 376 and 396 nm attributed to monomer emission increased and the intensity at 474 nm attributed to excimer emission decreased. As the fine structure of fluorescence spectrum of pyrene derivatives is affected by the polarity of its microenvironment, pyrene derivatives have been used as an indicator for studies on the microenvironment. The enhancement of 0–0 symmetry forbidden band (A) of pyrene molecules in polar media is induced by a decreasing symmetry due to either dipole-dipole interaction with the medium molecules. Thus, the ratio of the fluorescence intensity (B)/(A) is an indicator of the polarity of the microenvironment around pyrene molecules and the higher ratio indicates a less polar environment. Two typical peaks attributed monomer emission, 376 (A) and 396 nm (B) were obtained in the fluorescence spectra of PBA and myristic acid co-chemisorbed layer onto the anodic oxidized aluminum plate. Figure 3 shows the relationship between the ratio of the fluorescence intensity (B)/(A) and the [myristic acid]/[PBA] value. The ratio of (B)/(A) decreased with increasing the [myristic acid]/[PBA] value. Thus, the polarity of the microenvironment around PBA molecules increased by co-chemisorption of myristic acid and the excimer formation between PBA molecules was suppressed by the myristic acid layer onto nano-porous anodic oxidized aluminum plate. In all cases of PBA onto anodic oxidation of aluminum plate with myristic acid layer, the amount of chemisorbed PBA onto anodic oxidation of aluminum plate was estimated to be c.a. 10^{-9} mol cm^{-2} according to the previous reported method.[21] Since the area of PBA molecule is estimated to be c.a. 0.2 nm^2, the area PBA occupied onto 1 cm^2 of anodic oxidation of aluminum plate approximately is 1.2 cm^2. On the other hand, the total area of pore of anodic oxidized aluminum per 1 cm^2 is estimated to be c.a. 197 cm^2. Thus, the PBA and myristic acid layer chemisorbed onto anodic oxidation of aluminum plate will be formed the monolayer as shown in Figure 4.

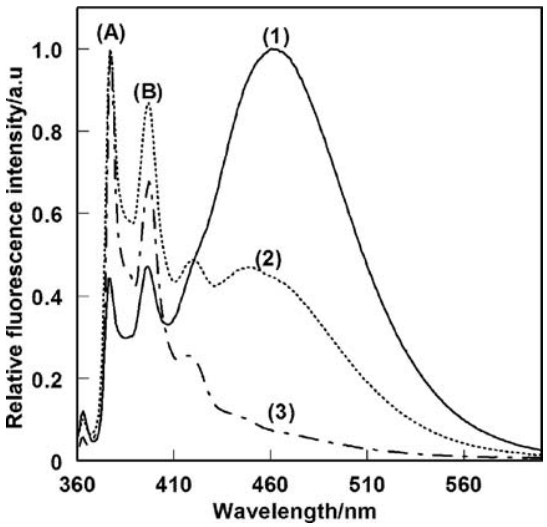

Fig. 2. Fluorescence spectra of PBA and myristic acid chemisorbed layer onto the anodic oxidized aluminum plate under argon saturated condition. The excitation wavelength was 340 nm. The spectra (1), (2), and (3) showed the 0, 2, and 10 of [myristic acid]/[PBA] value, respectively. A: Monomer, B: Excimer emission.

3.2. Oxygen-Induced Fluorescence Spectrum Change of PBA onto Anodic Oxidation of Aluminum Plate with Myristic Acid Layer

Figure 5 shows the fluorescence spectrum change of PBA onto anodic oxidation of aluminum plate with myristic

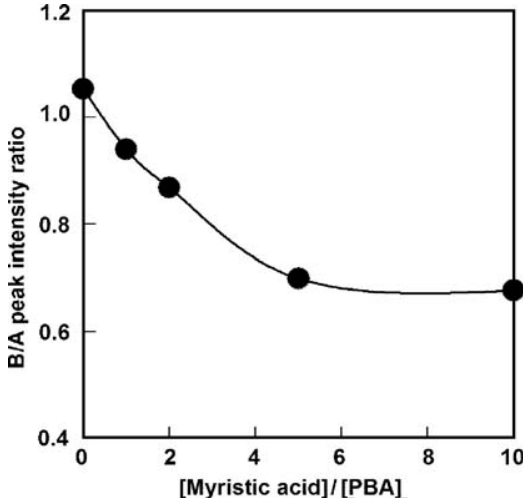

Fig. 3. Peak intensity ratio (B/A) dependent on the different molar composition ratios of myristic acid to PBA onto the anodic oxidized aluminum plate.

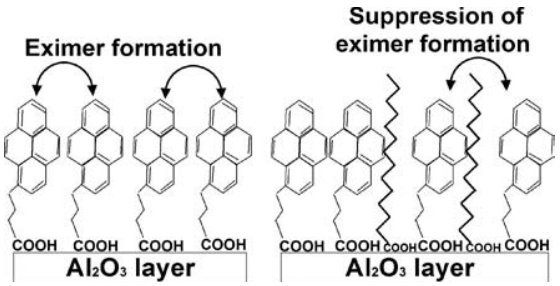

Fig. 4. Schematic representation of PBA and myristic acid layers onto anodic oxidation of aluminum plate.

acid layer by oxygen. The spectra (a) and (b) showed the 0 and 10 of [myristic acid]/[PBA] value, respectively. Both of fluorescence at 376, 396 (attributed to monomer emission) and 474 nm (attributed to excimer emission) were quenched by oxygen. For all cases of molar composition ratio of myristic acid to PBA, both of fluorescence at 376, 396, and 474 nm also were quenched by oxygen. The ratio I_0/I_{100}, where I_0 and I_{100} represent the detected fluorescence intensities from a substrate exposed to 100% argon and 100% oxygen, respectively, is used as an indicator of the sensitivity of the sensing film. In general, a sensor with I_0/I_{100} of more than 3.0 was a suitable oxygen-sensing device.[22] The I_0/I_{100} values of chemisorption layers with different molar composition ratios of PBA to myristic acid were summarized in Table I. The I_0/I_{100} values in monomer emission at 376 nm increased with increasing the ratio of myristic acid to PBA. In contrast, the I_0/I_{100} values in excimer emission at 461 nm decreased with increasing the ratio of myristic acid to PBA.

3.3. Oxygen Sensing Properties of PBA onto Anodic Oxidation of Aluminum Plate with Myristic Acid Layer

Stern-Volmer plot of the relationships between the fluorescence intensities of PBA and myristic acid chemisorbed layer and oxygen concentrations. The plots show nonlinear curve. Demas et al. reported a multi-site model in which the oxygen sensing film has some different oxygen-accessible sites.[23] According to this model, each site has

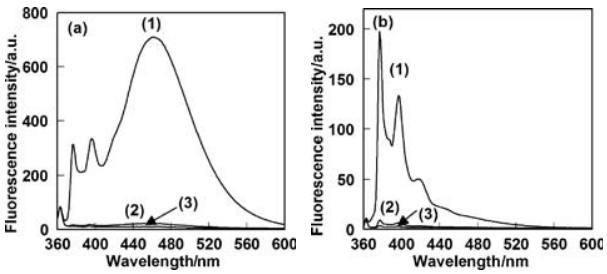

Fig. 5. Oxygen-induced fluorescence spectrum change of PBA onto anodic oxidation of aluminum plate with myristic acid layer. The excitation wavelength was 340 nm. The spectra (a) and (b) showed the 0, and 10 of [myristic acid]/[PBA] value, respectively, [O_2]: (1) 0, (2) 20, and (3) 100%.

Table I. The I_0/I_{100} values chemisorption layers with different molar composition ratios of myristic acid to PBA.

	I_0/I_{100}	
[Myristic acid]/[PBA]	376 nm	461 nm
0	27.9	73.4
1	37.7	47.2
2	56.6	39.6
5	60.0	11.9
10	62.6	9.6

its own individual characteristic-quenching constant. As the observed fluorescence intensity is the sum of emission from different oxygen-accessible sites with their own characteristic quenching constants, the Stern-Volmer relationship is given by

$$I_0/I = [\Sigma(f_n/(1+K_{SVn}[O_2]))]^{-1} \quad (2)$$

where n is an integer. f_n is the fractional contribution to each oxygen accessible site, and K_{SVn} is the quenching constant for each site. Assuming that there are k accessible (and n-k non-accessible) molecules with the same K_{SV}, one can then express equation (2) can be expressed as

$$\frac{I_0}{(I_0-I)} = \frac{1}{(fK_{SV}[O_2])} + \frac{1}{f} \quad (3)$$

where $f = \Sigma f_i$. This is the maximum mole fraction of pyrene molecules that are accessible to oxygen. If only a single class of pyrene molecules with the same accessibility to oxygen is present, $1/f$ in Eq. (3) should be 1. Figure 6 shows the modified Stern-Volmer plots for PBA and myristic acid chemisorbed layer plotted using Eq. (3). Figures 6(a) and (b) indicate the Stern-Volmer plot of monomer emission at 376 nm and excimer emission at 461 nm, respectively. The plot of $I_0/(I_0-I)$ against $1/[O_2]$ showed good linearity, which enhanced compared with the plot of I_0/I against oxygen concentrations. In order to obtain the f value, the regression line is extrapolated to $1/[O_2] = 0$. The value of f indicates the oxygen quenching mole fraction of the PBA molecule and $f = 1$ means that

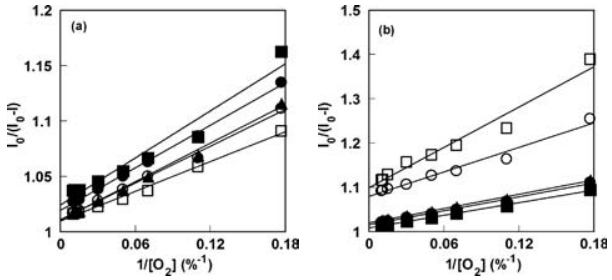

Fig. 6. Modified Stern-Volmer plots for PBA and myristic acid chemisorption layer onto anodic oxidation of aluminum plate monitored at (a) 376 nm and (b) 461 nm. The excitation wavelength was 340 nm. [myristic acid]/[PBA]=0 (closed circle), 1 (closed square), 2 (closed triangle), 5 (open circle), and 10 (open square).

Table II. The K_{SV} values chemisorption layers with different molar composition ratios of myristic acid to PBA.

	K_{SV}/%	
[Myristic acid]/[PBA]	376 nm	461 nm
0	1.4	2.3
1	1.6	2.0
2	1.8	1.8
5	1.9	1.2
10	2.1	0.84

all excited PBA molecules are quenched equally by oxygen. For all cases of molar composition ratio of myristic acid to PBA, both of f values at 376 and 474 nm were nearly to 1.0. The K_{SV} values of chemisorption layers with different molar composition ratios of PBA acid and myristic acid are summarized in Table II. The K_{SV} values at 376 nm due to monomer increased with increasing the ratio of myristic acid to PBA. In contrast, the K_{SV} values at 461 due to excimer nm decreased with increasing the ratio of myristic acid to PBA.

4. CONCLUSION

In this work we describe the fluorescence behavior of pyrene-1-butylic acid (PBA) chemisorption layer onto nano-porous anodic oxidized aluminum with myristic acid layer and its application as a fluorescence oxygen sensing material. When the [myristic acid]/[PBA] value increased, the fluorescence intensity due to monomer emission increased and the intensity due to excimer emission decreased. From the PBA fluorescence shape onto nano-porous anodic oxidized aluminum plate with myristic acid layer, the polarity of the microenvironment around PBA molecules increased by co-chemisorption of myristic acid and the excimer formation between PBA molecules was suppressed by the myristic acid layer onto nano-porous anodic oxidized aluminum plate. For all cases of molar composition ratio of myristic acid to PBA, both of fluorescence at 376, 396, and 474 nm also were quenched by oxygen. The I_0/I_{100} values in monomer emission increased with increasing the ratio of myristic acid to PBA. In contrast, the I_0/I_{100} values in excimer emission decreased with increasing the ratio of myristic acid to PBA. The oxygen sensing properties of PBA onto anodic oxidation of aluminum plate with myristic acid layer was investigated using Stern-Volmer theory. The PBA onto anodic oxidation of aluminum plates with myristic acid layer obey the modified Stern-Volmer equation. The K_{SV} values at monomer emission increased with increasing the ratio of myristic acid to PBA. On the other hand, the K_{SV} values at excimer emission decreased with increasing the ratio of myristic acid to PBA.

Acknowledgments: This work is partially supported by "Molecular Sensors for Aero-Thermodynamic Research (MOSAIC)," the Special Coordination Funds from the Ministry of Education, Culture, Sports, Science, and Technology Agency.

References and Notes

1. A. Ulman, An Introduction to Ultrathin Organic Films: From Langmuir-Blodgett to Self-Assembly, Academic Press, New York (**1991**).
2. G. Decher, J. D. Hong, and J. Schmitt, *Thin Solid Films* 210/211, 831 (**1992**).
3. P. Bertrand, A. Jonas, A. Laschewsky, and R. Legras, *Macromol. Rapid Commun.* 21, 319 (**2000**).
4. R. G. Nuzzo, F. A. Fusco, and D. L. Allara, *J. Am. Chem. Soc.* 109, 2358 (**1987**).
5. P. E. Laibinis and G. M. Whitesides, *J. Am. Chem. Soc.* 114, 1990 (**1992**).
6. K. D. Dobson and A. J. McQuillan, *Spectrochim. Acta A* 55, 1395 (**1999**).
7. K. D. Dobson and A. J. McQuillan, *Spectrochim. Acta A* 56, 557 (**2000**).
8. T. M. Freeman and W. R. Seitz, *Anal. Chem.* 53, 98 (**1981**).
9. T. Ishiji and M. Kaneko, *Analyst* 120, 1633 (**1995**).
10. A. Sharma and O. S. Wolfbeis, *Appl. Spect.* 42, 1009 (**1988**).
11. E. D. Lee, T. C. Werner, and R. Seitz, *Anal. Chem.* 59, 279 (**1987**).
12. E. Mohyi, J. Abu-Zeid, R. Lopez, P. Martinez, J. C. Acevedo, and R. Groff, *Chem. Phys. Lett.* 46, 558 (**1977**).
13. Y. Fujiwara and Y. Amao, *Sens Actuators B* 85, 175 (**2002**).
14. Y. Fujiwara and Y. Amao, *Sens Actuators B* 89, 59 (**2003**).
15. Y. Fujiwara and Y. Amao, *Sens Actuators B* 99, 130 (**2004**).
16. Y. Fujiwara and Y. Amao, *Sensor Lett.* 2, 232 (**2004**).
17. T. Ishiji, K. Kudo, and M. Kaneko, *Sens. Actuators* 22, 205 (**1994**).
18. E. Blatt, A. Launikonis, A. W. H. Mau, and W. H. F. Sasse, *Aust. J. Chem.* 40, 1 (**1987**).
19. K. Rajeshwar and M. Kaneko, *Langmuir* 5, 255 (**1989**).
20. K. Kalyanasundaram and J. K. Thomas, *J. Am. Chem. Soc.* 99, 2039 (**1977**).
21. A. Saeki, H. Sakai, K. Kamogawa, Y. Kondo, N. Yoshino, H. Uchiyama, J. H. Harwell, and M. Abe, *Langmuir* 16, 9991 (**2000**).
22. B. D. MacCraith, C. M. McDonagh, G. O'Keeffe, E. T. Keyes, J. G. Vos, B. O'Kelly, and J. F. McGilp, *Analyst* 118, 385 (**1993**).
23. J. N. Demas, B. A. DeGraff, and W. Xu, *Anal. Chem.* 67, 1377 (**1995**).

SENSOR LETTERS
Vol. 4, 144–154, 2006

RESEARCH ARTICLE

Superoxide Sensors

Takehiro Miyasaka[1,*], Kosuke Endo[2], Seiichi Mochizuki[3], and Kiyotaka Sakai[4]

[1] *Department of Cardiovascular Physiology, Okayama University Graduate School of Medicine, Dentistry, and Pharmaceutical Sciences, Okayama 700-8558, Japan*
[2] *Department of Physiology, Kawasaki Medical School, Okayama 701-0192, Japan*
[3] *Department of Medical Engineering, Kawasaki Medical School, Okayama 701-0192, Japan*
[4] *Department of Chemical Engineering, Faculty of Science and Engineering, Waseda University, Tokyo 169-8555, Japan*

(Received: 19 June 2005. Accepted: 19 July 2005)

The reactive oxygen species (ROS) have important physiological and protective roles in the maintenance of living systems. However, excessive production of ROS can impact cellular homeostasis and lead to oxidative stress. Superoxide has high reactivity acting as a reductant and an oxidant. Because of the pathophysiological roles of superoxide several methods for its detection have been developed. Spectrophotometric assay is nonspecific for superoxide, which limits its use. Chemiluminescent methods have been used frequently for vascular tissue samples because they are more sensitive than other conventional methods. Fluorescence-based assays have also been widely used in cultured cells and vascular tissues. Electron spin resonance (ESR) spectroscopy, also known as electron paramagnetic resonance (EPR), quantitatively measures superoxide concentration but is less suitable for its *in vivo* detection. Electrochemical sensors based on cytochrome c reduction or superoxide dismutase (SOD) enzymatic reaction have been developed for real-time monitoring, but lack adequate performance for *in vivo* superoxide measurement. Newly developed SOD-immobilized superoxide sensors reportedly have satisfactory performance for *in vitro* measurement. In this paper, we review superoxide measurement methods from the early spectrophotometric assays to the third generation of electrochemical sensors.

Keywords: Superoxide, Superoxide Dismutase, Superoxide Sensor, Electrochemical Sensor, Oxidative Stress.

1. INTRODUCTION

The use of oxygen in respiration has had a long and venerable prehistory; eukaryotes and prokaryotes first utilized oxygen perhaps as long ago as 2 billion years. The rapid and varied oxidation reactions make oxygen a very useful molecule in catabolic, and anabolic or biosynthetic pathways. However, oxygen is highly reactive and the resulting oxidative damage makes it toxic even to oxygen-dependent organisms. Organisms have developed extensive antioxidant defenses, and as awareness of the important roles of reactive oxygen species (ROS) in animal and plant pathology increases so does the interest of medical researchers, physiologists, and plant pathologists, in the antioxidant defense systems in cells and tissue.

Excessive production of ROS in mammals can affect cellular homeostasis and lead to oxidative stress, and is associated with inflammation,[1] hypercholesterolemia,[2] diabetes mellitus,[3] hypertension,[4] ischemic heart disease,[5] and chronic heart failure.[6] Figure 1 shows a schema of the process of oxidative stress. Table I shows the roles of ROS *in vivo*. Table II lists both oxygen radicals (superoxide anion radical, commonly called superoide: $O_2^{\cdot-}$, hydroxyl radical: $OH^{\cdot}$, etc.) and certain nonradicals (ozone: O_3, peroxynitrite: $ONOO^-$, singlet oxygen: $^1O_2$, hydrogen peroxide: H_2O_2) that are oxidant or are easily converted into other radicals and nonradicals. Some of the ROS of medical interest are known to have very short half-lives.[7]

The respiratory chain of enzyme activity in the mitochondria is the main intracellular source of $O_2^{\cdot-}$. Figure 2 shows the steps in the four-electron reduction of molecular oxygen (O_2) to water via $O_2^{\cdot-}$, H_2O_2, and $OH^{\cdot}$. $O_2^{\cdot-}$ is produced by the one-electron reduction of molecular O_2 as the first intermediate in this pathway. While $O_2^{\cdot-}$ is mainly produced by dihydronicotinamide adenine dinucleotide

*Corresponding author; E-mail: miyasaka@md.okayama-u.ac.jp

 1546-198X/2006/4/144/011 doi:10.1166/sl.2006.014

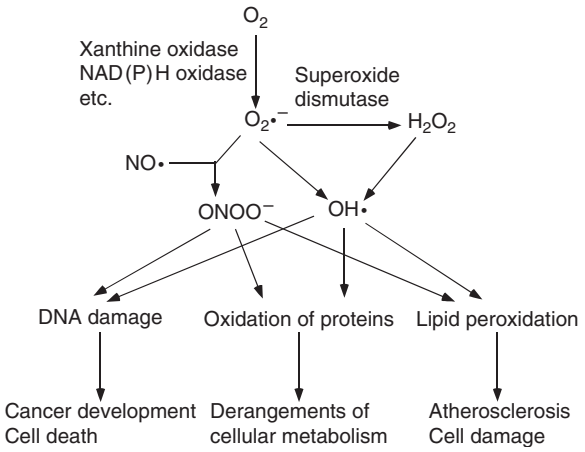

Fig. 1. Schematic illustration of mechanisms for the generation and elimination of ROS *in vivo*.

(NADH) dehydrogenase in mitochondria, other enzymes also produce $O_2^{\cdot -}$ such as reduced nicotinamide adenine dinucleotide phosphate (NADPH) oxidase in phagocytic cells, NADPH cytochrome P450 reductase in microsomes, and xanthine oxidase (XOD) and NAD(P)H oxidases in endothelial and vascular smooth muscle cells. For example, hypercholesterolemia increases endothelial production of $O_2^{\cdot -}$ by XOD activation.[8] Increased $O_2^{\cdot -}$ production may inactivate nitric oxide (NO) as endothelium-derived relaxing factor (EDRF) [9] contributing to the atherosclerotic process. In hypertension, oxidative stress is enhanced due to increased $O_2^{\cdot -}$ production by NAD(P)H oxidase and decreased scavenging of $O_2^{\cdot -}$ by extracellular superoxide dismutase (SOD).[10]

One family of highly-conserved enzymes has evolved to reduce $O_2^{\cdot -}$ is the SODs, which catalyze the reaction of $O_2^{\cdot -}$ with an electron and 2 protons to form H_2O_2.

$$2O_2^{\cdot -} + 2H^+ \xrightarrow{\text{SOD}} O_2 + H_2O_2 \qquad (1)$$

Three mammalian SODs have been identified: copper/zinc SOD (Cu/Zn SOD; SOD1), manganese SOD (Mn SOD; SOD2), and extracellular SOD (EC-SOD; SOD3). Cu/Zn SOD, the first member of the family discovered in mammals in 1969, is located in the cytosol and nucleus of all cell types.[10] Mn SOD, the second mammalian enzyme discovered from pig heart in 1973, is localized in the mitochondrial matrix.[11,12] The essential role of Mn

Table I. Roles of ROS *in vivo*.

Physiological condition (normal production)	Pathophysiological condition (overproduction)
By-product of ATP	Vascular dysfunction
Cytotoxicity against bacteria	Inflammation
Homeostatic regulation	DNA damage
Signal transfer of nerve system	Oxidation of proteins
	Lipid peroxidation

Table II. Reactive Oxygen Species.

Free radicals	
Superoxide	$O_2^{\cdot -}$
Hydroxyl	$OH^{\cdot}$
Hydroperoxyl	$HO_2^{\cdot}$
Peroxyl	$RO_2^{\cdot}$
Alkoxyl	$RO^{\cdot}$
Carbonate	$CO_3^{\cdot -}$
Carbon dioxide	$CO_2^{\cdot -}$
Nonradicals	
Hydrogen peroxide	H_2O_2
Hypobromous acid	HOBr
Hypochlorous acid	HOCl
Ozone	O_3
Singlet oxygen	$^1O_2$
Organic peroxides	ROOH
Peroxynitrite	ONOO$^-$
Peroxynitrous acid	ONOOH

SOD is maintaining mitochondrial function.[13] EC-SOD, the third and latest mammalian SOD discovered, was isolated from human lung by Marklund in 1982.[14] EC-SOD contains copper and zinc like Cu/Zn SOD but not manganese. Whereas the intracellular isoenzymes Cu/Zn SOD and Mn SOD are synthesized by virtually all mammalian cell types, important sources of EC-SOD are fibroblasts in peripheral tissues and glia cells in the central nervous system.[15] EC-SOD is secreted into the extracellular fluid (plasma, lymph, ascites, synovial fluid, and cerebrospinal fluid) [16] and reversibly binds to heparan sulphate proteoglycan ligands in the glycocalyx of the surface of most tissue cell types and in the interstitial matrix.[15] Table III lists these SODs.

$O_2^{\cdot -}$ also is eliminated by nonenzymatic antioxidant components such as tocopherol (vitamin E) and flavonoides.[17] Pietta et al. showed that ginkgoflavonol-glycosides and green tea (*Camellia sinensis*) catechins (types of tannin) metabolites have antioxidant capacity.[18] Of the many kinds of catechins in tea, such as (+)-catechin, (−)-epicatechin, (−)-epigallocatechin, (−)-epicatechin gallate, and (−)-epigallocatechin gallate, act as scavengers for $O_2^{\cdot -}$.[19] Catechins contained in green tea also directly scavenge NO, which is why green tea is reputed to be an excellent dietary source of antioxidant by virtue of its inhibitory effects on ROS metabolism.[20] Simonetti et al. showed that the levels of caffeic acid (hydroxycinnamic derivative) in human plasma increased linearly with dose of ingested of red wine, and that the caffeic acid concentrations correlated with the variation of plasma total antioxidant

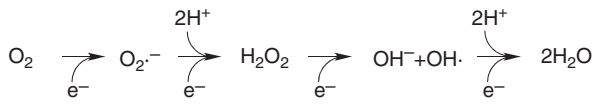

Fig. 2. Schematic illustration of one-electron reduction pathway of oxygen.

RESEARCH ARTICLE

Table III. Superoxide dismutase (SOD).

Type	Name	Metals	Subunit Size	Location
SOD1	Copper/zinc SOD	Cu/Zn	16 kDa	Cytosol and nucleus of all cell types
SOD2	Manganese SOD	Mn	16 kDa	Mitochondria
SOD3	Extracellular SOD	Cu/Zn	30 kDa	Fibroblasts, glial cells, and extracellular fluid

capacity.[21] Although such common foods may offer attractive targets for development of pharmaceutical products, they also are dietary sources of antioxidants that can act to confound *in vivo* investigations.

The high reactivity of $O_2^{\cdot-}$, abundant opportunities for auto-oxidation, and the scavenging system make the half-life of $O_2^{\cdot-}$ in biological systems extremely short. Real-time monitoring of $O_2^{\cdot-}$ production within the cell and in the extracellular matrix *in vivo* challenges current technological capacity. The reports about the sensors described in this article are of proof-of-concept studies of the production of $O_2^{\cdot-}$ in basic cellular processes. The methods include spectrophotometric assays, chemiluminescent detections, fluorescence-based assays, electron paramagnetic resonance (EPR) spectroscopy and spin trapping, electrochemical detection, and combinations of methods (Table IV). Table V lists the advantage and disadvantage of these ROS measurement systems. Published reviews on the measuring methods of vascular reactive species provide more detailed comparisons.[22–25]

Table IV. Methods of detecting superoxide.

Spectrophotometric assays	Cytochrome c
	Nitro blue tetrazolium (NBT)
Chemiluminescence assays	Luminol
	Coelenterazine
	2-methyl-6-phenyl-3,7-dihydroimidazo-[1,2-α]pyrazin-3-one (CLA)
	2-methyl-6-(4-methoxyphenyl)-3,7-dihydroimidazo[1,2-α]pyrazin-3-one (MCLA)
	Lucigenin
Fluorescence assays	Dihidroethidium (DHE)
	Dichlorofluorescein (DCF)
Electron spin resonance (ESR)	5,5-dimethylpyrroline-N-oxide (DMPO)
	5-dethoxyphosphoryl-5-methyl-1-pyrroline-N-oxide (DEPMPO)
Electrochemical detection = sensors	Catalase-based sensor
	Superoxide dismutase-based sensor

2. CONVENTIONAL METHODS FOR SUPEROXIDE DETECTION

2.1. Spectrophotometric Assays

Spectrophotometric assays measure the change of absorbance of reagents by reduction reaction with $O_2^{\cdot-}$, including cytochrome *c* (*cyt c*) reduction, and nitroblue tetrazolium (NBT) reduction, and aconitase reduction.

Cyt c reduction is a method widely used for measurement of $O_2^{\cdot-}$ production by various enzymes, tissue extracts, and cells. $O_2^{\cdot-}$ is measured as SOD-inhibitable reduction of *cyt c*, determined as an increase in absorbance of Fe(II)-*cyt c* at 550 nm.

$$Fe^{III}\,cyt\,c + O_2^{\cdot-} \rightarrow Fe^{II}\,cyt\,c + O_2 \qquad (2)$$

Several precautions to avoid overestimation are required in the use of this method, because *cyt c* is nonspecific for $O_2^{\cdot-}$, and reduced *cyt c* can be reoxidized by cytochrome oxidases, peroxidases and oxidants, including H_2O_2 and $ONOO^-$. The use of modified *cyt c* such as acetylated *cyt c* and succinoylated *cyt c* minimize these potentially misleading reactions.[26] However, modified *cyt c* cannot be used to measure $O_2^{\cdot-}$ released by uncoupled NO synthase (NOS) because neuronal NOS reduces native, acetylated and succinoylated *cyt c* by direct electron transfer.[27]

When *Cyt c* reduction is applied for the assay of SOD activity,[10,28] the reduction rate of *cyt c* by $O_2^{\cdot-}$ is monitored at 550 nm using the xanthine/XOD system as the source for $O_2^{\cdot-}$.

$$\text{Xanthine} + O_2 + H_2O \xrightarrow{\text{XOD}} \text{Uric acid} + 2H^+ + O_2^{\cdot-} \qquad (3)$$

SOD competes with *cyt c* for $O_2^{\cdot-}$ and decreases the reduction rate of *cyt c*. The rate of reduction of *cyt c*, inhibited by SOD, is plotted as reciprocal absorbance change per minute versus a standard concentration of SOD. One unit

Table V. Advantages and disadvantages of ROS measurement.

	Optical methods	Chemiluminescent methods	ESR(EPR)	Electrochemical methods
Object for detection	Spectrophotometry fluorescence	Chemiluminescence	Electron spin resonance spectrum	Electrode reaction
Easy and simple	yes	yes	no	yes/no
Quantitative	no	yes	yes	yes
Disadvantage	Qualitative	Probe selectivity Auto-oxidation	Complicated procedure	Hand-made
Real time monitoring	no	yes	no	yes
Real time *in vivo* monitoring	no	no	no	yes

of SOD is defined as that amount of enzyme, which inhibits the rate of *cyt c* reduction by 50%.

The formation of NBT reduced by $O_2^{\cdot-}$ to form monoformazan (NBT^+) can be monitored by spectrophotometer at 550 to 560 nm. NBT detects intracellular $O_2^{\cdot-}$; however, it is susceptible to reduction by several tissue reductases. The specificity for $O_2^{\cdot-}$ must be confirmed by inhibition of NBT staining by SOD. NBT has been shown to artificially generate $O_2^{\cdot-}$ by reacting with environmental O_2 under aerobic conditions. For these reasons, detection of $O_2^{\cdot-}$ in biological samples should not rely exclusively on NBT reduction.

2.2. Chemiluminescent Methods

Because chemiluminescent intensity is considered to be in proportion to $O_2^{\cdot-}$ concentration, it is an appropriate method of $O_2^{\cdot-}$ measurement.[29] And because they are more sensitive than other spectroscopic measurements, chemiluminescent methods frequently have been used for vascular tissue samples. Several chemiluminescent reagents have been used, including lucigenin (bis-*N*-methylacridinium), luminol (5-amino-2,3-dihydroxy-1,4-phthalayineione), coelenterazine [2-(4-hydroxybenzyl)-6-(4-hydroxyphenyl)-8-benzyl-3,7-dihydroimidazo [1,2-α]pyrazin-3-one],[30] and coelenterazine's analogs such as CLA (2-methyl-6-phenyl-3,7-dihydroimidazo[1,2-α]pyrazin-3-one) and MCLA [2-methyl-6-(4-methoxyphenyl)-3,7-dihydroimidazo[1,2-α] pyrazin-3-one].[31]

Among the chemiluminescent reagents, lucigenin has been used most widely to measure rapidly changing $O_2^{\cdot-}$ concentrations. The mechanism of $O_2^{\cdot-}$-dependent lucigenin chemiluminescence requires an initial one-electron reduction by which a lucigenin di-cation (Luc^{2+}) is transformed to a mono-cation radical ($Luc^{\cdot+}$). The mono-cation radical then reacts with $O_2^{\cdot-}$ to yield the unstable dioxetane ($LucO_2$), which spontaneously decomposes. This results in the formation of an electronically excited acridone, which emits light when it returns to a ground state (Fig. 3).

Guyllenhammar showed that lucigenin derived chemiluminescence possesses a high degree of specificity for $O_2^{\cdot-}$ produced from human neutrophils stimulated with a variety of soluble stimuli.[32] Auto-oxidation is negligible at low concentrations (<20 μmol/L[33] or 5 μM [34,35]). However, the concentrations of lucigenin must be controlled to avoid auto-oxidation at higher concentrations (up to 250 μmol/L), where redox cycling is favorable.[36]

$$Luc^{2+} \xrightarrow{\text{reduction}} Luc^{\cdot+} \quad (4)$$

$$Luc^{\cdot+} + O_2 \Leftrightarrow Luc^{2+} + O_2^{\cdot-} \quad (5)$$

Vásquez-Viar et al. demonstrated that lucigenin stimulates eNOS-dependent NADPH consumption and $O_2^{\cdot-}$ generation. In this reaction, lucigenin (Luc^{2+}) is reduced to the

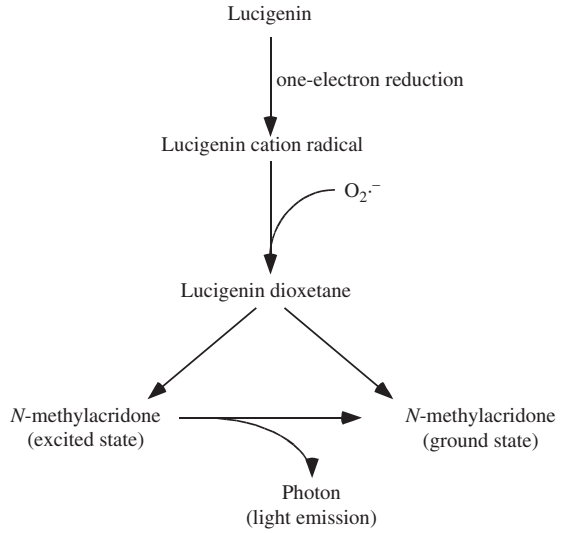

Fig. 3. Schematic illustration of the reaction pathway leading to lucigenin chemiluminescence.

$Luc^{\cdot+}$, which reacts with oxygen to regenerate lucigenin and $O_2^{\cdot-}$.[37]

$$NADPH/eNOS + Luc^{2+} \rightarrow Luc^{\cdot+} \quad (6)$$

$$Luc^{\cdot+} + O_2 \Leftrightarrow Luc^{2+} + O_2^{\cdot-} \quad (5)$$

Liochev and Fridovich showed that lucigenin (Luc^{2+}) is reduced to the $Luc^{\cdot+}$ by other enzymic reaction such as XOD + NADH, and glucose oxidase + glucose and then $Luc^{\cdot+}$ rapidly auto-oxidizes and produces $O_2^{\cdot-}$.[38] Because lucigenin undergoes a cycle of univalent reduction followed by auto-oxidation, the difficulties in controlling the possible enzymic reactions in cells and tissue limits its use in measuring $O_2^{\cdot-}$. Scheriber et al. performed real-time monitoring of $O_2^{\cdot-}$ production *in vitro* using lucigenin chemiluminescence[39] in brain slices during and after hypoxia, however the results were qualitative.

The mechanism of $O_2^{\cdot-}$-dependent luminol chemiluminescence requires an initial one-electron reduction by which a luminol is transformed to a luminol radical. The luminol radical reacts with $O_2^{\cdot-}$ to yield an unstable endoperoxide. The luminol endoperoxide decomposes to N_2 and aminophthallate. The aminophthallate, in an electronically exited state, relaxes into a ground state and emits a photon.

Luminol-derived chemiluminescence may be induced by a variety of ROS including $O_2^{\cdot-}$, $OH^{\cdot}$, and H_2O_2.[40] Thus, various scavengers such as uric acid for $ONOO^-$ and catalase for H_2O_2 are necessary to identify which ROS is responsible for the signal produced by luminol.

The above conventional chemiluminescent methods are useful for *in vitro* $O_2^{\cdot-}$ measurement in isolated tissues, isolated vessels or cultured cells. Recently, some of chemiluminescent methods have been applied *in vivo*, including the monitoring of $O_2^{\cdot-}$ production from the surface of rabbit

RESEARCH ARTICLE

heart and cat brain by the MCLA chemiluminescence;[41, 42] however, precise quantitation is problematic with the *in vivo* method.

2.3. Fluorescence-Based Assays

Fluorescence-based assays also have been widely used for detection of ROS in cultured cells and vascular tissues. Although these approaches are semi-quantitative, they provide important information on the localization of ROS in sample tissues and cells. Cells can be analyzed by a micro plate reader or by a fluorescence-activated cell sorter (FACS).[43] Fluorescent intensity provides quantitative information on ROS formation. Dihydrothidium (DHE) and dichlorofluorescein (DCF) are common fluorescent probes used to measure $O_2^{\cdot-}$. DHE is cell-membrane permeable and reacts with intracellular $O_2^{\cdot-}$ to form an intermediate product, which in turn interacts with DNA producing nuclear fluorescence at an excitation wavelength of 500–530 nm and an emission wavelength of 590–620 nm. Zhao et al. discovered another fluorescent product (excitation, 480 nm; emission, 567 nm) by the reaction of DHE and $O_2^{\cdot-}$.[44] DHE may react with $OH^{\cdot}$ and H_2O_2, it shows reasonable specificity to $O_2^{\cdot-}$. Oxidation transforms 2′,7′-dichlorodihydrofluorescein (DCFH) to the highly fluorescent 2′,7′-dichlorofluorescein (DCF). DCFH may also be auto-oxidized to form H_2O_2 and requires special precautions to avoid overestimation. DCF has been used to detect ROS in cultured cells, but the cell-membrane permeable type (DCF-diacetate: DCF-DA) must be used for tissue studies. Although DCF is not specific to $O_2^{\cdot-}$, and can fluoresce in response to a variety of ROS including H_2O_2, other peroxides, and $ONOO^-$, it is a useful marker of ROS.[45, 46]

2.4. Electron Spin Resonance Spectroscopy Methods

Electron spin resonance (ESR) spectroscopy, also known as electron paramagnetic resonance (EPR), detects molecules with unpaired electrons by means of spin-trap reagents, which incorporate radical molecules into their structure. Common spin trap reagents are nitrones such as 5,5-dimethylpyrroline-N-oxide (DMPO), which form –OH and –OOH adducts on reaction with the hydroxyl and $O_2^{\cdot-}$ radicals, respectively.[47] A more $O_2^{\cdot-}$-specific and stable spin trap reagent, 5-dethoxyphosphoryl-5-methyl-1-pyrroline-N-oxide (DEPMPO) has proven useful in measuring $O_2^{\cdot-}$ concentration in aqueous solution using liquid nitrogen freezing.[48] 5-ethoxycarbonyl-5-methyl-pyrroline-N-oxide (EMPO)-$O_2^{\cdot-}$ adduct (EMPO-OOH) is more stable than DEPMPO-$O_2^{\cdot-}$ adduct (DEPMPO-OOH). Zhang et al. showed that the signal-to-noise ratio of the ESR spectrum of EMPO-OOH is further enhanced by labeling the nitrone group in EMPO with a nitrogen-15 atom ([^{15}N]-EMPO).[49] However, some spin-trap reagents are more specific for $O_2^{\cdot-}$ than others. In the presence of reductants in tissues such as ascorbate, the spin active adducts are rapidly reduced to ESR silent species. Probe instability, tissue metabolism, lack of spin trap specificity and the high cost of ESR spectrometers make this technique more suitable for the *in vitro* detection of free radicals in small volume samples.

3. ELECTROCHEMICAL SENSORS FOR SUPEROXIDE MEASUREMENT

3.1. Cytochrome *c*-Based Sensors

In an early sensor design, McNeil et al. developed a monolayer gold disc electrode surface-modified with 4,4′-dithiobipyridine to monitor the reduction of *cyt c* by $O_2^{\cdot-}$.[50] The principle of this method is to measure the change in electric current by the reoxidation of reduced *cyt c* by $O_2^{\cdot-}$ at −25 mV. In this method, *cyt c* was not immobilized on the gold electrode but was only dissolved in sample solutions. They showed that the reduction of *cyt c* was specific to $O_2^{\cdot-}$, and the measured current was proportional to the spectrophotometric assay by *cyt c*. The measured current was proportional to the number of neutrophils that produce $O_2^{\cdot-}$, and then they concluded that this method is applicable to measurement of $O_2^{\cdot-}$ in biological samples.

Subsequently, McNeil et al. developed reagentless sensor system that is applicable to continuous direct monitoring $O_2^{\cdot-}$ concentration *in vitro*.[51] *Cyt c* was immobilized by passive adsorption to a monolayer, platinised activated carbon electrode (PACE). The rate of current production during reoxidation of *cyt c* reduced by $O_2^{\cdot-}$ was monitored using both xanthine/XOD and stimulated neutrophils as sources of $O_2^{\cdot-}$.

Fabian et al. showed that the PACE *cyt c* electrode is sensitive and responsive enough for real-time *in vivo* qualitative measurement of $O_2^{\cdot-}$ in brain tissue.[52, 53] To improve the measurement limit of enzymatic and cellular $O_2^{\cdot-}$ production, Tammeveski et al. adapted a 3,3′-dithiobis(sulfosuccinimidylpropionate) (DTSSP)-monolayer modified gold electrode and immobilized *cyt c* on the electrode.[54] Although the PACE electrode type sensor could not achieve real-time monitoring because of the small measurement area of the electrode, the DTSSP electrode had a larger area which enabled real-time monitoring of $O_2^{\cdot-}$. They applied this electrode to a quantitative *in vitro* analysis of $O_2^{\cdot-}$ released from lipopolysaccharide-activated human glioblastoma cells and demonstrated the relationship between $O_2^{\cdot-}$ and NO.[55]

Ge and Lisdat immobilized *cyt c* on a mercaptoundecanoic acid/mercaptoundecanol-modified gold wire electrode to improve electron transfer between *cyt c* and the electrode.[56] Büttemeyer et al. applied this *cyt c*-based sensor to real-time *in vivo* measurement in the gastrocnemius muscle tissue during reperfusion after ischemia, and demonstrated stable signals specific to $O_2^{\cdot-}$ during reperfusion injury.[57]

Lisdat et al. later designed a monolayer *cyt c* sensor for the measurement of antioxidant activity in analytical grade substances.[58] They used the $O_2^{\cdot-}$ produced by xanthine/XOD reaction, and the antioxidant activity quantified as a percentage of the signal decrease to determine the 50% inhibition value for flavonoids. The antioxidant activity was arranged in the order, flavanols > flavonols > flavones > flavonones > isoflavonones. Subsequent experiments using the same sensor design compared the *in vitro* $O_2^{\cdot-}$ scavenging activity and the *in vivo* antioxidant potential of methanolic extracts prepared from 10 Chinese tonifying herbs.[59] For the measurement of $O_2^{\cdot-}$ scavenging activity *in vitro*, they used hypoxanthine/XOD, and a *cyt c*-modified gold electrode $O_2^{\cdot-}$ sensor to measured the current changes caused by the addition of herbal extracts. They used CCl_4 hepatotoxicity model mice in experiments measuring the *in vivo* antioxidant potential of the herbal extracts. Plasma alanine aminotransferase activity and glutathione regeneration capacity were measured as the indices of antioxidant potential of the herbal extracts. They showed the $O_2^{\cdot-}$ scavenging activity *in vitro* and antioxidant activity of the herbal extracts fed to the mice, respectively, but the *in vitro* $O_2^{\cdot-}$ scavenging activity did not correlate well with the *in vivo* antioxidant activity in the mouse model.

3.2. The Basics of SOD-Based Sensors

Several SOD-immobilized sensors using the reaction of $O_2^{\cdot-}$ with SOD have been developed since 1989. McNeil et al. immobilized bovine Cu/Zn-SOD on a PACE monolayer sensor by passive adsorption.[51] The principle of $O_2^{\cdot-}$ measurement is as follows: SOD eliminates $O_2^{\cdot-}$ by the following reaction:

$$2O_2^{\cdot-} + 2H^+ \xrightarrow{\text{SOD}} O_2 + H_2O_2 \qquad (1)$$

These sensors determine $O_2^{\cdot-}$ concentration indirectly by measuring the amount of H_2O_2 produced by this enzymatic reaction.

$$H_2O_2 \xrightarrow{\text{electrode}} O_2 + 2H^+ + 2e^- \qquad (7)$$

Campanella et al. developed an SOD-immobilized biosensor.[54] SOD was physically entrapped in a kappa-carrageenan gel membrane, and then immobilized on the monolayer electrode. Figure 4 shows the structure and reaction mechanisms of SOD-immobilized $O_2^{\cdot-}$ sensor. They used the Clark electrode and an Ag/AgCl anode, between which −650 mV was applied. The Clark electrode and anode are covered with a polypropylene gas-permeable thin-film membrane. O_2 and H_2O_2 are produced by elimination reaction of $O_2^{\cdot-}$ by SOD [Eq. (1)]. The O_2 produced passes through the gas-permeable membrane and is measured by the electrode, so that the value of measurement indicates the amount of $O_2^{\cdot-}$. But O_2 also is consumed by $O_2^{\cdot-}$ product reactions such as the xthantine/XOD

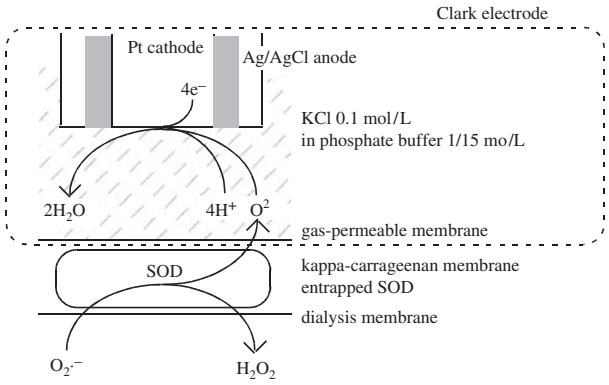

Fig. 4. Superoxide sensor with the Clark electrode by Campanella et al.

reaction [Eq. (3)], and accurate measurement of $O_2^{\cdot-}$ concentration with this type sensor is difficult.

An improved version of the sensor used a classical amperometric monolayer gold wire electrode for H_2O_2 as an indicator of $O_2^{\cdot-}$ production.[61] Figure 5 shows the structure and reaction mechanisms of this sensor. H_2O_2 produced by SOD [Eq. (1)] in the membrane surface diffuses through the membrane and reacts with the electrode. The SOD/H_2O_2 biosensor could measure $O_2^{\cdot-}$ concentration, and was used in a study of the activity of scavengers for $O_2^{\cdot-}$ (ascorbate, glutathione, and cysteine). The SOD/ H_2O_2 biosensor measured the $O_2^{\cdot-}$ released from homogenized healthy and cancerous kidney tissues, and showed that the amount of $O_2^{\cdot-}$ released from cancerous kidney tissues was greater than that from healthy tissue.[61]

Campanella et al. used the improved amperometric SOD biosensor *in vitro* to evaluate antioxidant properties of several fruits and vegetables obtained at a local market: garlic, shallot, onion, Japanese garlic, chilli, aloe, cauliflower, radish, carrot, tomato, kiwi fruit, mandarin, orange, lemon, grapefruit, and strawberry.[62] $O_2^{\cdot-}$ was produced by xanthine/XOD system in pH 7.5 PBS solution, and the calibration curve of the SOD sensor was recorded. The scavenging properties of these foods were evaluated from the percent ratio of slope values of the calibration curve

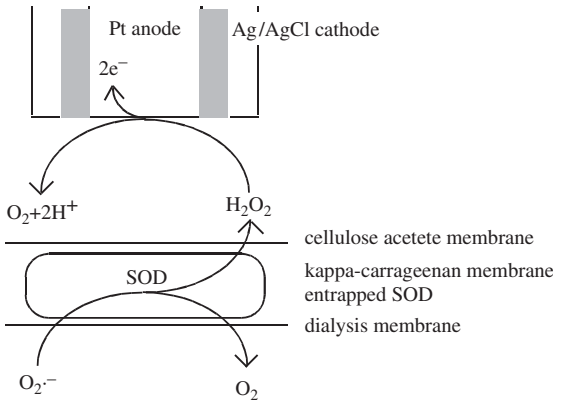

Fig. 5. Superoxide sensor with a classical amperometric electrode for H_2O_2 by Campanella et al.

RESEARCH ARTICLE

both in the absence and presence of each food. In the results, the slope values decreased from 18.7 to 78.1%. In related studies, Campanella et al. applied this amperometric SOD biosensor to determine the antioxidant capacity of different kinds of teas and herbal products such as decaffeinated (detheinated) tea, ordinary tea, green tea, and different fresh aromatic herbs, varieties of olives, and types of fresh fruits.[63,64] They concluded that the results obtained by the SOD biosensor were in good agreement with the results obtained by other methods such as the *cyt c* reduction method, and the spectrophotometric-NBT method.

Ge et al. used two types of SOD-immobilized sensors, CuZnSOD and FeSOD, in which each enzyme was immobilized on a 3-mercaptopropionic acid (MPA)-modified gold electrode, respectively.[65] $O_2^{\cdot-}$ was obtained via the hypoxanthine and XOD reaction, which had no catalytic current in the cyclic voltammogram, but had significant influence on the peak currents of oxidation and reduction of $O_2^{\cdot-}$.

3.3. Other Sensors

Campanella et al. developed a tyrosinase-immobilized biosensor for $O_2^{\cdot-}$ detection by applying a gaseous diffusion electrode for oxygen.[66] Phenol is converted to *o*-quinone through the reaction catalyzed by tyrosinase.

$$\text{phenol} + O_2 \xrightarrow{\text{tyrosinase}} \text{o} - \text{quinone} + H_2O \qquad (8)$$

The O_2 consumed in this reaction is immediately detected by the electrode.

$$O_2 + 4H^+ + 4e^- \xrightarrow{\text{electrode}} 2H_2O \qquad (9)$$

$O_2^{\cdot-}$ inhibits the tyrosinase reaction, and the percentage of inhibition is proportional to $O_2^{\cdot-}$ concentration.

Galactose oxidase (GAO) was used in a similar manner for $O_2^{\cdot-}$ detection.[66] GAO separately catalyses both the oxidation of primary alcohol to its aldehyde, and the reduction of O_2 to H_2O_2. This catalytic activity is inhibited in the presence of certain free radicals.

$$RCH_2OH + O_2 \xrightarrow{\text{GAO}} RCHO + H_2O_2 \qquad (10)$$

The percentage of inhibition of this oxidation reaction can be used to determine free radical concentration such as $O_2^{\cdot-}$ and NO. GAO is not specific enough for use under complex conditions.

4. PREPARATION OF AN SOD-IMMOBILIZED $O_2^{\cdot-}$ SENSOR

A sensitive and stable $O_2^{\cdot-}$ sensor[67] uses the specificity of the enzymatic reaction of SOD with $O_2^{\cdot-}$ without any effect from other oxidants and reductants. The electron mediator, ferrocene-carboxaldehyde was used for efficient electron transfer.[68–70] The SOD sensor directly measures the current produced by reoxidation of SOD instead of the current from electrode reaction with H_2O_2 (Fig. 6).

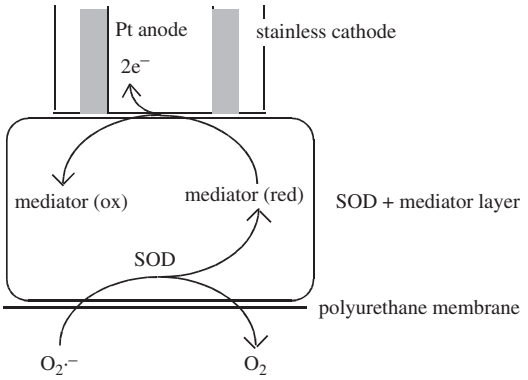

Fig. 6. SOD-immobilized superoxide sensor with a platinum wire electrode.

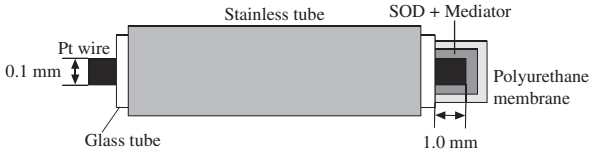

Fig. 7. Detailed schematic illustration of the SOD-immobilized superoxide sensor with a platinum wire electrode.

Figure 7 shows the structure of a simple SOD-immobilized $O_2^{\cdot-}$ sensor. The sensor consists of a polyurethane-coated platinum wire (diameter: 0.1 mm, and effective length: 1 mm) as the working electrode, a glass tube as the insulator, and a stainless tube (inner diameter: 0.94 mm) as the counter electrode. SOD (Mn-type) and the modulated ferrocene-carboxaldehyde mediator are immobilized on the electrode.

5. CALIBRATION OF THE SOD-IMMOBILIZED $O_2^{\cdot-}$ SENSOR

The SOD-immobilized $O_2^{\cdot-}$ sensor in Figure 7 is calibrated with $O_2^{\cdot-}$, which is enzymically produced in phosphate buffer saline (PBS) solution. The enzymatic reaction of xanthine and XOD synthesizes $O_2^{\cdot-}$ [Eq. (3)] as it does *in vivo*.[71] Figure 8 shows the experimental setup for calibration. The $O_2^{\cdot-}$ sensor is located in the detection chamber. Xanthine-PBS solution is perfused into the chamber at 2.8 ml/min. PBS solution with or without XOD is added at 0.2 ml/min to control $O_2^{\cdot-}$ production. Xanthine concentration in the detection chamber is 100 μM, and XOD concentration is controlled between 0 and 50 mU/ml by changing the flow rate. A charge of +0.5 V is applied to the working electrode, and the change in the current produced by the reoxidation reaction of SOD, which is reduced by dismutation of $O_2^{\cdot-}$, is measured by a potentiostat.

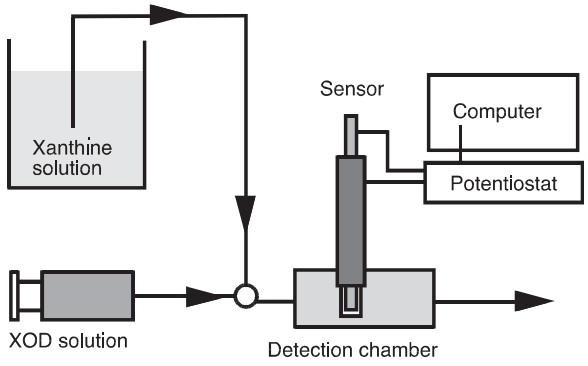

Fig. 8. Experimental setup for calibration of the SOD-immobilized superoxide sensor using superoxide produced by xanthine/XOD (see Fig. 7 for electrode detail).

Figure 9 shows typical traces of the measured current. When xanthine and XOD are mixed and injected into the chamber, the current gradually increases to the plateau level. When the XOD supply is stopped, the current decreases to baseline.

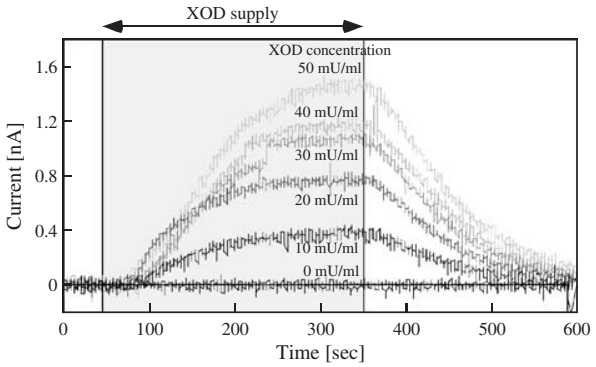

Fig. 9. Time courses of the current responses for superoxide produced by xanthine/XOD (0-50 mU/ml).

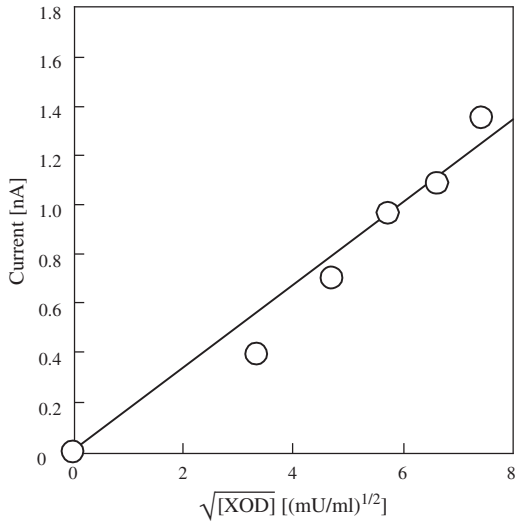

Fig. 10. Relationship of the peak current and XOD concentration (xthantine concentration: 100 μM, flow rate: 3 ml/min) measured by the SOD-immobilized superoxide sensor.

The plateau state level of $O_2^{\cdot-}$ $[O_2^{\cdot-}]$ plateau is expressed by equation 11:

$$[O_2^{\cdot-}]_{plateau} = \sqrt{\frac{k_1}{2k_2}}[XOD] \quad (11)$$

Where k_1 is the apparent rate constant of $O_2^{\cdot-}$ generation and k_2 is the non-enzymatic rate constant of dismutation reaction of $O_2^{\cdot-}$.[65] $[O_2^{\cdot-}]$ plateau is proportional to the square root of XOD concentration. Figure 10 shows the relationship between the plateau-level current and the square root of XOD concentration. A good linear relationship has been reported ($r^2 = 0.99$).[67]

6. MEASUREMENT OF $O_2^{\cdot-}$ RELEASED FROM ISOLATED ORGAN TISSUES

Oxidative stress is induced by a variety of factors such as toxic exposure to drugs, xenobiotics including endotoxin and carbon tetrachloride (CCl_4). It is known that XOD and NAD(P)H oxidase is activated by endotoxins, which increases $O_2^{\cdot-}$ production.[72,73] Miyasaka et al. used an endotoxin (lipopolysaccheide) in a rat model to measure increases in $O_2^{\cdot-}$ production by different organs.

Figure 11 shows the experimental setup for $O_2^{\cdot-}$ detection. The tissue samples heart, kidney, or liver of rat were put into a chamber located before the detection chamber. The working electrode was applied +0.5 V versus counter electrode, and the response current was monitored. After perfusion through the bypass and stabilization of the current, the flow channel was switched to the tissue-packed chamber. The $O_2^{\cdot-}$concentration in the perfusates was measured for 100 seconds, and then the flow channel was switched back to the bypass channel.

Figure 12 shows typical records of the measured current for isolated tissues (A: heart, B: liver, C: kidney). The large differences in the response currents were detected only in the endotoxin-shock group, indicating an increase in $O_2^{\cdot-}$ production by endotoxin in the kidney and liver.

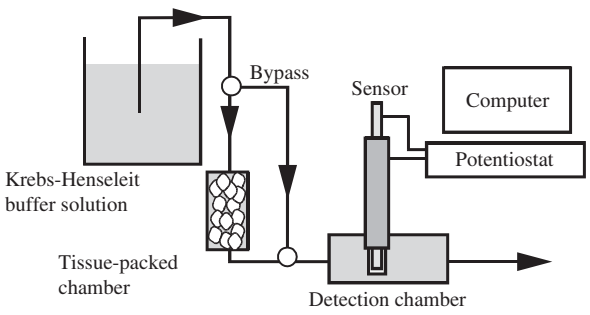

Fig. 11. Experimental setup for monitoring supeoxide released from isolated tissues.

RESEARCH ARTICLE

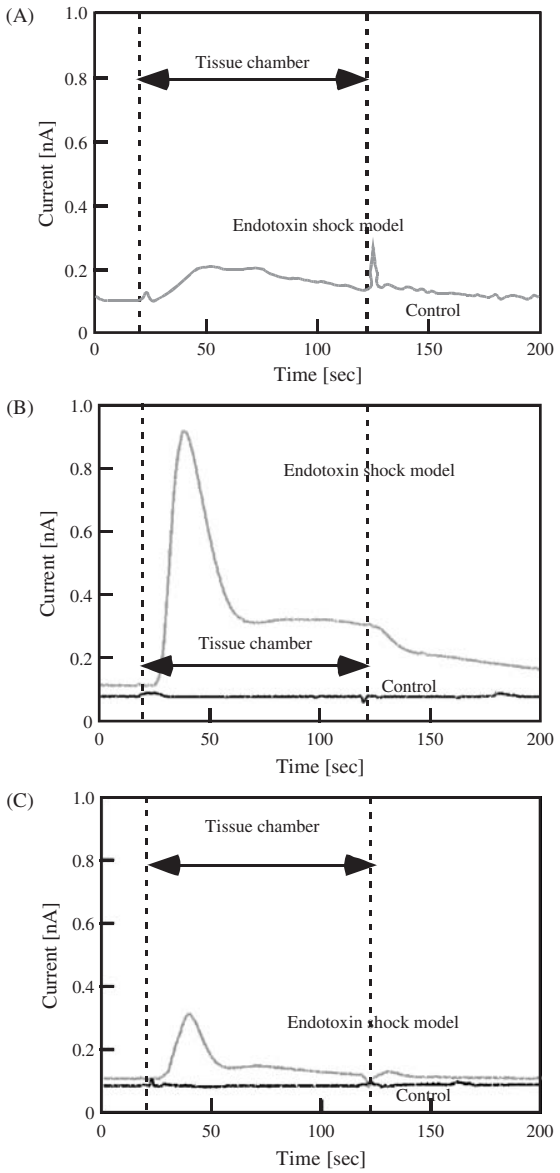

Fig. 12. Time courses of monitored superoxide released from isolated tissues: (A) heart, (B) liver, and (C) kidney.

7. THE FUTURE OF $O_2^{\cdot-}$ SENSORS

Krylow et al. miniaturized a disposable sensor that used a *cyt c*-modified thick-film electrode in the $O_2^{\cdot-}$ sensor, and measured H_2O_2 concentration by changing the applied potential.[74] They used a monolayer screen-printed gold-electrode on a ceramic substrate, which made the working electrode surface approximately three times larger than the geometrical area. Then they electroactively immobilized *cyt c* and measured re-oxidation current of *cyt c* reduced by $O_2^{\cdot-}$ like *cyt c*-based sensors. The sensitivity of this sensor was reported to be increased by a factor of about four compared with a metal-substrate sensor.

The monolayer *cyt c* electrodes are limited by the amount of *cyt c* immobilized on the electrode surface.[75] Beissenhirtz et al. immobilized 2–15 layers in an assembly of *cyt c* and a polyelectrolyte on a gold wire electrode.[75] This sensing mechanism was based on an electron transfer-modified gold electrode on which *cyt c* was immobilized.[56, 58] The best sensitivity for $O_2^{\cdot-}$ produced by hypoxanthine/XOD reaction was gained by a six-layer electrode in their series. Furthermore, thermal treatment at 45 °C for 30 min of the multilayer assembly offered sufficient electrode stability for serial sensor application and storage.

In a simplified approach to electrode preparation, Di et al. developed an SOD immobilized sensor based on a thin silica-PVA sol–gel film on a gold electrode.[76] The direct electron transfer between SOD and gold electrode occurred without any mediators or promoters, which enabled a fast response rate. The measurement mechanism of this sensor was based on the catalytic current of SOD immobilized on the electrode. These sensors would need to be biocompatible for *in vivo* use.

8. CONCLUSIONS

The key developments of $O_2^{\cdot-}$ sensors and the preliminary studies described in this review traces the progression of simple electrodes of coated wire, to carbon or ceramic substrates, micro arrays, and other chip designs. A number of design issues pertain to the next steps in moving beyond the proof-of-concept level if reliable, sensitive and specific simultaneous monitoring of intra- and extracellular $O_2^{\cdot-}$, production in real time *in vivo* is to be achieved. In practical terms, the sensitivity, and storage life of the electrodes must increase significantly. Electrode preparation time must be reduced through kits or mass production of complete electrodes. Further improvements in the self-assembly of multiple or mono-layers of electron-transfer promoters such as cysteine in thin film or thick-film designs could bring reproducible, quantitative applications within reach of researchers in small laboratories. $O_2^{\cdot-}$ sensors can be expected to be reported in basic and wider applications that include clarification of the oxygen-sensing pathway and regulatory relationships, identification of additional SOD family members, and characterization of effects of expression in various species in normal tissues, under disease conditions, and in response to drugs.

Lessons learned from development of the various $O_2^{\cdot-}$ sensors can be applied to other important molecules for other medical purposes such as subcutaneous monitoring. However, the long-term biocompatibility of the implant components remains an important hurdle to overcome.

References and Notes

1. C. A. Gunnett, D. D. Heistad, D. J. Berg, and F. M. Faraci, *Am. J. Physiol. Heart Circ. Physiol.* 279, H1555 (**2000**).
2. Y. Ohara, T. E. Peterson, H. S. Sayegh, R. R. Subramanian, J. N. Wilcox, and D. G. Harrison, *Circulation.* 92, 898 (**1995**).

3. N. N. Orie, W. Zidek, and M. Tepel, *Am. J. Hypertens.* 12, 1169 (**1999**).
4. J.-Z. Sun, X.-L. Tang, S.-W. Park, Y. Qiu, J. F. Turrens, and R. Bolli, *J. Ciln. Invest.* 97, 562 (**1996**).
5. K. Nakazono, N. Watanabe, K. Matsuno, J. Sasaki, T. Sato, and M. Inoue, *Proc. Natl. Acad. Sci.* 88, 10045 (**1991**).
6. Y. Taniyama and K. K. Griendling, *Hypertension* 42, 1075 (**2003**).
7. I. Fridovich, *Ann. NY Acid. Sci.* 893, 13 (**1999**).
8. Y. Ohara, T. E. Peterson, and D. G. Harrison, *J. Clin. Invest.* 91, 2546 (**1993**).
9. G. M. Rubanyi and P. M. Vanhoutte, *Am. J. Physiol. Heart Circ. Physiol.* 250, H822 (**1986**).
10. J. M. McCord and I. Fridovich, *J. Biol. Chem.* 241, 6049 (**1969**).
11. R. A. Weisiger and I. Fridovich, *J. Biol. Chem.* 248, 3582 (**1973**).
12. R. A. Weisiger and I. Fridovich, *J. Biol. Chem.* 248, 4793 (**1973**).
13. Y. Li, T.-T. Huang, E. J. Carlson, S. Melov, P. C. Ursell, J. L. Olson, L. J. Noble, M. P. Yoshimura, C. Berger, P. H. Chan, D. C. Wallace, and C. J. Epstein, *Nat Genet.* 11, 376 (**1995**).
14. S. L. Marklund, *Pro. Natl. Acad. Sci. USA* 79, 7634 (**1982**).
15. S. L. Marklund, *Biochem. J.* 266, 213 (**1990**).
16. S. L. Marklund, E. Hollme, and L. Hellner, *Clin. Chim. Acta.* 126, 41 (**1982**).
17. E. A. Ostrakhovitch and I. B. Afanas'ev, *Biochem. Pharmacol.* 62, 743 (**2001**).
18. P. Pietta, P. Simonetti, C. Gardana, and P. Mauri, *J. Pharm. Biomed. Anal.* 23, 223 (**2000**).
19. F. Nanjo, M. Mori, K. Goto, and Y. Hara, *Biosci. Biotechnol. Biochem.* 63, 1621 (**1999**).
20. T. Nakagawa and T. Yokozawa, *Food Chem. Toxicol.* 40, 1745 (**2002**).
21. P. Simonetti, C. Gardana, and P. Pietta, *J. Agric. Food Chem.* 49, 5964 (**2001**).
22. M. M. Tarpey and I. Fridovich, *Circ Res.* 89, 224 (**2001**).
23. T. Münzel, I. B. Afanas'ev, A. L. Kleschyov, and D. G. Harrison, *Arterioscler Thromb. Vasc. Biol.* 22, 1761 (**2002**).
24. M. M. Tarpey, D. A. Wink, and M. B. Grisham, *Am. J. Physiol. Regul. Integr. Comp. Physiol.* 286, R431 (**2004**).
25. B. Halliwell and M. Whiteman, *Br. J. Pharmacol.* 142, 231 (**2004**).
26. M. J. Green and H. A. O. Hill, *Methods in Enzymology* 105, 3 (**1984**).
27. J. Weaver, P. Tsai, G. L. Cao, L. J. Roman, and G. M. Rosen, *Anal. Biochem.* 320, 141 (**2003**).
28. L. Flohé and F. Ötting, *Methods in Enzymology.* 105, 93 (**1984**).
29. I. B. Afanas'ev, E. A. Ostrakhovitch, E. V. Mikhal'chik, and L. G. Korkina, *Luminescence.* 16, 305 (**2001**).
30. M. M. Tarpey, C. R. White, E. Suarez, G. Richardson, R. Radi, and B. A. Freeman, *Circ Res.* 84, 1203 (**1999**).
31. Y. Kambayashi and K. Ogino, *J. Toxicol. Sci.* 28, 139 (**2003**).
32. H. Gyllenhammar, *J. Immunol. Methods.* 97, 209 (**1987**).
33. Y. Li, H. Zhu, and M. A. Trush, *Biochim. Biophys. Acta.* 1428, 1 (**1999**).
34. Y. Li, H. Zhu, P. Kuppusamy, V. Roubaud, J. L. Zweier, and Michael A. Trush, *J. Biol. Chem.* 273, 2015 (**1998**).
35. M. P. Skatchkov, D. Sperling, U. Hink, A. Mülsch, D. G. Harrison, I. Sindermann, T. Meinertz, and T. Münzel, *Biochem. Biophys. Res. Commun.* 254, 319 (**1999**).
36. I. B. Afanas'ev, E. A. Ostrachovitch, and L. G. Korkina, *Arch. Biochem. Biophys.* 366, 267 (**1999**).
37. J. Vásquez-Vivar, N. Hogg, K. A. Pritchard, Jr., P. Martasek, and B. Kalyanaraman, *FEBS Letters* 403, 127 (**1997**).
38. S. I. Liochev and I. Fridovich, *Arch. Biochem. Biophys.* 337, 115 (**1997**).
39. S. J. Schreiber, D. Megow, A. Raupach, I. V. Victorov, and U. Dirnagl, *Brain Res.* 703, 227 (**1995**).
40. M. A. Trush, M. E. Wilson, and K. Van Dyke, *Methods Enzymol.* 57, 462 (**1978**).
41. S. Ushiroda, Y. Maruyama, and M. Nakano, *Jpn. Heart J.* 38, 91 (**1997**).
42. K. Yamaguchi, D. Uematsu, Y. Itoh, S. Watanabe, and Y. Fukuuchi, *Keio J. Med.* 51, 201 (**2002**).
43. G. Rothe and G. Valet, *J. Leukoc. Biol.* 47, 440 (**1990**).
44. H. Zhao, S. Kalivendi, H. Zhang, J. Joseph, K. Nithipatikom, J. Vásquez-Vivar, and B. Kalyanaraman, *Free Radic. Biol. Med.* 34, 1359 (**2003**).
45. O. Myhre, J. M. Andersen, H. Aarnes, and F. Fonnum, *Biochem. Pharmacol.* 65, 1575 (**2003**).
46. H. Possel, H. Noack, W. Augustin, G. Keilhoff, and G. Wolf, *FEBS Lett.* 416, 175 (**1997**).
47. P. Wang and J. L. Zweier, *J. Biol. Chem.* 271, 29223 (**1996**).
48. M. Dambrova, L. Baumane, I. Kalvinsh, and J. E. S. Wikberg, *Biochem. Biophys. Res. Commun.* 275, 895 (**2000**).
49. H. Zhang, J. Joseph, J. Vasquez-Vivar, H. Karoui, C. Nsanzumuhire, P. Martásek, P. Tordo, and B. Kalyanaraman, *FEBS Letters* 473, 58 (**2000**).
50. C. J. McNeil, K. A. Smith, P. Bellavite, and J. V. Bannister, *Free Rad. Res. Comms.* 7, 89 (**1989**).
51. C. J. McNeil, K. R. Greenough, P. A. Weeks, C. H. Self, and J. M. Cooper, *Free Rad. Res. Comms.* 17, 399 (**1992**).
52. R. H. Fabian, D. S. DeWitt, and T. A. Kent, *J. Cereb. Blood Flow Metab.* 15, 242 (**1995**).
53. R. H. Fabian, J. R. Perez-Polo, and T. A. Kent, *J. Neurosci. Res.* 60, 795 (**2000**).
54. K. Tammeveski, T. T. Tenno, A. A. Mashirin, E. W. Hillhouse, P. Manning, and C. J. McNeil, *Free Rad. Biol. Med.* 25, 973 (**1998**).
55. P. Manning, C. J. McNeil, J. M. Cooper, and E. W. Hillhouse, *Free Rad. Biol. Med.* 24, 1304 (**1998**).
56. B. Ge and F. Lisdat, *Anal. Chim. Acta* 454, 53 (**2002**).
57. R. Büttemeyer, A. W. Philipp, J. W. Mall, B. Ge, F. W. Scheller, and F. Lisdat, *Microsurgery* 22, 108 (**2002**).
58. S. Ignatov, D. Shishniashvili, B. Ge, F. W. Scheller, and F. Lisdat, *Biosens. Bioelectron.* 17, 191 (**2002**).
59. M. K. Beissenhitz, R. C. H. Kwan, K. M. Ko, R. Renneberg, F. W. Scheller, and F. Lisdat, *Phytother. Res.* 18, 149 (**2004**).
60. L. Campanella, G. Favero, and M. Tomassetti, *Anal. Lett.* 32, 2559 (**1999**).
61. L. Campanella, G. Favero, L. Persi, and M. Tomassetti, *J. Pharm. Biomed. Anal.* 23, 69 (**2000**).
62. L. Campanella, G. Favero, L. Persi, and M. Tomassetti, *J. Pharm. Biomed. Anal.* 24, 1055 (**2001**).
63. L. Campanella, A. Bonanni, and M. Tomassetti, *J. Pharm. Biomed. Anal.* 32, 725 (**2003**).
64. L. Campanella, A. Bonanni, G. Favero, and M. Tomassetti, *Anal. Bioanal. Chem.* 375, 1011 (**2003**).
65. B. Ge, F. W. Scheller, and F. Lisdat, *Biosens. Bioelectron.* 18, 295 (**2003**).
66. L. Campanella, L. Persi, and M. Tomassetti, *Sensors and Actuators B* 68, 351 (**2000**).
67. K. Endo, T. Miyasaka, S. Mochizuki, S. Aoyagi, N. Himi, H. Asahara, K. Tsujioka, and K. Sakai, *Sensor and Actuators B* 83, 30 (**2002**).
68. T. Miyasaka, Y. Taniyama, K. Sakai, and Y. Yoshimi, *ASAIO J.* 43, M505 (**1997**).
69. T. Miyasaka, Y. Yoshimi, and K. Sakai, *J. Chem. Eng. Jpn.* 31, 29 (**1998**).
70. S. Aoyagi, Y. Suzuki, K. Sakai, T. Miyasaka, and Y. Yoshimi, *Electrochem.* 69, 251 (**2001**).
71. I. Fridovich, *J. Biol. Chem.* 245, 4053 (**1970**).

72. P. M. Hassoun, F.-S. Yu, C. G. Cote, J. J. Zulueta, R. Sawhney, K. A. Skinner, H. B. Skinner, D. A. Parks, and J. J. Lanzillo, *Am. J. Respir. Crit. Care Med.* 158, 299 **(1998)**.
73. R. P. Brandes, G. Koddenberg, W. Gwinner, D.-Y. Kim, H.-J. Kruse, R. Busse, and A. Mügge, *Hypertension.* 33, 1243 **(1999)**.
74. A. V. Krylow, M. Beissenhirtz, H. Adamzig, F. W. Scheller, and F. Lisdat, *Anal. Bioanal. Chem.* 378, 1327 **(2004)**.
75. M. K. Beissenhitz, F. W. Scheller, and F. Lisdat, *Anal. Chem.* 76, 4665 **(2004)**.
76. J. Di, S. Bi, and M. Zhang, *Biosens. Bioelectron.* 19, 1479 **(2004)**.

SENSOR LETTERS
Vol. 4, 155–159, 2006

Efficient Taste Sensors Made of Bare Metal Electrodes

Carlos E. Borato[1,2], Fábio L. Leite[1,2], Osvaldo N. Oliveira, Jr.[1,*], and Luiz H. C. Mattoso[2]

[1] *Instituto de Física de São Carlos, Universidade de São Paulo, Caixa Postal 369, 13560-970 São Carlos, SP, Brazil*
[2] *EMBRAPA Instrumentação Agropecuária, CP 741, 13560-970, São Carlos, SP, Brazil*

(Received: 22 March 2006. Accepted: 13 April 2006)

In attempts to reduce cost and increase sensitivity of taste sensors we have found out that a novel, inexpensive set of chrome-deposited electrodes may be used in impedance spectroscopy measurements for sensing with great performance. High sensitivity is demonstrated by detecting, reproducibly, μM amounts of NaCl, HCl, sucrose, which represent basic tastes, and Cu^{2+} ions. This high sensitivity can also be used to distinguish complex liquids such as wines. Surprisingly, there was no need to cover the metal electrodes with nanostructured films of organic sensitive materials, which further reduces the cost of the sensing units. This sensitivity is attributed to interface effects between the metal electrodes and the liquid samples, which may be investigated with atomic force spectroscopy as illustrated in this paper.

Keywords: Chrome-Deposited Electrodes, Basic Taste, Heavy Metal, Taste Sensors.

RESEARCH ARTICLE

1. INTRODUCTION

The advent of taste sensors based on impedance spectroscopy with sensing units obtained with nanostructured films has brought considerable advances in terms of sensitivity to detect trace amounts of substances in a solution and the ability to distinguish among complex liquids such as different types of wine, coffee, juices, and milk.[1–4] Among the advantages of this type of taste sensor are no need of a reference electrode and the possibility to analyze non-electrolyte liquids.[5] The main challenge now is to evolve from prototypes to costly-effective industrial production, which is being pursued in our group. A number of steps may be taken in order to optimize the sensor performance and reduce costs, including the search for materials that bring higher performances at lower costs, tests of reproducibility and robustness of the sensing units, and cheaper systems for measuring the electrical response. In this communication we show that an inexpensive array of chrome-deposited electrodes can be used to detect low amounts (μM) of substances representing basic tastes and a heavy metal. This sensitivity also makes it possible to distinguish between different wines.

2. EXPERIMENTAL DETAILS

The electrodes were obtained by electrochemical deposition of chrome on a glass slide, according to a pre-printed pattern of 5 pairs of fingers with dimensions of $27.25 \times 2.40 \times 0.04$ mm, separated by 0.1 mm from each other. Five units of such electrodes—with no deposited film on top of the chrome—were assembled on a fiberglass slide to form an array. The electrodes were connected to the measuring apparatus through a Card edge connector. The array was placed onto a small trough in which the liquid sample is placed. Figure 1 shows the sensor array and the trough to hold the liquid samples. The solutions of NaCl, HCl, and sucrose were prepared from a stock solution of 50×10^{-3} mol/L in distilled water, from which dilutions were made to achieve concentrations of 20, 10, 5, 1×10^{-3} mol/L and 10^{-6} mol/L. Measurements were also performed with solutions of $CuSO_4 \cdot 5H_2O$ in Milli-Q water at various concentrations, as will be presented in the next Section. The red and white wines were provided by Brazilian producers Embrapa, Miolo, and Salton, and used as received. Impedance measurements were carried out with a Solartron 1260A impedance/gain phase analyzer at 200, 400, 600, 800, and 1 KHz, and bias voltage of 50 mV, with the electrodes being immersed into the liquid samples. The array remained immersed for 20 minutes in each of the solution before the measurements, carried out at 25 °C. After each measurement the units were washed with distilled water. Principal components analysis was employed to analyze the data obtained from the various sensing units for each liquid studied, using MATLAB version 6.1 (for a detailed description of PCA analysis see Ref. [6]).

*Corresponding author; E-mail: chu@if.sc.usp.br

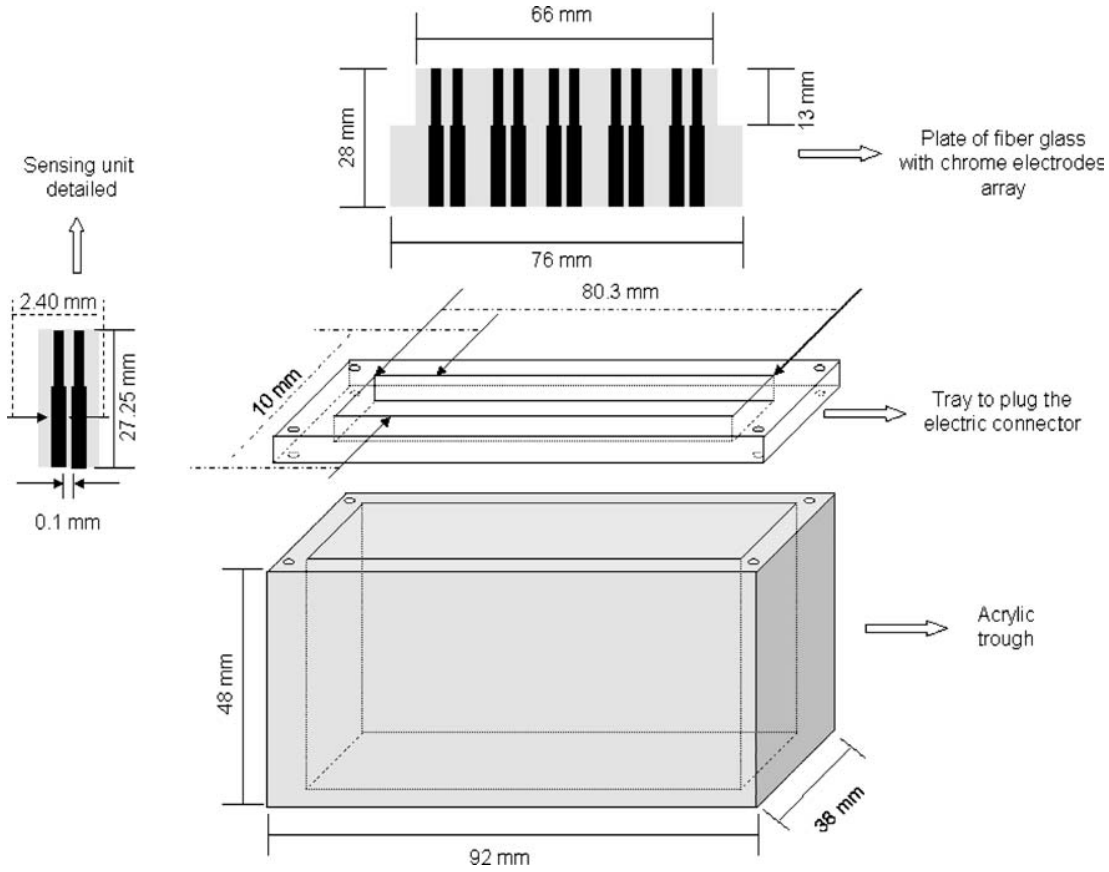

Fig. 1. Detailed diagram of the sensing units of electrodeposited chrome and the trough made to hold the liquid sample and insert the sensor array.

3. RESULTS AND DISCUSSION

The sensitivity to μM concentrations of the basic tastes, namely sweet, salty, and sour is illustrated in PCA plots of Figure 2. For these measurements, an array of 5 sensors was employed, none of which had a film adsorbed on them; they were made of bare metal. The data were extracted from impedance spectroscopy measurements, and refer to the capacitance of the system at 200 Hz. For all frequencies studied, viz. 200, 400, 600, 800, and 1000 Hz, it is possible to distinguish between the different tastes. However, only at low frequencies (see results for 200 Hz in Fig. 2) is it possible to distinguish solutions at the μM concentrations from pure water. The reason for the higher sensitivity at 200 Hz is associated with the physical phenomena governing the electrical response. Taylor and MacDonald[7] showed that at higher frequencies (>10 kHz), the response is dominated by the electrode capacitance. At 1 kHz, the response from the film dominates, whereas at 100–200 Hz the double-layer governs the response. Because the high sensitivity appears to be associated with surface phenomena, changes in the double layer are expected to be more prone to occur when the liquid is modified by trace amounts of substances.

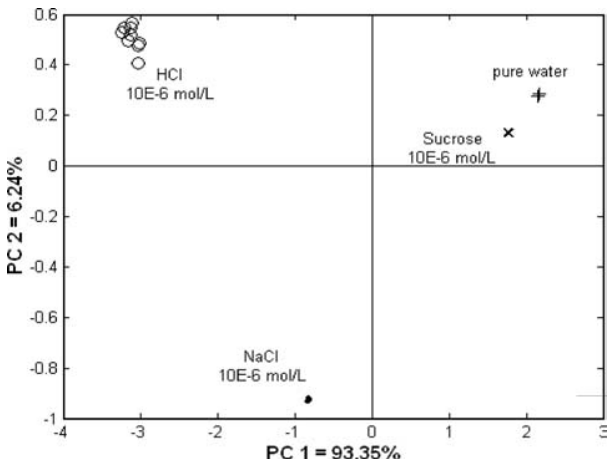

Fig. 2. PCA plots for sweet ($\times$), salt ($\bullet$), sour ($\circ$), and pure water ($+$) substances at $f = 200$ Hz.

It is surprising that the array could be made of sensing units that were nominally identical. (By "nominally identical" we mean that the chrome electrodes were produced with the same experimental procedure of electrodeposition. However, with this method the electrodes are not very homogeneous, varying particularly in morphology or oxide

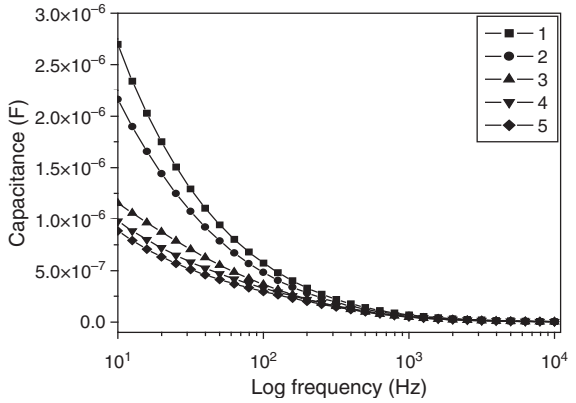

Fig. 3. Capacitance versus frequency plot showing that each of the sensing units has a characteristic electric curve. NaCl solution of $C = 5 \times 10^{-3}$ mol/L. The symbols corresponding to the sensing units 1 through 5 are given in the inset.

layer coating the metal). Therefore, because the electrical response depends on the interface effects, distinct responses were obtained for these nominally identical electrodes, as depicted in Figure 3. Cross-sensitivity can then be achieved with electrodes of the same metal, but with different morphologies. The capacitance decreases with increasing frequencies, as illustrated in Figure 3 for NaCl, and is higher for higher concentrations of NaCl, KCl, and HCl while for sucrose the capacitance decreases with increasing concentrations (results not shown). For each of the tastants, a pattern is observed regardless of the concentration. Also observed is a large difference in capacitance for sucrose in comparison to the other substances because sucrose solution contains almost no ions (it is not an electrolyte).

In order to prove that the cross-sensitivity obtained with bare metal electrodes could be useful in distinguishing samples with low detection limits, we performed a series of experiments (including control experiments) varying the substances. For instance, the distinguishing ability of the sensor array for concentrations at the μM level was tested for $CuSO_4$, with measurements taken on different days and with samples prepared in different days. The results shown in Figure 4 illustrate dispersion in the measurements for pure water if the time for equilibration differs, though it is clear that the samples containing $CuSO_4$ could be distinguished. We felt, however, that we had to check whether the differences in the pure water samples could not jeopardize the conclusions drawn so far, and decided to perform a number of control experiments. The results of these control experiments may be summarized as follows.

The mere manipulation of water in changing from one flask to the other may generate pure water samples that are distinguishable in the electrical measurements, probably because impurities are non-deliberately included. The electrical response may also vary with time due to ageing affects (e.g., from oxygen uptake). In fact, the electrical

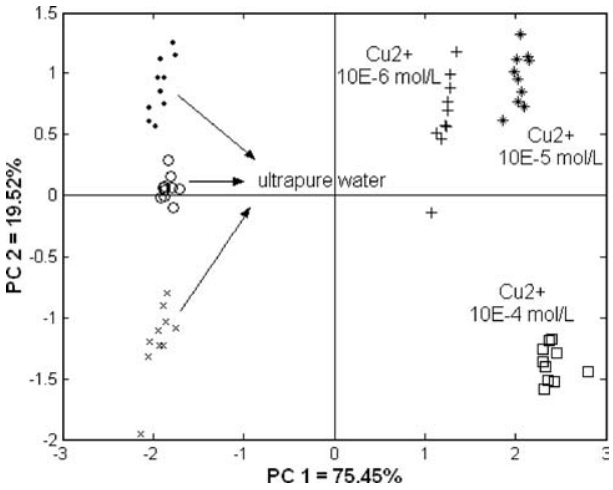

Fig. 4. PCA plot showing the addition of amounts of Cu^{2+} in ultrapure water: (•), (○), (×) pure water, (+) 10^{-6} mol/L of Cu^{2+}, (∗) 10^{-5} mol/L of Cu^{2+} and (□) 10^{-4} mol/L of Cu^{2+}.

measurements serve as excellent control tool for the water purity, similarly to what Taylor et al.[8] suggested for lateral conductance in Langmuir monolayers, which was found to be affected strongly by trace amounts of impurities in the water subphase. In order to be sure that we could detect small amounts of tastants or ions deliberately introduced in the liquid samples, we performed the experiments depicted in Figure 5. In one set, measurements were taken with a pure water sample within intervals of 30 min. For the 31st measurement, pure water was added to the sample (i.e., no impurity was deliberately introduced, but the sample suffered manipulation). A change in capacitance could be measured, but this was negligible if the scales used were chosen to accommodate the data for the incorporation of 1 μM of $CuSO_4$, which was done in the other set of experiments. The results of the latter are shown in the upper curve, indicating that the measured capacitance changed more appreciably when adding the Cu^{2+} ions. If a lower concentration of $CuSO_4$ was used in the measurement, then it was difficult to distinguish between this solution or a manipulated sample of pure water (with addition of

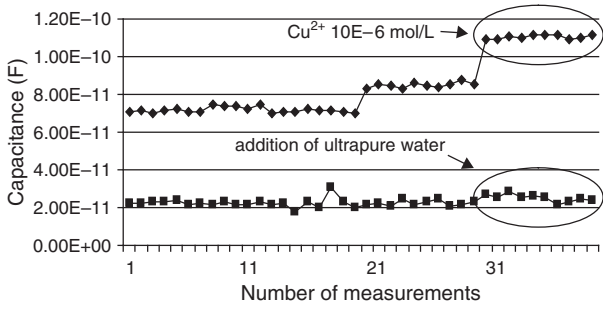

Fig. 5. Comparison among addition of 10^{-6} mol/L of Cu^{2+} (◆) and ultrapure water (■) in ultrapure water. Note in the circled regions that addition of 10^{-6} mol/L of Cu^{2+} can be distinguished from the control measurements, while the addition of pure water cannot.

RESEARCH ARTICLE

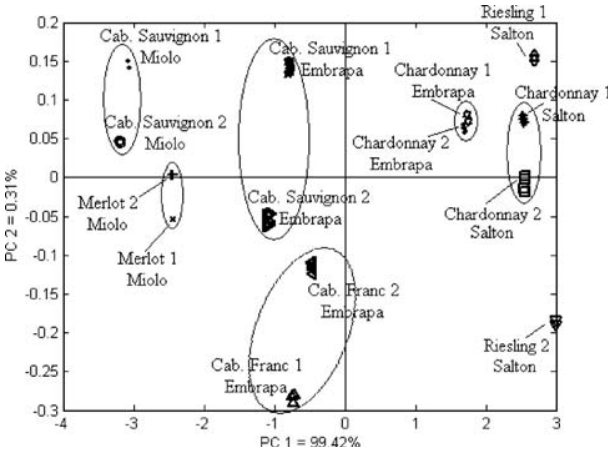

Fig. 6. PCA plots for capacitance data at 1 kHz for red wine samples of Cabernet Sauvignon Miolo 2000, Merlot Miolo 2000, Cabernet Sauvignon Embrapa 1999, Cabernet Franc Embrapa 1999, in addition to white wines Chardonnay Salton 1999, Chardonnay Embrapa 1999, Riesling Salton 1998. In each case measurements were made with 2 bottles, named 1 and 2. The results indicate that the sensor is capable of distinguishing wines of different grapes, and wines from the same grape but different producers (e.g., Embrapa and Miolo for Cabernet Sauvignon).

more pure water). From these results we infer that incorporation of $CuSO_4$ in concentrations below 1 μM could not be distinguished from the dispersion in the data due to mere manipulation of water samples, but the efficacy of the sensor array was demonstrated for concentrations equal to or above 1 μM.

Analogously to previous works,[2,9] we exploited the sensitivity of the taste sensors to distinguish among wines. The PCA plots in Figure 6 indicate that the sensor array is able to distinguish between wines of the same brand but different grapes, namely Cabernet Sauvignon and Merlot from the company Miolo (Brazil), and wines of the same grape but different produces (e.g., Cabernet Sauvignon from Miolo and Embrapa).

The explanation for the high sensitivity of the sensor arrays (electronic tongues) may lie on the strong dependence of electrical properties of interface systems on the liquid environment next to the interface. This is actually similar to the findings by Taylor et al.,[8] who pointed out that bulk measurements were not sufficient to detect the level of impurities in the water that surface measurements could do. Indeed, with force spectroscopy measurements carried out with an atomic force microscope (AFM) we show that water is aged upon exposure to air. Figure 7a is typical force curve obtained in water on mica surface (pH $\sim$ 7), which shows the presence of van der Waals interactions for short times (<1 h) (see more details on force spectroscopy in Ref. [10]). We employed a mica substrate in this experiment, rather than the chrome electrodes, because at the pH of water the appearance of the double-layer force is readily appreciated, being illustrative of the importance of interface effects.

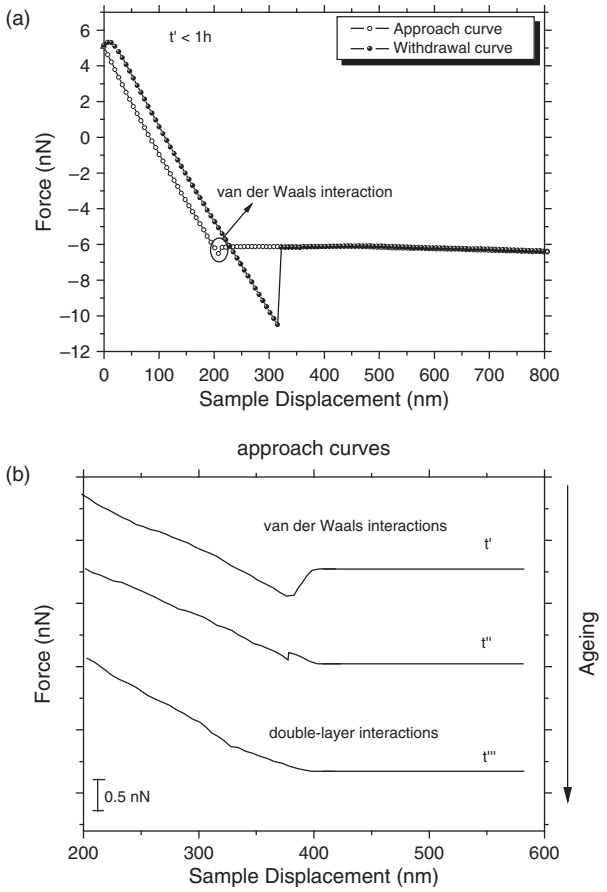

Fig. 7. (a) Typical force curve for a AFM tip and mica sample immersed in water and (b) schema (approach curves) showing water ageing for various periods of time (increasing in the direction $t' < t'' < t'''$). The difference between each of two times, $t' - t''$ or $t'' - t'''$ is 2 h.

The presence of impurities in the cell is found to affect the force curves. Here we employed pure water to investigate water ageing during several times, which are significantly altered as shown schematically in Figure 7b. For short periods, the curve displays a minimum with the distance between the tip of silicon nitrite ($\varepsilon_{\text{tip}} = 7.4$, $k_c = 0.03$ N m^{-1}) and a flat mica surface ($\varepsilon_{\text{mica}} = 5.4$),[11] which indicates the predominance of attractive van der Waals interactions. For longer times, repulsive double-layer forces dominate until the force curve is practically purely repulsive (for t'''). The double-layer contribution is repulsive for the following reason: It is energetically favorable for a surface charge to be surrounded by a medium with large dielectric constant like water. If the tip approaches the double layer region it replaces the water. Since the tip material has a lower dielectric constant than water, the situation is now energetically unfavorable and the tip is repelled by the double layer charge.[12] Ageing of the water is accompanied by a change to lower pH values, which then increases the charge of the silicon nitrite tip (whose isoelectric point is at pH 6.3[12]), whereas mica is negatively charged. The net result is an increase in the repulsive, double-layer force.

4. CONCLUSIONS

The results from atomic force spectroscopy indicate clearly that a very thin layer of water adjacent to the metallic substrates is affected when small changes occur in the liquid, as was the case of the ageing of water. This may be behind the high sensitivity of the sensing units, for interface phenomena—particularly those associated with double-layers—dominate the electrical response of the sensor at the frequency (200 Hz) where sensitivity was maximum. It is also consistent with the finding that sensitivity was decreased when nanostructured films deposited onto the electrodes were replaced by cast, thicker films.[13] The surprising feature of the sensing units used here was the absence of any sensitive organic material. It appears that, being a predominantly interface effect, the changes in morphology due to irregularities in the chrome deposition are sufficient to lead to distinct electrical responses that can be exploited to produce as a characteristic fingerprint of a given liquid in a sensor array. The sensitivity toward basic tastes of the sensor array presented here is similar to that obtained with interdigitated gold electrodes covered with nanostructured films,[13] while the distinguishing ability for different wines also compares with previous works.[2, 9, 14] The obvious advantage of the array made with bare metal electrodes is the simplicity and low cost. It should be stressed, nevertheless, that state-of-the-art sensors are expected to include coating materials that may also respond specifically to the analyte, as indicated by arrays containing immobilized enzymes.[15]

Acknowledgments: This work was supported by FAPESP, CNPq, Rede Nanobiotec256 and CT-Hidro/MCT (Brazil). The authors are grateful to Dr. Wilson T. Lopes for useful discussions.

References and Notes

1. B. Lawton and R. Pethig, *Measure. Sci. Technol.* 4, 38 (**1993**).
2. A. Riul, Jr., H. C. Souza, R. R. Malmegrim, D. S. Santos, Jr., A. C. P. L. F. Carvalho, F. J. Fonseca, O. N. Oliveira, Jr., and L. H. C. Mattoso, *Sens. Actuators B Chem* 98, 77 (**2004**).
3. C. E. Borato, A. Riul, Jr., M. Ferreira, O. N. Oliveira, Jr., and L. H. C. Mattoso, *Instrumentation Science and Technology* 32, 21 (**2004**).
4. A. Legin, A. Rudnitskaya, Y. Vlasov, C. Di Natale, F. Davide, and A. D'Amico, *Sens. Actuators B Chem.* 44, 291 (**1997**).
5. A. Riul, Jr., R. R. Malmegrim, F. J. Fonseca, and L. H. C. Mattoso, *Biosens. Bioelectron.* 18, 1365 (**2003**).
6. K. R. Beebe, R. J. Peel, and M. B. Seasholtz, Chemometrics: A Pratical Guide, John Wiley and Sons, New York (**1998**).
7. D. M. Taylor and A. G. MacDonald, *J. Phys. D.-Appl. Phys.* 20, 1277 (**1987**).
8. D. M. Taylor, O. N. Oliveira, Jr., and H. Morgan, *Thin Solid Films* 173, L141 (**1989**).
9. A. Riul, Jr., D. S. Dos Santos, Jr., K. Wohnrath, R. Di Thommazo, A. A. C. P. L. F. Carvalho, F. J. Fonseca, O. N. Oliveira, Jr., D. M. Taylor, and L. H. C. Mattoso, *Langmuir* 18, 239 (**2002**).
10. F. L. Leite and P. S. P. Herrmann, *J. Adhesion Sci. Technol.* 19, 365 (**2005**).
11. T. J. Senden and C. J. Drummnond, *Colloids Surf. A* 94, 29 (**1995**).
12. E. F. De Souza, G. Ceotto, and O. Teschke, *J. Mol. Catalysis A* 167, 235 (**2001**).
13. M. Ferreira, A. Riul, Jr., K. Wohnrath, F. J. Fonseca, O. N. Oliveira, Jr., and L. H. C. Mattoso, *Anal. Chem.* 75, 953 (**2003**).
14. A. Guadarrama, J. A. Fernández, M. Íñiguez, J. Souto, and J. A. de Saja, *Analytica Chimica Acta* 411, 193 (**2000**).
15. V. Zucolotto, A. P. A. Pinto, T. Tumolo, M. L. Moraes, M. S. Baptista, A. Riul, Jr., A. P. U. Araújo, and O. N. Oliveira, Jr., *Biosens. Bioelectron.* 21, 1320 (**2006**).

SENSOR LETTERS
Vol. 4, 160–164, 2006

RESEARCH ARTICLE

Kinetic Assay of Trypsin with a Wireless Magnetoelastic Sensor

Shihui Wu[1], Qingyun Cai[1,*], and Craig A. Grimes[2]

[1] *Department of Chemistry, State Key Laboratory of Chemo/Biosensing and Chemometrics, Hunan University, Changsha 410082, P. R. China*
[2] *Department of Electrical Engineering, and Department of Materials Science and Engineering, The Pennsylvania State University, University Park, Pennsylvania 16802, USA*

(Received: 2 February 2006. Accepted: 15 February 2006)

A wireless magnetoelastic trypsin sensor is fabricated by first coating a magnetoelastic ribbon-like sensor with a pH-sensitive polymer and then upon it a layer of trypsin. In response to an externally applied time-varying magnetic field, the magnetoelastic sensor mechanically vibrates at a characteristic frequency that is inversely dependent upon the mass of the attached film. As the magnetoelastic sensor is magnetostrictive, the mechanical vibrations of the sensor launch magnetic flux that can be detected remotely from the sensor using a pickup coil. The trypsin-catalyzed hydrolysis of N-α-benzoyl-L-arginine ethyl ester (BAEE) decreases the ambient pH, resulting in the pH-responsive polymer shrinking, and consequently the resonance frequency of the sensor increasing due to the decreased mass loading. The optimum pH and temperature are investigated. The kinetic parameters of both the immobilized and free trypsin are measured. Immobilization of trypsin resulted in the enzyme activity decreasing by about 50%. The magnetoelastic sensor demonstrates a linear shift in resonance frequency with trypsin concentration between 24 U/ml and 360 U/ml with a trypsin detection limit of 24 U/ml, and can be used to detect the substrate BAEE ranging from 0.4 mM to1.5 mM.

Keywords: Trypsin, Enzyme, Remote Sensor, Magnetoelastic Biosensor.

1. INTRODUCTION

Trypsin is a widely used pancreatic serine protease, commonly used for protein cleavage because of its high specificity and ability to digest insoluble or adsorbed protein. Trypsin cleaves peptide bonds at the carboxylate terminal side of lysine and arginine residues. Much attention has been paid to proteases in relation to bacterial identification.[1–3] Protease in serum or other body fluids provides important information on various pathological conditions, particularly in the diagnosis of human pancreatic diseases.[4] The detection and immobilization of trypsin are of great interests since trypsin can not be easily retrieved from the reaction systems.

Immobilized trypsin are widely employed in the field of food and clinical testing industries, such as the electrochemical trypsin sensors for the rapid and quantitative measurement of protein solution,[5,6] the analysis of enzyme inhibitors[7] and as microreactors for peptide mapping.[8] A variety approaches have been developed for trypsin immobilization: trypsin covalently immobilized on epoxy-modified silica monolithic support with a single reaction step,[9] poroszyme immobilized trypsin cartridges,[10] and trypsin-encapsulated sol–gel,[11,12] to cite but a few examples. Several methods have been proposed for the kinetic detection of trypsin, such as capillary electrophoresis (CE),[8] fluorimetry,[13] surface acoustic wave-impedance sensing analysis,[14] electrochemical assay of trypsin with protamine as substrate and polymer membrane as sensing layer[15,16] and immunoradiometric assay using two monoclonal antibodies directed to human trypsin 1 for the measuring of trypsin (ogen) in biological fluids.[17] These methods differ markedly in sensitivity.

In this work a low cost, easily fabricated, wireless magnetoelastic trypsin sensor was fabricated and used for the kinetic detection of trypsin. In a time-varying magnetic field, magnetoelastic materials efficiently translate magnetic to mechanical energies, so the magnetoelastic ribbon longitudinally vibrates at a fundamental characteristic resonance frequency f_r that inversely depends on the sensor

*Corresponding author; E-mail: qycai0001@hnu.cn

 1546-198X/2006/4/160/005 doi:10.1166/sl.2006.010

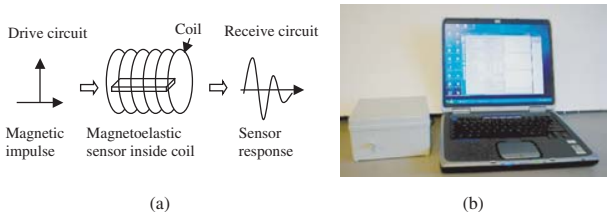

Fig. 1. Schematic showing operation of the wireless magnetoelastic sensor (a) and the magnetoelastic sensor-reader box (b, on left) connected to a portable computer via a RS232 port. The computer interface allows for user-control of measurement parameters, data display, and data storage.

length L. With sensor width and thickness given by: much smaller than length Young's modulus E, and density ρ[18] the resonance frequency is

$$f_r = \sqrt{\frac{E}{\rho}}\frac{1}{2L} \tag{1}$$

A small mass load Δm evenly deposited on a sensor of mass m_0 shifts the measured resonant frequency by:[18]

$$\Delta f = -f_r\frac{\Delta m}{2m_0} \tag{2}$$

The frequency shift is downward with increasing mass. Figure 1 illustrates the operating principle of the magnetoelastic sensor. A magnetic field is used to excite the sensor, causing it to mechanically vibrate at a resonance frequency which shifts in response to mass loading.[19, 20] The mechanical vibrations of the magnetostrictive material, in turn, generate a magnetic flux that can be remotely detected using a simple pick-up coil. A frequency counting technique, previously described,[21] implanted by use of micro-processor based electronics is employed to determine the resonance frequency of the magnetoelastic sensor. No physical connections between the sensor and the detection system are required for signal telemetry, nor is precise alignment necessary per optical telemetry systems The facile wireless capabilities of the magnetoelastic sensor platform makes it a powerful tool for *in situ* and *in vivo* analyses. Published applications include glucose, microbial biosensors[22, 23] and blood coagulation monitoring.[24]

The trypsin biosensor in this paper is fabricated by first coating the magnetoelastic sensor with a pH-sensitive polymer and then upon it a layer of trypsin. The trypsin catalyzed hydrolysis of BAEE results in the formation of H^+ which cause the pH responsive polymer to shrink and, in turn, consequently increase the resonance frequency due to the decreased sensor mass load. The sensor transduction signal is derived from the polymer mass difference between its relatively shrunken state in acidic solution and relatively swollen state in alkaline solution. In alkaline solution, the polymer is electrically charged due to acrylic acid dissociation and additional swelling arises from the osmotic pressure exerted by the charged carboxylic group and its mobile counterions.[25] Water molecules enter the polymer to lower the concentration of network ions until an equilibrium of osmotic pressure is achieved both inside and outside the polymer.

The effect of pH and temperature on the enzymatic activity of trypsin were investigated with kinetic parameters (the Michaelis-Menten constant, K_m, and the maximum initial rate V_{max}) estimated by using the Lineweaver-Burk plot.[26] As the immobilization process generally causes a decrease in enzyme activity that is a key factor while trypsin is used as microreactors for peptide mapping, the effect of immobilization on the trypsin activity was investigated. Using the proposed sensor the enzymatic hydrolysis process can be wirelessly monitored.

2. EXPERIMENTAL DETAILS

2.1. Materials

Trypsin (EC3.4.21.4, 1000∼1500 BAEE units/mg), bovine serum albumin (BSA) were obtained from Sigma Co., *N*-α-Benzoyl-L-arginine ethyl ester hydrochloride(BAEE), glutaric dialdehyde (25 wt% in water) were purchased form Sinopharm Chemical Reagent Co., Ltd. (China), Acrylic acid, poly (ethylene glycol) diacrylate (PEGD), and isooctyl acrylate were purchased from Aldrich (Milwaukee, WI) and the inhibitor, monomethyl ether hydroquinone was removed using an inhibitor remover disposable column (Aldrich) prior to use. 2,2′-Azobis(isobutyronitrile) (AIBN), dimethylaminopropyl-3-ethylcarbodiimide (EDC), and *N*-hydroxysuccinimide (NHS) were purchased from Aldrich and used as received. Bayhydrol 110, an anionic dispersion of an aliphatic polyester urethane resin in water/*N*-methyl-2-pyrrolidone solution (50% w/v) was purchased from Bayer Corp. (Pittsburgh, PA). Deionized and distilled water were used throughout the experiment. Trypsin and BAEE solution were freshly prepared before use. A 28-μm-thick ribbon of Metglas alloy 2826 MB, alloy composition $Fe_{40}Ni_{38}Mo_4B_{18}$, was used as received from Honeywell Corp. The sensors, 20 mm × 6 mm × 28 μm rectangles, were cut from the ribbon. The resonance frequency of an uncoated sensor in air is approximately 105 kHz.

2.2. Sensor Fabrication

The pH-sensitive polymer is a copolymer synthesized by free radical copolymerization of acrylic acid and isooctylacrylate in dimethylformamide, as described in Ref. [22]. The magnetoelastic sensors were ultrasonically cleaned in Micro-Cleaning solution, followed by a water and acetone rinse, and then dried in a stream of nitrogen. About 10 μl Bayhydrol 110 was applied to both sides of the cleaned sensors by dip-coating. The polyurethane-coated sensors were dried in air and then heated at 150 °C for 2 h to form a robust protective membrane, which offers a NH group for binding the pH-sensitive polymer and protects the iron-rich magnetoelastic substrate from corrosion.

RESEARCH ARTICLE

The polyurethane-protected sensor was then coated with 12 μl of 23 g/l pH-sensitive polymer in ethanol, which contains 0.46 g/l EDC and 0.38 g/l NHS. The polymer coated sensors were dried in air and then heated in a vacuum at 120 °C to form the amide bond between the pH-sensitive polymer and polyurethane. While the pH-sensitive polymer-coated sensor can be used to detect free trypsin activity, in this work it was further coated to achieve the working trypsin biosensor. The pH-polymer coated sensor was dipped in 0.02% EDC and NHS solution in water, rinsed with water, and upon it was applied 10 μl of pre-crosslinked trypsin solution, containing 19.2 g/l trypsin, 12.5 g/l BSA, and 0.1% glutaric dialdehyde in water, on both sides. The sensor was then placed in a refrigerator (4 °C) for over 20 h to allow the cross-linking reaction to proceed, as trypsin can undergo autolysis and lose its activity. Unreacted trypsin was removed by rinsing the sensor with PBS buffer. The as-prepared sensor was then dried in air at room temperature and stored at 4 °C.

2.3. Measurement

Prior to use the functionalized sensor was immersed in 0.05 M pH 7.0 PBS buffer for 20 min to wet the polymer, which resulted in a 100 Hz drop in resonance frequency. The wetted sensor was immersed in a small vial that fit into the magnetoelastic sensor reader box, containing 0.005 M phosphate buffer solution (containing 10 mM NaCl) and incubated at 25 °C for about 10 min to stabilize the reaction response. This step is necessary since increasing salt concentration results in the pH polymer shrinking due to osmotic pressure.[22] As an electrolyte, the substrate BAEE can cause a small response even in the absence of trypsin. Blank experiments without trypsin indicate that 1 mM BAEE can cause a frequency increase of about 80 Hz. Therefore in this work 10 mM NaCl was added as the supporting electrolyte to stabilize any osmotic effect. Finally 10 μl BAEE solution was added to the detection cell and the resonant frequency recorded as a function of time with a magnetoelastic sensor reader.[27]

3. RESULTS AND DISCUSSION

3.1. Sensor Response Profiles

The hydrolysis of BAEE produces H^+, resulting in shrinking of the pH responsive polymer and, in turn, increasing the resonance frequency due to the decrease in sensor mass loading. A linear shift in frequency was observed between pH 4.0 and 9.0 with a slope of 250 Hz/pH. Figure 2 shows the frequency shift when BAEE is hydrolyzed by the immobilized trypsin. The frequency shift rate, $\Delta F/\Delta t$ in Hz/min, over the first 4 min is used to express the enzymatic hydrolysis rate, since the trypsin-catalyzed hydrolysis rate was relatively constant over the first 4 min. It takes about 10 min to complete the hydrolysis reaction; the frequency shift within the first 10 min is also recorded to characterize the enzyme activity.

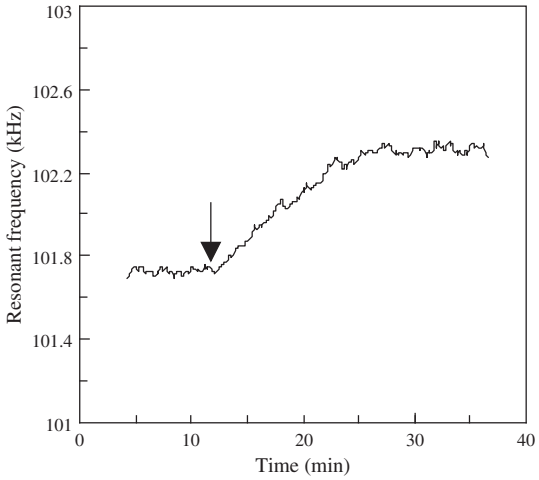

Fig. 2. Typical response curves of magnetoelastic sensor during the enzymatic hydrolysis of BAEE at a concentration of 1 mM. (the down arrow refers to addition of BAEE).

3.2. The Effect of Reaction Time on Sensor Sensitivity

In the sensor fabrication process trypsin was chemically bonded on BSA through glutaric dialdehyde, and BSA was then bonded to the pH polymer through amide bond. Trypsin, BSA, and glutaric dialdehyde were first mixed in water in a glass vial to start the cross-linking reaction. As trypsin can undergo autolysis and lose its activity, the cross-linking reaction was proceeded at 4 °C within a refrigerator. When the reaction time is less than half an hour, little responses were observed due to inadequate trypsin immobilization; when the reaction time is about an hour, the sensors exhibit good sensitivity, but are unstable, the sensitivity declined fast with usage times; when the reaction time is more than 20 h, stable and good sensitivity were obtained. In this work the reaction time for cross-linking was 20 h. However longer reaction periods could cause excess cross-linking reducing the enzyme activity.

3.3. The Effect of pH and Temperature

Figure 3 shows the pH-dependent trypsin activity, determined by the frequency shift during the first 10 min upon addition of one milliliter of 1 mM BAEE solution that was hydrolyzed by the immobilized trypsin on the magnetoelatic sensor. The tested pH value ranged from 6.5 to 8.8. The maximum response (ΔF) appears with a pH of approximately 7.7. The optimum temperature for trypsin was also investigated under the same experimental conditions. Figure 4 shows that trypsin has an activity maximum near 25 °C. So the succeeding experiments were carried out under pH 7.7 and 25 °C.

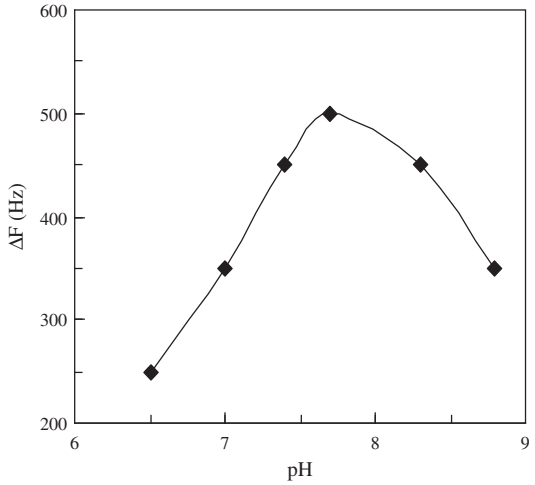

Fig. 3. Effect of pH on trypsin activity at 25 °C.

3.4. The Effect of Immobilization on the Trypsin Activity

The effect of the immobilization on the trypsin activity was investigated by measuring the kinetic parameters of both the immobilized and the free trypsin using the Lineweaver-Burk equation:[26]

$$\frac{1}{V} = \frac{K_m}{V_{\max}} \times \frac{1}{[S]} + \frac{1}{V_{\max}} \tag{3}$$

Where V and $V_{\max}$ are the initial hydrolysis rate and the maximum hydrolysis rate in Hz/min, respectively, K_m is the Michaelis-Menten constant and $[S]$ the BAEE concentration in mM.

The initial hydrolysis rate (V) was obtained by linear fitting the ΔF-t data within the first 4 min. As shown in Figure 5, $1/V$ is linear to $1/[S]$ for both the immobilized and free trypsin in the investigated BAEE concentrations of $0.4 \sim 1.5$ mM. The determined kinetic parameters are: $K_m = 9$ mM, $V_{\max} = -833.3$ Hz/min ($n = 6$, $r = 0.997$) for immobilized trypsin; and $K_m = 4.5$ mM, $V_{\max} = -270.3$ Hz/min ($n = 6$, $r = 0.996$), for free trypsin. The higher Michaelis-Menten constant value of the immobilized trypsin indicates that the immobilization reduces trypsin activity by about 50%.

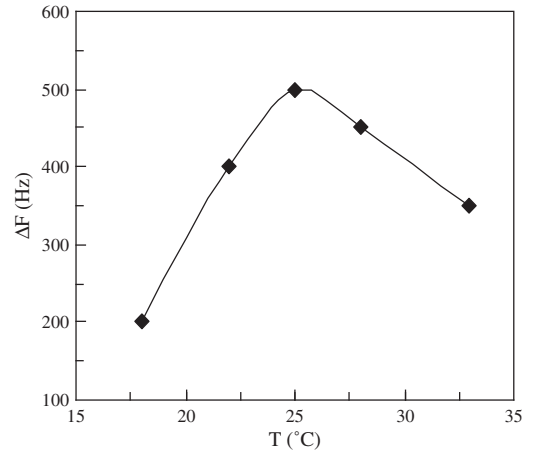

Fig. 4. Effect of temperature on trypsin activity at pH 7.7.

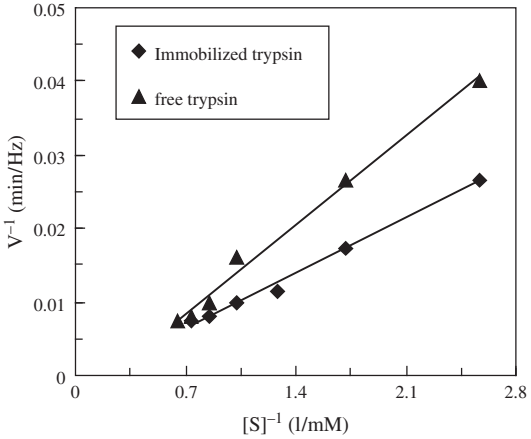

Fig. 5. The dependence of the reciprocal of enzymatic hydrolysis rate on the reciprocal of concentration of BAEE (25 °C, pH 7.7).

3.5. Detection of Trypsin and BAEE

The magnetoelastic sensor response to trypsin ranging from 24–720 U/ml was investigated in this work. Frequency shift rates, $\Delta F/\Delta t$ in Hz/min, over the first 4 min is linear to trypsin activity in solution over the range of 24–360 U/ml, as shown in Figure 6. The detection sensitivity for trypsin of the magnetoelatic sensor is more sensitive than the colorimetric titration method,[28] which is based on the measurement of *p*-nitrophenol released by the irreversible reaction of trypsin with specific active cite of the titrant *p*-nitrophenyl-*p*-guanidinobenzoate (500–25,000 U/ml); comparative to electrode methods (10–200 U/ml[15] and 5.4–108 U/ml[16]), but less sensitive than surface

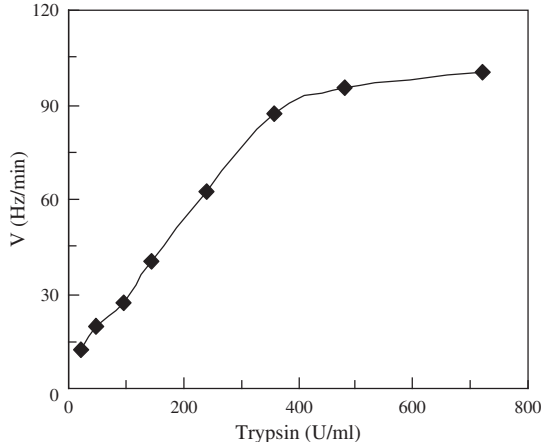

Fig. 6. A calibration curve for determination of trypsin activity. The hydrolysis rates (V) were estimated by measuring the frequency increase within the first 4 min caused from the hydrolysis of 1 mM BAEE under pH 7.7 and 25 °C.

RESEARCH ARTICLE

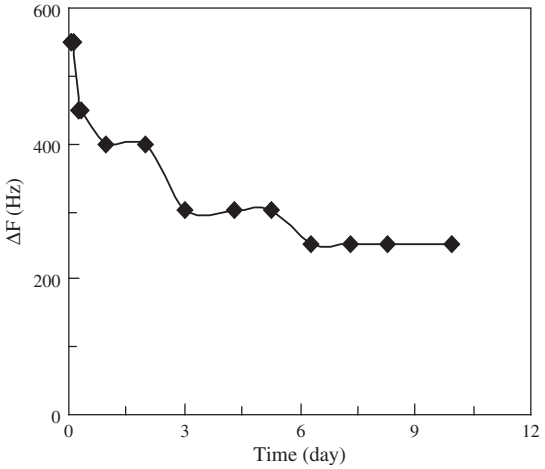

Fig. 7. The long-term stability by measuring the frequency shift (ΔF) within the first 10 min caused from the hydrolysis of 1 mM BAEE under pH 7.7 and 25 °C.

acoustic wave sensor[14] (0.3U/ml). The magnetoelastic sensor, however, can be used for wireless and remote detection, which is particularly useful for *in situ* clinical assay.

BAEE in solution was detected using the trypsin-immobilized magnetoelastic sensor. Linear response was observed in the concentration range of 0.4–1.5 mM.

The long-term stability of the trypsin sensor was tested by repeatedly measuring the frequency shift within the first 10 min (ΔF) resulted from the trypsin-catalyzed hydrolysis of 1 mM BAEE under pH 7.7 and 25 °C. As shown in Figure 7, the sensor response decreased rapidly in the first three days and then became stable. The sensor sensitivity was reduced by 33% in the first 3 days, and 50% over the first 5 days primarily due to the trypsin dissolving. sThe relative stability in the following days indicates that the immobilized trypsin is stable.

4. CONCLUSIONS

A wireless remote magnetoelastic trypsin biosensor is described based on the enzymatic hydrolysis of BAEE by the immobilized trypsin. The pH change of the solution caused the coated pH-sensitive polymer to shrink, and consequently resulted in aresonant frequency change. The optimum pH and temperature were investigated to be pH 7.7 and 25 °C, respectively. The magnetoelastic sensor can be used to detect trypsin at 24 U/ml to 360 U/ml and BAEE at 0.4 mM to 1.5 mM, which is more sensitive than the colorimetric titration method and comparative to electrode methods. The kinetic parameters of both the immobilized and free trypsin were determined. The immobilization of the enzyme reduced the activity by about 50%. The sensor sensitivity, however, was relatively stable after first uses.

Acknowledgments: We are grateful for the financial support from the National Science Foundation of China under the grant 20475016, the Specialized Research Fund for the Doctoral Program of Higher Education under grant 20050532024, and the Scientific Research Foundation of Hunan University. C. A. Grimes gratefully acknowledges partial support of this work by the National Science Foundation under grant BES-0426170.

References and Notes

1. J. P. Dworzanski, A. P. Snyder, R. Chen, H. Zhang, D. Wishart, and L. Li, *Anal. Chem.* 76, 2355 (**2004**).
2. L. M. Ben, B. van, A. G. Hulst, A. L. de Jong, and E. R. J. Wils, *J. Chromatogr. A* 970, 95 (**2002**).
3. T. Larsson, J. Bergström, C. Nilsson, and K. A. Karlsson, *FEBS Lett.* 469, 155 (**2000**).
4. D. M. Goldberg, *Clin. Chim. Acta* 291, 201 (**2000**).
5. S. J. Setford, S. F. White, and J. A. Bolbot, *Biosens. Bioelectron.* 17, 79 (**2002**).
6. P. Sarkar, *Microchem. J.* 64, 283 (**2000**).
7. J. Borch and P. Roepstorff, *Anal. Chem.* 76, 5243 (**2004**).
8. E. Bonneil, M. Mercier, and K. C. Waldron, *Anal. Chim. Acta* 404, 29 (**2000**).
9. E. Calleri, C. Temporini, E. Perani, C. Stella, S. Rudaz, D. Lubda, G. Mellerio, J. L. Veuthey, G. Caccialanza, and G. Massolini, *J. Chromatogr. A* 1045, 99 (**2004**).
10. S. Hara, V. Katta, and H. S. Lu, *J. Chromatogr A.* 867, 151 (**2000**).
11. K. Sakai-Kato, M. Kato, and T. Toyo'oka, *Anal. Chem.* 75, 388 (**2003**).
12. M. T. Dulay, Q. J. Baca, and R. N. Zare, *Anal. Chem.* 77, 4604 (**2005**).
13. E. W. Voss, C. J. Workman, and M. E. Mummert, *Biotechniques* 20, 286 (**1996**).
14. Q. Y. Cai, R. H. Wang, L. Y. Wu, L. H. Nie, and S. Z. Yao, *Microchem. J.* 55, 367 (**1997**).
15. J. H. Yun, M. E. Meyerhoff, and V. C. Yang, *Anal. Biochem.* 224, 212 (**1995**).
16. H. S. M. Abd-Rabboh, S. A. Nevins, N. Durust, and M. E. Meyerhoff, *Biosens. Bioelectron.* 18, 229 (**2003**).
17. P. Lafont, O. Guy-Crotte, C. Paulin, D. Galvain, S. Mertani, C. Frigarella, and Y. Barbier, *Clin. Chim. Acta.* 235, 197 (**1995**).
18. S. Schmidt and C. A. Grimes, *Sens. Actuators A* 94, 189 (**2001**).
19. Q. Y. Cai and C. A. Grimes, *Sens. Actuators B* 71, 112 (**2000**).
20. C. A. Grimes and D. Kouzoudis, *Sens. Actuators A* 84, 205 (**2000**).
21. K. F. Zeng, K. G. Ong, C. Mungle, and C. A. Grimes, *Rev. Sci. Instrum.* 73, 4375 (**2002**).
22. Q. Y. Cai, K. F. Zeng, C. M. Ruan, T. A. Desai, and C. A. Grimes, *Anal. Chem.* 76, 4038 (**2004**).
23. C. M. Ruan, K. F. Zeng, O. K. Varghese, and C. A. Grimes, *Anal. Chem.* 75, 6494 (**2003**).
24. L. G. Puckett, G. Barrett, D. Kouzoudis, C. Grimes, and L. G. Bachas, *Biosens. Bioelectron.* 18, 675 (**2003**).
25. A. R Khokhlov, S. G. Starodubtzev, and V. V. Vasilevskaya, *Adv. Polym. Sci.* 109, 123 (**1993**).
26. H. Lineweaver and D. J. Burk, *J. Am. Chem. Soc.* 56, 658 (**1934**).
27. K. Sankar, C. M. Ruan, K. F. Zeng, and C. A. Grimes, *Sens. Actuators B* 107, 640 (**2005**).
28. T. Chase and E. Shaw, *Biochem. Biophys. Res. Commun.* 29, 508 (**1967**).

SENSOR LETTERS
Vol. 4, 2006

Selected Peer-Reviewed Papers from International Conference of Thermal, Mechanical, and Multiphysics Simulation and Experiments in Microelectronics and Microsystems (EUROSIME'2005)

This special section includes selected papers presented at the *International Conference of Thermal, Mechanical, and MultiPhysics Simulation and Experiments in Microelectronics and Microsystems (EuroSimE)* held in Berlin, 18–20 April 2005. The annual EuroSimE conference was initiated in 2000, as the only international conference focusing on mechanical, thermal, and thermo-mechanical simulation and experiments in microelectronics and microsystems, in order to meet the growing needs and challenges of this rapidly progressing field. This edition features the addition of a parallel track in multiphysics simulation. In total, the conference had more than 100 technical papers divided in 22 sessions.

Selected papers were submitted to an independent peer-review process. They cover significant contributions concerning the use of advanced modeling and simulation techniques relevant for the computer aided design of microsystems.

The conference was possible, thanks to the kind sponsorhip of IEEE, FhG-IZM-Berlin, Philips, Nokia, and Robert Bosch GmbH, and the efforts of the organizing and local committees. I would like to thank specially G. Q. Zhang, L. J. Ernst, P. Rodgers, M. Meuwissen, and last but not least, O. de Saint Leger.

I would like to thank also the following reviewers for their valuable contribution: M. Salleras, S. Mijalkovic, E. Lemaire, D. Elata, A. Wymyslowski, J. P. Polizzi, G. Schrag, E. Rudnyi, N. Cordero, C. Tsamis, and E. Ferraris.

Dr. Santiago Marco,
Guest Editor
Sistemes d'Instrumentació i Communicacions
Departament d'Electrònica, Universitat de Barcelona
Martí i Franqués 1, 08028-Barcelona, Spain
E-mail: santi@el.ub.es

ABOUT THE GUEST EDITOR

Dr. Santiago Marco is Associate Professor (Profesor Titular) at the Departament d'Electronica of Universitat de Barcelona since 1995. He received the degree in Physics from the Universitat de Barcelona in 1988. From 1989 to 1990 he was working in the electro-optical characterization of deep levels in GaAs. From 1990 to 1993 he was regular visitor of the Centro Nacional de Microelectrònica, Bellaterra, Spain. In 1993, he received his Ph.D. (honor award) degree from the Departament de Física Aplicada i Electrònica, Universitat de Barcelona, for the development of a novel silicon sensor for *in-vivo* measurements of the blood pressure. In 1994, he was a post-doc researcher at the Department of Electronic Engineering, Universita di Roma 'Tor Vergata', working in Data Processing for Artificial Olfaction. He has published about 60 papers in scientific journals and books, as well as more than 100 conference papers. His current research interests are twofold: chemical instrumentation based on intelligent signal processing and microsystem modeling.

 1546-198X/2006/4 doi:10.1166/sl.2006.009

SENSOR LETTERS
Vol. 4, 165–173, 2006

Parametric Model Reduction for Fast Simulation of Cyclic Voltammograms

Lihong Feng[1,*], Darius Koziol[2], Evgenii B. Rudnyi[2], and Jan G. Korvink[2]

[1] *ASIC and System State-key Laboratory, Microelectronics Department, Zhangjang Campus, Fudan University, Pudong new District, Shanghai, China*
[2] *IMTEK-Institute for Microsystem Technology, University of Freiburg, Freiburg, Germany*

(Received: 4 January 2006. Accepted: 12 April 2006)

Model order reduction is a well-established technique for fast simulation of large-scale models based on ordinary differential equations, especially those in the field of integrated circuits and micro-electro-mechanical systems. In this paper, we propose the use of parametric model reduction for fast simulation of a cyclic voltammogram. Instead of being considered as a time varying system, the model for a cyclic voltammogram is treated as a system with a parameter (applied voltage) which is to be preserved during model reduction. Because voltage is preserved in the symbolic form during model reduction, we can simulate the cyclic voltammogram with a reduced system and therefore invest much less time and memory as compared with direct simulation based on the original large-scale model. We present our approach for a case study based on scanning electrochemical microscopy.

Keywords: Model Order Reduction, Compact Model, Simulation, Scanning Electrochemical Microscopy (SECM), Voltammogram.

RESEARCH ARTICLE

1. INTRODUCTION

During the last 15 years, Scanning Electrochemical Microscopy (SECM) has evolved from a basic feedback application to a powerful tool for analyzing local electrochemical properties or for modifying surfaces.[1] In recent years, the addition of submicron-scale spatial resolution has increased its capacity for interdisciplinary applications. For example, the technique has been used to measure local kinetics and study chemical reactivity and topology of samples or micro fabrications. In particular, SECM finds many applications in current problems in the biological field. For instance, procedures to characterize surfaces with high local resolution and chemical sensitivity are of great importance for biotechnology, biomedicine, and biosensors. With the combination of chemical specificity and spatial resolution, SECM offers a unique basis for studying surface properties in the sub-μm range.

Quantitative mathematical models have been developed for different operating modes of the SECM, for example, feedback and generator/collector modes, steady state and transient measurements, diffusion-controlled or kinetic-controlled processes.[2,3] However, except for some very specific problems, like the diffusion-controlled current on a circular electrode far away from the border, solutions can only be obtained by numerical simulation, which is based on discretization of the model in space by an appropriate method like finite differences,[4] finite elements,[5] or boundary elements.[6,7] After discretization, a high-dimensional system of ordinary differential equations is obtained. Its high dimensionality leads to high computational cost. This results in a situation where an accurate model is available in principle but is hard to use in practice.

In recent years, several model order reduction (MOR) methods[8–10] have been proposed in order to get a quick and accurate simulation of very large-scale integrated circuits and micro-electro-mechanical systems (for a quick overview see.[11]) They have proved to be very efficient but to our knowledge, they have not yet been applied to electrochemical simulation. One of the reasons is that there are at least two additional problems that should be solved before model reduction can be employed in electrochemistry.

In order to derive a mathematical model for electrochemistry, at least one reaction between two species should be considered. Therefore, it is impossible to set the initial state of all the species equal to zero. Hence, the initial condition of the ordinary differential equations is always nonzero. It happens that for such a system, the

*Corresponding author; E-mail: lhfeng@fudan.edu.cn

conventional model order reduction methods[8–11] cannot be applied immediately because they deal only with systems possessing the zero initial condition. In this paper, we propose a transformation technique, which avoids the nonzero initial condition so that the methods above can be successfully applied to obtain an accurate solution.

Another problem is that, during simulation of a voltammogram, the voltage that changes in time enters the system matrices. Formally speaking, this makes a dynamic system time varying and hence conventional model reduction methods[8–11] cannot be applied. There are special model reduction methods for time varying systems[12, 13] but, in our view, one can suggest much more efficient solution by exploring the special structure of the dynamic system in the case of electrochemistry by relying on parametric model reduction methods.[14, 15] In the present paper, we will show that, after proper modification, the time varying electrochemical model for voltammogram simulation can be successfully reduced by the parametric model reduction technique.

The paper is arranged as follows. In Section 2, we describe our case study and the derivation of the discretized ordinary differential equations (the starting point for model order reduction). It is worthy to note two points here. First, we use a model based on scanning electrochemical microscopy. In this case one can ignore convection and this simplifies modeling. However otherwise, our setup is common to many typical experiments in electrochemistry. Second, our goal is to perform research on model reduction. As a result, we make comparison between the original full scale and reduced models only. The validation of the original model is beyond the scope of the present paper.

In Section 3, we review conventional model order reduction methods based on a projection technique and show its limitations when dealing nonzero initial conditions and time varying systems. Then we propose a transformation technique, which solves the problem with nonzero initial conditions. Then we show how to apply parametric model reduction to solve the electrochemical model when system matrices depend on voltage changing in time. The efficiency of parametric model order reduction is presented in Section 4 with numerical simulation results. Finally, some conclusions are drawn.

2. CASE STUDY

We consider a cylindrical electrode as shown in Figure 1. The computation domain under the 2D-axisymmetrical approximation includes the electrolyte under the electrode. We assume that the concentration does not depend on the rotation angle. A single chemical reaction takes place on the electrode:

$$Ox + e^- \underset{k_b}{\overset{k_f}{\Leftrightarrow}} \mathrm{Red} \tag{1}$$

where k_f and k_b are reaction rates for the forward and backward reactions accordingly.

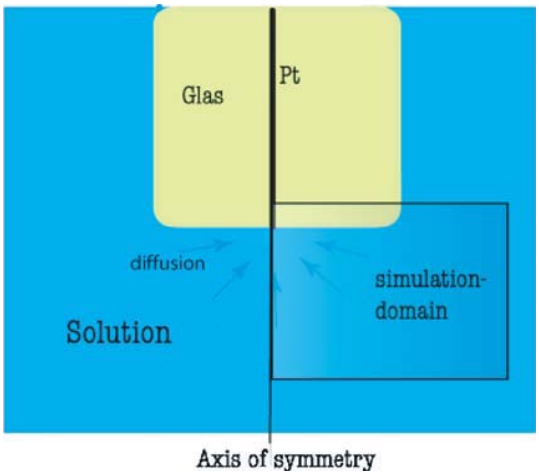

Fig. 1. The computational geometry.

According to the theory of SECM,[2] the species transport in the electrolyte is described by diffusion only. The diffusion partial differential equation is given by the second Fick law as follows

$$dc_1/dt = D_1 \cdot \nabla^2 c_1 \tag{2}$$

$$dc_2/dt = D_2 \cdot \nabla^2 c_2 \tag{3}$$

where $c_1(r, z, t)$ is the concentration field of species Ox and $c_2(r, z, t)$ is the concentration field of species Red, D_1 and D_2 are the respective species diffusion coefficients, t is the time. The initial conditions are

$$c_1(0) = c_{1,0}, \quad c_2(0) = c_{2,0} \tag{4}$$

Conditions at the glass and the bottom of the bath are described by the Neumann boundary conditions of zero flux

$$\nabla c_1 \cdot \vec{n} = 0 \qquad \text{and} \qquad \nabla c_2 \cdot \vec{n} = 0$$

Conditions at the border to the bulk are described by Dirichlet boundary conditions of constant concentration, equal to the initial conditions

$$c_1 = c_{1,0}, \quad c_2 = c_{2,0}$$

To describe the reaction rate on electrode surfaces for chemical reaction (1), the Buttler-Volmer equation has been used,

$$j = k_f \cdot c_{Ox} - k_b \cdot c_{\mathrm{Red}} \tag{5}$$

The reaction constants for the forward reaction and the backward reaction are given as follows

$$k_f = k^0 e^{(\alpha z F(U-U^0)/RT)} \tag{6}$$

$$k_b = k^0 e^{(-(1-\alpha) z F(U-U^0)/RT)} \tag{7}$$

where k^0 is the heterogeneous standard rate constant, and α is an empirical transmission factor for a heterogeneous reaction. F is the Faraday-constant, R is the gas constant, T is the temperature and z is the number of exchanged

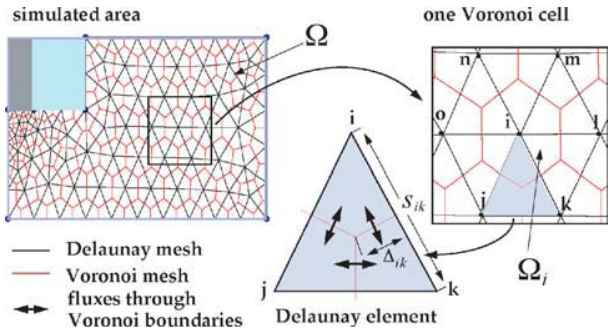

Fig. 2. The discretization scheme.

electrons per reaction. $u = U - U_0$ is the difference between the electrode potential and the reference potential. This difference, to which we refer below as voltage, is changed during the measurement of a voltammogram. This allows us to write the boundary conditions at the electrode as follows,

$$\nabla c_1 \cdot \vec{n} = j \qquad \text{and} \qquad \nabla c_2 \cdot \vec{n} = -j \tag{8}$$

The control volume method has been used for the spatial discretization of (2) and (3) (see Fig. 2). The considered domain Ω is covered by a grid consisting of N_n nodes with $x_i \in \Omega, i = 1, 2, \ldots, N_n$. These nodes are connected by edges as shown in Figure 2. The resulting triangular mesh, in which no angle is bigger than 90° is of type Delaunay, also known as the primary mesh.

Around each node i, we construct a box Ω_i whose edges are composed of the mid-perpendiculars of all the edges terminating in node i. These boxes form the secondary or Voronoi mesh. The resulting equations for the discretization are given as follows:

$$V_i \dot{c}_{1,i} = D_1 \sum_j \frac{S_{ij}}{\Delta_{ij}} (c_{1,j} - c_{1,i}) \tag{9}$$

$$V_i \dot{c}_{2,i} = D_2 \sum_j \frac{S_{ij}}{\Delta_{ij}} (c_{2,j} - c_{2,i}) \tag{10}$$

where i stands for the i-th node and the sum over j includes all neighboring nodes. S_{ij} is the distance between the nodes i and j. Δ_{ij} is the length of the part of Voronoi mesh which belongs to the Delaunay element and the nodes i and j. V_i is the volume (in 2D the area) of the Voronoi cell which belongs to node i.

Equations (9) and (10) are not yet coupled. The coupling arises from the discretization of the mixed boundary conditions at the electrode. The resulting system of ordinary differential equations is as follows

$$E\, d\vec{c}/dt + K(\mathrm{u}(t))\vec{c} = F, \vec{c}(0) = \vec{c}_0 \neq 0 \tag{11}$$

where E and $K(\mathrm{u}(t))$ are system matrices, $K(\mathrm{u}(t))$ is a function of voltage that in turn depends on time. The voltage appears in the system matrix due to the boundary conditions (8) where, in turn, the voltage comes from Eqs. (5) to Eq. (7). $\vec{c} \in R^n$ is the vector of unknown concentrations, R^n means that there are n elements in the real-valued vector $\vec{c}$, n is usually referred to as the dimension of the system (11). The vector $\vec{c}$ includes both the Ox and Red species. The vector F is the load vector, which arises as a consequence of the Dirichlet boundary conditions imposed at the bulk boundary of the electrolyte. The total current is computed as an integral (sum) over the electrode surface.

3. MODEL ORDER REDUCTION

3.1. General Idea of Model Order Reduction

The dimension n of system (11) is usually around 10^4–10^6. It is always time consuming if we use conventional numerical integration methods, for example backward Euler, to directly simulate (11) time step by time step over a typical time interval. The model order reduction technique replaces the original large dimensional system (11) with a compact model and at the same time, makes sure that the solution computed from the compact model is as accurate as that computed directly from the original large system.

Most often, model order reduction is based on a projection technique when the projection basis is found by implicit moment matching.[8–10] We refer below to these methods as conventional model reduction. It should be noted that there are other approaches for model reduction like balanced truncation approximation and proper orthogonal decomposition (see review[11] for details). However, the parametric model reduction introduced in Section III.D is the generalization of implicit moment matching and at present it is unclear how to preserve parameters in other model reduction approaches. As a result, we limited ourselves in the present paper to model reduction methods based on implicit moment matching.

It should be noted here that conventional model reduction can deal with models with constant system matrices only. In other words, in Eq. (11), it is required that the matrices E, K, F do not depend on time or some other parameters. For simplicity, we assume in this section that the matrix K is formed at a constant voltage value. The basic idea of model order reduction is to find a projection matrix V such that $V^T V = I$ and the unknown vector $\vec{c}$ can be sufficiently approximated by $\vec{c} \approx V\bar{z}$, with a rectangular matrix $V \in R^{n \times q}$ such that the number of columns much less than the number of rows, $q \ll n$. This gives us

$$EV\, d\bar{z}/dt + KV\bar{z} = F \tag{12}$$

After multiplying (12) by V^T from the left, we obtain the final reduced small system (compact model) with unknown vector $\bar{z} \in R^q$, which is of much smaller dimension q:

$$V^T EV\, d\bar{z}/dt + V^T KV\bar{z} = V^T F \tag{13}$$

RESEARCH ARTICLE

3.2. Conventional Projection Technique

In order to perform model order reduction described in subsection *A*, the projection matrix V needs to be computed. With the assumption that the initial condition of the system is zero ($\vec{c}_0 = 0$), the conventional method of constructing V is based on the transfer function of the original system (11). In the case of system (11), we are not interested in the complete concentration vector $\vec{c}$ but in a few outputs computed as linear combinations of concentrations, i.e.

$$\bar{y} = L\vec{c} \tag{14}$$

Natural choice for electrochemistry here is the current that is computed directly from the concentration vector as a linear combination.

Provided that the matrix K is constant, the Laplace transformation of (11) and (14) with initial condition $\vec{c}_0 = 0$ is as follows

$$\begin{aligned} sEC(s) + KC(s) &= F\mathrm{U}(s) \\ Y(s) &= LC(s) \end{aligned} \tag{15}$$

The transfer function is defined as

$$H(s) = Y(s)/U(s) = L(sE+K)^{-1}F \tag{16}$$

By choosing an expansion point, $s = s_0 + \sigma$, $H(s)$ can be expanded into series around s_0,

$$H(\sigma) = \sum_{i=0}^{\infty} LM^i r\sigma^i \tag{17}$$

where $M^i = -(s_0E+K)^{-1}E$, $r = (s_0E+K)^{-1}F$.

The projection matrix V is constructed as follows

$$spancolumn\{V\} = span\{(r, Mr, \ldots, M^j r\} \tag{18}$$

by satisfying $V^TV = I$. In Eq. (18), *spancolumn* means the subspace spanned by the columns in V; *span* means the subspace spanned by $r, Mr, \ldots M^j r$. The condition $V^TV = I$ means that the columns in V form a group of orthonormal vectors for the subspace spanned by $r, Mr, \ldots M^j r$. Usually, the reduced system (13) can approximate the original system (11) quite well even for small j. The reduced system will be more accurate if more terms are included in the right hand side of Eq. (18). Detailed theoretical proof is given elsewhere.[9]

The conventional method of computing V has an assumption that the initial condition of the system must be zero so that a transfer function in the form of Eq. (16) can be obtained. However, from the Laplace transformation of the system in Eq. (11), we have that

$$\int_0^\infty E\dot{\vec{c}}e^{-st}dt + \int_0^\infty K\vec{c}e^{-st}dt = \int_0^\infty Fe^{-st}dt$$

After integration, we actually obtain

$$\begin{aligned} sEC(s) + KC(s) &= FU(s) + E\vec{c}_0 \\ Y(s) &= LC(s) \end{aligned}$$

and

$$\begin{aligned} H(s) = Y(s)/U(s) &= L(sE+K)^{-1}F \\ &+ L(sE+K)^{-1}E\vec{c}_0/U(s) \end{aligned} \tag{19}$$

The expression in Eq. (19) contains $\vec{c}_0$. When $\vec{c}_0 = 0$, it is the same as Eq. (16). However when $\vec{c}_0$ is nonzero, only the first part in Eq. (19) would be considered to construct the projection matrix V as is done in Eq. (18) and the resulting reduced model might be inaccurate.

Another reason is that with the reduced model we cannot describe well all possible initial conditions. We mean that Eq. (11) can be considered as a family of initial value problems with different $\vec{c}_0 \neq 0$. A normal way to obtain the initial condition of the reduced system is by projection $\vec{z}_0 \approx V^T\vec{c}_0$. However, if we use such $\vec{z}_0$ to compute the initial condition of the original system we obtain $\vec{c}_0 \approx V\vec{z}_0 = VV^T\vec{c}_0$. It is clear that we can only obtain an approximation of the nonzero initial condition $\vec{c}_0^r = VV^T\vec{c}_0$. $\vec{c}_0^r$ is a projection of the original $\vec{c}_0$ to the low-dimensional subspace and it will be very inaccurate if $\vec{c}_0$ is far away from the subspace spanned by V. Such a situation is shown in Figure 3, where $\vec{c}_0^r = VV^T\vec{c}_0$ is in the subspace spanned by V, *span{V}* , while the original $\vec{c}_0$ is not. This happens to be also the case in our example.

From the above analysis, we can conclude that there are two important difficulties to overcome before conventional model reduction can be employed for the model described by Eq. (11). First, the initial condition of the system is always nonzero in our case, i.e., $\vec{c}_0 \neq 0$. Second, in Eq. (11), the matrix $K(\mathrm{u}(t))$ depends on the voltage that in turn depends on time in the simulation of a cyclic voltammogram. This feature must be preserved in the reduced model. In the following subsections, we will first propose a transformation technique to validate the conventional model reduction method for the nonzero initial condition. Then, we review the parametric model reduction technique to deal with the voltage dependent case. Finally, we combine the parametric model reduction technique with the transformation technique to obtain a reduced model for Eq. (11).

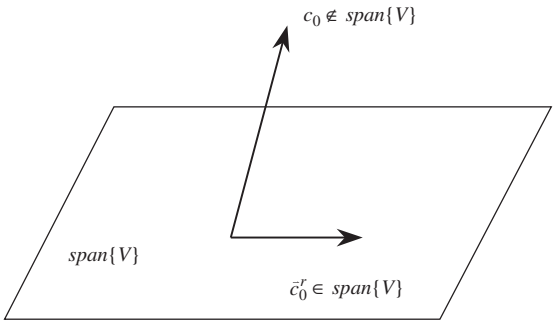

Fig. 3. Inaccuracy of initial condition caused by conventional projection technique.

3.3. Projection Technique with Transformation

The natural solution for a problem above is to transform system (11) to the standard state-space formulation. Let us define a new unknown vector $\tilde{\vec{c}} = \vec{c} - \vec{c}_0$ and then obtain a new system for $\tilde{\vec{c}}$

$$\begin{aligned} E\dot{\tilde{\vec{c}}} + K\tilde{\vec{c}} &= F - K\vec{c}_0, \tilde{\vec{c}}(0) = 0 \\ \tilde{Y}(t) &= L\tilde{\vec{c}} \end{aligned} \tag{20}$$

It is clear that the transformed system (20) possesses zero initial conditions by definition so that the conventional projection technique of subsection *B* can be employed to perform model reduction on this new system. One can prove that

$$H(s) = L(sE + K)^{-1}\tilde{F} = \sum_{i=0}^{\infty} M^i \tilde{r}\sigma^i$$

where $\tilde{F} = F - K\vec{c}_0$, $\tilde{r} = (s_0 E + K)^{-1}\tilde{F}$, M is defined as in Eq. (17). The projection matrix $\tilde{V}$ can be computed in a similar way as

$$spancolumn\{\tilde{V}\} = span\{(\tilde{r}, M\tilde{r}, \ldots, M^j\tilde{r}\} \tag{21}$$

The same way as in Eq. (12) and (13), we obtain a small dimensional reduced system as follows

$$\tilde{V}^T E\tilde{V}\dot{\tilde{z}} + \tilde{V}^T K\tilde{V}\tilde{z} = \tilde{V}^T F \tag{22}$$

The unknown vector $\vec{c}$ for the original system (11) can be restored by

$$\vec{c} = \tilde{\vec{c}} + \vec{c}_0 \approx \tilde{V}\vec{z} + \vec{c}_0 \tag{23}$$

In this way the nonzero initial condition is preserved exactly, because from $\vec{z}_0 = \tilde{V}^T\tilde{\vec{c}}_0 = 0$ we have that $\tilde{\vec{c}}_0^r = \tilde{V}\vec{z}_0 = 0$, then we obtain $\vec{c}_0^r = \tilde{\vec{c}}_0^r + \vec{c}_0 = c_0$, which means that the initial condition $\vec{c}_0^r$ computed from the reduced system (22) is identical to the exact initial condition $\vec{c}_0$. In the end, the accuracy of the reduced system (22) will only depend on the accuracy of projection matrix $\tilde{V}$, which is easily met by adding more terms into the right hand side of Eq. (21).

3.4. Parametric Model Reduction

In this subsection, we review recently developed model reduction methods which can preserve parameters during the model reduction process. We will show how they can be applied to the time varying electrochemical model in Eq. (11) in the next subsection.

The parametric model reduction method proposed in Ref. [13] deals with a two-parameter system in the following form

$$\begin{aligned} (s_1E_1 + s_2E_2 - E_0)x &= b\mathrm{w} \\ y &= cx \end{aligned} \tag{24}$$

where corresponding reduced model is

$$\begin{aligned} (s_1\hat{E}_1 + s_2\hat{E}_2 - \hat{E}_0) &= \hat{b}\mathrm{w} \\ \hat{y} &= \hat{c}x \end{aligned} \tag{25}$$

where

$$\begin{aligned} &\hat{E}_1 = V^T E_1 V, \hat{E}_2 = V^T E_2 V, \\ &\hat{E}_0 = V^T E_0 V, \hat{b} = V^T b, \hat{c} = cV \end{aligned}$$

The projection matrix V is computed from the transfer function of (24) where we explicitly write that it depends on both parameters

$$h(s_1, s_2) = c(s_1E_1 + s_2E_2 - E_0)^{-1}b \tag{26}$$

$h(s_1, s_2)$ can be expanded into series of both s_1 and s_2,

$$\begin{aligned} h(s_1, s_2) &= -c[I - (E_0^{-1}E_1s_1 + E_0^{-1}E_2s_2)]^{-1}E_0^{-1}b \\ &= -c\sum_{i=0}^{\infty}(E_0^{-1}E_1s_1 + E_0^{-1}E_1s_2)^iE_0^{-1}b \\ &= -c\sum_{j=0}^{\infty}\sum_{k=0}^{j}[F_k^j(E_0^{-1}E_1, E_0^{-1}E_2)s_1^{j-k}s_2^k]E_0^{-1}b \end{aligned}$$

where F_k^j is the matrix before $s_1^{j-k}s_2^k$. For example,

$$\begin{aligned} &F_0^1 = E_0^{-1}E_1, F_1^1 = E_0^{-1}E_2, F_0^2 = (E_0^{-1}E_1)^2 \\ &F_1^2 = (E_0^{-1}E_1)(E_0^{-1}E_2) + (E_0^{-1}E_2)(E_0^{-1}E_1) \\ &F_2^2 = (E_0^{-1}E_2)^2, \ldots \end{aligned} \tag{27}$$

The moments for both parameters are as follows

$$-cF_k^j(E_0^{-1}E_1, E_0^{-1}E_2)E_0^{-1}b \tag{28}$$

the projection matrix V is computed based on the moments in Eq. (28), that is

$$colspan\{V\} = span\left\{\bigcup_{m=0}^{j}\bigcup_{k=0}^{m}F_k^m(E_0^{-1}E_1, E_0^{-1}E_2)E_0^{-1}b\right\} \tag{29}$$

Theorem 4 in Ref. [14] guarantees the accuracy of the reduced model by proving that a certain number of the moments in the reduced model (25) will match the corresponding moments in the original model (24):

$$\begin{aligned} cF_k^m(P^{-1}E_1, P^{-1}E_2)P^{-1}b = \hat{c}F_k^m(\hat{P}^{-1}\hat{E}_1, \hat{P}^{-1}\hat{E}_2)\hat{P}^{-1}\hat{b} \\ 0 \le k \le m \le j+1 \end{aligned}$$

This method was extended to systems with any number of parameters in Ref. [15], where a linear system with p parameters is defined as

$$\begin{aligned} (s_1E_1 + s_2E_2 + \cdots + s_pE_p - E_0)x &= b\mathrm{w} \\ y &= cx \end{aligned} \tag{30}$$

Since c does not contribute the projection matrix V, the series expansion of x instead of the transfer function is considered in Ref. [15]. From (30) we have

$$\begin{aligned} x &= -[I - (s_1E_0^{-1}E_1 + \cdots + s_pE_0^{-1}E_p)]^{-1}E_0^{-1}b\mathrm{w} \\ &= -\sum_{m=0}^{\infty}[s_1E_0^{-1}E_1 + \cdots + s_pE_0^{-1}E_p]^mE_0^{-1}b\mathrm{w} \end{aligned}$$

RESEARCH ARTICLE

$$= \sum_{m=0}^{\infty} \sum_{k_2=0}^{m-(k_3+\cdots+k_p)} \cdots \sum_{k_{p-1}=0}^{m-k_p} \sum_{k_p=0}^{m} [F_{k_2,\cdots k_p^m}(E_0^{-1}E_1,\ldots,E_0^{-1}E_p)b\mathrm{w}]s_1^{m-(k_2+\cdots+k_p)}s_2^{k_2}\cdots s_p^{k_p}$$

where $F_{k_2,\ldots,k_p^m}$ is similarly defined as in Eq. (27).

The projection matrix V is constructed by the terms of the series above, that is

$$colspan(V) = span\left\{\bigcup_{m=0}^{m_q}\bigcup_{k_2=0}^{m-(k_p+\ldots+k_3)}\cdots\bigcup_{k_{p-1}=0}^{m-k_p}\bigcup_{k_p=0}^{m} F_{k_2,\ldots k_p}^{m}E_0^{-1}b\right\} \tag{31}$$

or alternatively,

$$\begin{aligned} colspan(V) = span\{&E_0^{-1}b,(E_0^{-1}E_1)E_0^{-1}b,(E_0^{-1}E_2)E_0^{-1}b\ldots,\\ &(E_0^{-1}E_p)E_0^{-1}b,(E_0^{-1}E_1)^2E_0^{-1}b,\\ &[(E_0^{-1}E_1)(E_0^{-1}E_2)+(E_0^{-1}E_2)(E_0^{-1}E_1)]E_0^{-1}b,\ldots,\\ &[(E_0^{-1}E_1)(E_0^{-1}E_p)+(E_0^{-1}E_p+E_0^{-1}E_1)]E_0^{-1}b,\\ &(E_0^{-1}E_2)^2E_0^{-1}b,[(E_0^{-1}E_2)(E_0^{-1}E_3)\\ &+(E_0^{-1}E_3)(E_0^{-1}E_2)]E_0^{-1}b,\ldots,[(E_0^{-1}E_2)(E_0^{-1}E_p)\\ &+(E_0^{-1}E_p)(E_0^{-1}E_2)]E_0^{-1}b,\ldots,(E_0^{-1}E_p)^mE_0^{-1}b\} \end{aligned}$$

In this way of computing V, there is another theorem in Ref. [15] which proves that the moments included in Eq. (31) are conserved by the reduced model. In the next subsection, we will show the applicability of this method to the model of Eq. (11).

3.5. Application to the Electrochemical Model

For the electrochemical model in Eq. (11), the system matrix K depends on the voltage which in turn plays the role of an input function that changes in time. According to the theory from Section 2, we can express this dependence as follows

$$K = G + s_1D_1 + s_2D_2$$

where G, D_1, D_2 are constant matrices and s_1 and s_2 are the functions of the voltage applied to the electrode

$$s_1(t) = e^{u(t)}, \quad s_2(t) = e^{-u(t)}$$

with $u(t) = v(t) - v_0$ and where v_0 is the reference voltage.

As result, the system (11) can be re-written as follows:

$$E\,d\vec{c}/dt + G\vec{c} + (s_1D_1 + s_2D_2)\vec{c} = \mathrm{F} \tag{32}$$

where the two scalar functions $s_1(t), s_2(t)$ are considered as parameters.

Taking into account that the initial condition of system (11) is a nonzero vector, $\vec{c}_0 \neq 0$, the Laplace transformation for Eq. (32) produces

$$(sE + s_1D_1 + s_2D_2 + G)x(s) = \mathrm{F}U(s) + E\vec{c}_0 \tag{33}$$

where $x(s)$ is the Laplace transformation of $\vec{c}$. By comparison, (33) is different from (30) when $p = 3$. This means that (31) cannot be used yet to construct the projection matrix for Eq. (32). However, as has been discussed in subsection C, we can first transform the vector in Eq. (32) as $\tilde{\vec{c}} = \vec{c} - \vec{c}_0$ without loss of accuracy and obtain a new system with respect to $\tilde{\vec{c}}$,

$$E\,d\tilde{\vec{c}}/dt + G\tilde{\vec{c}} + (s_1D_1 + s_2D_2)\tilde{\vec{c}} = \mathrm{F} + G\vec{c}_0 + s_1D_1\vec{c}_0 + s_2D_2\vec{c}_0 \tag{34}$$

For the new system, the initial condition is exactly zero, $\tilde{\vec{c}}_0 = \vec{c}_0 - \vec{c}_0 = 0$. After Laplace transformation, (34) becomes,

$$sEx(s) + Gx(s) + (s_1D_1 + s_2D_2)x(s) = \widetilde{F}U(s) \tag{35}$$

with $\widetilde{F} = F + G\vec{c}_0 + s_1D_1\vec{c}_0 + s_2D_2\vec{c}_0$.

Equation (35) is of almost the same form as Eq. (30), except that the vector b in Eq. (30) is not related with the parameters, whereas the vector $\widetilde{F}$ is dependent on two parameters. However, one can deal with this just after inspecting Eq. (31). In Eq. (31), the vector b is one of the base vectors to span the subspace for matrix V, in Eq. (35) the vector $\widetilde{F}$ is acting the same role as b. $\widetilde{F}$ is actually the linear combination of the three vectors, $(F + G\vec{c}_0)$, $D_1\vec{c}_0$, $D_2\vec{c}_0$. Therefore, when we construct the projection matrix V according to Eq. (31), we can replace the vector b in Eq. (30) by the three vectors above, that is, define a new matrix $B = (F + G\vec{c}_0, D_1\vec{c}_0, D_2\vec{c}_0)$ so that it is independent of the parameters. We construct the projection matrix V for Eq. (35) according to Eq. (31) as

$$\begin{aligned} colspan(V) = span\{&G^{-1}B,(G^{-1}E)G^{-1}B,(G^{-1}D_1)G^{-1}B,\ldots,\\ &(G^{-1}D_2)G^{-1}B,(G^{-1}E)^2G^{-1}B,\\ &[(G^{-1}E)(G^{-1}D_1)+(G^{-1}D_1)(G^{-1}E)]G^{-1}B,\ldots,\\ &[(G^{-1}E)(G^{-1}D_2)+G^{-1}D_2+G^{-1}E)]\\ &G^{-1}B,(G^{-1}D_1)^2G^{-1}B,\ldots,(G^{-1}D_2)^jG^{-1}B\} \end{aligned}$$

The final reduced model is

$$\widehat{E}\,dz/dt + \widehat{G}z + (s_1\widehat{D}_1 + s_2\widehat{D}_2)z = \widehat{F} \tag{36}$$

where

$$\widehat{E} = V^TEV, \quad \widehat{G} = V^TGV, \quad \widehat{D}_1 = V^TD_1V,$$
$$\widehat{D}_2 = V^TD_2V, \quad \widehat{F} = V^T\widetilde{F}$$

After obtaining the solution z in Eq. (36), we return back to the solution $\tilde{\vec{c}}$ in Eq. (34) via $\tilde{\vec{c}} \approx Vz$, the original solution $\vec{c}$ in Eq. (11) can be computed by $\vec{c} = \tilde{\vec{c}} + \vec{c}_0$.

In the next section, we will show the efficiency of parametric model reduction for the simulation of a voltammogram with numerical simulation results for the case study described in Section 2.

4. NUMERICAL EXPERIMENTS

In this section, we present simulation results to show both the accuracy of the proposed transformation technique to deal with nonzero initial conditions and the efficiency of the parametric model order reduction method combined with the transformation technique.

Figure 1 and Figure 2 show the layout of the scanning electrochemical microscope for which the partial differential equations in Eqs. (2) and (3) are derived (see Section 2). Figure 1 is the computational unit and Figure 2 is the discretization scheme of the control volume method. The resulted system in Eq. (11) is of dimension 16912, that is $\vec{c} \in R^{\mathrm{n}}$, and $n = 16912$. We have limited the dimension of the system on purpose, as our goal was to research on the method rather than to develop a scalable implementation. In the figures below, q represents the dimension of the reduced small system, that is, the unknown vector $\vec{z} \in R^{q}$.

In order to give clear and simple description for the transformation technique, we simulated the current after imposing voltage $E - E_0 = 0.1$ V, that is, we set the system matrix K in Eq. (11) as a constant matrix. The simulation results for the transformation technique are shown in Figures 4–9.

In Figure 4, we show the plot of the solution for the current. We compare the solution by conventional projection technique and the solution by the proposed transformation technique with the solution computed by direct simulation. One can see that for the conventional projection technique (dotted line), the reduced system of dimension 100 cannot reproduce the initial condition of the current. At the same time, the solution derived by the proposed transformation technique is indistinguishable from the solution computed by traditional direct simulation.

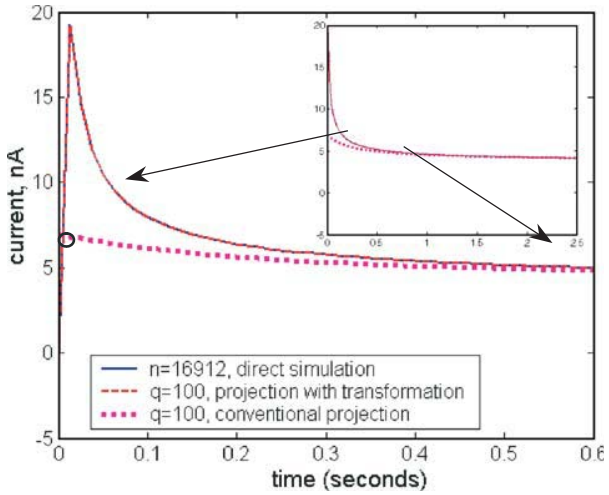

Fig. 4. Comparison between direct simulation and model reduction for the electrode current. The small circle on the vertical axis indicates the mismatch of the conventional projection method for initial condition.

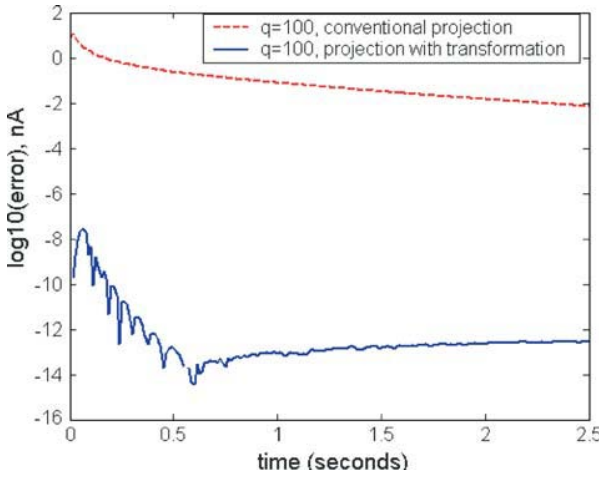

Fig. 5. Errors of model reduction with two different projection techniques for the solution of electrode current.

The simulation errors of the two model order reduction techniques are displayed in Figure 5. The error is defined as

$$error = |y(t) - \hat{y}(t)| \tag{37}$$

where $y(t)$ is the current computed by direct simulation for system (11), $\hat{y}(t)$ is the current computed by reduced system in Eqs. (13) or (22). In order to put the errors of the two different model order reduction techniques into one figure, we use a logarithmic plot. The dashed line is the error of the reduced system in Eq. (13) by the conventional projection technique. The solid line is the error of the reduced system in Eq. (22) by the proposed transformation technique. They again show that the results of the model reduction with transformation technique are very accurate.

In Figure 6 and Figure 7, we further show the accuracy of model order reduction with simulation results for the current obtained from several reduced models of different

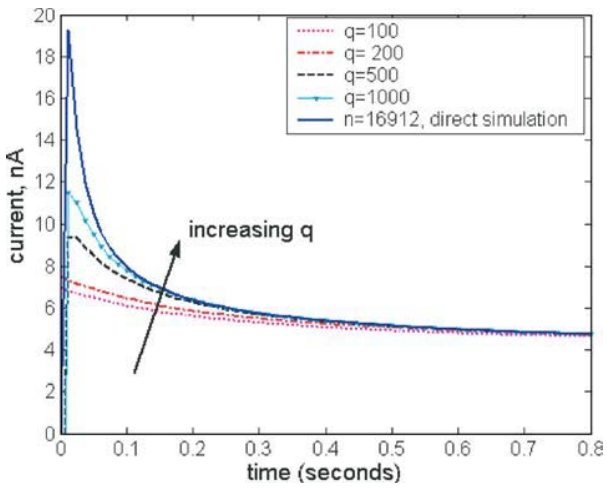

Fig. 6. Solution for electrode current by different dimensions of reduced models with conventional model reduction.

RESEARCH ARTICLE

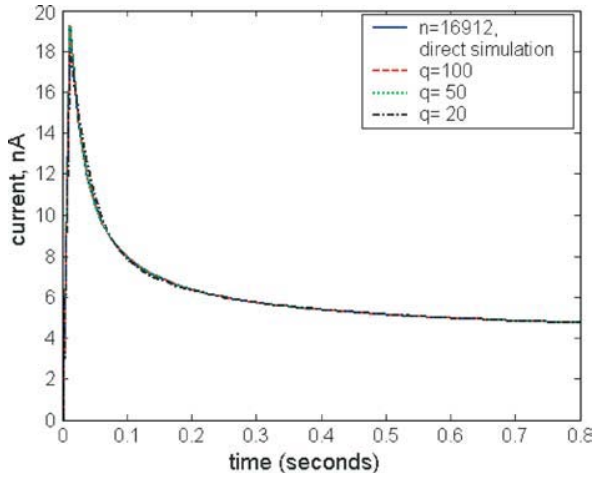

Fig. 7. Solution for electrode current by different dimensions of reduced models with proposed transformation technique.

dimensions. In Figure 6, the simulation results are from four different reduced models of dimension 100, 200, 500, and 1000, respectively by the conventional projection technique. In Figure 7 we plot simulation results, which are from three different reduced models of respective dimensions 20, 50, 100 by the proposed transformation projection technique. From Figure 6, we can see that the results of the reduced models by conventional projection technique are not accurate even if we increase the dimension of the reduced model to 1000. For the proposed transformation technique, it can be seen that the results of the reduced model are still very accurate even if the dimension of the reduced model is very small ($q = 20$). The errors of the reduced models by the proposed transformation technique are all below 10^{-6} for the three cases.

Figures 8–11 show the simulation results of the original full-scale model and the reduced model obtained by the parametric model reduction method combined with the proposed transformation technique for the cyclic

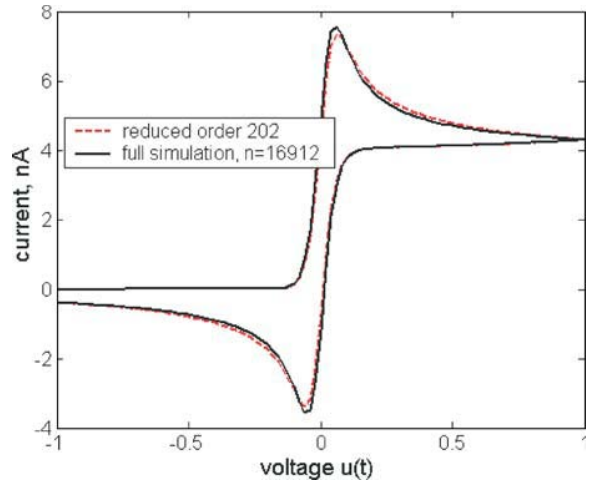

Fig. 8. Simulated cyclic voltammogram for $du/dt = \pm 0.5$.

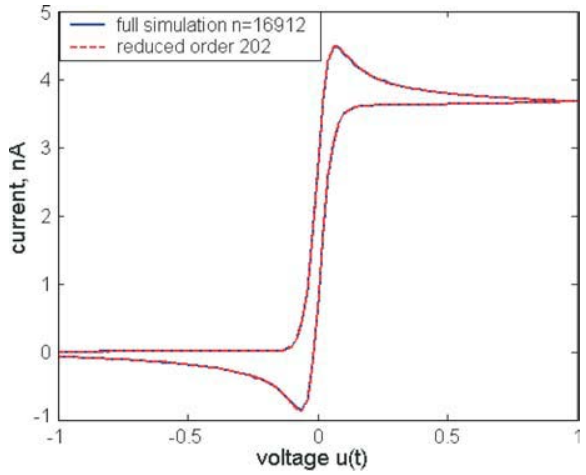

Fig. 9. Simulated cyclic voltammogram for $du/dt = \pm 0.05$.

voltammogram. The dimension of the reduced model is $q = 202$. The voltage follows a symmetric triangular waveform:

$$\begin{cases} u = u_0 + at, & 0 < t < t_{u_{\max}} \\ u = u_0 - at, & t_{u_{\max}} < t < 2t_{u_{\max}} \end{cases}$$

The figures display the current as a function of voltage (not in time) as this is the usual way to represent voltammograms. The solid line is the result computed by full simulation of the original large model, the dashed line is the result computed by the small reduced model. The results of the reduced model are accurate for a wide range of the dynamic behavior when the value of du/dt changes by three orders of magnitude (0.0005–0.5).

The major cost to integrate a system of ordinary differential Eq. (11) is the solution of a system of linear equations during time stepping. Let us compare the timing between a solution of a linear system of dimension $n = 16912$ for the original problem and dimension $q = 100$, 50, 20 for the reduced system. We use the sparse solver

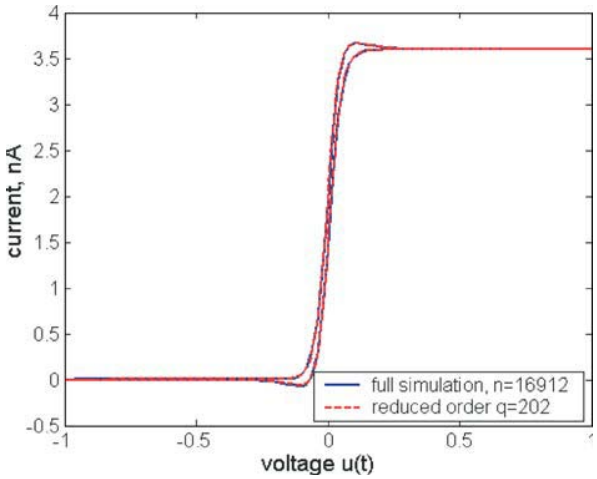

Fig. 10. Simulated cyclic voltammogram for $du/dt = \pm 0.005$.

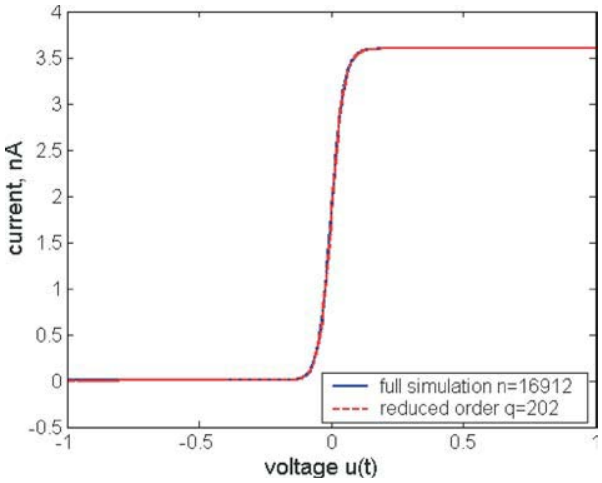

Fig. 11. Simulated cyclic voltammogram for $du/dt = \pm 0.0005$.

UMPACK[16] to solve a linear system for the original system, and LAPACK[17] to simulate the reduced system on the same workstation. The solution time on Sun Sparc Ultra-80 for the original system is 1.5 seconds, whereas solution of the reduced small model costs only 0.003, 0.0007, 0.0003 seconds respectively with respective speed factors 500, 2143, and 5000.

5. CONCLUSION

We have shown that it is feasible to apply model reduction in electrochemistry by addressing two major challenges: nonzero initial conditions and changes of the applied voltage in time. As was already mentioned, our case study is straightforward. However, it includes all features of a typical experiment in cyclic voltammetry and we believe that it is representative enough for this conclusion.

First, we have demonstrated that nonzero initial conditions are, mathematically speaking, far away from the low dimensional subspace that captures the system dynamics. The transformation technique presented in the paper allowed us to solve this problem and obtain a very accurate but low dimensional reduced system.

Second, we have introduced a parametric model order reduction technique in order to build a compact model to describe a voltammogram scan. Parametric model order reduction preserves the parameters in the original model in the reduced small model in the symbolic form so that the reduced small model can replace the original large model in simulation of a wide range of parameter values. At the same time, the reduced model produces solutions as accurate as the solution computed directly from the original large model.

Acknowledgments: This research is supported partly by NSFC research project 90307017, 60176017, 90207002, partly by the National Basic Research Program of China under the grant 2005CB321701, partly by Synopsys Inc., partly by Cross-Century Outstanding Schoolar's fund of Ministry of Education of China, partly by National 863 plan projects 2004AA1Z1050, Shanghai Science and Technology committee Key project 04JC14015 and Shanghai AM R&D fund 0418 and partly by a fund of the Alfried Krupp von Bohlen und Halbach-Stiftung of Germany.

References and Notes

1. A. J. Bard and M. V. Mirkin (Eds.), Scanning Electrochemical Microscopy, John Wiley and Sons, New York **(2001)**.
2. M. V. Mirkin, Theory in Scanning Electrochemical Microscopy, edited by A. J. Bard and M. V. Mirkin, John Wiley and Sons, New York **(2001)**, pp. 145–199.
3. A. L. Whitworth, D. Mandler, and P. R. Unwin, *Phys. Chem. Chem. Phys.* 7, 356 **(2005)**.
4. J. Heinze, M. Stoerzbach, Digital Simulation of Mass Transport to Ultramicroelectrodes. NATO ASI Series, Series E **(1991)**, Vol. 197, pp. 99–122.
5. T. Nann and J. Heinze, *Electrochem. Comm.* 1, 289 **(1999)**.
6. O. Sklyar and G. Wittstock, *J. Phys. Chem. B* 106, 7499 **(2002)**.
7. O. Sklyar, A. Kueng, C. Kranz, B. Mizaikoff, A. Lugstein, E. Bertagnolli, and G. Wittstock, *Analytical Chemistry* 77, 764 **(2005)**.
8. L. M. Silveira, M. Kamon, and J. White, Efficient Reduced-Order Modeling of Frequency-Dependent Coupling Inductances Associated with 3-D Interconnect Structures, *IEEE Transactions on Components Packaging and Manufacturing Technology Part B-Advanced Packaging*, **(1996)**, Vol. 19, pp. 283–288.
9. R. W. Freund, Reduced-Order Modeling Techniques Based on Krylov Subspaces and Their use in Circuit Simulation, in *Applied and Computational Control Signals and Circuits*, edited by B. N. Datta, Birkhauser, Boston **(1999)**, Vol. 1, pp. 435–498.
10. A. Odabasioglu, M. Celik, and L. T. Pileggi, PRIMA: Passive Reduced-Order Interconnect Macromodeling Algorithm, *IEEE Transactions On Computer-Aided Design of Integrated Circuits and Systems* **(1998)**, Vol. 17, pp. 645–654.
11. E. B. Rudnyi and J. G. Korvink, Review: Automatic Model Reduction for Transient Simulation of MEMS-Based Devices, Sensors Update **(2002)** Vol. 11, p. 3–33.
12. J. Roychowdhury, Reduced-Order Modeling of Time-Varying Systems, *IEEE Transactions On Circuits and Systems II-Analog and Digital Signal Processing* **(1999)**, Vol. 46, pp. 1273–1288.
13. J. R. Phillips, Projection-Based Approaches for Model Reduction of Weakly Nonlinear, Time-Varying Systems, *IEEE Transactions on Computer-Aided Design of Integrated Circuits and Systems* **(2003)**, Vol. 22, pp. 171–187.
14. D. S. Weile, E. Michielssen, E. Grimme, and K. Gallivan, *Appl. Math. Lett.* 12, 93 **(1999)**.
15. L. Daniel, O. C. Siong, L. S. Chay, K. H. Lee, and J. White, A Multiparameter Moment-Matching Model-Reduction Approach for Generating Geometrically Parameterized Interconnect Performance Models, *IEEE Trans. Computer-Aided Design of Integrated Circuits and Systems* **(2004)**, Vol. 23, pp. 678–693.
16. T. A. Davis. Algorithm 832: UMFPACK V4.3, an Unsymmetric-Pattern Multifrontal Method. ACM Transactions on Mathematical Software **(2004)**, Vol. 30, pp. 196–199.
17. E. Anderson, Z. Bai, C. Bischof, J. Demmel, J. Dongarra, J. Du Croz, A. Greenbaum, S. Hammarling, A. McKenney, S. Ostrouchov, and D. Sorensen. LAPACK Users' Guide. SIAM, Philadelphia, PA **(1995)**, 2nd edn.

SENSOR LETTERS
Vol. 4, 174–183, 2006

RESEARCH ARTICLE

Computer Assisted Design Study of a Non-Silicon Capacitive Pressure Sensor System

M. H. H. Meuwissen*, E. P. Veninga, M. W. W. J. Tijdink, and M. G. H. Meijerink

TNO Science and Industry, P. O. Box 6235, NL 5600 HE Eindhoven, The Netherlands

(Received: 11 September 2005. Accepted: 4 December 2005)

The application of numerical techniques for the design of a capacitive pressure sensor system in non-silicon materials is described. These techniques have been used to address issues related to the thermo-mechanical performance of the sensor system. This comprises the selection of the materials and dimensions used for the sensor itself and the substrate on which it is mounted. Moreover, simulations are applied to aid in the selection of suitable solder interconnect materials and dimensions. Where possible, the accuracy of the numerical predictions is assessed by comparing them to experiments on physical prototypes. The application of numerical simulations allowed for a reduction in the number of physical tests and thereby a reduction in design time and costs. A sensor system was specified based on the outcome of the design studies. It proved to meet the functional demands imposed by the targeted application on a laboratory scale.

Keywords: Non-Silicon Pressure Sensor System, Numerical Modelling, Soldering, Assembly and Packaging.

1. INTRODUCTION

Micromachined pressure sensors are already commercially available for many years.[1,2] However, they are typically fabricated in silicon which warrants their use only for applications in which they can be manufactured in large volumes because of the high costs for production facilities. In order to enable the production of low- and mid-volume series at reasonable unit prices, the materials and production costs have to be reduced considerably. This could possibly be achieved by the use of other materials and processes that are commonly applied and proven in micro-electronics.

The work presented in this paper is part of a project targeted at the development of a low-cost pressure sensor in non-silicon materials. The principle of this sensor is schematically shown in Figure 1.

The sensor basically consists of a thin circular membrane placed parallel to a rigid reference plane. The membrane and the rigid plane act as the two electrodes of a capacitor. Deflection of the membrane due to a pressure difference results in a change in capacity. The capacity changes are logged and used to calculate the pressure on the membrane.

The pressure sensor is to be applied for monitoring the ageing of a solid rocket propulsion material. For this particular material, ageing is accompanied by volumetric shrinkage. Since the material is stored in a rigid container, volumetric shrinkage causes a change of hydrostatic pressure which exerts a pulling load on the sensor membrane as shown in Figure 1.

Next to the low unit-price, other typical demands set for this application are: Ability to operate in a temperature domain ranging from −40 °C to +60 °C, ability to measure pressures of up to 5 bar, and ability to function over a time span of more than one year.

The pressure sensor is mounted on a Low-Temperature Co-fired Ceramic (LTCC) substrate. LTCC technology is readily available for the realisation of complex electronic circuits. In addition to the features of standard thick-film technology, LTCC allows for the integration of interconnect, actives, and passives inside the substrate, thereby creating a compact way of packaging and interconnecting electronic components. Apart from these benefits, it is characterised by other advantages such as hermeticity, bio-compatibility, close thermal matching with silicon, and advantages in high-frequency applications because of its low-loss tangent and high dielectric constant which is also stable over a broad range.[3]

For the current application, the substrate is used to accommodate the logging, interface, and transmission circuitry and the power supply. The LTCC substrate is placed as a lid on a box-shaped housing to protect the support electronics and power unit from environmental attacks. The set up is schematically shown in Figure 2.

*Corresponding author; E-mail: marcel.meuwissen@tno.nl

 1546-198X/2006/4/174/010 doi:10.1166/sl.2006.018

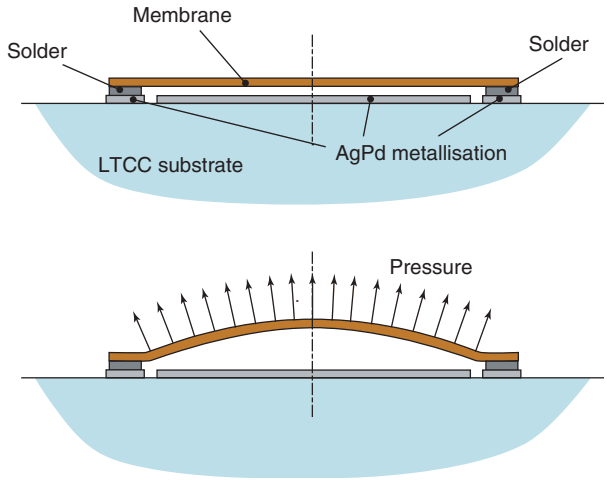

Fig. 1. Pressure sensor consisting of a thin circular membrane mounted onto a Low-Temperature Co-fired Ceramic (LTCC) substrate. In the intended application, a pulling load is exerted on the membrane resulting in an upward deflection.

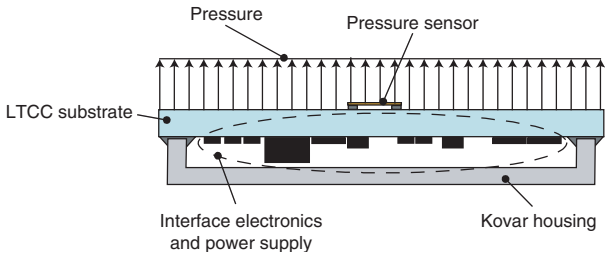

Fig. 2. Schematic layout of the pressure sensor, its supporting electronics, and power supply.

During the design phase of the autonomous pressure sensor, several aspects had to be addressed related to its thermo-mechanical behaviour. Finite element techniques were applied in addition to experiments on physical prototypes to arrive at a thermo-mechanically sound pressure sensor design. In particular, this concerns the following aspects:

- Sensor membrane: (i) response (deflection) to applied pressure, (ii) selection of suitable material and dimensions, (iii) selection of solder interconnect to the LTCC substrate (material and layout).
- LTCC substrate: estimation of its probability of failure under pressure load and selection of suitable dimensions.
- Interconnect between LTCC substrate and Kovar housing: feasibility study.

2. SENSOR MEMBRANE

Simulations of the mechanical response of the sensor membrane and its interconnect to the substrate are aimed at two aspects:
(i) determination of suitable membrane material and dimensions, and
(ii) selection of a suitable solder interconnect material and determination of a feasible interconnect layout.

2.1. Calculated Response of the Sensor Membrane to an Applied Pressure

Because of the simple shape of the sensor membrane, a straightforward analytical model can be derived to describe its mechanical and electrical response to pressure changes. As mentioned in the introduction, a change in pressure difference is detected electrically by a change in capacity. The capacity C for the current configuration is determined from:

$$C(p) = \int_{r=0}^{R_e} \frac{2\pi r \varepsilon}{h(r,p)}\, dr \qquad (1)$$

where, R_e is the radius of the rigid reference plane, ε the dielectric constant of the medium between the two electrodes, p is the pressure, and h is the distance between the upper and lower electrode (see Fig. 3).

The distance between the lower electrode and the membrane is the sum of the initial distance at zero pressure (h_0) and the deflection of the membrane due to the applied pressure. For a clamped circular plate loaded by a uniform pressure, the deflection w is given by[4]:

$$w(r) = \frac{p(R_m^2 - r^2)^2}{64D} \qquad (2)$$

with R_m the radius of the membrane and D the flexural rigidity:

$$D = \frac{Et^3}{12(1-\nu^2)} \qquad (3)$$

where E is the Young's modulus, t is the plate thickness, and ν the Poisson's ratio.

Using Eqs. (1) to (3), the membrane deflection and capacity changes can be calculated for different configurations. The results are summarised in Table I.

The lowest sensitivity is found for a thick Kovar membrane (250 μm) with a small radius (2.5 mm). In addition, the thick copper (200 μm) and LTCC (270 μm) membranes with the same diameter have a relatively low

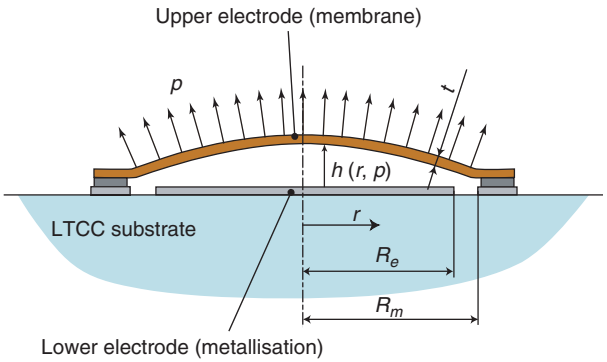

Fig. 3. Explanation of symbols.

RESEARCH ARTICLE

Table I. Maximal deflection and capacity change due to an applied pressure of 5 bar for several configurations (membrane dimensions and materials). Initial gap height h_0 is 40 μm and lower electrode radius $R_e = 1.5$ mm for all configurations.

Configuration			Capacity change [pF]	Maximal deflection of centre [μm]
Material	t [μm]	R_m [mm]		
Cu	200	2.5	0.10	3.5
Cu	100	2.5	1.57	27.7
Fe	100	2.5	0.64	16.6
LTCC	270	2.5	0.05	1.7
LTCC	270	3.5	0.24	6.5
LTCC	135	2.5	0.48	13.6
Kovar	250	2.5	0.04	1.5

sensitivity as well. The other configurations have significantly higher sensitivities.

2.2. Measured Response of the Sensor Membrane to an Applied Pressure

Figure 4 shows the results of an actual experiment using an LTCC membrane. In the experiment an LTCC membrane (thickness 270 μm, radius 2.5 mm) is subjected to a constant pressure for nearly 3 days. The sensor membrane is attached to the substrate by an SnAg3Cu0.5 solder alloy. The electrical capacity is measured with a 0.001 pF resolution.

For the unloaded membrane, the capacity is approximately 2.015 pF. From Eq. (1), the initial electrode distance h_0 is estimated at 31 μm. Using this estimate, the calculated capacity at 5 bar pressure is 2.09 pF, whereas the measured value is slightly less than 2.06 pF.

The sensor shows some capacity drift over the 3 day period (approximately 0.005 pF). This drift may possibly be attributed to time dependent behaviour of the solder material. After removal of the pressure, the membrane does not fully recover to its original deflection. This also indicates the presence of one or more irreversible mechanisms.

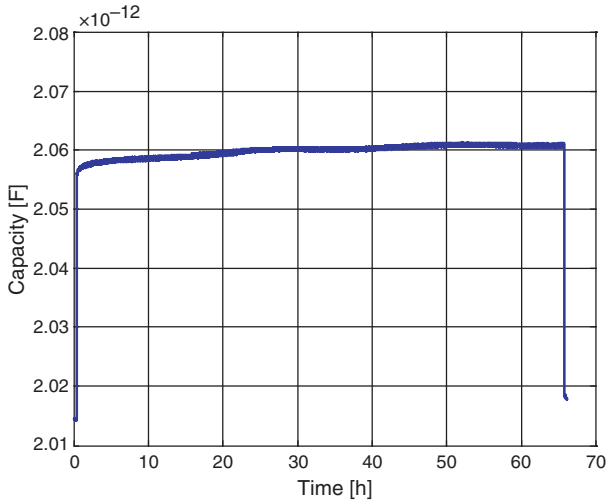

Fig. 4. Measured capacity of a 270 μm thick LTCC (membrane radius $R_m = 2.5$ mm) during testing. At $t = 0$ hours 5 bar pressure is applied, held constant for nearly 66 hours, and removed again.

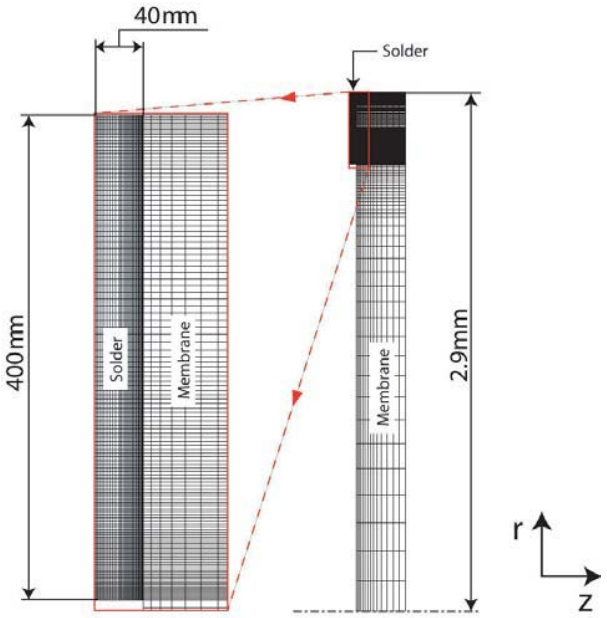

Fig. 5. Finite element mesh used for the axi-symmetric model consisting of the sensor membrane and a solder ring.

2.3. Finite Element Model

In order to gain some insight in the observed drift in the response of the sensor, an axi-symmetric model is implemented in a finite element package. This model comprises of the sensor membrane and a ring of solder material placed at the periphery of the membrane. Characteristics of the mesh of this model are shown in Figure 5. The width of the solder ring is 400 μm and its height is 40 μm. The radius of the membrane is 2.9 mm.

The membrane is assumed to behave linear elastistically whereas a creep law is adopted for the solder material. Simulations are carried out for both SnAgCu solder and eutectic SnPb solder. For the SnAgCu solder, the following creep law is used:[5]

$$\frac{d\varepsilon_{cr}}{dt} = C_1[\sin h(C_2\sigma)]^n \exp\left(\frac{E_{act}}{RT}\right) \qquad (4)$$

where R is the universal gas constant, ε_{cr} the creep strain, σ the stress, and T the temperature. The parameters in Eq. (4) are taken from literature[6] and summarised in Table II.

Table II. Parameters used in the creep Eq. (4) applied for the SnAgCu solder alloy.

Parameter	Value
C1	$7.925 \cdot 10^{+5}$
C2	0.0356 MPa^{-1}
E_{act}	$6.79 \cdot 10^{+4}$ J/mol
n	6

Table III. Parameters in the creep Eq. (5) applied for the eutectic SnPb solder.

Parameter	Value
C	16.534 K mm^2/N s
α	751
Q	$8.78 \cdot 10^{-20}$ J
n	3.3

For describing the creep behaviour of the eutectic SnPb solder the following creep law is applied:[7]

$$\frac{d\varepsilon_{cr}}{dt} = C\frac{G}{T}\left[\sin h\left(\alpha\frac{\sigma}{G}\right)\right]^n \exp\left(\frac{-Q}{kT}\right) \qquad (5)$$

where G is the shear modulus and k is Bolzmann's constant. The other parameters are taken from literature[5] and summarised in Table III. The plastic behaviour of the solder material is neglected in the current simulations. The other parameters required for the model are taken from literatur[8] and summarised in Table IV.

The top surface of the LTCC membrane is loaded by a uniform pressure which is increased linearly from 0 to 5 bar in 100 s and maintained at that level for 3 days.

Figure 6 shows the deflection of the centre of the membrane as a function of time for the two solder alloys. For the SnAgCu solder, the deflection increases by 0.11 μm over 3 days due to creep. From the experiments, the drift was estimated at 0.1 μm. Given the relatively large scatter on LTCC substrate thickness, the unknown thickness h_0, and the relatively crude approximation of the creep behaviour (only second level creep included), the numerical value compares well to the experimental one. For the eutectic SnPb solder alloy, the calculated creep over the 3 day period is much higher: about 0.88 μm.

The calculated stresses in the solder material remained well below the yield stress of the material, indicating that the inclusion of plastic behaviour in the model for the solder is unnecessary.

Figure 7 shows a part of the SnAgCu solder material in the region where the accumulated equivalent creep strain attains the highest values after 3 days. It can be seen that the maximal creep strain is concentrated in a corner-point (singular point). The peak values should thus be treated with care since they are mesh dependent. The strains somewhat further away are approximately 1%.

From the experimental and numerical investigations, it can be concluded that drift leads to an unacceptable

Table IV. Parameters used for the elastic part of the models. The parameters are taken from literature.

Material	Young's modulus [GPa]	Poisson's ratio [−]
Solder (SnAgCu)	38	0.40
Solder (SnPb)	30	0.37
LTCC (membrane)	100	0.30

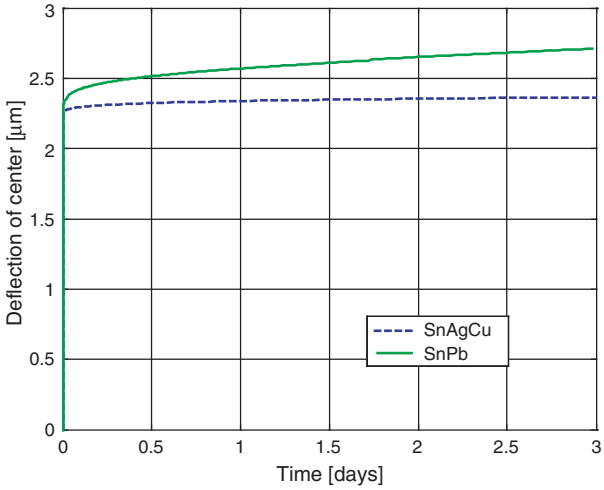

Fig. 6. Calculated deflection of the centre of the membrane during application of a uniform pressure (5 bar).

disturbance of the measurements. After 3 days, the drift on the out-of-plane displacement of the membrane is already 5% whereas a drift of less than 1% is acceptable for the intended application. The simulations support the hypothesis that the drift is caused by creep in the solder interconnect.

The sensor must be able to operate at temperatures up to 60 °C over time periods of up to one year. Higher temperatures generally lead to more pronounced creep behaviour

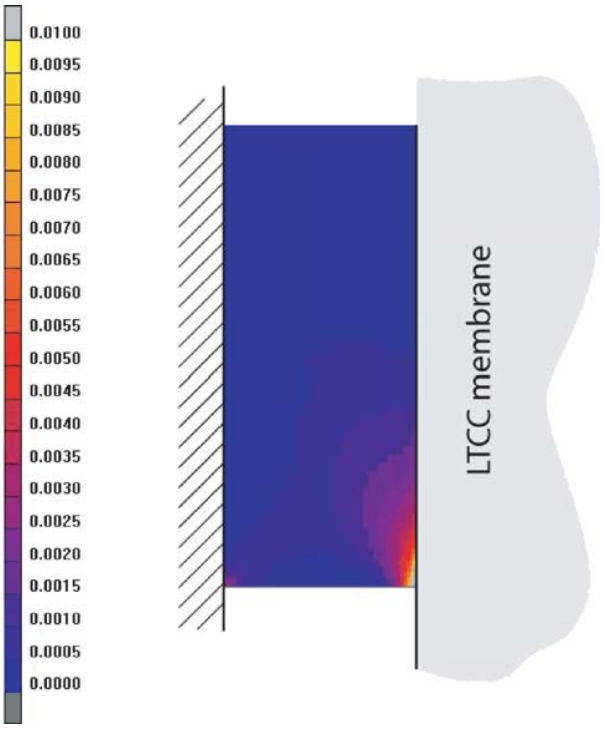

Fig. 7. Accumulated creep strain in the SnAgCu solder interconnect after 3 days under a constant pressure load of 5 bar on the membrane surface.

RESEARCH ARTICLE

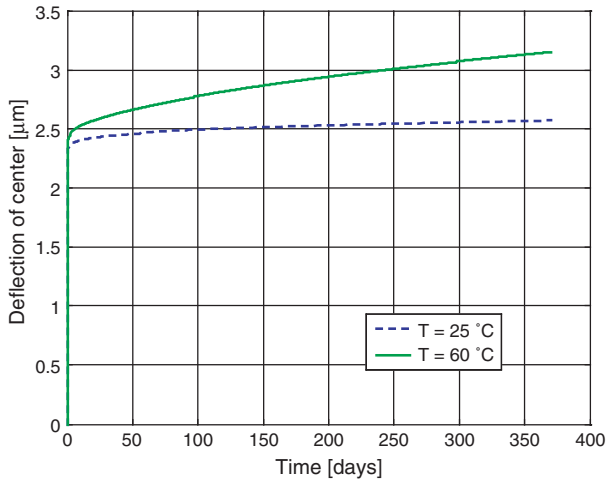

Fig. 8. Calculated displacement of the centre of the membrane as a function of time at a constant pressure on the surface (5 bar) at 25 °C and 60 °C.

in the solder material. The previous analysis is repeated for a time period of 1 year at 25 °C and 60 °C for the SnAgCu solder. It should be noted that 5 bar pressure over 1 year is a worst case scenario for the present application. In practice, it is loaded for much shorter time spans at this pressure level. Figure 8 shows the calculated displacement of the centre of the membrane as a function of time. At 25 °C the drift over a one year time span is 14% whereas the drift has increased to nearly 40% at 60 °C. These high drift values are not acceptable for the current application.

Even for the SnAgCu solder, the drift of the out-of-plane displacement of the membrane is quite high, especially at higher temperatures. The additional deflection is caused by creep deformation in a fairly localised domain in the interconnect. For reducing the creep strains in this region, it is investigated whether a geometrical change of the membrane as shown in Figure 9 can improve the situation.

It is expected that the addition of a reinforcement ring will reduce the localised stress levels in the solder ring and thereby the accumulated creep strain over time.

Initial simulations using this new configuration indeed showed a reduction of drift of the centre of the membrane. These simulations were carried out with relatively arbitrarily values selected for the different geometrical parameters.

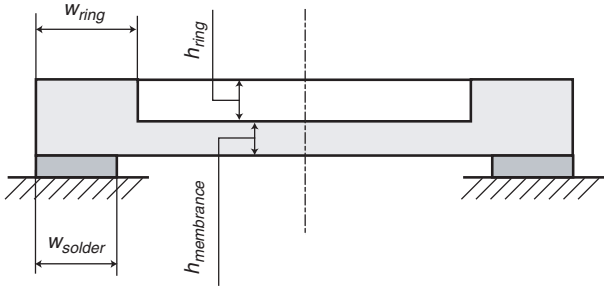

Fig. 9. Adjustments to the LTCC membrane (addition of a reinforcement ring) aimed at reducing the creep strains in the solder interconnect.

In order to determine the sensitivity of these parameters on the drift of the membrane deflection, a Design of Experiments (DoE) approach is utilised.[9] An L8 orthogonal scheme is used. The parameters to be varied are (see Figure 9):

(i) width of the solder ring w_{solder} (low/high: 0.4 mm/0.6 mm),

(ii) width of the reinforcement ring w_{ring} (low/high: 0.7 mm/1.1 mm),

(iii) height of the reinforcement ring h_{ring} (low/high: 405 μm/810 μm),

(iv) thickness of the membrane t_{membrane} (low/high: 135 μm/270 μm.

Within this scheme the following interactions are taken into account: i×ii, i×iii and i×iv.

The relative out-of-plane displacement drift of the membrane (displacement drift divided by initial displacement) over a one year period is used as output for the DoE. The main effects resulting from the DoE analysis are summarised in Figure 10. The optimal configuration is given by $w_{\text{solder}} = 0.6$ mm, $w_{\text{ring}} = 1.1$ mm, $h_{\text{ring}} = 810$ μm, and $t_{\text{membrane}} = 135$ μm.

In the next step, possible interactions with factor w_{solder} have been investigated and depicted in an interactions plot (Fig. 11). The nearly parallel lines for the interactions with the factors w_{ring} and t_{membrane} indicate that there is no significant interaction effect. A rather strong interaction effect can however be seen between the factors w_{solder} and h_{ring}. Since the combination of levels which yield the lowest drift is going to be included in the optimum configuration, no further measures have been taken.

The optimal configuration was not a setting used for the DoE runs. A simulation run with the optimal settings showed a displacement drift of 0.25% over a one year period. For a temperature increase to 60 °C this value increases to 0.5%. Both values are within the design limits.

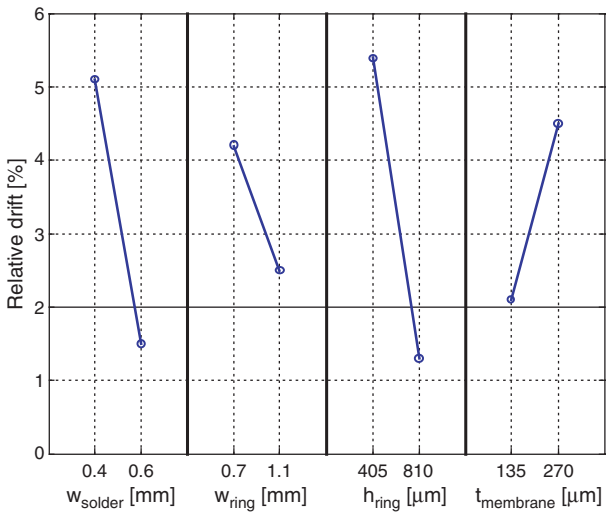

Fig. 10. Main effects of parameters on relative drift.

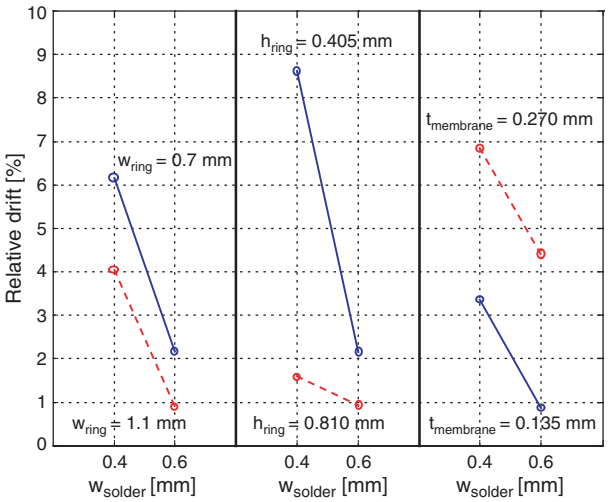

Fig. 11. Interactions between parameters on relative drift.

As a disadvantage of this solution, the additional cost required for fabricating membranes with reinforcement rings should be mentioned. An alternative is investigated in parallel in which use is made of another solder material with lower creep sensitivity: AuSn20. Unfortunately, the creep behaviour of this material has not been as thoroughly investigated as that for the more commonly used SnPb37 and SnAgCu alloys. Due to the lack of appropriate creep models for this material, it was not possible to assess its performance by numerical simulations and therefore physical prototypes incorporating this solder material were built and tested. An example of the response of a membrane attached to the surface with this solder material is shown in Figure 12. The drift in the measured capacity is significantly reduced compared to samples soldered with SnAgCu solder (see for example Fig. 4).

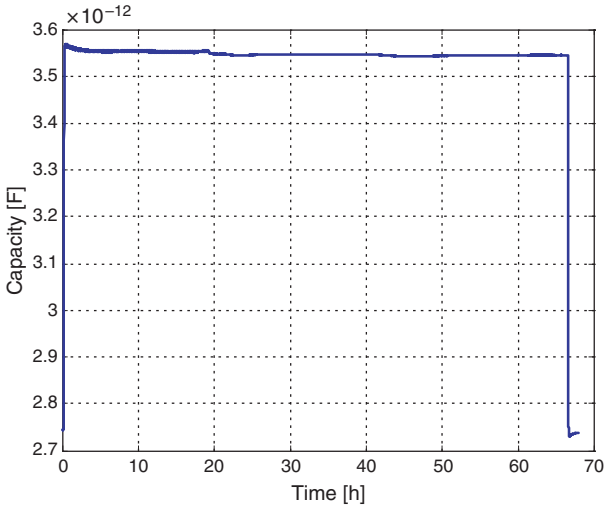

Fig. 12. Capacity measured on a membrane (stainless steel, $t = 200\ \mu$m, $R_m = 2.5$ mm) soldered to the LTCC substrate using AuSn20. At $t = 0$ hours, 5 bar pressure is applied, attained for nearly 70 hours and removed again. The slight drop in capacity is due to a slight reduction in applied pressure during the experiment.

3. LTCC SUBSTRATE

3.1. Probability of Failure

In order to accommodate all electronic components on the backside of the LTCC substrate, the width and length dimensions have to be set to at least 24×55 mm^2. The thickness is determined by the maximal load the substrate has to withstand (5 bar). In order to determine the minimal required thickness, finite element simulations were performed in combination with experiments on the LTCC material.

Among other factors, the critical tensile stress of the LTCC substrate is determined by the materials properties (homogeneity), processing conditions and the particular layout of the layers (orientation, presence of inclusions such as electrically conductive tracks, *et cetera*). Since there is some scatter on these parameters from sample to sample, it can be expected that there will be scatter in the critical strength of the samples as well. Here, the strength of the LTCC material is characterised by applying a Weibull approach.[10, 11] In this approach, the probability of failure is assumed to be a function of the applied stress and the volume under stress:

$$F = 1 - \exp\left[-\int_v \left(\frac{\sigma}{\sigma_0}\right)^m dV\right] \tag{6}$$

where F is the probability of failure, V is the volume, σ is the stress, and σ_0 and m are two parameters to be determined from measurements.

For determining the parameters σ_0 and m, three point bending experiments are carried out on samples with dimensions $10 \times 55 \times 1.6$ mm^3, which were supported on two rollers placed 27 mm apart. These samples were cut

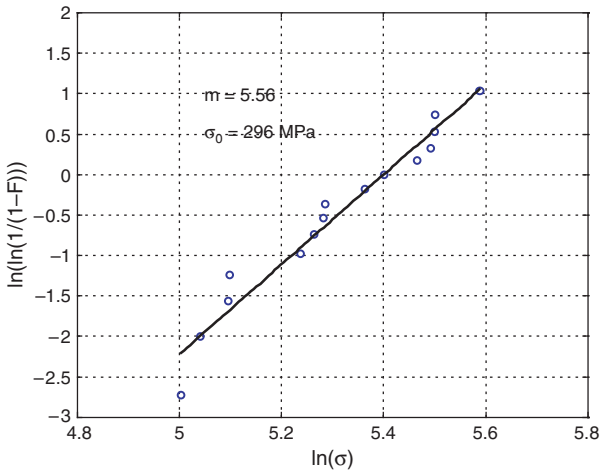

Fig. 13. Measurements and fitted Weibull curve.

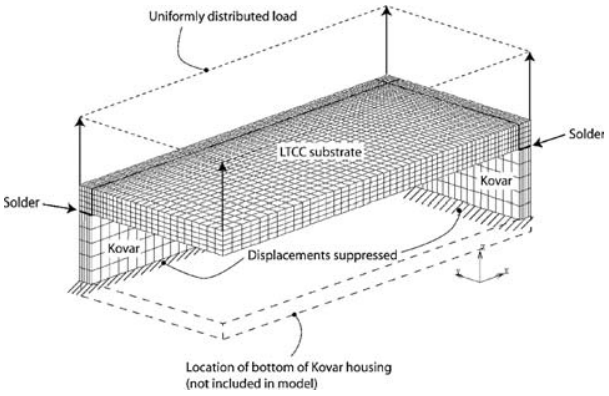

Fig. 14. 3D finite element mesh used for calculating the probability of failure of the LTCC substrate.

from larger LTCC substrates by laser. The characteristics of the sample material were similar to those of the final design (in terms of number of layers, presence of vias, and type of metallization materials).

The results of the bending tests are summarised in Figure 13. This figure also shows the fitted Weibull curve Eq. (6). The fit was determined by linear least squares regression.

The Weibull parameters are used in combination with finite element simulations to determine the probability of failure of a substrate with particular dimensions. For all design variants, the lateral dimensions of the LTCC substrate are set to 24×55 mm.[2] Several thickness values are evaluated in the range from 0.8 mm to 1.6 mm Eq. (6) is used to calculate the probability of failure for a design using for σ the maximal principal strain in a point as calculated with the finite element model. If the maximal principal strain in a point of the substrate is smaller than 0, σ at that location is set to 0 in order to accommodate for the fact that the LTCC material will be able to withstand compressive stresses much better than tensile stresses.

The finite element model for one of the configurations is shown in Figure 14. The model includes the LTCC substrate, a part of the (Kovar) housing and the solder interconnect between the housing and the substrate. The top surface of the substrate is assumed to be loaded by a uniform pressure (directed upward) which is increased from 0 to 5 bar. The displacements on the bottom face of the Kovar housing are suppressed. Due to symmetry in the assembly only one quarter is modelled. The bottom of the Kovar housing was not included in the model as this is

Table V. Parameters used for the elastic part of the constitutive models. The values are taken from literature.

Material	Young's modulus [GPa]	Poisson's ratio[−]
Solder (SnPb)	30	0.37
Kovar	137	0.31
LTCC	100	0.30

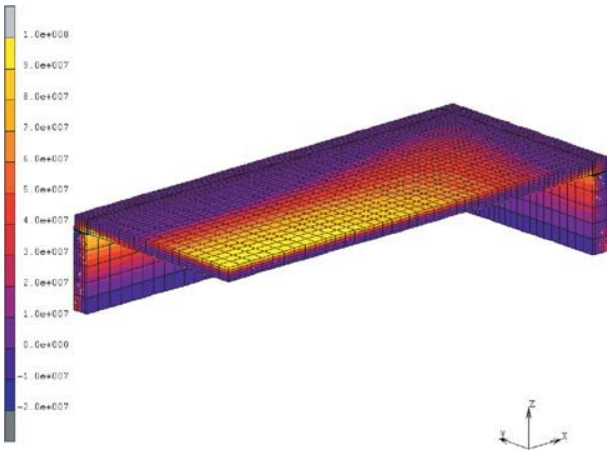

Fig. 15. Maximal principal stress in the assembly at a pressure load of 5 bar for an LTCC substrate thickness of 0.8 mm.

expected to have only a marginal influence on the deformations of the LTCC substrate.

The LTCC and Kovar materials are assumed to behave elastically whereas an elasto-plastic model with bi-linear kinematic hardening is taken for the SnPb solder material.[12] The parameter values are taken from literature and summarised in Table V.

Figure 15 shows the distribution of the maximal principal stresses in the assembly for an LTCC substrate thickness of 0.8 mm and a maximal load of 5 bar.

Using the calculated stresses and the Weibull equation fitted on the measurements, the probability of failure for different configurations can be calculated. The probability of failure is shown in Figure 16 for several values for the LTCC substrate thickness. It can be seen that for the 0.8 mm LTCC thickness, the probability of failure of the substrate at 5 bar pressure is approximately 12.5% whereas this value has dropped to less than 0.04% for the 1.6 mm thickness.

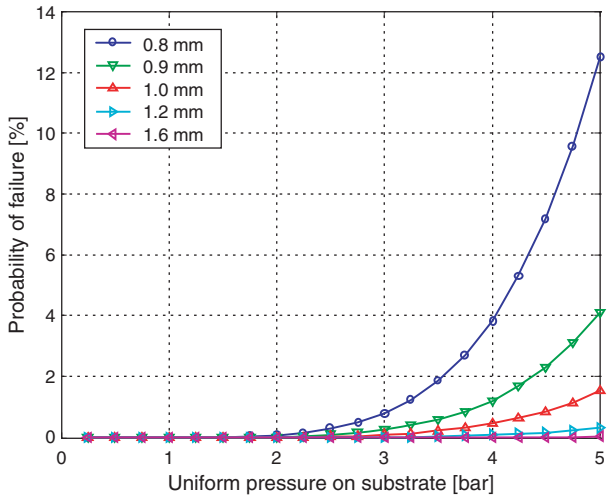

Fig. 16. Probability of failure of the LTCC substrate versus applied pressure for different substrate thicknesses.

4. INTERCONNECT BETWEEN LTCC SUBSTRATE AND KOVAR HOUSING

The second critical solder interconnect in the assembly is that of the LTCC substrate to the Kovar housing (see Fig. 2). In order to investigate the stress levels that develop in this interconnect during pressure load, a finite element model is created of the assembly.

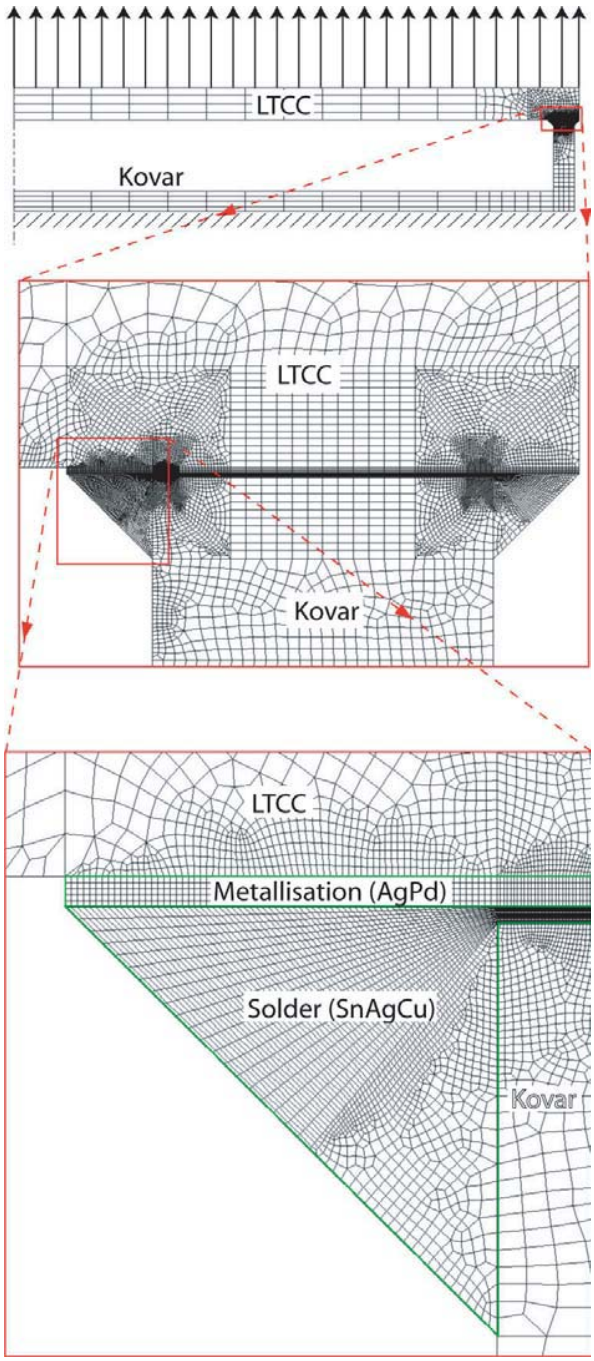

Fig. 17. Finite element model of the LTCC substrate and Kovar housing.

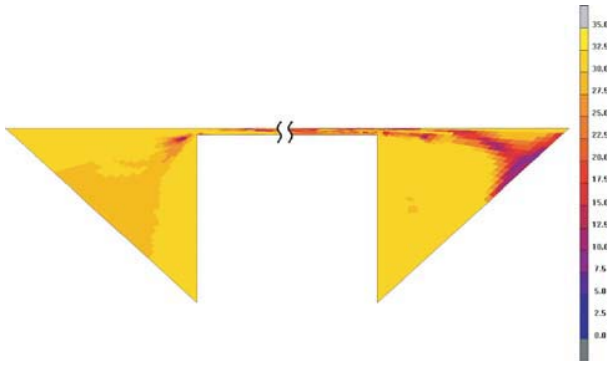

Fig. 18. Equivalent Von Mises stress in the solder interconnect at maximal pressure on substrate surface.

For time efficiency reasons, an axi-symmetric model is used although the assembly actually has a rectangular shape. Given the intended use of this initial model, this simplification is deemed acceptable. Figure 17 shows some details of the finite element mesh.

The LTCC substrate is loaded by a maximal pressure of 5 bar. The bottom (right side in Fig. 17) of the Kovar housing is fixed.

Figure 18 shows the equivalent Von Mises stress in the solder interconnect. The maximal stress is approximately 35 MPa which is well above the initial yield strength of the material (approximately 23 MPa).

As a measure for reducing the stresses on the solder interconnect, the interior of the Kovar housing is filled with an epoxy resin. Repeating the analysis for this new configuration, the maximal stresses in the solder interconnect reduce to an acceptable level of 2 MPa.

A new problem introduced by filling the cavity with epoxy is the thermal mismatch between this material and the other components. This is studied using the same model for a thermo-mechanical analysis. For this analysis, the materials in the assembly are assumed to behave linear elastically except for the solder material which is assumed to behave elasto-plastically.[12] The parameters for the elastic domain were taken from literature except for the epoxy material and AgPd metallisation. For the latter two materials, estimates were made. All parameters used in the simulations are given in Table VI.

Table VI. Parameters in elastic domain. The parameters for the epoxy and metallization materials are estimates. The other parameters are taken from literature.

Component	Young's modulus [GPa]	Poisson's ratio [−]	Coefficient of thermal expansion [ppm/°C]
Solder	38	0.40	23.0
LTCC	100	0.30	6.5
Kovar	138	0.31	3.5
Epoxy	5	0.35	30.0
Metallization	76	0.37	19.6

RESEARCH ARTICLE

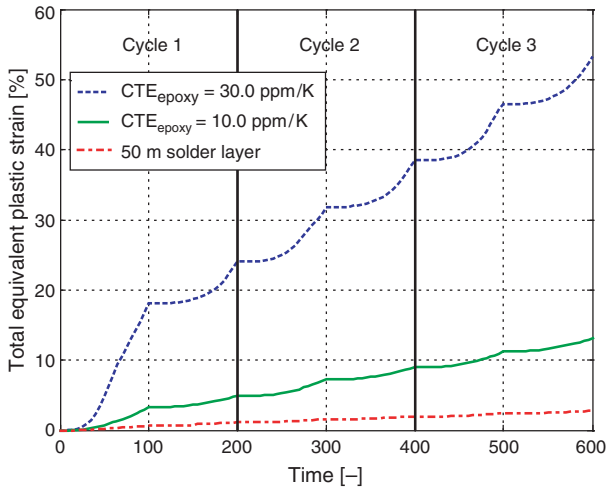

Fig. 19. Equivalent plastic strain in the solder interconnect for two values of the coefficient of thermal expansion (CTE) of the epoxy material.

A uniform temperature is assumed over the whole domain. This temperature is varied in time between −40 °C and 60 °C. A total of 3 cycles is simulated.

Figure 19 shows the development of the equivalent plastic strain during the three temperature cycles. Using the initial value for the coefficient of thermal expansion (30.0 ppm/°C) for the epoxy material, the accumulated strains in one cycle are unacceptably high (around 14%). Choosing the coefficient of thermal expansion of the epoxy material closer to that of the other materials in the assembly (10 ppm/°C), leads to a significant reduction of accumulated plastic strain. It should be mentioned however, that this value is extremely low as the coefficient of thermal expansion of commercially available filled epoxies is typically in the range of 20 to 25 ppm/°C below the glass transition temperature. Nevertheless the strain accumulation is still about 4% per cycle. This strain accumulation is mainly caused by the local thermal mismatch between the solder material and the other materials.

By increasing the solder layer thickness, this strain accumulation can be reduced even further. As an example, Figure 19 also shows the accumulated strain for a solder layer thickness of 50 μm instead of 10 μm. In this situation the accumulated plastic strain is reduced to 0.8% per cycle.

5. PHYSICAL PROTOTYPE

Figure 20 shows a functional prototype of the autonomous system with on top of the LTCC substrate the pressure sensor membrane and the antenna. The LTCC substrate is fabricated in panel form by Via Electronic. The membranes are mounted using a flip chip bonder. This enables both accurate alignment in x- and y-direction and the possibility to maintain the required assembly height of the membrane during soldering. The solder material is AuSn20 which is

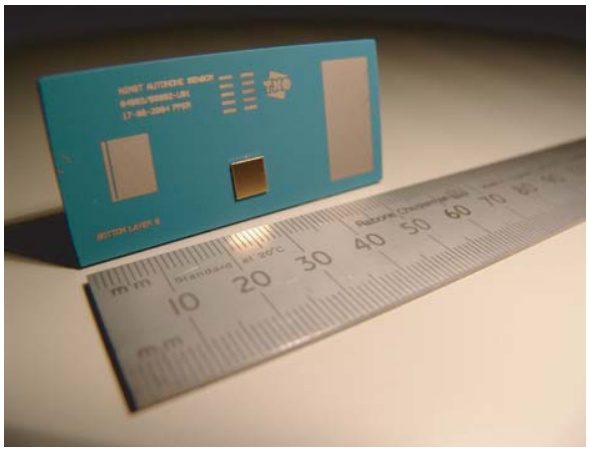

Fig. 20. Complete autonomous system including the sensor membrane, LTCC substrate, and Kovar.

applied as preform. Before further assembly, the pressure sensors are tested by a specially designed tool which can load the sensors in panel form by air pressure. The SMT-components on the secondary substrate side are mounted using a standard refow-soldering process. During this operation the interconnection of the sensor membrane will not re-melt due to the 280 °C melting temperature of AuSn20. After SMT-assembly the systems are cut out by laser and functionally tested. To finally close the systems, a ring of solder paste is printed on the edges of the LTCC substrate, a Kovar housing is placed and subsequently reflow soldered to seal the package. In case a filling is needed, the Kovar housings are provided with laser cut holes. The prototypes proved to meet the functional requirement to measure pressures of up to 5 bar with sufficient sensitivity. Figure 21 shows the results of a step-stress test.

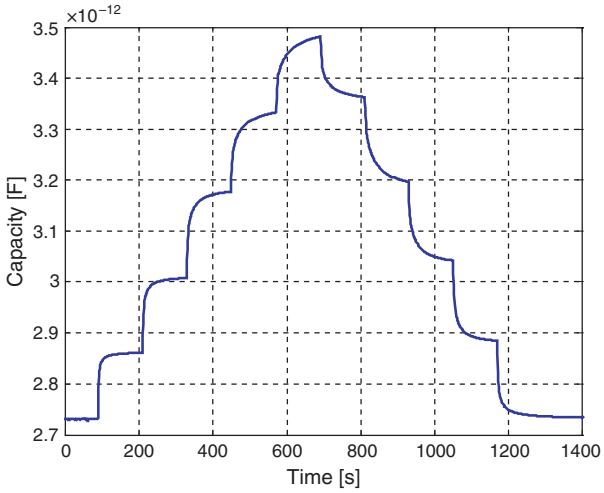

Fig. 21. Response of a pressure sensor to a step-stress test. The relaxation-like variation of the capacity versus time is caused by the testing equipment and the way in which the pressure is applied onto and removed from the sensor membrane.

6. CONCLUSIONS

Numerical simulations have been applied in combination with experiments in the thermo-mechanical design of a pressure sensor. The simulations were applied for the selection of suitable dimensions for the sensor-membrane and LTCC substrate onto which the sensor is mounted. Furthermore, they were applied for determining suitable solder interconnect materials and dimensions.

Initial experiments on a sensor prototype showed an unacceptably high drift of the out-of-plane displacement of the sensor membrane over time. Simulations were conducted to assess several geometrical design changes to reduce this drift. From these simulations it was concluded that the suggested changes did indeed lead to an improved design. However, the design change (addition of reinforcement ring) would also increase the cost of the sensor membrane fabrication. The application of a more creep resistant solder (AuSn20) was investigated as an alternative. Tests on physical prototypes with this solder alloy showed the drift to be reduced within acceptable limits.

The dimensions of the LTCC substrate was partly (width and length) determined by the number and size of the components (logging, interface, and transmission electronics, power supply) that had to be accommodated on it. The thickness of the substrate has been selected based on Weibull statistics.

Finally, the interconnect between the LTCC substrate and the Kovar housing was investigated. It was found that special precautions had to be taken in order to reduce the stresses in the solder interconnect.

The application of simulation techniques led to a significant reduction of the effort required for building and testing of physical prototypes, which in turn reduced design time and costs.

Future work will include life testing of prototypes to assess their long term stability and (thermo-mechanical) reliability.

Acknowledgments: The authors would like to thank Via Electronic GmbH in Germany for their technical support and for producing the LTCC test structures.

References and Notes

1. S. M. Sze, Semiconductor Sensors, John Wiley and Sons Inc. (**1994**).
2. S. A. Campbell and H. J. Lewerenz, Semiconductor Machining, Fundamentals and Technology (**1998**).
3. P. K. Khanna, B. Hornbostel, T. Jäger, and W. Schäfer, *MST News* 4/04, 40 (**2004**).
4. S. P. Timoshenko and S. Woinowsky-Krieger, Theory of Plates and Shells, McGraw-Hill (**1959**).
5. J. H. Lau, Ball Grid Array Technology, McGraw-Hill Inc., New York (**1995**), Chap. 13.
6. J. P. Clech, Review and Analysis of Lead-Free Solder Material Properties (**2004**).
7. R. Darveaux and K. Banerji, *IEEE Trans. Components, Hybrids, Manufact. Technol.* 15, 1013 (**1992**).
8. T. Siewert, S. Liu, D. R. Smith, and J. C. Madeni, Database for Solder Properties with Emphasis on New Lead-Free Solders (**2002**).
9. R. Roy, A Primer on the Taguchi Method, Van Nostrand Reinhold (**1990**).
10. W. Weibull, *J. Appl. Mech.* 18, 293 (**1951**).
11. D. W. Richerson, Modern Ceramic Engineering: Properties, Processing, and Use in Design, Marcel Dekker, Basel (**1992**).
12. S. Wiese, S. Rzepka, and E. Meusel, EuroSimE 2002, Paris (**2002**), p. 79.

SENSOR LETTERS
Vol. 4, 184–190, 2006

RESEARCH ARTICLE

Out of Plane Flexural Behaviour of Thin Polysilicon Films: Mechanical Characterization and Application of the Weibull Approach

Fabrizio Cacchione[1], Alberto Corigliano[1,*], Biagio De Masi[2], and Marco Ferrera[2]

[1] *Department of Structural Engineering, Politecnico di Milano, Piazza L. da Vinci 32, 20133 Milano, Italy*
[2] *MEMS Business Unit. STMicroelectronics, via Tolomeo 1, 20010 Cornaredo, Milano, Italy*

(Received: 6 December 2005. Accepted: 12 April 2006)

A new MEMS for on-chip mechanical testing of 0.7 μm thick polysilicon film has been designed, modelled, and fabricated. The polysilicon film is electrostatically loaded under bending until rupture in the out of plane direction, by means of electrostatic attraction in the direction orthogonal to the substrate. This is at difference with previous works of the same Authors, in which results relevant to in plane loading conditions have been presented. 3D Finite Element (FE) and Boundary Element (BE) models of the structure were used during the design and data reduction phases. Tests were carried out at room temperature and at atmospheric humidity. The measured Young's modulus obtained on 20 tested polysilicon specimens was 174 ± 9 GPa. Rupture stress computed after 21 tests, treated with the Weibull statistical theory, gave Weibull material parameters $\sigma_0 = 2237$ MPa, with a Weibull modulus $m = 5.1$.

Keywords: MEMS, Polysilicon, Mechanical Characterization, Bending Tests, Weibull Approach.

1. INTRODUCTION

The development of polysilicon MEMS technology and the large and fast diffusion of relevant applications, have forced researchers in the direction of a complete and correct characterization of polysilicon at the scale of micron.[1,2] In particular, the issue of MEMS reliability and mechanical characterization of polysilicon has become very important in the recent scientific literature.[3–14] Many approaches have been proposed in order to obtain parameters characterizing the mechanical response of polysilicon: Elastic parameters, rupture strength, and fracture properties under monotonic and cyclic loading.

The Authors have recently proposed a fully on-chip procedure for the characterization of polysilicon, based on *ad hoc* designed MEMS for mechanical testing.[13–16,20] The main advantage of on-chip approaches with respect to out of chip ones is related to the possibility of precisely characterising the same material which is used to produce MEMS without any disturbance induced by the manipulation of small specimens in the laboratory. Another advantage consists in the possibility of avoiding complicate gripping systems and data acquisition methods. In spite of the above mentioned advantages, a series of disadvantages still affect the on-chip methodologies, mainly related to the technological limitations associated to the MEMS production and to the limited possibility to load the specimens in various conditions.

The purpose of the present paper is to present recent results which aim at partially overcoming the limitations on loading conditions related to on-chip approaches. A MEMS has been designed with a parallel plate electrostatic actuator which loads (up to rupture) under out-of plane bending a couple of beam-shaped specimens. By means of a data reduction procedure based on the measurement of the capacitance variation, it is possible to obtain the value of the Young's modulus of the polysilicon specimen and that of the maximum stress at rupture.

The particular loading conditions chosen in the present study have been motivated by two main reasons: The necessity to precisely control an electrostatically actuated movement in the direction orthogonal to the substrate and the need to verify the existence of differences in the elastic and rupture properties of polysilicon for in plane and out of plane bending, possibly related to the anisotropy of the particular structure of the material originated by the production process.

*Corresponding author; E-mail: alberto.corigliano@polimi.it

 1546-198X/2006/4/184/007 doi:10.1166/sl.2006.016

An outline of the paper is as follows. In Section 2 the layout and the main properties of the out-of-plane electrostatic actuator are briefly described. Section 3 is devoted to the description of the data reduction procedure and of numerical simulations. The obtained experimental results and the adopted Weibull approach are discussed in Section 4. Section 5 contains some closing remarks.

2. OUT OF PLANE ELECTROSTATIC ACTUATOR

The purpose of the present work has been the mechanical characterization of thin polysilicon films produced by means of the surface micromachining process called Thelma™ developed and used by the MEMS Business Unit of ST-Microelectronics.[14]

A set of test structures for on-chip fracture characterization of 0.7 μm thick polysilicon film have been designed, modelled, and fabricated. Figure 1 shows the whole device, while Figure 2 is a zoom of the central part where the beam specimens are placed. An holed plate of 15 μm thick polysilicon is suspended on the substrate by means of four elastic springs placed at the four corners. The holed plate is also connected to the thin polysilicon film specimens placed at the centre, as shown in Figure 2. The two symmetric specimens are in turn connected on one side to the holed plate, while on the other are rigidly connected to the substrate. The two specimens are therefore equivalent to a couple of doubly clamped beams. The holes in the plate are due to the etching process for the elimination of the sacrificial layer, thus allowing for movement of the holed plate with respect to the substrate.

The movement in the direction orthogonal to the substrate is obtained by electrostatic attraction of the holed plate towards the substrate. The whole plate and the

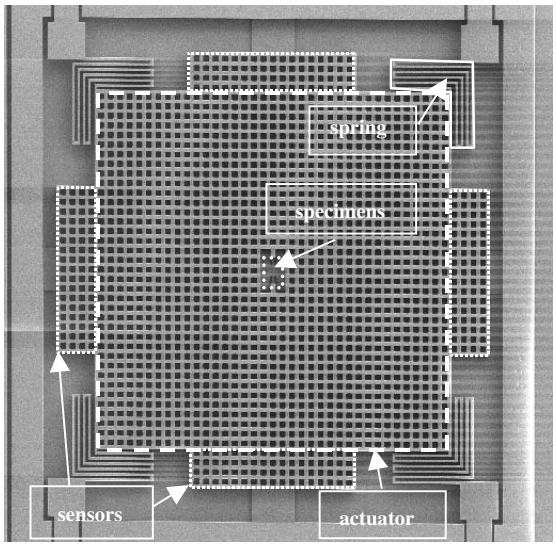

Fig. 1. Parallel plate actuator for out of plane bending tests: general view.

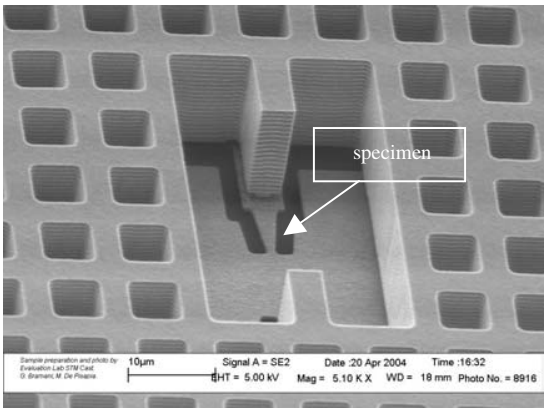

Fig. 2. Parallel plate actuator for out of plane bending tests: detail of one of the specimens.

substrate thus act as a parallel plate electrostatic actuator. When the plate moves towards the substrate, the couple of specimens bend, as schematically depicted in Figure 3.

It is important to remark that only the squared part of the holed plate acts as an actuator (see Fig. 1), while the holed rectangular parts added to each side of the plate act as sensors; these in turn allow for the experimental determination of the capacitance variation and of the vertical movement, as discussed in Section 3.

The choice of on-chip electrostatic actuation was driven by the advantage of great precision and absence of misalignment due to external manipulation.

The length of each specimen is 7 μm; in order to force the rupture in an *a priori* chosen section, their cross section changes with a linearly varying width which decreases from 3 μm to 1 μm (see Fig. 2).

Due to the end constraint of the specimens, the internal stresses were not released. The length of the specimen was kept short enough to avoid Eulerian buckling due to the internal stresses. An estimation of the residual stress gradient was done measuring with a profilometer the deformed shape of released cantilevers fabricated on the same die of the test structure. In order to measure the residual stress, an array of doubly clamped beams with different length was used. The residual stress was then extracted from the buckling load of the shorter beam of the array which undergoes buckling.

A linear elastic 3D FE model of a quarter of the central part of the structure was used during the design phase, in order to optimize the shape of the specimen with the goal to obtain rupture; Figure 4 shows some details of the FE mesh.

Fig. 3. Specimens loaded in bending.

RESEARCH ARTICLE

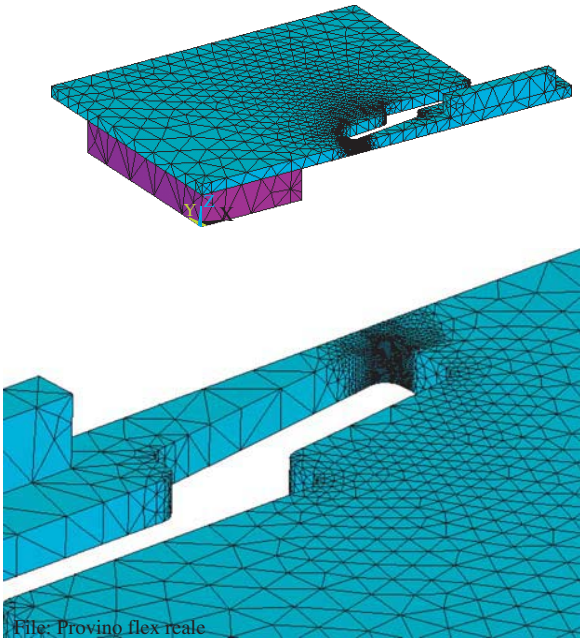

Fig. 4. Details of the Finite Element Mesh.

3. DATA REDUCTION SCHEME AND NUMERICAL SIMULATIONS

Tests were carried out at room temperature and at atmospheric humidity, with a probe station mounted on an optical microscope (see also[14, 20] for further details on the experimental setup). A slowly increasing voltage was applied in order to induce quasi-static loading conditions in the specimen. The input voltage given to the structure and the variation of the capacitance induced by the displacement of the rotor was measured connecting an Agilent Precision LCR Meter between two pads. The LCR resolution, in the range of measures of interest in this work, is ± 1 fF.

The experimentally determined capacitance versus voltage plots were transformed in force versus displacement plots by making use of relationships between capacitance and displacement and between voltage and electrostatic force, respectively. These relations were obtained by means of accurate electrostatic BE and FE simulations given the complex geometry of the actuator and of the sensing system and the subsequent difficulty in applying analytical formulae.

A series of electrostatic BE simulations on one of the lateral sensors allowed for the determination of a capacitance variation versus vertical gap plot, which was directly used in order to transform experimental capacitance variation data in vertical displacements. The analyses were carried out decreasing the gap between the rotor and the stator part of the sensing electrodes from the value 1.8 μm until 0.2 μm, with a step equal to 0.1 μm. Figure 5 shows the BE discretization of one of the sensors, while in Figure 6

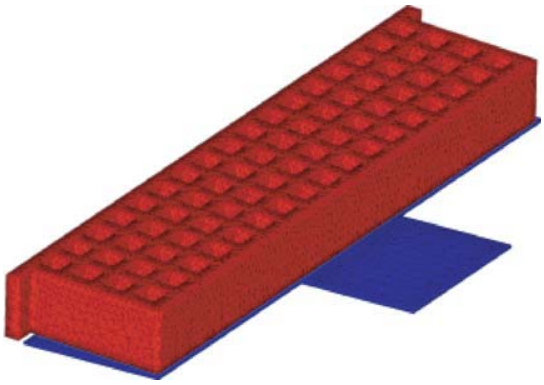

Fig. 5. BE discretization for one of the sensors.

it is shown the obtained sensing capacitance versus gap plot. The BE results were fitted with the expression below, also plotted in Figure 6:

$$g = \frac{0.2598}{C^2 + 1.3112\,C - 0.0315} \tag{1}$$

where g is the gap and C the measured capacitance. Notice that Eq. (1) can be used for values of C greater than 0.0236 pF, which is one of the zeros of the denominator.

FE electrostatic simulations were used in order to obtain the vertical force of attraction on the square holed plate acting as a rotor. In Figure 7 it is shown the 3D model used to this purpose: A quarter of a representative volume containing 100 holes was modelled, surrounded by a large volume of air. The electrostatic field was then found in the air surrounding the polysilicon plate, applying an imposed voltage as boundary conditions.

The analyses were carried out varying the gap between the plate and the substrate, in order to get the force versus gap relationship. The direct result of the analysis was the electrostatic energy of the system. The numerical results were fitted by means of a 6th order polynomial; computing the derivative of the energy with respect to the displacement, it was possible to obtain the force.

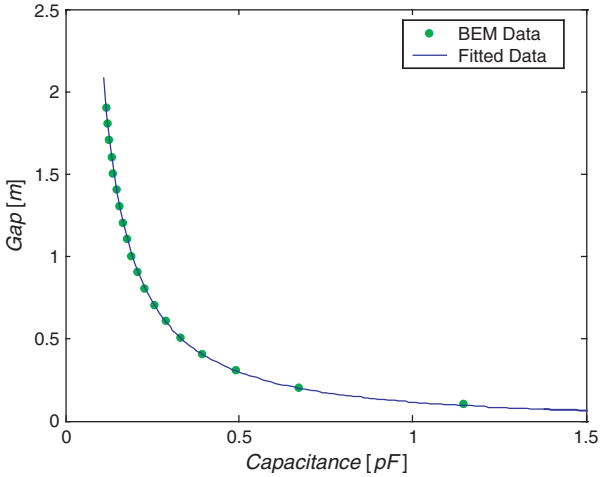

Fig. 6. Sensing capacitance versus gap plot.

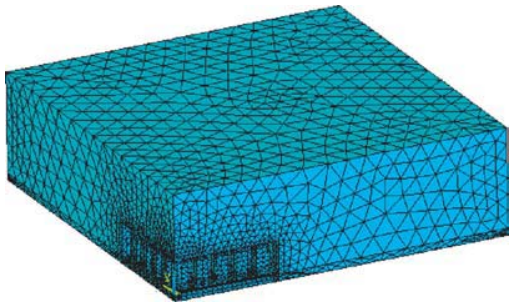

Fig. 7. FE discretization of the air surrounding a part of the actuator.

These results were compared (see Fig. 8) with the analytical formula for the electrostatic force developed by an infinitely thin square plate, without holes, with the same lateral dimensions, taking into account perimetrical fringing effects:

$$F_{\text{act}} = \frac{1}{2}\varepsilon_0\left[\frac{l^2}{(g_0-x)^2} + \frac{P}{2\pi}\frac{1}{(g_0-x)}\right]V^2 \qquad (2)$$

where ε_0 is the permittivity of vacuum, l the side of the plate, V the applied voltage, P the perimeter of the plate, g_0 the gap at rest and x the displacement.

As it is possible to see in Figure 8, in the gap range available for the actuation ($2.8 \div 4.2$ μm), the two curves are almost superposed. From the results of FE electrostatic simulations it was therefore deduced that the attractive vertical force can be computed by making use, with negligible error, of the analytical relation (2).

By means of the above briefly described procedure, the experimental capacitance versus voltage plot was transformed for each test in a force versus displacement one, as in the example shown in Figure 9.

Starting from the force-displacement plot, the force acting on the specimens was obtained by subtracting the part equilibrated by the elastic suspension springs in the four corners of the holed plate (see Fig. 1). An elastic 3D FE solution of the specimen under bending in the vertical plane (Fig. 10) was then used to relate the global stiffness of the specimen to the Young's modulus and the force at rupture to the maximum tensile stress in the specimen. Experimental values of Young's modulus and rupture stress were therefore finally obtained.

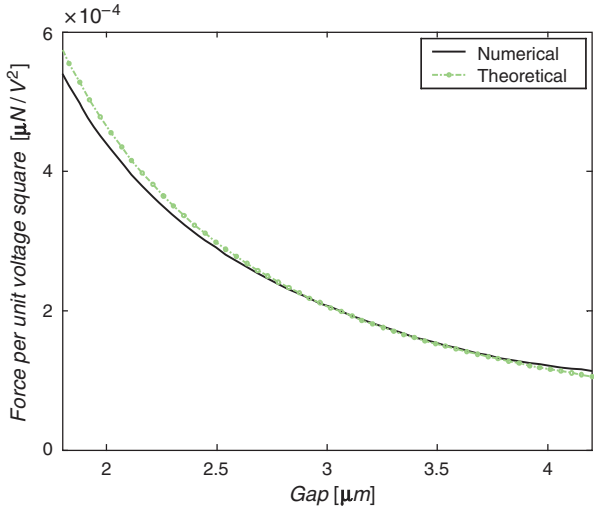

Fig. 8. Actuation force versus gap plots.

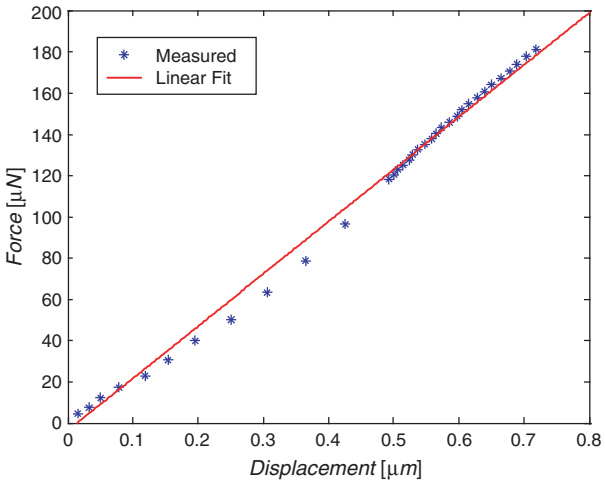

Fig. 9. Force-displacement plots obtained after the data reduction procedure.

The above briefly described data reduction procedure is analogous to that adopted in the previous paper[16] where it is described with more details.

A key point in the data reduction procedure, is the high sensitivity of the results to the value of the vertical gap between the holed plate and the substrate. In order to have an idea of this sensitivity, in Figure 11 a plot of the relative variation of the obtained Young's modulus $\Delta E/E$ versus the relative variation of the gap $\Delta g/g$ is shown. The results of Figure 11 have been obtained by considering the reference values $E = 175$ GPa, $g = 1.6$ μm with g variable in the range $1.5 \div 1.7$ μm. As it can be appreciated from Figure 11, the relative variation of the Young's modulus

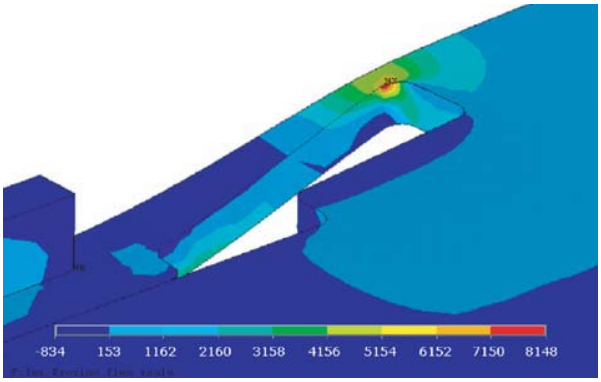

Fig. 10. Example of finite element results: deformed mesh and maximum principal stress (in MPa) obtained with an imposed vertical displacement = 1.4 μm.

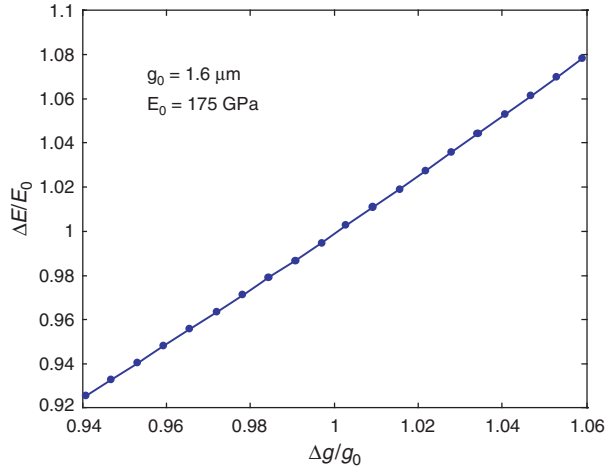

Fig. 11. Relative variation of the Young's modulus with respect to relative variation of the vertical gap.

with respecte to the relative variation of g is of the order of 100%. This fact must be carefully considered in the whole data reduction procedure also because the vertical gap cannot be easily measured on the real device and it can strongly depend on the quality of the etching process. In the results here presented a mean value of $g = 1.65\ \mu$m was used.

4. EXPERIMENTAL RESULTS AND APPLICATION OF WEIBULL APPROACH

The value of Young's modulus obtained from 20 tests was 174 ± 9 GPa, as shown in Figure 12.

The data concerning rupture of the specimens were interpreted in the framework of the Weibull approach for brittle materials,[18, 19] extending what already done in[14] (see also the parallel work.[20]) The application of the Weibull approach allows for a satisfying interpretation of stress gradient and size effects in the experimental rupture data.

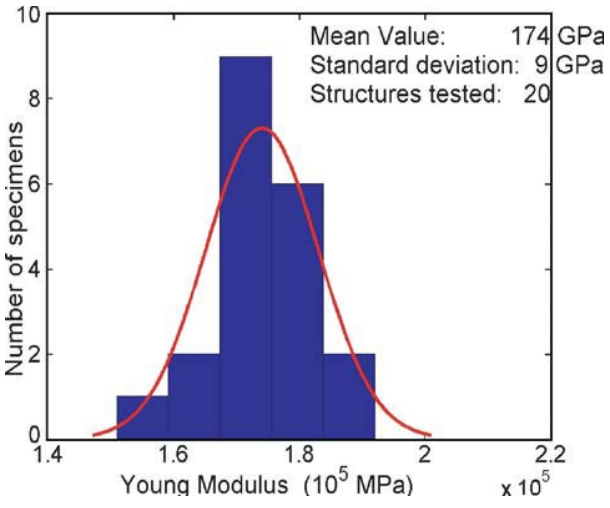

Fig. 12. Distribution of experimental results for the Young modulus.

In the case of a multi-axial, non uniform stress state it is usually assumed that cracks form in the planes normal to the principal stresses $\sigma_1(\mathbf{x})\sigma_2(\mathbf{x})$, $\sigma_3(\mathbf{x})$; the probability of failure is then given by:

$$P_f = 1 - \exp\left[-\frac{1}{\Omega_r}\int_\Omega \sum_{i=1}^{3}\left\langle\frac{\sigma_i(\mathbf{x}) - \sigma_u}{\sigma_0}\right\rangle_+^m d\Omega\right] \quad (3)$$

where Ω is the volume of the solid, Ω_r is a statistically uniform representative volume, σ_u, σ_0, and m are material parameters, $\langle\bullet\rangle_+$ denotes the positive part of $\bullet$ ($\langle\bullet\rangle_+ = \bullet$ if $\bullet > 0$; $\langle\bullet\rangle_+ = 0$, if $\bullet \leq 0$). Equation (3) is obtained from the one usually considered for a uniformly stressed uniaxial bar iterating the hypothesis of statistical uniformity of every volume and computing the joint probability of survival for every infinitesimal volume; a recent discussion can be found in Refs. [19, 20].

The general expression (3) is here applied under the assumption that $\sigma_u = 0$, which means that all level of stresses have an influence on the probability of failure. Equation (3) is then re-written in a more compact way as:

$$P_f = 1 - \exp\left[-\frac{1}{\Omega_r}\int_\Omega \left(\frac{\tilde{\sigma}(\mathbf{x})}{\sigma_0}\right)^m d\Omega\right] \quad (4)$$

once the equivalent stress $\tilde{\sigma}(\mathbf{x})$ is defined by:

$$\tilde{\sigma}(\mathbf{x}) \equiv \left(\sum_{i=1}^{3}\langle\sigma_i(\mathbf{x})\rangle_+^m\right)^{1/m} \quad (5)$$

The above relations can be used in order to estimate the probability of failure P_f of a given structure or solid once the *Weibull parameters* m and σ_0 are known and the elastic distribution of stresses has been computed via analytical formula or numerical solutions, e.g., the FE method.

Parameters m and σ_0 are usually experimentally determined starting from a series of uniaxially tensile tests on cylindrical specimens of volume Ω and surface area A; in this simple case Eq. (3) reduces to:

$$P_f = 1 - \exp\left[-\frac{\Omega}{\Omega_r}\left(\frac{\sigma}{\sigma_0}\right)^m\right] \quad (6)$$

Weibull parameters can be identified also from a specimen or structure loaded in a multiaxial situation with a non-uniform stress distribution, like the one here considered. Let us re-write Eq. (3) in a form similar to (6):

$$\begin{aligned} P_f &= 1 - \exp\left[-\frac{1}{\Omega_r}\int_\Omega \left(\frac{\tilde{\sigma}(\mathbf{x})}{\sigma_0}\right)^m d\Omega\right] \\ &\equiv 1 - \exp\left[-\frac{\Omega}{\Omega_r}\left(\frac{\sigma_{\text{nom}}}{\sigma_0}\right)^m \beta^m\right] \end{aligned} \quad (7)$$

where β is defined by

$$\beta^m \equiv \frac{1}{\sigma_{\text{nom}}^m \Omega}\int_\Omega \sum_{i=1}^{3}\langle\sigma_i(\mathbf{x})\rangle_+^m d\Omega \equiv \frac{1}{\Omega}\int_\Omega (h(\mathbf{x}))^m d\Omega \quad (8)$$

and σ_{nom} represents a nominal stress in the non uniformly stressed specimen or structure, which acts as a scaling parameter for the elastic response. Notice that function $h(\mathbf{x})$ defined by Eq. (8b) depends only on the normalized stress distribution in the linear elastic response and is therefore independent of the load level.

In order to compare the behaviour of different structures, it is possible to define a critical stress level as the nominal stress level $\sigma_{\text{nom}\,0}$ evaluated in the structure when the probability of failure is equal to 63.2%, in full equivalence to the interpretation of σ_0 for a uniaxially, uniformly loaded specimen. From Eq. (6b) it thus follows

$$\sigma_{\text{nom}\,0} = \frac{\sigma_0}{\beta}\left(\frac{\Omega_r}{\Omega}\right)^{1/m} \tag{9}$$

Given two structures (1) and (2), it is therefore possible to write

$$(\sigma_{\text{nom}\,0})_1 = \frac{\sigma_0}{\beta_1}\left(\frac{\Omega_r}{\Omega_1}\right)^{1/m}; \quad (\sigma_{\text{nom}\,0})_2 = \frac{\sigma_0}{\beta_2}\left(\frac{\Omega_r}{\Omega_2}\right)^{1/m};$$
$$\frac{(\sigma_{\text{nom}\,0})_1}{(\sigma_{\text{nom}\,0})_2} = \frac{\beta_2}{\beta_1}\left(\frac{\Omega_2}{\Omega_1}\right)^{1/m} \tag{10}$$

Relations (10) allow us for a direct comparison of the behaviour of structures with different volumes and stress distributions. The variation of parameter $\sigma_{\text{nom}\,0}$ with the volume clarifies the kind of size effect related to the statistical uniform distribution of defects described by a Weibull approach. $\sigma_{\text{nom}\,0}$ is inversely proportional to the volume and this dependence increases with decreasing m; at the limit, by letting m to infinite, the statistical size effect disappears. Noteworthy is also the dependence of $\sigma_{\text{nom}\,0}$ on the parameter β, which in turn depends on the stress non-uniformity.

Further details on the particular application of Weibull theory can be found in the parallel paper.[20] Starting from the experimental values of rupture stress, the statistical treatment implied in the Weibull approach was applied

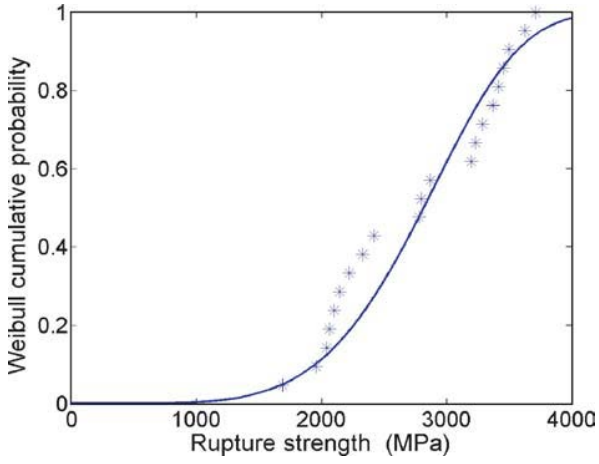

Fig. 13. Weibull cumulative probability of rupture strength.

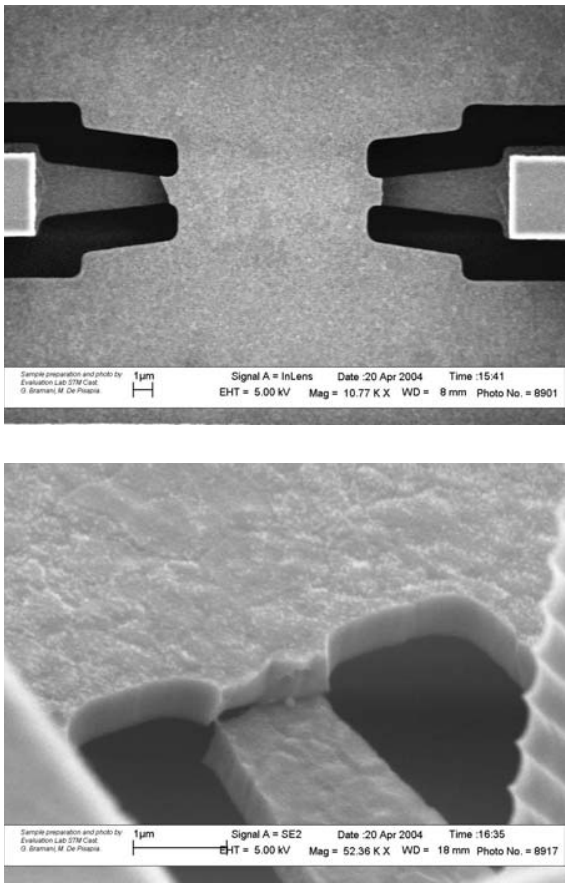

Fig. 14. Specimens after rupture.

taking into account the non-uniformity of the stress field in the specimens; this in turn implies the computation of volume integrals in Eq. (8) on the whole specimen volumes. The whole procedure was based on the 3D FE model already used during the design phase and for the evaluation of rupture stress. Volume integrals were computed by means of a numerical Gaussian integration on each tethraedral FE with quadratic displacement field.

21 specimens have been brought to rupture; the obtained Weibull parameters are $\sigma_0 = 2237$ MPa; $m = 5.1$, while the nominal stress value of Eq. (8) is $\sigma_{\text{nom}\,0} = 3026$ MPa. The experimental results and the cumulated Weibull plot are shown in Figure 13. An example of specimens after rupture is shown in Figure 14 where it can be clearly observed a specimen broken in the thinner cross section, as expected during the design phase.

5. DISCUSSION AND CONCLUSIONS

The results presented in the paper concern an ongoing research activity based on the use of on-chip tests for the mechanical characterization of thin polysilicon films.

A set of test structures was designed and fabricated to characterize the flexural behaviour of polysilicon films in a plane orthogonal to the substrate and to evaluate the

possible influence of grain morphology on the mechanical response. The device has been based on a holed parallel plate actuator which is attracted by the substrate in the direction orthogonal to it. A system of elastic springs keeps the holed plate suspended over the substrate. A couple of bending specimens is placed at the centre of the device.

The electrostatic actuation in the vertical direction developed loads large enough to break the specimen, as expected during the design phase.

In parallel works,[16, 20] results concerning the rupture properties of polysilicon captured by means of in-plane loading have been recently published. In particular, results concerning 0.7 μm thick polysilicon film with have been discussed.[20] The Weibull parameters there obtained are $\sigma_0 = 1840$ MPa; $m = 6.2$, which are different from those obtained in the present work for out of plane loading: $\sigma_0 = 2237$ MPa; $m = 5.1$. A possible explanation for the remarkable difference obtained in the two sets of Weibull parameters can be the influence of different loading conditions which could locally initiate different rupture mechanisms. As already discussed at the end of Section 3, an additional reason for possible discrepances in the results can be found in the influence of geometrical parameters like the gap between the holed plate and the stator.

Careful consideration and possible improvements in the whole data reduction procedure seem to be necessary before judging the present preliminary results as representative of the possibly remarkable difference between in plane and out of plane behaviour of polysilicon films.

Acknowledgment: The contribution of EU NoE Design for Micro and Nano Manufacture (PATENT-DfMM), contract n°: 507255 is gratefully acknowledged.

References and Notes

1. J. W. Gardner, V. K. Varadan, and O. O. Awadelkarim, Microsensors MEMS and Smart Devices, Wiley, Chichester **(2001)**.
2. S. E. Lyshevski, MEMS and NEMS, Systems Devices and Structures, CRC Press, Boca Raton **(2002)**.
3. S. Greek, F. Ericson, S. Johansson, and J. A. Schweitz, *Thin Solid Films* 292, 247 **(1997)**.
4. P. M. Oostemberg and S. D. Senturia, *J. Microelectromech. Syst.* 6, 107 **(1997)**.
5. W. N. Sharpe, K. T. Turner, and R. L. Edwards, *J. Exp. Mech.* 39, 162 **(1999)**.
6. H. Kahn, R. Ballarini, R. L. Mullen, and A. H. Heuer, *Proc. R. Soc. Lond. A* 455, 3807 **(1999)**.
7. H. Kahn, N. Tayebi, R. Ballarini, R. L. Mullen, and A. H. Heuer, *Sens. Actuators A* 82, 274 **(2000)**.
8. T. Ando, M. Shikida, and K. Sato, *Sens. Actuators A* 93, 70 **(2001)**.
9. I. Chasiotis and W. G. Knauss, *Exp. Mech.* 42, 51 **(2002)**.
10. J. Bagdahn and W. N. Sharpe, Jr., *J. Microelectromech. Syst.* 12, 302 **(2003)**.
11. D. Gao, C. Carraro, V. Radmilovic, and R. T. Howe, *J. Microelectromech. Syst.* 13, 972 **(2004)**.
12. C. S. Oh, H. J. Lee, S. G. Ko, S. W. Kim, and H. G. Ahn, *Sens. Actuators* 117, 151 **(2005)**.
13. A. Villa, B. De Masi, A. Corigliano, A. Frangi, and C. Comi, *Proceedings Second MIT Conference on Computational Fluid and Solid Mechanics*, Boston, Elsevier **(2003)**, Vol. 1, P. 722.
14. Corigliano, B. De Masi, A. Frangi, C. Comi, A. Villa, and M. Marchi, *J. Microelectromech. Syst.* 13, 200 **(2004)**.
15. B. De Masi, A. Villa, A. Corigliano, A. Frangi, C. Comi, and M. Marchi, *Proceedings MEMS04*, Maastricht **(2004)**.
16. F. Cacchione, B. De Masi, A. Corigliano, and M. Ferrera, *Sens. Lett.* 4, 38 **(2006)**.
17. W. Weibull, *J. Appl. Mech.* 18, 293 **(1951)**.
18. P. Stanley and E. Y. Inanc, Probabilistic Methods in the Mechanics of Solids and Structures. in *Proceedings Symposium to the memory of W. Weibull*, Stockholm, Springer-Verlag, Berlin **(1984)**.
19. Z. Bažant, Y. Xi, and S. Reid, *J. Eng. Mech. ASCE* 117, 2609 **(1991)**.
20. A. Corigliano, F. Cacchione, B. De Masi, and C. Riva, *Meccanica.* 40, 485 **(2005)**.

SENSOR LETTERS
Vol. 4, 191–199, 2006

Multiphysics for Structural Topology Optimization

Zhenyu Liu[1,*], Jan G. Korvink[1], and Michael L. Reed[2]

[1] Department of Microsystems Engineering, University of Freiburg-IMTEK, Freiburg D-79110, Germany
[2] Department of Electrical and Computer Engineering, University of Virginia, Charlottesville, VA, USA

(Received: 28 November 2005. Accepted: 12 April 2006)

Coupled simulation environment for MEMS devices are already available in a variety of commercial and freeware software packages. However, structural optimization for the multiphysics case has not been fully discussed yet. In most published cases, the optimization algorithm merely follows the traditional single-field problem case, in which design variable and sensitivity are updated sequentially. This paper presents a promising method to implement structural topology optimization via a fully coupled partial differential equation (PDE) expression. The multiphysical structural optimization is integrated via derivation of a suitable Lagrangian-Euler equation. The update of the structural topology is implemented through evolving material boundaries with the level set method. The accuracy of the boundary position is preserved with the h-adaptive mesh refinement method. A benchmark example of structural topology optimization which includes coupled effects is presented in order to demonstrate the feasibility of this method.

Keywords: Topology Optimization, Level Set Method, Moving Mesh Method, Finite Element Method, FEMLAB.

RESEARCH ARTICLE

1. INTRODUCTION

Microelectromechanical systems (MEMS) are miniaturized devices that consist of both mechanical and electrical parts. These systems can sense and actuate on a micro scale and can function individually or be arrayed on a macro scale.[1–3] A realistic physical model for a MEMS device can compose all areas of continuum physics, such as the mechanical, thermal, and electromagnetic energy domains. On accurate numerical simulation for MEMS device should include a single mathematical expression for each energy domain and possible interactive coupling among all the energy domains (Fig. 1).[4] Because of the complexity of coupling effects, an efficient numerical algorithm to solve the coupled PDE is a key point in order to obtain a reasonable numerical solution. Generally, there are two methods to discretize the coupled PDEs. The first is the sequentially de-coupled method by which the coupled PDEs are de-coupled and then all the PDEs are solved sequentially. The second is the direct method in which the coupled PDEs are discretized together and all the unknowns are solved simultaneously. For the sequentially de-coupled method, it is easy to find a suitable algorithm for each PDE. However, the solving sequence of the de-coupled PDEs will influence the convergence and accuracy of the numerical solution. In the case of direct discretization, the coupling effect is directly included in the discretized equations. However, this procedure will result in a large scale nonlinear equation system which needs an efficient numerical algorithm to obtain a converged solution. Nonlinear algorithms have experienced major progress and the direct discretization method is becoming more popular in MEMS simulation.

To date, fully coupled simulation environments have been implemented in several commercial and freeware software packages.[5–7] However, structural optimization for multiphysics has not been discussed adequately. The optimization algorithm merely follows the traditional single-field problem case, in which the optimization procedure is implemented by iterations of sequentially coupled solvers for direct physical problems and sensitivity analysis. Because of the multiphysical interaction, the sensitivity of coupled problem is really complicated in most cases.[8–12] An integrated and efficient simulation and optimization methodology for multiphysics is needed for MEMS devices. In this paper, we discuss a coupled optimization method for a single objective function, a single constraint and multiple fields in MEMS. All the numerical examples in this paper are implemented in the software environment FEMLAB.[6]

*Corresponding author; E-mail: zhenyu@imtek.de

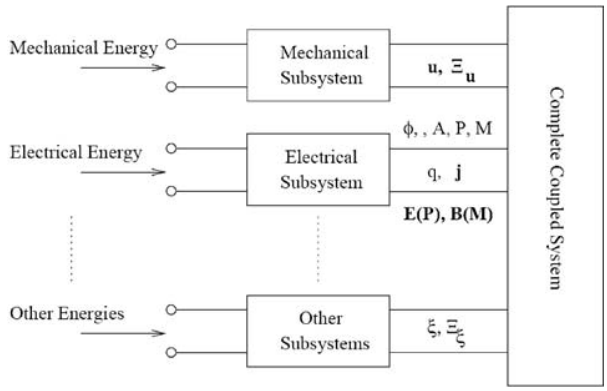

Fig. 1. Coupled physical domains in MEMS device.

2. FULLY COUPLED PDE FORMULATION FOR SINGLE-FIELD STRUCTURAL TOPOLOGY OPTIMIZATION

Structural optimization has great potential to improve the performance of MEMS device. Generally, one has to follow the optimization procedure as shown in Figure 2. Because of the complexity of coupled effects in MEMS devices, the sensitivity analysis is very complicated in most cases. Typically, the element density type method, such as the SIMP (solid isotropic microstructures with penalization) method is used to implement structural topology optimization.[13] However, the expression of the structural layout is non-smooth because of piece-wise constant density value is used to express the material domain. Even though this will not cause serious numerical problems for the structural optimization of pure mechanical problems, a material non-smooth expression will lead to unexpected results for other types of structural optimization, such as thermal problems.[14] One of the simplest remedies to overcome the problem of a material non-smooth expression is the nodal density type method, where material density is interpolated smoothly with nodal density values.[15] In MEMS simulation, the actuation force is normally either a body force or a surface force. During structural topology optimization, these two kinds of forces are referred to as design-dependent loads, which mean that the load vector changes with the evolution of the structural layout.[16] With either the element or nodal density type method, there is no explicitly defined material boundary. So the implementation of the design-dependent load is not straightforward. Basically, the level set method belongs to the shape optimization method. Because of its ability to merge holes during the optimization, it has recently become popular in structural topology optimization. When compared with the density type method, one of the distinguishing advantages of the level set method is that the material boundary is expressed with the zero level set contour, therefore the design dependent load is easily implemented during the optimization procedure.[17, 18] Here we introduce the use of the level set method to transform a typical optimization procedure to a coupled PDEs expression, so that the structural optimization procedure can be solved as a pseudo-time dependent coupled PDE problem.

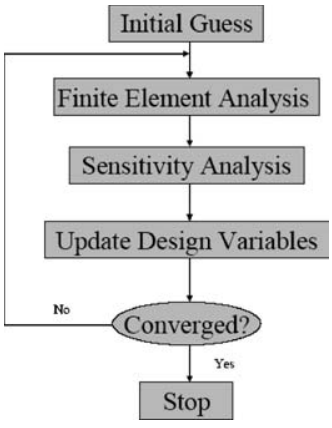

Fig. 2. The procedure of structural optimization.

2.1. Mechanical Problem

A typical structural topology optimization problem for 2D compliance minimization can be written as

$$\left.\begin{aligned} \min: \quad & C(\phi,\varepsilon)=\int_\Omega \frac{1}{2}E(\phi)\varepsilon^T D\varepsilon d\Omega \\ \text{s.t.} \quad & \nabla\cdot(E(\phi)\sigma)=f \\ & \int_\Omega H(\phi)d\Omega=\mathrm{Vol}^* \end{aligned}\right\} \tag{1}$$

where the design domain is represented by Ω, the linear elastic equilibrium equation is used to calculate the displacement field u, strain tensor is ε and stress tensor is σ, E is the design variable which is defined by the level set surface Φ as $E(\phi)=H(\phi)+(1-H(\phi))E_{\min}$, where $E_{\min}$ is a small number, such as 0.001, to avoid singularity of the stiffness matrix, D is the elasticity matrix in which the material Young's modulus is E_0, and Vol^* is the material volume constraint in the design domain. The Heaviside function $H(\phi)$ is defined as

$$H(\phi(x))=\begin{cases} 0 & \phi\le 0 \\ 1 & \phi>0 \end{cases} \tag{2}$$

and the derivative of the Heaviside function, $\delta(\phi)$ is defined as

$$\delta(\phi(x))=\frac{dH(\phi(x))}{d\phi} \tag{3}$$

The level set function $\phi(x)$ is an implicit function for a given domain Ω with smooth boundary which satisfies

$$\left.\begin{aligned} &\phi(x)>0 \quad x\in\Omega^+ \text{ (material)} \\ &\phi(x)=0 \quad x\in\partial\Omega \text{ (boundary)} \\ &\phi(x)<0 \quad x\in\Omega^- \text{ (hole)} \end{aligned}\right\} \tag{4}$$

The area constraint condition which is typically used in compliance minimization design is presented. The

optimization problem (1) can be solved by the level set method.[19, 20] To derive the level set equation which moves the material boundaries, we combine the objective function and constraints together by using a Lagrangian formulation, and then derive a corresponding Euler-Lagrangian equation.

Using the Lagrangian multiplier λ, we can rewrite problem (1) as

$$J(\varepsilon, \phi, \lambda) = \int_\Omega \left[\frac{1}{2} E(\phi) \varepsilon^T D \varepsilon + \lambda \left(H(\phi) - \frac{\text{Vol}^*}{\text{Vol}^\Omega} \right) \right] d\Omega \tag{5}$$

where Vol^Ω is the area of the entire design domain. From classical calculus, we know that the extrema of functional (5) is attained at the position where $J' = 0$. To obtain the level set equation which uses a level set surface to express the structural topology implicitly, we need to calculate the variation of the level set surface. For the variation of a material domain which is expressed by the Heaviside function of the level set surface ϕ, we have

$$\delta H(\phi) = \frac{\partial H(\phi)}{\partial \phi} \delta\phi = \delta(\phi)\delta\phi = \delta\phi|_{\phi=0} \tag{6}$$

Where $\delta\phi$ is the variation of ϕ, and $\delta(\phi)$ is the Dirac delta function. Based on knowledge of structural shape optimization, only the normal velocity on the material boundary will influence the change of the shape, the tangential velocity will not influence the deformation of the geometry, merely its parameterization. We assume that the zero level set contour ($\phi = 0$) moves only in the normal direction. For an infinitesimal variation δl which is along the normal direction $\bar{n}$, a new zero level set is ϕ' and we have

$$\begin{aligned} \delta\phi|_{\phi=0} &= \phi'(x) - \phi(x) = \phi(x + \delta l \cdot \bar{n}) - \phi(x) \\ &= \nabla\phi \cdot (\delta l \cdot \bar{n}) = |\nabla\phi| \delta l \end{aligned} \tag{7}$$

where the normal vector $\bar{n} = \nabla\phi / |\nabla\phi|$. For problem (5), the variation of the level set surface on the material boundary can be expressed as

$$\delta_\phi J = \int_\Omega \left[\frac{1}{2}(1 - E_{\min}) \varepsilon^T D \varepsilon + \lambda \right] \delta(\phi) |\nabla\phi| \delta l \, d\Omega \tag{8}$$

The corresponding Euler-Lagrangian equation at the extreme value point is

$$\left[\frac{1}{2}(1 - E_{\min}) \varepsilon^T D \varepsilon + \lambda \right] \delta(\phi) |\nabla\phi| = 0 \tag{9}$$

In most cases, it is impossible to solve Eq. (9) directly. One general technique is to solve the level set equation numerically

$$\frac{\partial \phi}{\partial t} - \left[\frac{1}{2}(1 - E_{\min}) \varepsilon^T D \varepsilon + \lambda \right] \delta(\phi) |\nabla\phi| = 0 \tag{10}$$

The auxiliary variable t is used as pseudo time. The method is also called gradient descent flow. In the case of a well-posed optimization problem, the solution can hopefully converge to a local minimum based on different initial values. As a result, we can solve the coupled PDEs. So the 2D compliance minimization topology optimization problem can be transformed into the following coupled plane stress equation and time-dependent reaction-diffusion equation

$$\left.\begin{aligned} &\nabla \cdot (E(\phi)\sigma) = f \\ &\frac{\partial \phi}{\partial t} - \left[\frac{1}{2}(1 - E_{\min}) \varepsilon^T D \varepsilon + \lambda \right] \delta(\phi) |\nabla\phi| = \alpha \Delta\phi \end{aligned}\right\} \tag{11}$$

with a suitable initial condition for ϕ_0. Here an artificial diffusion term $\alpha\Delta\phi$ is added to overcome numerical oscillations during the evolution of level set surface. The coefficient α is proportional to the mesh size and reaction term. The Lagrangian multiplier is expressed as

$$\lambda = -\frac{\int_\Omega [1/2(1 - E_{\min}) \varepsilon^T D \varepsilon] \delta^2(\phi) |\nabla\phi| d\Omega}{\int_\Omega \delta^2(\phi) |\nabla\phi| d\Omega} \tag{12}$$

Here we call the first equation in Eq. (11) the state equation for the direct problem and the second equation the optimization equation for the structural optimization problem. Figure 3 is a typical example of a compliance minimization structural topology optimization problem. The short cantilever beam is clamped on the left side and a vertical force acts on the midpoint of the right side. The area constraint condition is 0.3 Vol^Ω. The design domain is discretized with 2466 triangular linear elements.

2.2. Electrostatic Problem

In topology optimization, one of the most commonly used objective functions is the stored potential energy inside a

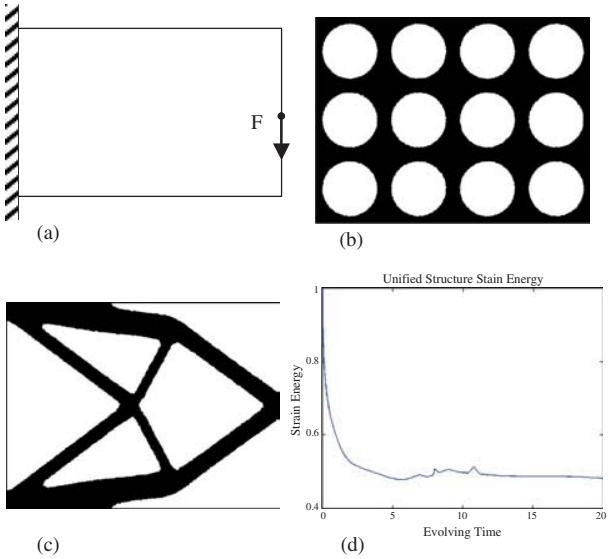

Fig. 3. Structural topology optimization of a purely mechanical problem. (a) design domain (b) initial structural topology (c) optimized structural topology (d) optimization procedure of the structural strain energy.

design domain. For the electrostatic problem, the electric energy can be expressed as $\mu(\phi)\nabla V^T \nabla V/2$, where V is the electric potential, ∇V is the electric field vector, μ is dielectric permittivity which is defined by a level set surface Φ as $\mu(\phi) = \mu_{\text{mat}} H(\phi) + (1 - H(\phi))\mu_{\text{air}}$ where μ_{air} is the dielectric permittivity of the air and μ_{mat} is the dielectric permittivity of the design material. The equilibrium equation which controls the electrostatic problem is the Poisson equation. Following a similar procedure as for the mechanical problem, a maximization of the electrostatic energy problem can be expressed as

$$\left.\begin{aligned} \max: \quad & C(\phi, \nabla V) = \int_\Omega \frac{1}{2}\mu(\phi)\nabla V^T \nabla V d\Omega \\ \text{s.t.} \quad & \nabla \cdot (\mu(\phi)\nabla V) = 0 \\ & \int_\Omega H(\phi) d\Omega = \text{Vol}^* \end{aligned}\right\} \tag{13}$$

A fully coupled PDE expression of topology optimization for the electric potential energy problem with area constraint can be similarly expressed as

$$\left.\begin{aligned} & \nabla \cdot (\mu(\phi)\nabla V) = 0 \\ & \frac{\partial \phi}{\partial t} - \left[\frac{1}{2}(\mu_{\text{mat}} - \mu_{\text{air}})\nabla V^T \nabla V + \lambda\right]\delta(\phi)|\nabla \phi| = \alpha \Delta \phi \end{aligned}\right\} \tag{14}$$

where

$$\lambda = -\frac{\int_\Omega [1/2(\mu_{\text{mat}} - \mu_{\text{air}})\nabla V^T \nabla V]\delta^2(\phi)|\nabla \phi| d\Omega}{\int_\Omega \delta^2(\phi)|\nabla \phi| d\Omega} \tag{15}$$

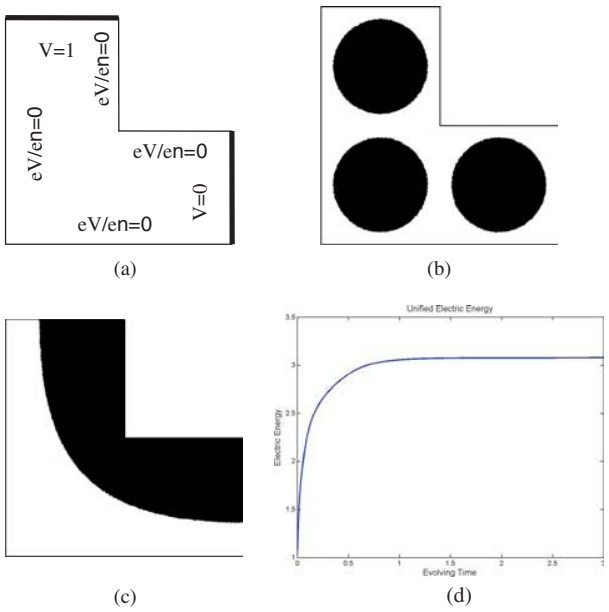

Fig. 4. Structural topology optimization of a purely electrostatic problem for maximum stored energy. (a) design domain (b) initial structural topology (c) optimized structural topology (d) optimization procedure of the electric energy.

For the same reason as for the mechanical problem, an artificial diffusion term is added in the right hand of the second equation in Eq. (14). Figure 4 is a typical example of an energy maximization structural topology optimization problem. The L-shape domain is chosen as design domain with given potential and insulation boundary conditions. The area constraint condition is 0.5 Vol^Ω. The design domain is discretized with 2561 triangular linear elements. Since we know that the electrical field is concentrated at the inner bend of the L-shaped domain, we see that the optimized structure is correct, since the optimization procedure places the material with higher dielectric constant here.

3. H-ADAPTIVE MESH REFINEMENT FOR STRUCTURAL TOPOLOGY OPTIMIZATION

The application of the level set method to structural topology optimization has provided a new level of flexibility in expressing the change of topology when compared with the element density method. Usually, a design domain with regularly distributed mesh is discretized and the whole iterative procedure is based on this fixed mesh. The accuracy of the finite element solution and the position of the boundaries are largely dependent on the mesh density. Thus one has to discretize the design domain with a reasonable number of elements in order to balance the computational cost and the accuracy of boundary position. Mesh adaptation has become an indispensable tool in the numerical solution of partial differential equation in order to improve the computational accuracy and efficiency. This is especially useful in domain in which time-dependent gradient concentration or large solution variations occur within the physical solutions.

There are three methods in which the dynamic mesh adaptation can be implemented, p-adaptation, h-adaptive mesh refinement (H-AMR) and the r-adaptive moving mesh (R-AMM) method. In the H-AMR the mesh is remeshed locally or globally based on error estimates in order to capture the significant part of the solution.[21, 22] In R-AMM the moving mesh is based on the solution of a moving mesh equation.[23, 24] The mesh topology is kept unchanged but the mesh grids are shifted throughout the region to best approximate the solution globally. In Ref. [25], we discussed how to implement R-AMM structural topology optimization. In this paper, we will focus on the H-AMR structural topology optimization within the framework of fully coupled PDE formulation.

The key point when combining structural topology optimization and the H-AMR method is to define a remeshing strategy. This will guarantee the quality of the finite element solution and smooth the expression of the material domain, while keeping a reasonable number of design variables. Generally, the error estimator is used to determine the adaptation strategy, since the exact solution of the

direct problem is unknown in general. For a linear elastic equation the error estimator by Zienkiewicz and Zhu[26] can be expressed as

$$\|e\|_{\text{energy}} \approx \int_{\Omega} (\sigma^* - \sigma^h)^T C^{-1} (\sigma^* - \sigma^h) d\Omega \qquad (16)$$

where σ^* is the smoothed stress in the Gaussian points, σ^h is the approximated nodal stress and C is the material tensor. Equation (16) measures the strain energy error in an average sense over all elements. However, for structural topology optimization with the level set method, the accuracy of the Heaviside and Dirac delta function of the level set surface, which are used to capture the material domain and boundary, cannot be improved by the strain energy error estimator. A specified error estimator which is based on the property of the level set surface can be defined as

$$\|e\|_{\text{ls}} \approx \int_{\Omega} (\nabla H(\phi)^* - \nabla H(\phi)^h)^T (\nabla H(\phi)^* - \nabla H(\phi)^h) d\Omega \qquad (17)$$

where $\|e\|_{\text{ls}}$ is the error estimator for the material domain which is expressed by a level set surface. Figure (5) shows the different effects of two different error estimators of the short cantilever beam example. The beam is clamped on the left side and a fixed force acts on the right-down corner. Both cases are remeshed to use a similar number of elements. The final optimal topologies are quite similar to each other in that the convergence of structural optimization with mesh adaptation is not affected by the error estimators we used. Meanwhile, the overall computational cost for structural optimization is reduced when compared with using a global refined mesh. One can choose one of the error estimators to mesh the design domain for different purposes. In the next section, the error estimator in Eq. (17) is used.

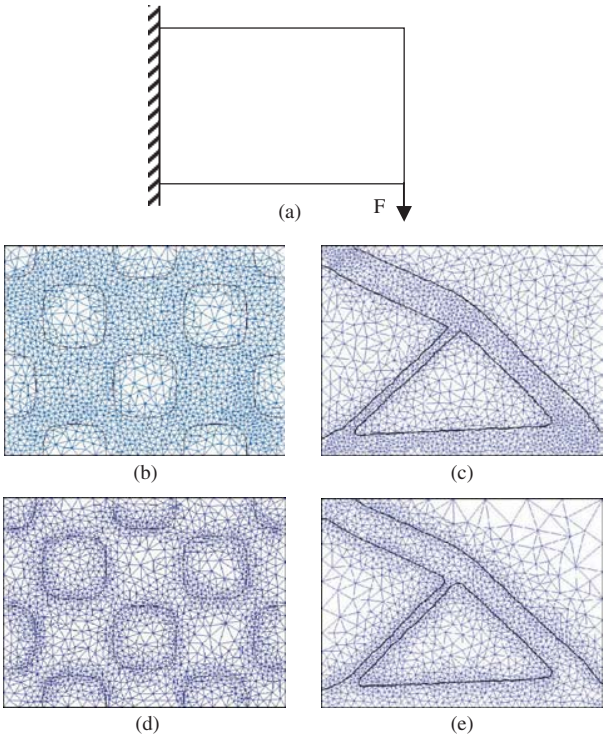

Fig. 5. Structural topology optimization with H-AMR method of a classical benchmark problem. (a) design domain, (b) and (c) Initial and optimized structure topology and meshing (3384 and 3374 triangular elements) using the strain energy error estimator, (d) and (e) Initial and optimized topology and meshing (3085 and 3275 triangular elements) use the level set surface error estimator.

4. FULLY COUPLED PDE FORMULATION FOR ELECTRO-MECHANICAL STRUCTURAL TOPOLOGY OPTIMIZATION

Typically, the compliance minimized topology optimization problem is presented with a constant load force. In MEMS, the electrostatic force is often used to actuate devices. In this case, the amplitude and direction of the electrostatic force will change with the update of a structure's topology and its deformation. Hence we have a coupled optimization problem. Here we present two examples for compliance minimized topology optimization with an electrostatic actuation force.

The design domain and mechanical boundary conditions of the first example are shown in Figure 6a and the electrostatic boundary conditions in Figure 6b. In this example, we assume that the deformation of the structure is small enough so that the electrostatic force will not be changed by the deformation of the structure. The coupling effect between the mechanical and electrostatic problem merely comes from the electrostatic force which will be controlled by the structural topology inside the design domain. So the electrostatic force is a design-dependent load. This is completely different from the fixed load vector case.

For the finite element analysis, the two coupled equations, mechanical and electrostatic, are given by

$$\left.\begin{aligned} \nabla \cdot (\mu \nabla V) &= 0 \\ \nabla \cdot \sigma &= F_{\text{fixed}} + F_{\text{ele}} \end{aligned}\right\} \qquad (18)$$

where F_{fixed} is a fixed load vector and the F_{ele} is the electrostatic force which is dependent on the distribution of the material. The material inside the design domain is SiO_2. The optimization objective is to minimize the deformation of the whole structure with area constraint. The electrostatic force is used to decrease the deformation of the structure. For this kind of weakly coupled optimization problem, the sequential analysis and optimization method has been discussed in Ref. [27]. To make a clear comparison of the traditional sequential method and the fully coupled PDE formulation method we proposed in this paper, we derive the sensitivity expression with the traditional method first.

When using the typical element density design variable method to implement the structural topology optimization,

RESEARCH ARTICLE

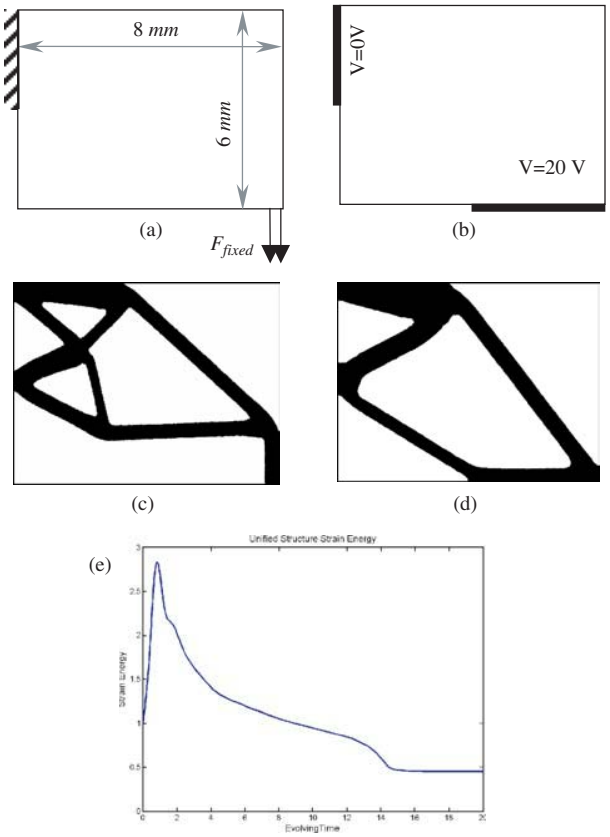

Fig. 6. Compliance minimized topology optimization of a cantilever beam. (a) mechanical design domain and boundary conditions, (b) electrostatic design domain and boundary conditions, (c) optimized material distribution when only the fixed load vector F acts upon the structure, (d) optimized material distribution when both the load vector F and the electrostatic forces act upon the structure, (e) optimization procedure of the structural strain energy of Figure 6d.

both equations in Eq. (18) depend on element design variable ρ_i^p

$$\left.\begin{aligned}\nabla\cdot(\mu(\rho)\nabla V)=0\\ \nabla\cdot(E(\rho)\sigma)=F_{\text{fixed}}+F_{\text{ele}}(\rho,\nabla V)\end{aligned}\right\} \tag{19}$$

One can add Eq. (19) into the original objective function via the finite element discretized expression

$$U_{\text{out}}=U^T K^{\text{ME}}U+\lambda_1 K^{\text{PO}}V+\lambda_2(K^{\text{ME}}U-F_{\text{fixed}}-F_{\text{ele}}) \tag{20}$$

where λ_1 and λ_2 are Lagrangian vectors, K^{PO} and K^{ME} are the stiffness matrices of the electrostatic equation and the linear elastic equation, U is mechanical displacement vector and V is scalar electrical potential. Using the adjoint method, the sensitivity is:

$$\begin{aligned}\frac{\partial U_{\text{out}}}{\partial\rho_i^p}&=2^*U^T K^{\text{ME}}\frac{\partial U}{\partial\rho_i^p}+U^T\frac{\partial K^{\text{ME}}}{\partial\rho_i^p}U+\lambda_1\frac{\partial K^{\text{PO}}}{\partial\rho_i^p}V\\&\quad+\lambda_2\left[\frac{\partial K^{\text{ME}}}{\partial\rho_i^p}U-\frac{\partial F_{\text{ele}}}{\partial\rho_i^p}\right]+\lambda_1 k^{\text{PO}}\frac{\partial V}{\partial\rho_i^p}+\lambda_2 K^{\text{ME}}\frac{\partial U}{\partial\rho_i^p}\end{aligned} \tag{21}$$

To remove the terms $\partial U/\partial\rho_i^p$ and $\partial V/\partial\rho_i^p$ in the sensitivity, the following expressions should be set to zero

$$\begin{aligned}(2*U^T K^{\text{Me}}+\lambda_2 K^{\text{ME}})=0\\ \lambda_1 K^{\text{PO}}=0\end{aligned} \tag{22}$$

With the solution for λ_1 in terms of λ_2, the sensitivity can be simplified as

$$\begin{aligned}\frac{\partial U_{\text{out}}}{\partial\rho_i^p}&=U^T\frac{\partial K^{\text{ME}}}{\partial\rho_i^p}U+\lambda_1\frac{\partial K^{\text{PO}}}{\partial\rho_i^p}V\\&\quad+\lambda_2\frac{\partial K^{\text{ME}}}{\partial\rho_i^p}U-\lambda_2\frac{\partial F_{\text{ele}}}{\partial\rho_i^p}\end{aligned} \tag{23}$$

To obtain the sensitivity in Eq. (23), one has to solve the displacement and electric potential solution first with Eq. (19) and then calculate two adjoint vectors with Eq. (22). The expression of the sensitivity is relatively complicated even for this weakly coupled problem. Because the traditional optimization method solves the direct physical problem first and then derives sensitivity sequentially, the state variables (displacement and electric potential) are treated as implicit functions of the design variables. Then sensitivity analysis should include the derivative terms of the state variables and the design variables. Several papers and books discuss the derivation of sensitivity in the case where displacement is treated as an implicit function of the design variables.[9, 10, 27]. In this paper, we set the displacement and electric potential as independent of the design variables, that is, the state and design variables are defined in a composite vector. This method is called the simultaneous analysis and design (SAND) method.[28] One of the distinguished advantages of the SAND method is that the derivation of the sensitivity is relatively straightforward, especially when one wants to implement structural optimization in which the state variables are controlled by multi-physical problems. For example, equilibrium equations could include mechanics, electrostatics, and thermo-electric effects. The state variables include displacement, electrostatic field, thermal stress, etc. The coupling effects include surface coupling of mechanism and electrostatics, domain coupling of mechanics and thermo-electric effects. In this case, the sensitivity analysis of the traditional method is extremely complicated. However, the expression of the SAND method is much simpler for coupled problems, especially in which the load vector is design-dependent. One remaining question is how to establish the relationship between the de-coupled state and design variables. One of the possibilities is to derive a corresponding optimization equation based on the specified objective function and to solve the fully coupled equilibrium equation and optimization equation simultaneously.

When using the fully coupled PDE formulation, we do not need to calculate the Lagrangian vectors (Eq. 22)

explicitly. The structural topology optimization problem can be expressed with the level set method as

$$\left.\begin{aligned} \text{min:} \quad & C(\phi, \varepsilon, \nabla V) = \int_\Omega \frac{1}{2} E(\phi)\varepsilon^T D\varepsilon d\Omega \\ \text{s.t.} \quad & \nabla \cdot (E(\phi)\sigma) = F_{\text{fixed}} + F_{\text{ele}} \\ & \nabla \cdot (\mu(\phi)\nabla V) = 0 \\ & \int_\Omega H(\phi)\, d\Omega = \text{Vol}^* \end{aligned}\right\} \quad (24)$$

In the optimization equation, the level set surface which expresses the evolving of the structural layout is not influenced by the design-dependent electrostatic force. The evolving of the level set surface still can be expressed by the coupling effect of the first two equations in Eq. (25). To sum up, the coupled PDE formulation to express structural topology optimization is:

$$\left.\begin{aligned} & \nabla \cdot (\mu(\phi)\nabla V) = 0 \\ & \nabla \cdot (E(\phi)\sigma) = F_{\text{fixed}} + F_{\text{ele}} \\ & \frac{\partial \phi}{\partial t} - \left[\frac{1}{2}(1 - E_{\min})\varepsilon^T D\varepsilon + \lambda\right]\delta(\phi)|\nabla\phi| = \alpha\Delta\phi \end{aligned}\right\} \quad (25)$$

Figure 6c shows the optimized structural topology when only F_{fixed} acts and Figure 6d is the optimized topology when both F_{fixed} and F_{ele} act on the structure. Figure 6e is the optimization procedure of the structural strain energy.

In MEMS, the electrostatic force is commonly used to actuate the slender structures. This is a typical self-consistent electromechanical analysis which involves determining mechanical displacement to balance the electrostatic force on the surface. There are two different methods to solve this surface coupling problem, the sequentially coupled solver and the directly coupled solver. To implement structural optimization with the coupled method, the directly coupled solver is used to calculate the structural deformation. The design domain is shown in Figure 7. There are two subdomains, subdomain 1 has fixed material property and subdomain 2 is the optimization domain. Here we discuss three different load cases. In the first case, a fixed load vector ($F_{\text{fixed}} = 1\mu N$) is added on the middle point of the upper surface of the whole domain. In the second case, the electrostatic force acts on the structure. In the last case, both the fixed load and electrostatic force act on the structure. The objective of structural optimization is still compliance minimization with area constraint. The material inside both subdomains is Aluminium with Young's modulus of 70 GPa and Poisson ration of 0.33.

For the first case, we still can use the compliance minimization model in Eq. (1). In addition, we consider the geometrically large deformation for the elastic equilibrium equation. So the strain tensor ε has a nonlinear relationship

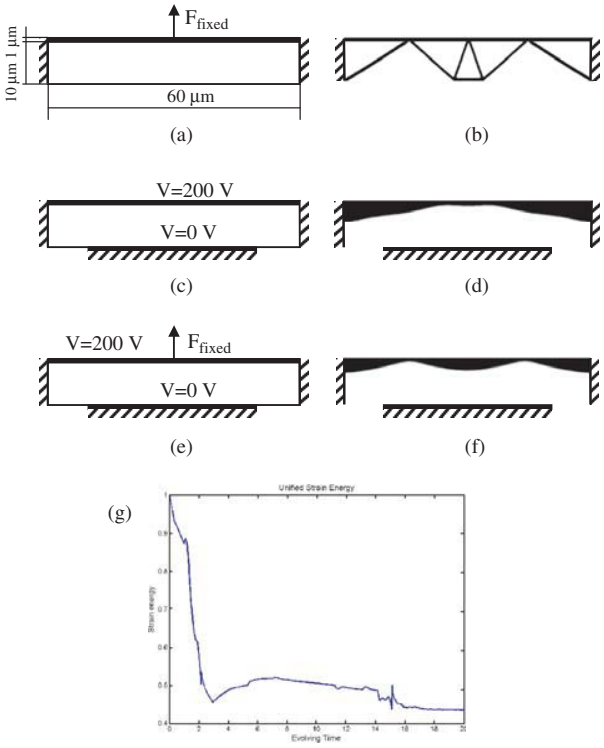

Fig. 7. Compliance minimized topology optimization of a fixed-fixed end beam. (a) and (b) initial design domain and optimized topology with fixed load vector, (c) and (d) initial design domain and optimized topology with electrostatic force, (e) and (f) initial design domain and optimized topology with both the fixed load vector and electrostatic force, (g) optimization procedure of the structural strain energy of Figure 7f.

with the displacement vector

$$\left.\begin{aligned} \varepsilon_x &= \frac{\partial u}{\partial x} + \left(\left(\frac{\partial u}{\partial x}\right)^2 + \left(\frac{\partial v}{\partial x}\right)^2\right) \\ \varepsilon_y &= \frac{\partial v}{\partial y} + \left(\left(\frac{\partial u}{\partial y}\right)^2 + \left(\frac{\partial v}{\partial y}\right)^2\right) \\ \varepsilon_{xy} &= \left(\frac{\partial u}{\partial y} + \frac{\partial v}{\partial x}\right) + \left(\frac{\partial^2 u}{\partial x \partial y} + \frac{\partial^2 v}{\partial x \partial y}\right) \end{aligned}\right\} \quad (26)$$

Since we use the SAND method in which the design variable ϕ and the displacement vector are independent of each other, the optimization equation is still same as the second equation in Eq. (11). The first equation in Eq. (11) is solved with a nonlinear iterative solver for large deformation analysis. The optimized structural topology is shown in Figure 7b.

For the second load case, a consistent solution for the electromechanical problem is needed. To coincide with the fully coupled optimization method we propose in this paper, we choose a direct coupled solver where the deformed mesh caused by the structural deformation is simulated by the ALE method.[4, 32] In FEMLAB, the

RESEARCH ARTICLE

coupled ALE method can be implemented with following coupled Eqs. [6]

$$\left.\begin{aligned}\nabla\cdot(\mu(\phi)\nabla V_X)&=0\\ \nabla\cdot(E(\phi)\sigma)&=F_{ele}\\ \nabla\cdot(G\nabla X)&=0\end{aligned}\right\} \tag{27}$$

where $\boldsymbol{X}$ expresses the deformed nodal position because of structural deformation, G is the mesh monitor function which controls the local property of the deformed mesh, V_X means that the value of the electrical potential is calculated for the deformed mesh and $\mu(\phi)=\mu_{\max}H(\phi)+(1-H(\phi))\mu_{\text{air}}$ where $\mu_{\max}$ is a large number to approximate the distribution of the electrical potential. In this example $\mu_{\max}=100$. Using the moving mesh equation (the third equation in Eq. (27)), all of the displacement, force and electrical potential boundary conditions can be implemented in the original coordinates. This method can deal with the electromechanical coupling directly before pull-in occurs. For the optimization examples we presented here, the fixed-fixed end beam in subdomain 1 is used to avoid the pull-in occurring during the optimization procedure with reasonable electrical potential conditions. The coupled optimization equations are

$$\begin{aligned}\nabla\cdot(\mu(\phi)\nabla V_X)&=0\\ \nabla\cdot(E(\phi)\sigma)&=F_{\text{ele}}\\ \nabla\cdot(\nabla X)&=0\\ \frac{\partial\phi}{\partial t}-\left[\frac{1}{2}(1-E_{\min})\varepsilon^T D\varepsilon+\lambda\right]\delta(\phi)|\nabla\phi|&=\alpha\Delta\phi\end{aligned} \tag{28}$$

Here the mesh monitor function is the unit function so that the mesh is smoothly modified on the whole design domain. On each mesh node, there are 6 degrees of freedom (dofs), two displacement dofs, one electrical potential dof, two moving mesh position dofs, and one level set surface dof. However, the optimization equation remains unchanged despite the complicated coupled forward problems. The optimized result is shown in Figure 7d.

In the last case, both the fixed load vector and electrostatic force act on the structure. So this is a multiple load optimization problem. Based on the analysis of the first two cases, the optimization equation for these two loads is

$$\begin{aligned}\nabla\cdot(E(\phi)\sigma_1)&=F_{\text{fixed}}\\ \nabla\cdot(\mu(\phi)\nabla V_X)&=0\\ \nabla\cdot(E(\phi)\sigma_2)&=F_{\text{ele}}\\ \nabla\cdot(\nabla X)&=0\\ \frac{\partial\phi}{\partial t}-\left[\frac{1}{2}(1-E_{\min})(\varepsilon_1^T D\varepsilon_1+\varepsilon_2^T D\varepsilon_2)+\lambda\right]&\\ \delta(\phi)|\nabla\phi|=\alpha\Delta\phi&\end{aligned} \tag{29}$$

where ε_1 and ε_2 are the strain vectors corresponding to two load cases. The optimized result is shown in Figure 7f.

5. CONCLUSION

This paper presents a procedure to implement single objective function, single constraint, and multiphysics structural topology optimization by a fully integrated PDE expression via the level set method. The optimization procedure is implemented through a pseudo-time dependent optimization equation. Expressing the sensitivity with the SAND method is much simpler than using the traditional sequential coupled algorithm. Several examples demonstrate the use of the method we proposed. The efficiency and accuracy of this optimization method strongly depends on the power of the nonlinear algorithm for large scale problems. Practical optimization of MEMS requires multi-objectives, multi-constraints, together with multiphysical problems. Our work will now focus on these issues.

Acknowledgments: This work is supported by Deutsche Forschungsgemeinschaft (DFG) 1883/5-3.

References and Notes

1. B. F. Romanowicz, Methodology for the Modeling and Simulation of Microsystems, Kluwer Academic Publishers **(1998)**.
2. S. D. Senturia, Microsystem Design, Kluwer Academic Publishers **(2000)**.
3. A. Nathan and H. Baltes, Microtransducer CAD, Physical and Computational Aspects, Springler-Verlag **(1999)**.
4. K. Zeng, Z. Liu, and J. G. Korvink, *Microsystem Technologies* 10, 387 **(2004)**.
5. http://www.ansys.com/.
6. http://www.femlab.com.
7. http://www.bsac.eecs.berkeley.edu/cadtools/sugar.
8. L. Yin and G. K. Ananthasuresh, *Sens. Actuators, A* 97, 599 **(2002)**.
9. O. Sigmund, *Comput. Methods Appl. Mech. Engrg.* 190, 6577 **(2001)**.
10. O. Sigmund, *Comput. Methods Appl. Mech. Engrg.* 190, 6605 **(2001)**.
11. E. C. N. Silva, J. S. O. Fonseca, and N. Kikuchi, *Computational Mechanics* 19, 397 **(1997)**.
12. S. Nishiwaki, M. I. Frecker, S. Min, and N. Kikuchi, *Int. J. Numer. Meth. Engrg.* 42, 535 **(1998)**.
13. G. I. N. Rozvany, *Struct. Multidisc Optim.* 21, 90 **(2001)**.
14. G. H. Yoon and Y. Y. Kim, *Int. J. Numer. Meth. Engrg.* **(2006)**, in press.
15. S. F. Rahmatalla and C. C. Swan, *Struct. Multidisc. Optim.* 27, 130 **(2004)**.
16. V. B. Hammer and N. Olhoff, *Struct. Multidisc. Optim.* 19, 85 **(2000)**.
17. T. Belytschko, S. P. Xiao, and C. Parimi, *Int. J. Numer. Meth. Engrg.* 57, 1177 **(2003)**.
18. M. Y. Wang, X. Wang, and D. Guo, *Comput. Methods Appl. Mech. Engrg.* 192, 227 **(2003)**.
19. J. A. Sethian and A. Wiegmann, *J. Comp. Phys.* 163, 489 **(1999)**.
20. G. Allaire, F. Jouv, and A. Toader, *J. Comp. Phys.* 194, 363 **(2004)**.
21. J. Costa and M. K. Alves, *Int. J. Numer. Meth. Engrg.* 58, 83 **(2003)**.
22. A. Schleupen, K. Maute, and E. Ramm, *Struct. Multidisc. Optim.* 19, 282 **(2000)**.
23. W. Cao, W. Huang, and R. D. Russell, *Appl. Numer. Math.* 47, 121 **(2003)**.
24. G. Beckett, J. A. Mackenzie, and M. L. Robertson, *J. Comp. Phys.* 182, 478 **(2001)**.

25. Z. Liu and J. G. Korvink, Adaptive Moving Mesh Level Set Method for Structure Topology Optimization (Research Report) **(2004)**.
26. O. C. Zienkiewicz and J. Z. Zhu, *Int. J. Numer. Meth. Engrg.* 24, 337 **(1987)**.
27. M. P. Bendsoe and O. Sigmund, Topology Optimization Theory, Methods and Applications, Springer **(2003)**.
28. J. S. Arora and Q. Wang, *Struct. Multidisc. Optim.* 30, 251 **(2005)**.
29. O. Sigmund, *Struct. Multidisc. Optim.* 21, 120 **(2001)**.
30. Z. Liu, J. G. Korvink, and R. Huang, *Struct. Multidisc. Optim.* 29, 407 **(2005)**.
31. S. Osher and R. Fedkiw, Level Set Methods and Dynamic Implicit Surfaces, Springer **(2002)**.
32. L. A. Jakobsen, E. Lund, and H. Møller, Shape Sensitivity Analysis of Time Dependent Fluid-Structure Interaction Problems Using the ALE Method, *Proc. 4th World Congress on Structural and Multidisciplinary Optimization* **(2001)**.

SENSOR LETTERS
Vol. 4, 200–205, 2006

RESEARCH ARTICLE

Spring Constant Models for Analysis and Design of MEMS Plates on Straight or Meander Tethers

Maryna Lishchynska*, Nicolas Cordero, Orla Slattery, and Conor O'Mahony

Tyndall National Institute, Lee Maltings, Prospect Row, Cork, Ireland

(Received: 28 November 2005. Accepted: 12 April 2006)

Comprehensive spring constant models are developed to analyse the electromechanical behaviour of elastically suspended MEMS plates. These models account for residual (post-fabrication) stress, finite stiffness of real anchors, and non-rigidity of the plate. Based on the models developed, the pull-in voltage of microfabricated switches is determined for a wide range of device geometries. Experimental measurements verify the accuracy of the models developed, which is within 11%. The results also show that significant errors (over 100%) in predicting the device pull-in behaviour may result if conventional models are applied to the plate-tethers system.

Keywords: Spring Constant, Elastically Suspended Plate, RF Switch, Pull-in Voltage, MEMS.

1. INTRODUCTION

Suspended plates find a wide range of applications as key elements in various microdevices such as MEMS varactors for wireless communication systems[1–6] and RF switches.[7–10] These plates are usually supported by spring-like suspensions such as cantilever (straight) or meander type tethers (Fig. 1). Although these types of structures have been previously modelled with conventional equations, the assumptions and simplifications inherent to those models make them unsuitable (or inaccurate) for use where a high degree of design accuracy is desired.

The primary goal of this paper is to develop models for accurate evaluation of the spring constant of suspended plates on straight or meander tethers. Such models incorporate fabrication non-idealities such as residual stress, real anchors, and also account for the plate compliance. This is achieved by extracting spring constant values from Finite Element Method (FEM) simulation data and experimental validation.

2. PREVIOUS/CONVENTIONAL MODELS

MEMS varactors and RF switches usually consist of a movable plate suspended above the ground on elastic elements or tethers (Fig. 2). Altering the vertical position of the plate using externally applied forces (e.g., thermal, electrostatic, piezoelectric, etc.) changes the capacitance of the structure and influences the electrical characteristics of the device. Removal of the applied forces allows the plate to return to its original undeflected position because of the mechanical restoring forces exerted by the tethers. Plates suspended by four tethers of two geometries, straight or meander (Fig. 3), are considered in this paper.

For small displacements the restoring force F from a spring displaced a distance δ is given by Hooke's law:[11]

$$F = -K\delta \tag{1}$$

where K is the spring constant.

The mechanical spring constant of micromachined structures controls the response of the devices to external influences such as pressure or voltage. Knowing the spring constant, such important behavioural characteristics as the pull-in voltage $V_{\text{pull-in}}$, the resonance frequency f_{res} and the deflection δ of the structure due to an externally applied force can be easily found using the following well-known expressions:[1, 12–13]

$$V_{\text{pull-in}} = \sqrt{\frac{8K^{\text{total}}h^3}{27\varepsilon A}} \tag{2}$$

$$f_{\text{res}} = \frac{1}{2\pi}\sqrt{\frac{K^{\text{total}}}{m}} \tag{3}$$

$$\delta = -\frac{F}{K^{\text{total}}} \tag{4}$$

where K^{total} is the spring constant of the entire structure, ε is the electrical permittivity, A is the common plate-electrode area, m is the mass, F is the applied force, and

*Corresponding author; E-mail: marynal@tyndall.ie

1546-198X/2006/4/200/006 doi:10.1166/sl.2006.011

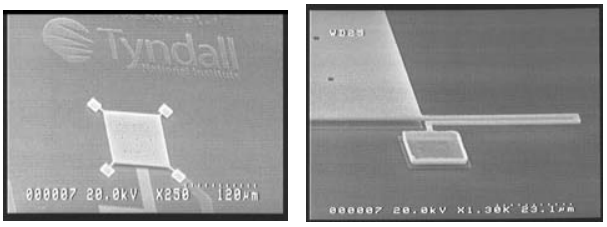

(a) (b)

Fig. 1. Micromachined plates suspended by (a) straight tethers and (b) meander tethers.

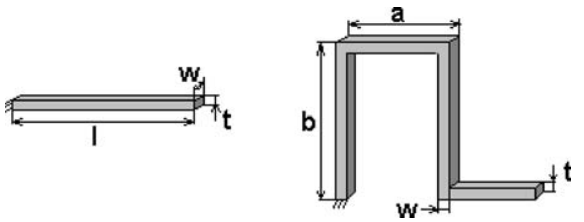

(a) (b)

Fig. 3. (a) Straight and (b) meander tethers typically used as micro-spring suspensions.

h is the electrical gap. Therefore, accurate evaluation of the spring constant is the key to accurate modelling and design of the structure.

Conventional models assume that the total spring constant of the structure, K^{total}, is the sum of the spring constants of the individual tethers,[1, 2, 7]

$$K^{\text{total}} = \sum k_0^s \tag{5}$$

where k_0^s are calculated using known expressions:

$$k_0^s = \begin{cases} \dfrac{Ewt^3}{l^3}, \quad \text{for a straight tether}^{7} & \text{(6a)} \\ \left(\dfrac{8a^3+2b^3}{3EI_x} + \dfrac{ab(3b+15a)}{3GJ} - \dfrac{a^2\left(\frac{2a}{EI_x}+\frac{3b}{GJ}\right)^2}{2\left(\frac{a}{EI_x}+\frac{b}{GJ}\right)} - \dfrac{b^2}{2}\left(\dfrac{a}{GJ}+\dfrac{b}{EI_x}\right)\right)^{-1}, \\ \quad \text{for a meander tether}^{13} & \text{(6b)} \end{cases}$$

Such models assume the plate to be rigid and do not account for the residual stresses and anchor compliance that are inevitable with most micromachining technologies.[7, 14, 15] As a result, large errors may occur when calculating the spring constant of the structure. This is clearly illustrated in Table I. Experimental studies also report a significant discrepancy.[7]

There are a number of factors causing this inconsistency, residual stress and non-rigidity of the plate being the most significant ones. Non-ideal anchors, typical in MEMS, also influence the spring constant.[14, 15] The following sections of this paper discuss the development of comprehensive spring constant models which take account of these factors.

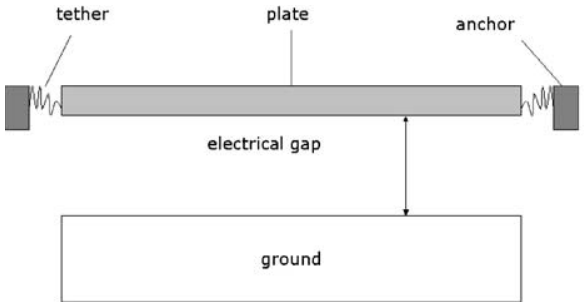

Fig. 2. Cross-section of the plate suspended on elastic elements.

3. STRESS ANALYSIS IN SUSPENDED PLATES

Residual stress is induced during the fabrication of most microstructures. Under this stress, deformations and changes in the mechanical behaviour of the structure occur. For instance, in-plane residual stress results in the stiffening of most microstructures,[16] an effect that is undesirable in many RF applications. Therefore, any residual stress present must be taken into account when modelling.

The generation of residual stress in micromachined structures is complicated and depends heavily on the specifics of the fabrication process. Furthermore, simulations undertaken in this work show that the stress in suspended structures redistributes after release. Consequently most of the post-release stress is concentrated in the tethers and the plate itself is nearly stress-free.

A more detailed look at the behaviour of straight tethers in a stressed device reveals not only stiffening of the cantilever-like suspensions (Fig. 4a), resulting in an increase of the spring constant, but also an extra bending of the anchor, implying a decrease in the spring constant (Fig. 4b). These two phenomena superpose in a complex way. Meander tethers, on the other hand, absorb much more stress through deformation (Fig. 5). All these effects should be taken into account when modelling the spring constant.

Table I. Comparison of FEM simulated and analytical (1), (2) values of spring constant (MPa · μm) for straight and meander suspended plates.

	Straight tethers; plate size, μm^2			Meander tethers; plate size, μm^2				
	100×100	200×200	300×300	10×10	50×50	100×100	200×200	300×300
Analytical	28.28	28.28	28.28	9.26	9.26	9.26	9.26	9.26
Simulated	14.7	13	11	7.75	6.58	5.68	4.18	3.27

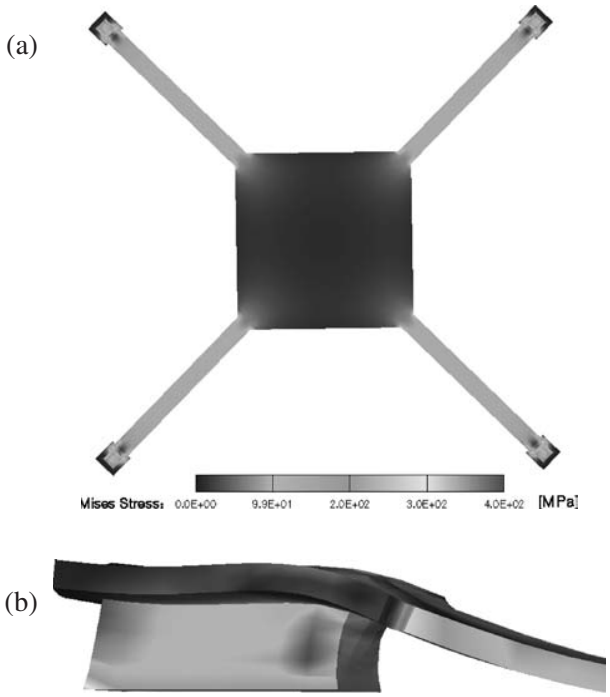

Fig. 4. Simulated stress redistribution in plate suspended by straight tethers (a) and local deformation (exaggerated) of the anchor of the pillar-supported guided-end cantilever due to the stress, no external load applied (b). Initial biaxial stress is 100 MPa. Lighter areas indicate higher residual stress, darker areas represent lower stress.

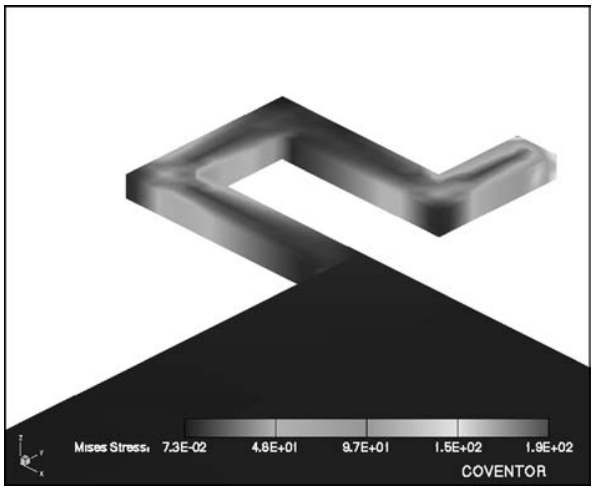

Fig. 5. Simulated stress redistribution (MPa) in plate suspended by meander tethers.

4. MODELLING THE SPRING CONSTANT

A previously described technique of extracting analytical models from FEM simulation data[17] was applied here. It can be roughly described in the following set of steps.

(1) A dimensional analysis is firstly undertaken. The purpose of this exercise is to establish a basic relationship between the dimensional parameters that have a significant role in the device performance. In the case when an exact solution exists for the ideal structure the dimensional part of a relation can be easily found. However, when there is no predefined equation for the ideal case, more investigation is needed. Dimensional analysis reduces the number of variables in the formula since the contribution of the main parameters is already found. The remaining variables are transformed into dimensionless ones, hence reducing their number further.
(2) FE simulation data relating the behaviour of structures of a given geometry to dimensionless parameters is generated. Parametric studies on all contributing parameters should be carried out as well.
(3) The final closed-form formula (function representation) is obtained by manipulation of the output data from FE simulation followed by accurate curve fitting.
(4) Experimental validation of the models is conducted where possible.

The following two subsections present the development of the spring constant model for straight tethers system in greater detail and provides the final model for meanders-plate system.

4.1. Plate on Straight Tethers

Expression (6a) assumes an ideally fixed guided-end cantilever (Fig. 3a) and does not account for the non-ideal anchors that are typical of MEMS structures. Nevertheless, according to our simulation study and experimental works of other authors,[14, 15] real anchors significantly affect the spring constant of the structure and need to be taken into account when modelling.

Consider an anchored guided-end cantilever (Fig. 6). This structure was modelled and its deflection under a concentrated load was simulated in Coventor.[18] As no experimental work on stress relaxation has been done in this study an elastic material model was used for simulations. Then, applying Hooke's law, the spring constant was calculated as

$$k_s = -\frac{F}{\delta} \tag{7}$$

A parametric study of the cantilever spring constant with varying dimensional parameters was carried out and the numerical data were interpolated by least square method (Microsoft Excel). Results revealed a linear dependence of the normalised spring constant (k_s/k_s^0) on h/l as $(k_s/k_s^0)^{-1} = 1 + 4h/l$. This yields the following equation for the spring constant of the guided-end cantilever with non-ideal anchor:

$$k^s = \frac{k_0^s}{1+4h/l} \tag{8}$$

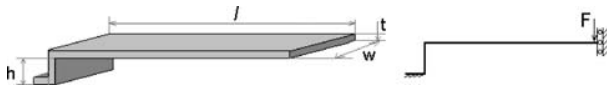

Fig. 6. Schematic of the anchored guided-end cantilever.

Micromachined beams that are prevented from stretching/shrinking by mounting conditions (e.g., doubly fixed beam, guided-end cantilever) are very sensitive to residual stress σ.[1,7] At the same time, non-ideal anchors allow more compliance and stress absorption than ideal ones, thus reducing the overall stiffness of the structure.[15] These two phenomena superpose but do not cancel each other. In fact, they significantly affect the spring constant of the structure. Since the classical model of the spring constant of the guided-end cantilever incorporating axial stress[13] does not account for non-ideal anchors, the following model allowing for the coupled effects of residual stress and non-ideal anchor was established in this work:

$$k^s = \frac{k_0^s}{\left(1+0.65\frac{\sigma}{E}\left(\frac{l}{t}\right)^2\right)^{-1} + \frac{4h}{l}\left(1+1.96e5\sqrt{\frac{\sigma}{E}}\frac{h^{0.22}w^{1.28}t}{l^{2.5}}\right)} \tag{9}$$

Here, the first term in the denominator is due to the stress stiffening of the cantilever. The second term represents the support post and its increased compliance due to biaxial residual stress σ. The value of k_0^s is calculated using (6a).

Applications of the conventional formula (5) are usually based on the assumption that the movable plate is rigid and that there is no localised deformation in connection (joint) areas. However, our simulation study shows that the movable plate does actually deform (Fig. 7), thus affecting the total spring constant of the device K^{total}. In this work, the spring constant of plates suspended on straight tethers was determined by loading the plate with a low pressure and converting the deflection into K^{total} via Hooke's law (7). Then the formula for the total spring constant of the structure (Fig. 1a) was established:

$$K^{\text{total}} = \frac{4k^s}{1+0.15wL^2/l^3} \tag{10}$$

where L is the plate side length. Together, Eqs. (9) and (10) comprise a closed-form model for the spring constant of a plate on straight suspensions (Fig. 1a).

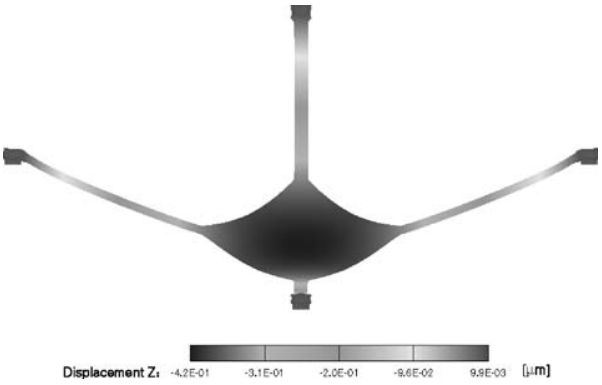

Fig. 7. Deformation of the plate suspended on straight tethers under uniform pressure; the dark area in the middle of the plate indicates its local deformation (exaggerated 100 times).

4.2. Plate on Meander Tethers

Because of an inherent complex cross-axis coupling in meander springs (Fig. 3b) and complex tethers-plate coupling, accurate modelling of plates with such tethers is a challenging task. The presence of biaxial residual stress affects the spring constant even more. FEM simulations revealed no tangible effect of residual stress on the spring constant of stand-alone meanders (less than 1%); it is only when meanders are in a plate-tethers system that the effect of residual stress becomes pronounced and substantial. This is because of the high compliance of the meanders and in-plane deformation of the device. In order to account for all these effects, the technique described in the beginning of this section was applied and the following formula for calculation of the spring constant of plates with meander tethers has been developed:

$$K^{\text{total}} = 4 * k_s^0 \frac{1+2.4(\sigma/E)(a/b)^{1.4}((w-1.5)^{0.8}L^{0.7})/(t^{1.5})}{1+58(a\sqrt{b}L\sqrt{w-1.95})/((3a+b)^3)} \tag{11}$$

where k_s^0 is calculated via (6b). As with any non-empirical equations, the models developed here require validation which is the aim of the next section.

5. EXPERIMENT/VERIFICATION AND SENSITIVITY ANALYSIS

RF switches microfabricated in the Tyndall National Institute (Fig. 1) were used to experimentally validate the models. The switches consisted of a 1 μm thick aluminium plate (100×100 μm^2 or 200×200 μm^2) suspended on either 50 μm $\times$ 5 μm cantilever or 10 μm $\times$ 8 μm $\times$ 2 μm meander tethers. Mechanical material properties assumed in calculations are presented in Table II. Using blanket film tests and the Stoney formula,[19] it was experimentally found that biaxial tensile stress induced during the fabrication process was of the order of 35 MPa. The pull-in voltage of the structures was measured using a capacitance-voltage test system. This voltage represents an electromechanical instability point at which time the switch collapses or "pulls-in" onto an underlying electrode.[15]

This voltage is predicted by the following expression

$$V_{\text{pull-in}} = \sqrt{\frac{8K^{\text{total}}h^3}{27\varepsilon A}} + V_{\text{offset}} \tag{12}$$

where the spring constant values were estimated via Eqs. (9), (10), (11). The zero-voltage airgap h was measured using white-light interferometry.[21] Note that formula (12) incorporates one extra term V_{offset}, not present in the conventional Eq. (2), which is a measured value of the

Table II. Material properties of Al thin film.

Young's modulus, GPa	Poisson's ratio	Ref.
74	0.34	[20]

RESEARCH ARTICLE

voltage offset ($V_{offset} = 0.55$ V) due to dielectric charging.[22] Measured and modelled results were found in very good agreement, with a maximum discrepancy of 11% (Fig. 8). It is also clear that significant errors (over 100%) may result in predicting pull-in voltage when the spring constant is calculated via the conventional model (5), (6). These models assume the plate to be rigid and neglect the effects of residual stress and non-ideal anchors.

In order to investigate combined effects of residual stress and non-ideal anchors (anchor compliance) on the spring constant a parameter sensitivity study was undertaken. Thus, the spring constant was calculated for variable values of residual stress and anchor height with all other parameters held constant. Analysis of the results, presented in Figure 9, shows a strong interaction between the two parameters that is reasonably anticipated. On the other hand, for zero stress K^{total} converges to the value predicted by the conventional model. Anchor height is found to be the most critical design parameter controlling low spring constant of a device incorporating residual stresses.

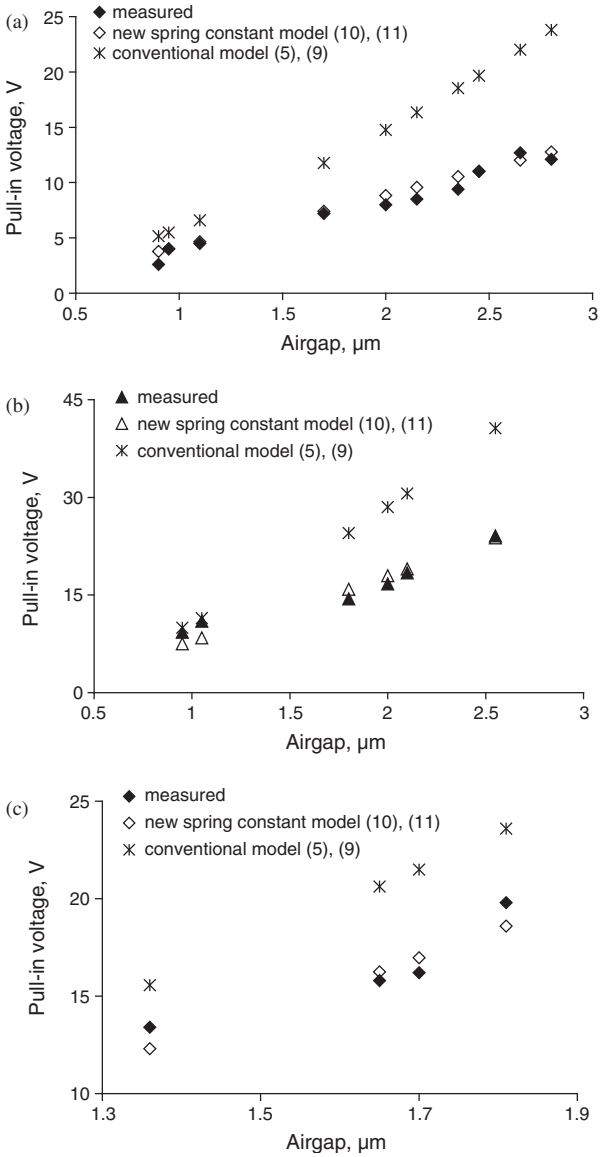

Fig. 8. Modelled and measured pull-in voltage for 100×100 μm^2 (a) and 200×200 μm^2 (b) plates suspended on straight tethers and 100×100 μm^2 plate on meander (10 $\mu m \times 8$ $\mu m \times 2$ μm) tethers (c).

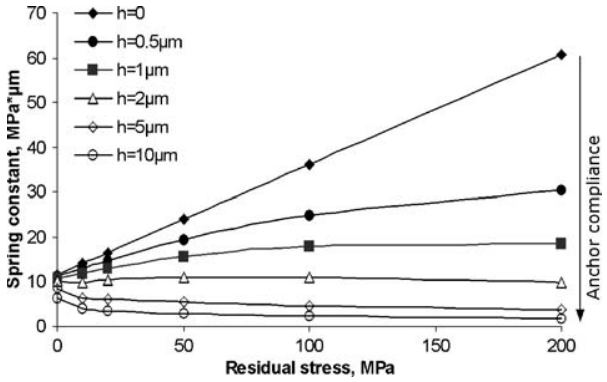

Fig. 9. Results of sensitivity study: Effect of coupling of residual stress and anchor compliance.

6. CONCLUSIONS

Comprehensive models for calculating the spring constant of a plate suspended by four straight or meander tethers, common to MEMS tunable capacitors and RF switches, have been developed. These models account for residual stress and non-ideal anchors typical of microfabricated structures, and were validated by comparison with experimentally measured values. Correlation to within 11% was achieved. The results also indicate that significant errors may result in predicting the spring constant when the combined effects of residual stress, non-ideal anchors, and non-rigidity of the plate are neglected or underestimated. The findings can be used for evaluation of the spring constant and consequently the pull-in voltage, the resonant frequency or the deflection of microstructures based on the suspended plate.

Acknowledgments: This work has been funded by Irish Research Council in Science, Engineering, and Technology. The RF switch fabrication has been carried out with the support of Enterprise Ireland under the ATRP program.

NOMENCLATURE AND ABBREVIATIONS

E—Young's modulus
L—plate side length
w—width of the cantilever suspension
t—thickness of the device
l—length of cantilever suspension
K^{total}—total spring constant of the suspended structure

k_s—spring constant of a pillar-supported guided-end cantilever
k_0^s—spring constant of an ideally fixed guided-end cantilever
h—anchor height/electrical gap
F—force
σ—fabrication residual stress
MEMS—microelectromechanical systems
RF—radio frequency
FEM—finite elements method

References and Notes

1. G. M. Rebeiz, *RF MEMS, Theory, Design, and Technology* Wiley, Hoboken **(2003)**.
2. A. Dec and K. Suyama, *IEEE Transactions on Microwave Theory and Techniques* 46, 12 **(1998)**.
3. Jun Zou, Chang Liu, Jose Shutt-Aine, Jinghong Chen, and Sung-Mo Kang, *International Electron Device Meeting*, San Francisco **(2000)**.
4. C. T.-C. Nguyen, *Proc. IEEE International Micro Electro Mechanical Systems Workshop*, Heidelberg, Germany **(1998)**.
5. H. Nieminen, V. Ermolov, K. Nybergh, S. Silanto, and T. Ryhänen, *J. Micromech. Microeng.* 12 **(2002)**.
6. Z. Olszewski, M. Hill, C. O'Mahony, R. Duanne, and R. Houlihan, *J. Micromech. Microeng.* 15, S122 **(2005)**.
7. D. Peroulis, S. P. Pacheco, K. Sarabandi, and L. P. B. Katehi, *IEEE Transactions on Microwave Theory and Techniques* 51, 1 **(2003)**.
8. C. O'Mahony, R. Duane, M. Hill, and A. Mathewson, *Proc. Design, Test, Integration and Packaging of MEMS/MOEMS Conference*, Montreux, Switzerland **(2004)**.
9. S. P. Pacheco, L. P. B. Katehi, and C. T.-C. Nguyen, *IEEE MTT-S Int. Microwave Symp. Dig.* 1 **(2000)**.
10. C. O'Mahony, R. Duane, M. Hill, and A. Mathewson, *Proc. 15th Micromechanics Europe*, Leuven, Belgium **(2004)**.
11. P. P. Benham, R. J. Crawford, and C. G. Armstrong, *Mechanics of Engineering Materials*, Pearson, Essex **(1996)**.
12. J. A. Pelesko and D. H. Bernstein, *Modeling MEMS and NEMS*, Chapman and Hall/CRC, Florida **(2002)**.
13. R. J. Roark and W. Young, *Formulas for Stress and Strain*, McGraw-Hill, New York **(2000)**.
14. B. D. Jensen, F. Bitsie, and M. de Boer, *Proc. SPIE Micromachining and Microfabrication*, Santa Clara, USA **(1999)**.
15. C. O'Mahony, M. Hill, R. Duane, and A. Mathewson, *J. Micromech. Microeng.* 13, S75 **(2003)**.
16. M. Gere and S. Timoshenko, *Mechanics of Materials*, Boston, PWS-Kent **(1990)**.
17. M. Lishchynska, N. Cordero, and O. Slattery, *Analog Integrated Circuits and Signal Processing* 44, 109 **(2005)**.
18. CoventorWare version 2005. *Reference Guides and Tutorials*, www.coventor.com
19. D. Campbell, Handbook of Thin Film Technology, edited by Maissel, Glang, McGraw-Hill, New York **(1970)**, Chap. 12.
20. M. Chilmungund, R. B. Inturi, and J. A. Barnard, *Thin Solid Films* 270, 260 **(1995)**.
21. C. O'Mahony, M. Hill, M. Brunet, R. Duane, and A. Mathewson, *Meas. Sci. Technol.* 14, 1807 **(2003)**.
22. C. O'Mahony, R. Duane, M. Hill, and A. Mathewson, *Electron. Lett.* 41 **(2005)**.

SENSOR LETTERS
Vol. 4, 206–213, 2006

RESEARCH ARTICLE

Coupled Electro-Mechanics Simulation Methodology of the Dynamic Pull-in in Micro-Systems

V. Rochus[1,*], D. J. Rixen[2], and J. C. Golinval[1]

[1] *University of Liège, Département d'Aérospatiale, Mécanique et Matériaux, LTAS-Vibrations et Identification des Structures, Chemin des chevreuils, 1, B52/3, B-4000 Liège, Belgium*
[2] *T. U. Delft, Faculty of Design, Engineering and Production Engineering Dynamics Mekelweg 2, 2628 CD Delft, The Netherlands*

(Received: 12 May 2005. Accepted: 4 December 2005)

The aim of this paper is to deal with multi-physics simulation of micro-electro-mechanical systems (MEMS) based on an advanced numerical methodology. MEMS are very small devices in which electric as well as mechanical and fluid phenomena appear and interact. Because of their microscopic scale, strong coupling effects arise between the different physical fields, and some forces, which were negligible at macroscopic scale, have to be taken into account. In order to accurately design such micro-electro-mechanical systems, it is of primary importance to be able to handle the strong coupling between the electric and the mechanical fields. In this paper, the finite element method (FEM) is used to model the electro-mechanical interactions and to perform static and transient analyses. The application example considered here is a micro-bridge consisting of a clamped-clamped beam suspended over a substrate (the lower electrode). When a voltage is applied between the beam and the substrate, electrostatic forces appear which force the beam to bend. When the applied voltage increases, the electrostatic forces become dominant and the plates stick together. The corresponding critical voltage is called the pull-in voltage. When the dynamic behaviour of the system is taken into account, it is shown that two new parameters have to be defined: the dynamic pull-in displacement and the dynamic pull-in time.

Keywords: Electro-Mechanical Coupling, Nonlinear, Finite Element Method, Micro-Electro-Mechanical Systems.

1. INTRODUCTION

To analyse the static and dynamic behaviour of electrostatically actuated Micro-Electro-Mechanical Systems (MEMS), the electromechanical coupling has to be accounted for. Since the electrostatic domain is influenced by the deformation of the structural components, the Finite Element discretisation of the electrostatic domain needs to be properly updated. The common approach is based on a staggered procedure, which consists on iterating between the mechanical domain and the electrostatic domain using separate software.[1] Boundary elements are also currently used in order to avoid moving mesh problems. Another approach consists in using predefined capacitance between structural nodes or applying structural reduction techniques together with finite difference evaluation of electrostatic coupling. However, such techniques cannot easily handle strong coupling effects in an accurate manner. In the present work, a fully coupled electro-mechanical formulation is proposed. The method provides fully consistent tangent stiffness matrices and allows static equilibrium positions to be found, to evaluate natural frequencies and to compute transient dynamic responses in a non-staggered way. An interesting application of the proposed method is the analysis of the dynamic behaviour of electrostatically actuated micro-bridges when a sudden voltage step is applied on the electrodes. The dynamic behaviour of this type of micro-systems is also studied by Nayfeh in Ref. [2] where an AC voltage is applied and by Dequesnes[3] for carbon nanotube based switches. In this paper it is shown that dynamic transients may lead to pull-in instabilities even though the applied voltage is smaller than the static pull-in voltage usually defined as design criterion and a characterisation of the dynamic pull-in voltage and the dynamic pull-in time is performed.

*Corresponding author; E-mail: V.Rochus@ulg.ac.be

 1546-198X/2006/4/206/008 doi:10.1166/sl.2006.017

2. ELECTRO-MECHANICAL COUPLING

In order to understand the physical phenomena of electro-mechanical coupling, the reference problem shown in Figure 1 is considered. It consists in a capacitor made of two parallel plates between which a voltage is applied. The upper plate is supported by a spring and the lower plate is grounded. This mass-spring model is representative of the mode of operation of electrostatically actuated MEMS devices.

For the sake of simplicity, the electrodes of the capacitor are considered as infinite planes and the electric charges are supposed to be evenly distributed on the surfaces. This approximation allows fringing fields to be neglected and to reduce the system to a one-dimensional problem. The capacitor is also considered to be in vacuum and no damping is considered in the model. The dynamic equilibrium equation of the system is:[4]

$$m\ddot{d} = -k(d - d_0) - \frac{1}{2}\varepsilon_0 \frac{V^2}{d^2} \tag{1}$$

where d is the distance between the two plates; m is the mass of the upper electrode; k is the spring stiffness and ε_0 is the permittivity of free space. It can be noted from the equation that the dynamic behaviour of the structure depends on the applied voltage V and on the initial gap between the plates d_0.

2.1. Static Pull-in Voltage

The static equilibrium equation of the system is the following:

$$k(d - d_0) + \frac{1}{2}\varepsilon_0 \frac{V^2}{d^2} = 0 \tag{2}$$

When the applied voltage increases, it creates an attraction force between the electrodes and the upper plate moves closer to the grounded plate. When the electrostatic forces in $1/d^2$ become dominant with respect to the mechanical force so that the plates stick together, a critical voltage is reached. This critical voltage is called the static pull-in voltage. The analytical expressions of the static pull-in voltage and of the corresponding pull-in distance are given in Ref. [4]:

$$V_{pi} = \sqrt{\frac{8}{27}\frac{kd_0^3}{\varepsilon_0}} \quad \text{and} \quad d_{pi} = \frac{2}{3}d_0 \tag{3}$$

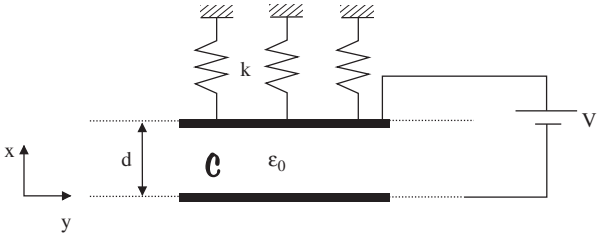

Fig. 1. Definition of the reference problem.

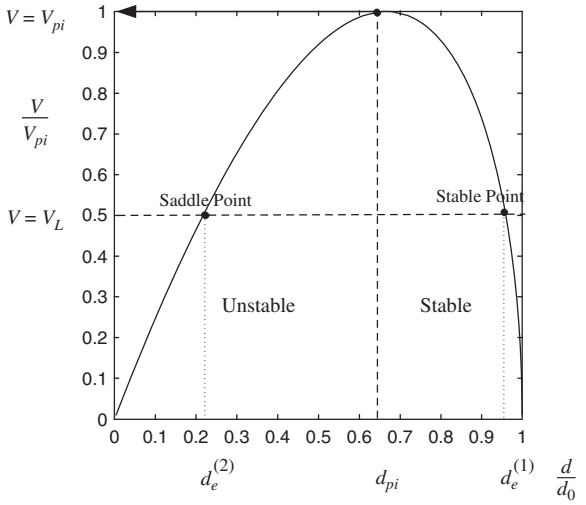

Fig. 2. Evolution of the normalized displacement with the normalized voltage.

When the applied voltage V is smaller than the pull-in voltage, two equilibrium positions exist: $d_e^{(1)}$ and $d_e^{(2)}$ as shown in Figure 2. When $V = Vpi$, the two equilibrium positions merge into one point (d_{pi}, V_{pi}). Beyond V_{pi}, no equilibrium position exists.

2.2. Dynamic Pull-in

The dynamic equilibrium equation may also be written in a non-dimensional form defining the following variables:

$$V^* = \frac{V}{V_{pi}} \quad d^* = \frac{d}{d_0}, \quad \omega_0^2 = \frac{k}{m} \tag{4}$$

The dynamic behaviour of the coupled system corresponding to different initial conditions are shown in the phase diagrams of Figures 3(a) to 3(d) (assuming $\omega_0 = 1$).

- (a): Phase diagram of the pure mechanical model. No voltage is applied, the system is stable.
- (b) and (c): a voltage $V < V_{pi}$ is applied. The system is stable near the equilibrium position and oscillates in a non-linear way. If the initial displacement is large enough, the moving plate can reach a position close to the fixed electrode so that the electrostatic forces become higher than the spring restoring force: the plates collapse on one another and stick together.
- (d): $V \geq V_{pi}$: For any initial condition, the system is unstable and the phase diagram diverges to two solutions: $d = 0$, $\dot{d} = \pm\infty$.

A second critical voltage is now defined. As stated in Ref. [4], when $V < V_{pi}$, a stable area may be observed in the phase diagram corresponding to the ellipsoid area in Figure 3(b). If we refer to the static pull-in definition, the system is stable. But if the dynamic behaviour is considered, the problem may become unstable. Indeed, if the system has enough energy to pass over a second characteristic point called the dynamic pull-in position, the

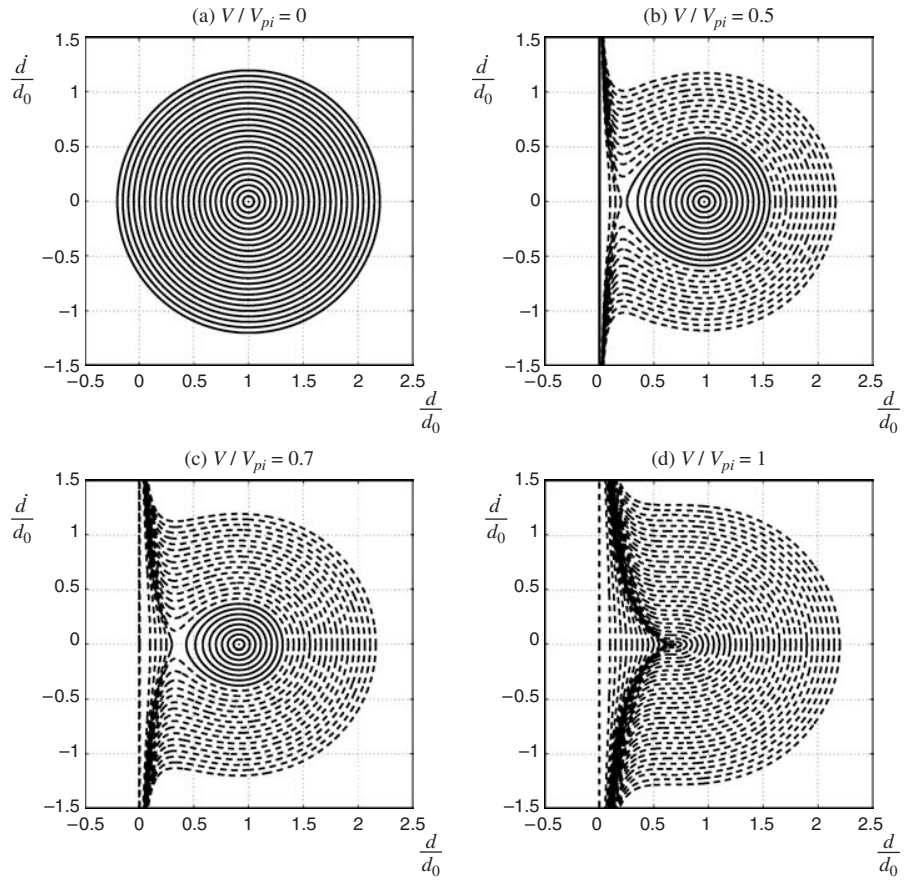

Fig. 3. Phase diagrams for different values of voltage.

system becomes unstable. The dynamic pull-in voltage is defined as the voltage for which the system becomes unstable when it is suddenly applied to the system at rest.

3. FINITE ELEMENT FORMULATION

To simulate electro-mechanically coupled systems, common software use weak coupling procedures in the sense that the electrostatic and the mechanical domains are discretised and treated iteratively in separate solvers. This basic iterative method is commonly presented in the literature (see e.g., Lee et al.[1]) In this paper, we propose a finite element formulation to solve the electrostatic and mechanical domains simultaneously in a strong coupled form. One of the advantages of this formulation is that the tangent stiffness matrix of the electro-mechanical problem can be explicitly constructed. Thus the natural frequency of the electro-mechanical system can be directly evaluated around a given equilibrium configuration and the transient dynamic response can be more easily computed.

The consistent way of deriving a finite element discretisation to model electro-mechanical coupling is using variational calculus. Starting from the energy of the coupled problem, nodal forces are obtained for an element by derivation of the energy. The tangent stiffness matrix of the coupled problem is then obtained by linearisation of the equilibrium equations in the vicinity of an equilibrium position (see in Ref. [4]):

$$\begin{pmatrix} \mathbf{K}_{uu}(\phi) & \mathbf{K}_{u\phi}(\phi) \\ \mathbf{K}_{\phi u}(\phi) & \mathbf{K}_{\phi\phi} \end{pmatrix} \begin{pmatrix} \Delta\mathbf{U} \\ \Delta\Phi \end{pmatrix} = \begin{pmatrix} \Delta\mathbf{f}_m \\ \Delta\mathbf{f}_e \end{pmatrix} \tag{5}$$

where subscripts u and ϕ refer respectively to the mechanical and electrostatic domains; $\Delta\mathbf{U}$ is the displacement vector and $\Delta\mathbf{f}_m$ is the vector of mechanical forces; $\Delta\Phi$ is the electric potential vector and $\Delta\mathbf{f}_e$ is the vector of electrostatic forces. It can be observed that the tangent stiffness matrix is symmetric and that coupling terms such as $\mathbf{K}_{u\phi}$ and $\mathbf{K}_{\phi u}$ appear between mechanical and electric degrees of freedom. It should be noted that the tangent stiffness matrix, unlike in the common approach, is not obtained by finite difference, but derives naturally from the variational approach and can be easily assembled using the finite element model. More details about the expression of the coupling matrix may be found in Ref. [4].

4. APPLICATION TO A MICRO-BRIDGE

The application of the proposed method is illustrated on the example of a beam-type micro-resonator composed of two electrodes: a clamped-clamped beam and a substrate

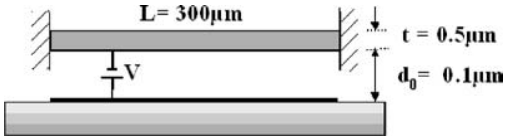

Fig. 4. Micro-Bridge.

as shown in Figure 4. The beam is made of silicon with a density of 2648.38 kg/m^3 and a Young's modulus of 77 GPa. Its length is 300 μm, its thickness is 0.5 μm and its width is about 10 μm. The initial gap d_0 between the electrodes is set to 0.1 μm. In that case, the displacements remain small so that linear structural deformation can be assumed. The only nonlinear effect comes from the electrostatic coupling. If d_0 is equal or bigger than 6 μm, geometrical nonlinear effect would be important as shown in Ref. [5]. In that case, the geometric nonlinearity induced by the mechanical displacement of the structure has to be taken into account in the formulation. For the sake of clarity, the small displacement assumption is considered in the following.

4.1. Finite Element Modelling

The system of Figure 4 is modelled using mechanical and electrostatic finite elements. The mechanical domain is discretised by non-compatible elements, which permits to take into account the bending of the beam.[6] The electrostatic domain is modelled using two types of elements: pure electrostatic elements for the surrounding environment of the beam and electro-mechanical coupling elements at the border with the beam. These coupling elements allow the mechanical structure to be loaded by the electrostatic forces. When the mechanical structure is displaced the mesh of the electrostatic domain is deformed. The method used to displace the nodes is to consider the electrostatic domain as a virtual structure which deforms under the action of the interface displacement.

4.2. Static Equilibrium

The static pull-in voltage is first computed by evaluating the static equilibrium position of the system when V is incremented. To this purpose, the classical Riks-Crisfields continuation technique is used to reach equilibrium positions in the unstable region.[4] The typical pull-in curve is plotted in Figure 5 where the voltage is given in function of the displacement at the middle of the beam. It is observed that the static pull-in voltage appears at 0.0397 Volt. For this particular example, the large displacement assumption would provide the same results.

4.3. Dynamic Behaviour

In this section, the transient dynamic response of the system is computed when the voltage is suddenly applied between

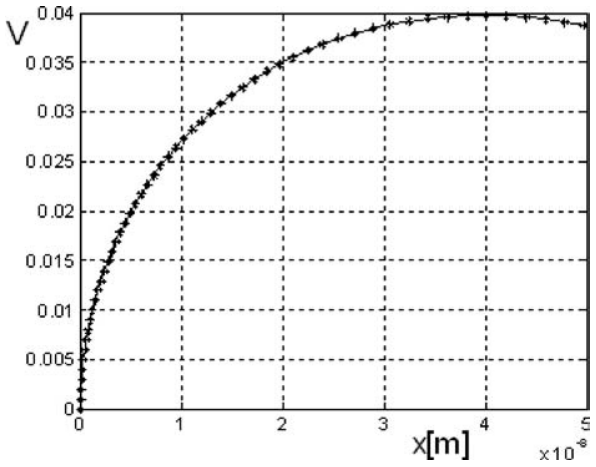

Fig. 5. Static Pull-in Voltage.

the two electrodes i.e., when the time-history of the voltage corresponds to a step function as illustrated in Figure 6.

The Newmark time-integration scheme has been used to calculate the time response of the system with a small numerical damping ($\alpha = 0.05$). The results obtained are depicted in the phase plot of Figure 7. Instability is observed for voltages higher than or equal to 0.0363 V. Thus the dynamic pull-in voltage may be defined as the voltage amplitude such that, when applied suddenly, it leads to the dynamical instability of the system. Another characteristic parameter of the system is the pull-in time, which is defined as the time needed for the plates to stick together when the pull-in voltage is applied. In this example, the difference between the static and the dynamic pull-in voltage is around 8.7% and the pull-in time is estimated to 20.7 μs.

4.4. Parametric Study

Approximate expressions are given in the literature for the static pull-in voltage of simple systems such as a clamped-clamped beam. They are very useful for the preliminary design of simple micro-systems. In the paper by Osterberg and Senturia,[7] an analytical formula is proposed to better match the experiment results:

$$V_{pi} = \sqrt{\frac{4\gamma_1 B}{\varepsilon_L^4 \gamma_2^2 [1 + \gamma_3 \frac{d_0}{b}]}} \tag{6}$$

with $\gamma_1 = 2.79$, $\gamma_2 = 0.97$, $\gamma_3 = 0.42$, and $B = Et^3 d_0^3$. The parameters γ_1, γ_2, and γ_3 were introduced in the formula

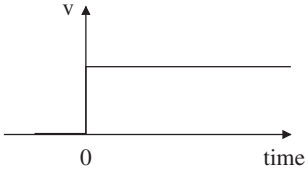

Fig. 6. Step of voltage.

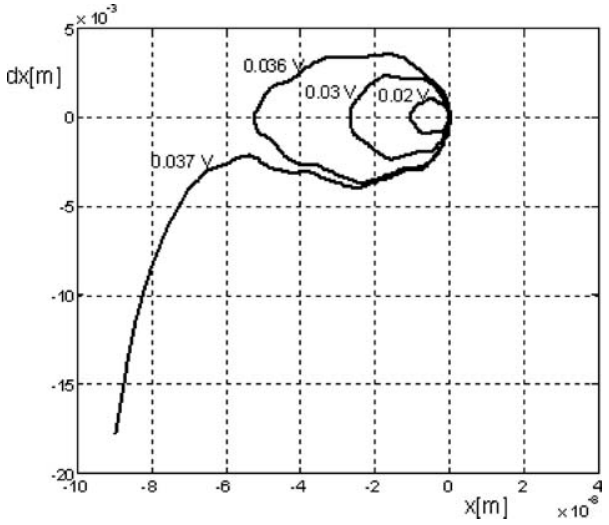

Fig. 7. Evolution of pull-in voltage with the thickness of the beam.

to fit the experiments. In the particular example considered here, the term $\gamma_3(d_0/b)$ is negligible.

The static pull-in voltage given by this semi-empirical formula is estimated to 0.0398 Volt, which is in very good agreement with our finite element simulation result. Regarding to the dynamic pull-in voltage, no analytical expression exists even for the one-dimensional problem. To build such relations for the dynamic pull-in voltage and the pull-in time, all the dimensions and structural parameters of the system have been modified independently in the following. The objective is to identify the dependency of the dynamic pull-in voltage and the pull-in time with the length L, the thickness t, the initial gap d_0, the Young's modulus E and the mass density ρ of the beam.

4.4.1. Variation of the Length of the Beam

Figure 8 shows the evolution of the static pull-in voltage (black points) and of the dynamic pull-in voltage (white

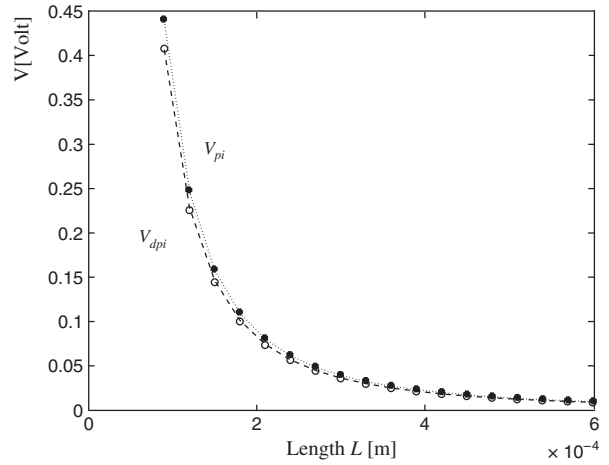

Fig. 8. Evolution of pull-in voltage with the length of the beam.

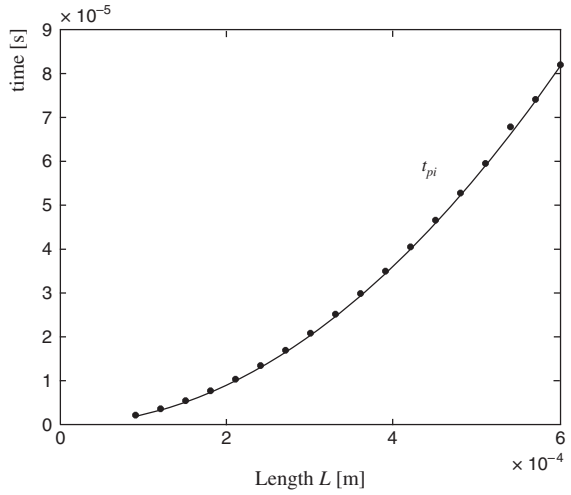

Fig. 9. Evolution of pull-in time with the length of the beam.

circles) with respect to the length of the beam. These results were obtained by finite element simulations. In the two cases, the pull-in voltages decrease when the length of the beam increases. The fitting of the results by the relation A_1/L^2 for the static pull-in voltage and by A_2/L^2 for the dynamic pull-in voltage gives the results: $A_1 = 3.57\ 10^{-9}$ V.m^2 and $A_2 = 3.3\ 10^{-9}$ V.m^2. Parameters A_1 and A_2 are very close and their difference does not provide any important information on the behaviour of the system. For this reason, they will not be considered in the following. The difference between the two pull-in voltages is about 8%.

The second dynamic parameter to fit is the pull-in time. The pull-in time is given in Figure 9 for different lengths of the beam. The black points are the Finite Element results. It is found to increase with the squared-length of the beam. The function used to fit the finite element results is BL^2 with $B = 228.37$ s/m^2.

4.4.2. Variation of the Thickness of the Beam

When the thickness t of the beam is varied from 0.1 μm to 1 μm, the pull-in voltage increases as shown in Figure 10. Indeed the increase of the thickness increases the stiffness of the structure so that it needs more voltage to bend it. It is found that both the static and the dynamic pull-in voltage are proportional to $t^{3/2}$. This relation is used to plot the dashed line and the dotted line which follows very well the finite element results in Figure 10. The evolution of the pull-in time with the thickness of the beam is plotted in Figure 11. It decreases when the thickness increases. The function used to fit the numerical results is inversely proportional to the thickness: $B\,(1/t)$.

4.4.3. Variation of the Initial Gap

In this subsection, the distance between the two electrodes is changed. That means that the structural behaviour of

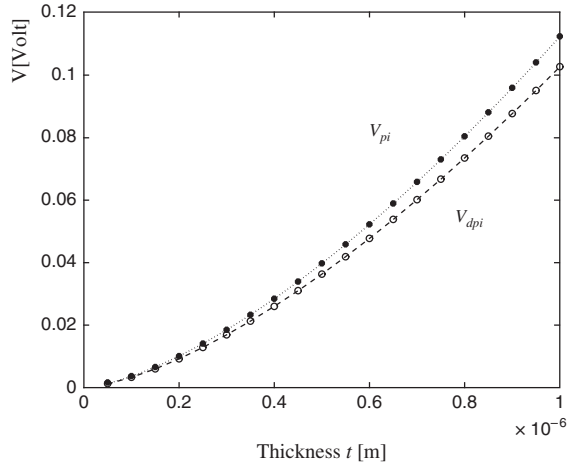

Fig. 10. Evolution of pull-in voltage with the thickness of the beam.

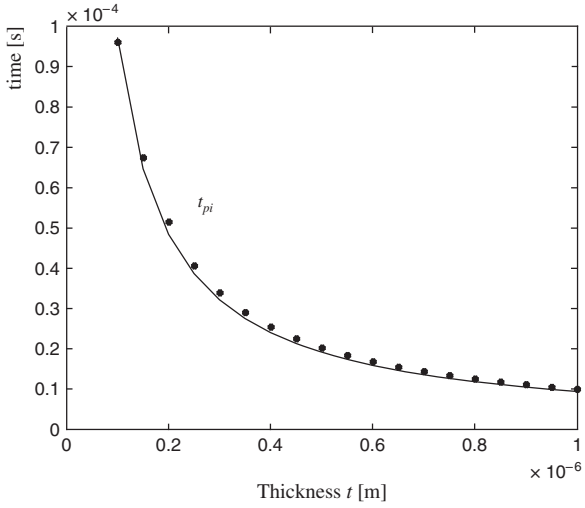

Fig. 11. Evolution of pull-in time with the thickness of the beam.

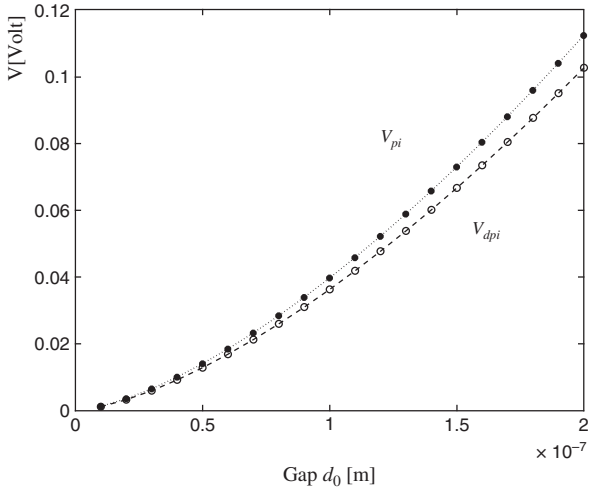

Fig. 12. Evolution of pull-in voltage with the gap between the electrodes.

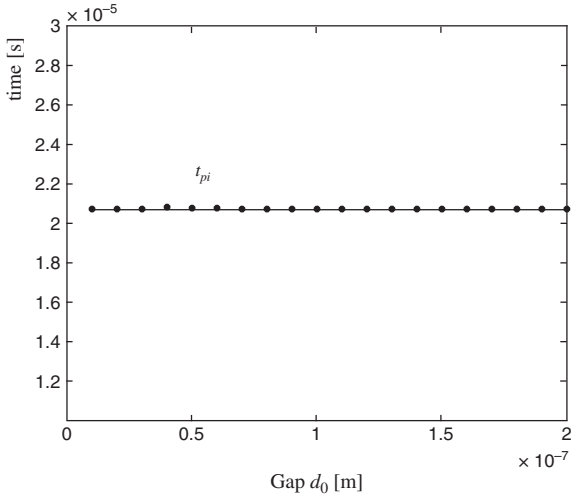

Fig. 13. Evolution of pull-in time with the gap between the electrodes.

the beam is not modified. Only the electrostatic forces are increased when the gap is reduced. The variations of the static and dynamic pull-in voltages with respect to the initial gap d_0 are shown in Figure 12. Both the static and the dynamic pull-in voltages are found to be proportional to $d_0^{3/2}$. When the gap is reduced the electrostatic forces are more important for the same structural stiffness. It needs then less voltage to achieve the pull-in voltage as shown in Figure 12. The plot in Figure 13 shows an important result: the pull-in time does not depend on the distance between the electrodes. Only the mechanical behaviour of the beam determines the value of the pull-in time.

4.4.4. Variation of Young's Modulus

In the two next subsections, the material characteristics of the beam are studied. The first one is the Young's modulus. It can be found easily that the static and dynamic pull-in voltages are proportional to $\sqrt{E}$ as shown in Figure 14 as already found in the one-dimensional analysis. When the Young's modulus increases, the stiffness of the structure increases and the pull-in voltages increases. Figure 15 shows that the pull-in time is proportional to $1/\sqrt{E}$.

4.4.5. Variation of the Mass Density

In Figure 16, it is observed that the static pull-in voltage as well as the dynamic pull-in voltage do not depend on the mass density of the beam. On one hand, in the case of the static pull-in voltage, it is understandable since this voltage is obtained from the static equilibrium equation. On the other hand, the dynamic pull-in voltage is obtained by a time-integration of the dynamic equilibrium equation for different values of voltage. Its independence with respect to the mass density is not expected. Figure 17 shows that the dynamic pull-in time increases when the mass density increases. It is proportional to $\sqrt{\rho}$.

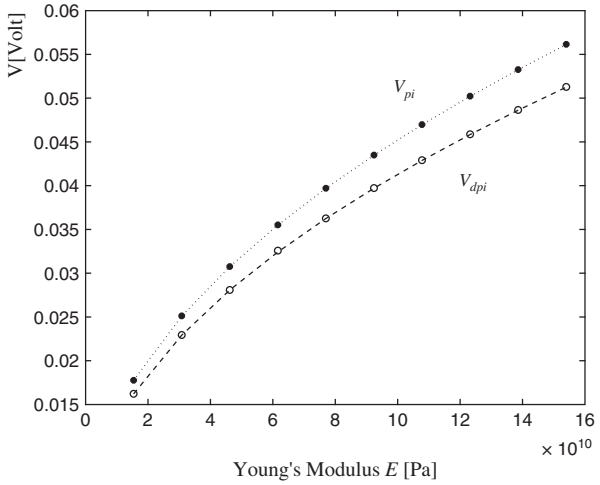

Fig. 14. Evolution of pull-in voltage with the Young's Modulus.

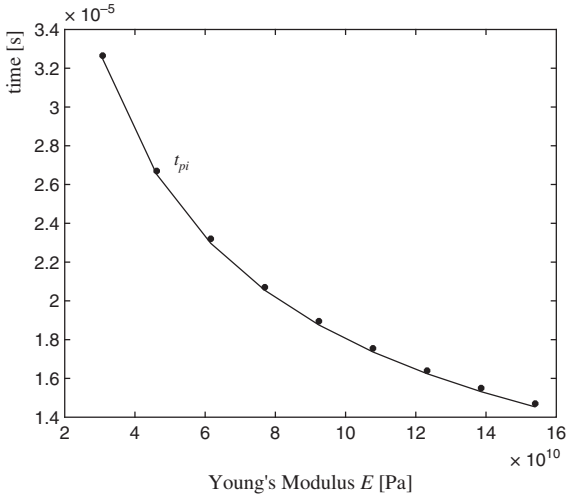

Fig. 15. Evolution of pull-in time with the Young's Modulus.

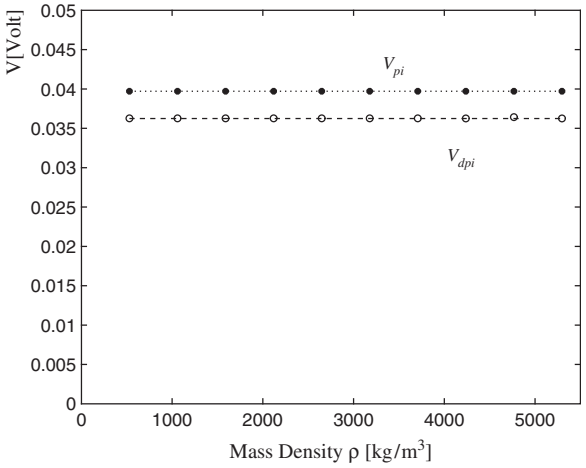

Fig. 16. Evolution of pull-in voltage with the mass density of the beam.

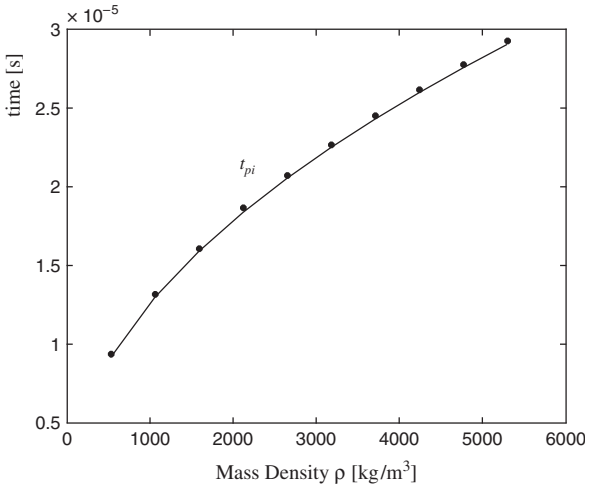

Fig. 17. Evolution of pull-in time with the mass density of the beam.

4.4.6. Variation of the Void Permittivity

On the graph of the evolution of the pull-in voltage with the permittivity presented in Figure 18 the pull-in voltages change as $1/\sqrt{\varepsilon}$. The pull-in time is totally independent of the permittivity as shown in Figure 19.

4.4.7. Discussions

The sensitivity of the static and dynamic pull-in voltages and of the pull-in time to all the parameters defining the micro-bridge was studied. By collecting all the results, expressions may be written for the pull-in voltages and pull-in time in the case of deep beams.

Static Pull-in Voltage:

$$V_{spi} = A_1\sqrt{\frac{Et^3d_0^3}{\varepsilon L^4}} \quad \text{with} \quad A_1 = 3.4196\ ([-]) \qquad (7)$$

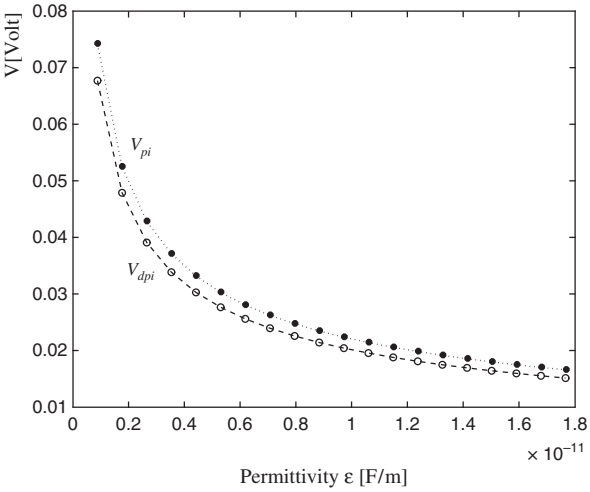

Fig. 18. Evolution of pull-in voltage with the permittivity.

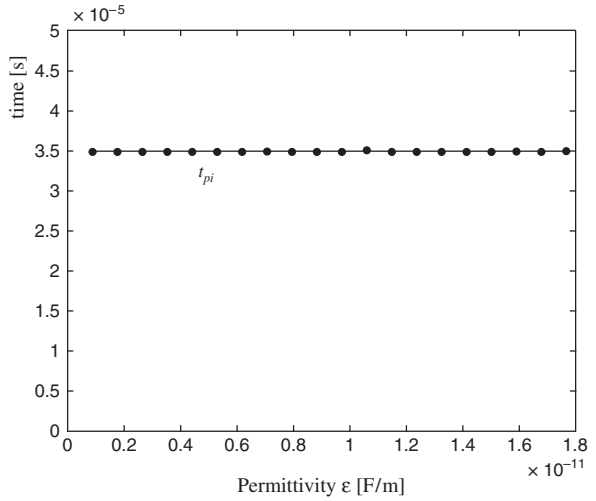

Fig. 19. Evolution of pull-in time with the permittivity.

Dynamic Pull-in Voltage:

$$V_{dpi} = A_2\sqrt{\frac{Et^3d_0^3}{\varepsilon L^4}} \quad \text{with} \quad A_2 = 3.152\ ([-]) \qquad (8)$$

Pull-in time:

$$t_{pi} = B\frac{L^2}{t}\sqrt{\frac{\rho}{E}} \quad \text{with} \quad B = 0.615\ ([\sqrt{m}]) \qquad (9)$$

The relation given here for the static pull-in voltage obtained here is very similar to the expression proposed in the first section. One remarkable result is the independence of the dynamic pull-in voltages with respect to the mass density and the independence of the pull-in time with respect to the distance between the electrodes.

5. CONCLUSIONS

The advantage of the methodology used in this paper compared to the common staggered approach found in commercial software is that the tangent stiffness matrix of the coupled problem is directly available. It permits to compute easily the static pull-in voltage with a good accuracy. It also allows the dynamic behaviour of the system to be simulated using time-integration algorithms. In a previous paper,[5] we have shown that there is a non-negligible difference between the static and the dynamic pull-in voltages. Here, some analytical expressions for the dynamic pull-in voltage and the pull-in time have been proposed. These expressions may be used for the design of electrostatically actuated micro-bridges.

Acknowledgments: The first author acknowledges the financial support of the Belgian National Fund for Scientific Research. Part of the work presented in this text is supported by the Communauté Française de Belgique—Direction Générale de la Recherche Scientifique in the framework Actions de Recherche Concertées (convention ARC 03/08-298). The second author acknowledges the financial support of the Koiter Institute form the Delft University of Technology, The Netherlands.

References and Notes

1. W. S. Lee, K. C. Kwon, B. K. Kim, J. H. Cho, and S. K. Young, *Journal of Modeling and Simulation of Micro-systems* 2, 83 **(2001)**.
2. A. H. Nayfeh and M. I. Younis, *Journal of Micromechanics and Microengineering*, 15, 1840 **(2005)**.
3. M. Dequesnes, Z. Tang, and N. R. Aluru, *Journal of Engineering Materials and Technology—Transactions of the ASME* 126, 230 **(2004)**.
4. V. Rochus, D. J. Rixen, and J. C. Golinval, *International Journal for Numerical Methods in Engineering*, (submitted to).
5. V. Rochus, D. J. Rixen, and J. C. Golinval, Electrostatic Coupling of MEMs Structures: Transient Simulations and Dynamic Pull-in. *The 2004 Workshop on Coupled Problems, Processes, and Phenomena: Modelling, Control, and Analysis*, Orlando **(2004)**.
6. O. C. Zienkiewicz, The Finite Element Method. *IE* **(1977)**, pp. 272–276.
7. P. M. Osterberg and Stephen D. Senturia, M-Test: A test Chip for Mems Material Property Measurement Using Electrostatically Actuated Test Structures. *IEEE*, **(1997)**, Vol. 6, pp. 107–118.